UNIVERSITAT POLITÈCNICA DE CATALUNYA

Programa de Doctorat:

AUTOMATITZACIÓ AVANÇADA I ROBÒTICA

PhD Dissertation

Energy Efficient Control of Electrostatically Actuated MEMS

Andreu Fargas Marquès

Director: Ramon Costa Castelló

November 2015

To my wife, Raquel, and my daughters, that have been patient all these years.

And to my Advisor, Ramon, without whom this wouldn't have been possible.

Acknowledgments

I would like to take this chance to express my deep thanks and appreciation to my Advisor Professor Ramon Costa-Castelló for his support and patience during all these years. Since his advise in my bachelor final project, our careers have crossed several times to finally produce this dissertation. I have been pleased to know him and enjoyed greatly his friendship.

This work wouldn't have been possible either without the help of my former Advisor, Professor Andrei Shkel. I was fortunate to share the beginning of his career as Professor in the University of California, Irvine and to have him as my Master Thesis advisor. He made me discover the world of MEMS. And thanks to his help and support, the results of this dissertation have reached the MEMS community. Moreover, he is the founder of the Microsystems Lab, where I met wonderful people that has helped me during my research on the MEMS field. Chris Painter, Cenk Acar, Adam Schofield and Alex Trusov all of them have helped at some point to make this work possible.

And finally, I also want to thank Professor Jasmina Casals-Terré. We met in the Microsystems Lab long time ago, and during all these years of research she has helped me in the pursuit of obtaining test results for my dissertation.

Contents

Nomenclature v

1 Introduction 1

1.1 Research motivation . . . 1

1.2 Problem description . . . 2

1.2.1 Designing a MEMS parallel-plate electrostatic actuator/sensor . . . 2

1.2.2 Simplified actuator model . . . 4

1.2.3 The pull-in limitation . . . 5

1.3 Research objective . . . 6

1.4 Dissertation outline . . . 7

2 Electrostatically actuated MEMS resonator model 9

2.1 Distributed parameters model formulation . . . 9

2.1.1 Mechanical model . . . 9

2.1.2 Electrostatic actuation . . . 12

2.1.3 Damping in MEMS . . . 15

2.1.4 Lumped system . . . 21

2.2 Evolution in MEMS modeling . . . 22

2.3 Concentrated parameters model formulation . . . 29

2.4 Conclusions . . . 32

3 Pull-in analysis in MEMS resonators 35

3.1 Introduction . . . 35

3.2 Static Pull-in case . . . 36

3.3 Dynamic Pull-in case . . . 39

3.4 Oscillatory Pull-in case . . . 42

3.4.1 Resonant Pull-in case . . . 42

3.4.2 Resonant Pull-in Condition 44
3.4.3 Experimental validation 47
3.5 Conclusions 51

4 Oscillation characterization of MEMS resonators 53
4.1 Introduction 53
4.2 Simulation characterization 53
4.2.1 Time response of the system 55
4.2.2 Phase-plot and energy evolution 59
4.2.3 Frequency response 62
4.2.4 Stability and Pull-in analysis 66
4.2.5 Analysis conclusions 71
4.3 Harmonic Balance characterization 73
4.3.1 Series expansion of system equations 73
4.3.2 Cases of study 75
4.3.3 Approach validation 78
4.4 Driving voltage characterization 84
4.4.1 Voltage types 84
4.4.2 Actuation error 89
4.5 Driving voltage analysis 93
4.5.1 Number of harmonics 94
4.5.2 Voltage magnitude 97
4.5.3 Energy consumption 101
4.5.4 Stability 107
4.6 Conclusions 109

5 Control of electrostatically actuated MEMS 111
5.1 A survey of prior work on MEMS control 111
5.1.1 MEMS oriented control strategies 111
5.1.2 Classical control strategies 116
5.1.3 Classical nonlinear control strategies 117
5.1.4 New nonlinear control strategies 120
5.2 Thesis proposed strategies 121

5.2.1 Proposed controller 122
5.2.2 Robust control strategy 123
5.2.3 Internal-Model-Principle based control strategy 124
5.2.4 Extremum seeking control strategy 126
5.2.5 Conclusion 127

6 Control architecture design 129

6.1 Introduction 129
6.2 System reformulation for control 129
6.2.1 System linearization 130
6.3 Robust control strategy 131
6.3.1 System uncertainties 131
6.3.2 H_∞ robust control 134
6.3.3 μ-analysis 136
6.4 Internal-Model-Principle based control strategy 143
6.4.1 Resonant control 144
6.5 Extremum seeking control strategy 152
6.5.1 Energy calculation 153
6.5.2 Extremum seeking controller 155
6.5.3 Convergence analysis 158
6.6 Conclusion 160

7 Verification of control strategy 161

7.1 Introduction 161
7.2 System performance 161
7.2.1 Stability 162
7.2.2 Robustness 169
7.2.3 Sinus-like oscillation 171
7.2.4 Minimum energy 174
7.2.5 Conclusion 179
7.3 Improvement of MEMS drive and sense for control applications 179
7.3.1 Full range oscillation 180
7.3.2 Full position feedback 183

7.4 Proposed laboratory testing . . . 192
7.4.1 MEMS resonator design . . . 193
7.4.2 Laboratory test set-up . . . 195

8 Conclusions **199**
8.1 Contributions of the dissertation . . . 200
8.2 Publications in the field . . . 202
8.3 Future work . . . 203

A Harmonic Balance formulations **231**
A.1 Linear case - second harmonic . . . 231
A.2 Nonlinear case - second harmonic . . . 232

Nomenclature

Constants

η Viscosity of the fluid

η_{eff} Corrected viscosity of the fluid, accounting for rarefication effects

λ Mean free path of a fluid molecule

ν Poisson's ratio of the transverse contraction of a beam when axially stretched

ρ Density of beam material

E Young Modulus of the material of beams

E′ Extended Young Modulus of the material for a wide microbeam, E' $= \mathrm{E}/(1-\nu^2)$

g Gravity acceleration

K_n Knudsen number, $\mathrm{K}_n = \lambda/\mathrm{g}_{sq}$

ε Permittivity constant of the dielectric element between the plates in non free space

ε_0 Permittivity constant of the dielectric element between the plates in free space

Parameters

ω_{sq} Cut-off squeeze film damping frequency

σ_d Squeeze number for squeeze film damping

α_{f} Normalized stretching force parameter, $\alpha_{\mathrm{f}} = 6\left(\frac{\mathrm{g}_0}{\mathrm{h}}\right)^2$

β Nonlinear spring factor of a beam, $\beta = \mathrm{K}/(\mathrm{K}_3\,\mathrm{g}_0^2)$

ϵ Aspect ratio comparing the gap size to beam length, $\epsilon = \frac{\mathrm{g}_0}{\mathrm{L}}$

κ Non-dimensional cubic nonlinear mechanical spring constant, $\kappa = \frac{\mathrm{K}_3\mathrm{g}_0^2}{\mathrm{M}}$

ω_{n} Natural frequency of the system, $\omega_{\mathrm{n}}^2 = \frac{\mathrm{K}}{\mathrm{M}}$

ω_d Desired or set-point frequency for the system

A	Area of the cross-section of a beam, $\mathrm{A} = \mathrm{b} \cdot \mathrm{h}$
a_b	Aspect ratio of the beam comparing length and width, $a_b = \frac{L}{b}$
A_c	Area of the capacitor plates
A_{ov}	Area of overlap between two opposite plates
B	Damping force parameter
b	Width of the section of a beam
C	Driving capacitance in non-free space, $C = \frac{\varepsilon A_c}{g_0}$
C_0	Driving capacitance in free space, $C_0 = \frac{\varepsilon_0 A_c}{g_0}$
C_n	Fringing field capacitance correction parameter
C_p	Capacitance of parasitics coupling between input and output of MEMS resonator
C_s	Capacitance of the sensing capacitor
DPV	Dynamic pull-in voltage
f_k	Electrostatic force normalized constant, $f_k = \frac{C_0}{2g_0}$
g_0	Gap between the capacitor plates at non-load conditions
g_s	Gap between the capacitor plates in sensing combs
g_{cou}	Gap between the plates that suffer couette flow
g_k	Inertia normalized constant, $g_k = \frac{1}{g_0 M}$
g_{sq}	Static gap between the plates that suffer squeeze film damping
h	Height of the section of a beam
I	Moment of inertia of the cross-section of a beam ($I = bh^3/12$)
K	Linear mechanical spring constant of the system
K_3	Cubic nonlinear mechanical spring constant
L	Longitude of a beam
L_{ov}	Longitude of beam overlap in lateral comb fingers
M	Moving mass of the system
N_l	Number of lateral comb fingers sensing pairs
N_p	Number of parallel-plate sensing fingers pairs

Q Quality factor, $\mathrm{Q} = \frac{1}{2\zeta} = \frac{\omega_{\mathrm{n}}\mathrm{M}}{\mathrm{B}}$

RPC Resonant pull-in condition

R_{amp} Resistance used in the transimpedance amplifier

R_{vs} Resistance associated to the voltage source and the actuation wiring

SPV Static pull-in voltage

T Time constant, $\mathrm{T} = (\rho \mathrm{A}\ \mathrm{L}^4/(\mathrm{E'}\ \mathrm{I}))^{1/2}$

$\mathrm{V_{AC}}$ Magnitude of the alternating voltage applied between the capacitor plates. In sinusoidal actuation, magnitude of the first harmonic

$\mathrm{V_{DC}}$ Constant voltage load applied between the capacitor plates

ϑ Aspect ratio between gap and beam width, $\vartheta = \mathrm{g}_0/\mathrm{b}$

ζ Damping constant of the system

f_{n} Natural frequency for the system (Hz), $f_n = \frac{\omega_{\mathrm{n}}}{2\pi}$

f_d Desired or set-point frequency for the system (Hz), $f_d = \frac{\omega_d}{2\pi}$

Variables

$\breve{G}_n$ Non-dimensional n-harmonic Fourier series amplitude in exponential form, $\breve{G}_n = \frac{G_n}{2j}\, e^{j\, n\, \phi_n}\ \ n = 1..\infty$

δ Variable uncertainty

$\hat{\phi}_i(\hat{x})$ Position-dependent modal shape for the oscillation mode i

$\hat{\psi}$ Electrostatic potential field between the plates of the capacitor

$\hat{g}(\hat{t})$ Gap between the capacitor plates

$\hat{N}(\hat{t})$ Axial force in a beam

$\hat{q}_i(\hat{t})$ Time-dependent modal displacement for the oscillation mode i

$\hat{t}$ Time

$\hat{w}(\hat{t})$ Displacement of the center of the moving capacitor plate from the static position g_0 (y-direction)

$\hat{w}(\hat{x}, \hat{t})$ Displacement of a beam from the static position g_0, depending on the beam point

$\hat{x}$ X direction component of the movement (length of the beam)

$\hat{y}$ Y direction component of the movement (oscillation of the beam)

$\hat{z}$ Z direction component of the movement (width of the beam)

ψ Non-dimensional electrostatic potential field between the plates of the capacitor, $\psi = \frac{\hat{\psi}}{V}$

ρ_m Mass-density of the fluid that surrounds the device

τ Shear stress in a fluid

E Total energy of the system

F_d Damping force in the system

F_e Electrostatic force in the system

F_{int} Internal axial force due to stretching in a beam

g Non-dimensional gap between the plates of the capacitor, $g = 1 - y = \frac{\mathrm{g}_0 - \hat{y}}{\mathrm{g}_0}$

G_0 Non-dimensional gap static bias

G_1 Non-dimensional first harmonic oscillation amplitude

G_n Non-dimensional n-harmonic oscillation amplitude

g_1, g_2 Normalized gap between the driving capacitor plates of the two-sided actuator

I_s Current generated by the movement of the plates of the sensing capacitor

I_{vs} Current generated between the voltage source and the driving capacitor

L Energy Lagrangian of the system

N Normalized axial force in a beam, $N = \frac{\hat{N}\mathrm{L}^2}{\mathrm{E'I}}$

P Pressure of the fluid

P_a Static pressure of the fluid

Q Charge stored between the plates of a capacitor

Q_s Charge stored between the plates of the sensing capacitor

T Kinetic energy of the system

t Non-dimensional time, $t = \frac{\hat{t}}{\mathrm{T}}$

U Potential energy of the system

U_e Electrostatics potential energy

U_k Spring potential energy

U_{def} Potential energy of the lateral deformation of a beam

U_{int} Potential energy associated to the internal deformation of a beam

V Total voltage applied between the driving capacitor plates. Also $V(t)$ or V_d. In most cases, $V(t) = \mathrm{V_{DC}} + V_{AC}(t)$

V_+^2 Positive valued part of V^2: $V_+^2 = V^2$ if $V^2 > 0$ and $V_+^2 = 0$ if $V^2 \leq 0$

V_-^2 Absolute value of the negative valued part of V^2: $V_-^2 = -V^2$ if $V^2 < 0$ and $V_-^2 = 0$ if $V^2 \geq 0$

V_0 Fixed voltage applied at the input, also indicated as $V_0 = \mathrm{V_{DC}}$

V_1 First harmonic input voltage amplitude. If the input is a pure sinusoidal, $V_1 = \mathrm{V_{AC}}$

V_n n-harmonic input voltage amplitude

V_s Voltage applied between the plates of the sensing capacitor

$V_{AC}(t)$ Alternating voltage applied between the capacitor plates

V_{d1}, V_{d2} Total voltage applied between the driving capacitor plates of the two-sided actuator

V_{vs} Voltage generated by the voltage source to charge and discharge the driving capacitor

W Work generated for the non-conservative forces of the system

$w(t)$ Normalized displacement ($\hat{w}/\mathrm{g_0}$) of the moving capacitor plate (y-direction)

w_k Non-dimensional frequency, $w_k = \frac{\omega}{\omega_\mathrm{n}}$

x Non-dimensional X direction component of the movement, ($\hat{x}$/L)

y Non-dimensional Y direction component of the movement, ($\hat{y}/\mathrm{g_0}$)

z Non-dimensional Z direction component of the movement, ($\hat{z}$/b)

Vectors

$\hat{\mathbf{e}}$ Electrostatic vector field, $\hat{\mathbf{e}} = -\nabla\hat{\psi}$

$\mathbf{a}$ Vector example, $\mathbf{a} = \begin{pmatrix} a_1 \\ a_2 \end{pmatrix}$

$\mathbf{e}$ Normalized Electrostatic vector field, $\mathbf{e} = -\nabla\psi$

$\mathbf{v}$ Velocity of the fluid, $\mathbf{v} = \begin{pmatrix} v_x \\ v_y \end{pmatrix}$

$\mathbf{v}_{cou}$ Velocity of the fluid in couette flow

Matrices

Δ Uncertainty matrix

$\mathbf{A}$ Matrix example, $\mathbf{A} = \begin{pmatrix} a_{11} & a_{12} \\ a_{21} & a_{22} \end{pmatrix}$

Functions

$\bar{\sigma}$ Matrix singular value

$\frac{\partial}{\partial x}$ Partial derivative

$\frac{d}{dt}$ Time derivative

$\int_v$ Volume integral

μ_Δ Structured singular value of uncertainty

∇ Gradient operator

∇^2 Laplacian operator, $\nabla^2 \equiv \frac{\partial}{\partial \hat{x}} + \frac{\partial}{\partial \hat{y}} + \frac{\partial}{\partial \hat{z}}$

Chapter 1

Introduction

1.1 Research motivation

The field of Micro-Electro-Mechanical Systems (MEMS) has undergone a startling revolution in the last twenty years. It is now possible to produce accelerometers less than one millimeter long, functioning motors that can only be seen with the aid of a microscope, gears smaller than a human hair, and needles so tiny they can deliver an injection without stimulating nerve cells. However, important challenges are still to be solved.

Lots of MEMS devices are actuated using electrostatic forces, and specially, parallel-plate actuators are extensively used. Building a capacitor with the existing MEMS fabrication methods is straightforward. One must put together two parallel surfaces and then apply a potential difference between the two parts. If one of the two sides of the capacitor is attached to a movable system, we obtain a parallel-plate electrostatic actuator (Figure 1.1). At the same time, these same parallel-plate capacitors can be used for sensing movement, detecting the current that runs through them.

Nevertheless, the electrostatic actuation has some limitations due to the non-linearity of the generated force. This force is directly proportional to the square of the applied voltage and inversely proportional to the square of gap between the capacitor plates.

Consequently, as the potential difference between the plates is increased, the attraction force between the plates increases. This force translates to motion of the moving plate and gap reduction. Due to the dependence of the force on the gap distance, this gap reduction also generates an increment in the generated force. This non-linearity leads to the fact that at some point the restoring mechanical forces of the system cannot balance the electrostatic force anymore. Once reached this state, the electrodes will snap one

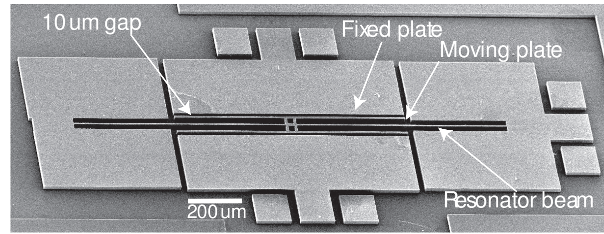

Figure 1.1: A beam MEMS resonator with parallel-plate electrostatic actuation and sensing. This MEMS resonator has been designed, fabricated and tested by the author. Fabrication was carried out by the *Centro Nacional de Microelectrònica - Barcelona*. The device has been used to experimentally verify the *Resonant Pull-in Condition* [62].

against the other, and in most cases, the system would be permanently disabled. This actuation instability phenomenon is known as *pull-in*, and the associated critical voltage is called the Pull-in Voltage.

The non-linear force implications are even more complex in oscillating systems like resonant accelerometers or gyroscopes. Apart from the pull-in instability, the non-linearity influences the pattern of the oscillation, becoming not symmetric. To solve both problems, MEMS systems are usually oscillated with low amplitudes.

Added problems appear with the sensing of the movement. Parallel-plate capacitors are also used, and although movement is proportional to capacitance variation, parasitics interfere with the read-out. Consequently, if the system is oscillated with low amplitude, this translates to reduced sensitivity/performance.

The dissertation studies the electrostatic non-linearities in the case of oscillating devices, extending the previous approaches that concentrate on static or positioning applications. The goal is to model and analyze the oscillatory behavior of MEMS devices, in order to provide a suitable control law to obtain stable sinus-like oscillations of the full gap amplitude with the minimum required energy, and consequently, improving MEMS sensors sensitivity and performance.

1.2 Problem description

1.2.1 Designing a MEMS parallel-plate electrostatic actuator/sensor

A basic building block of any electrostatically driven device is a microbeam. It forms one side of a variable capacity air-gap capacitor. Opposite to the microbeam lays the driving electrode that completes the capacitor. If a voltage difference is applied between

the capacitor plates, a force is generated on the beam that deflects under this action. Examples of the typical configurations are shown in Figure 1.2.

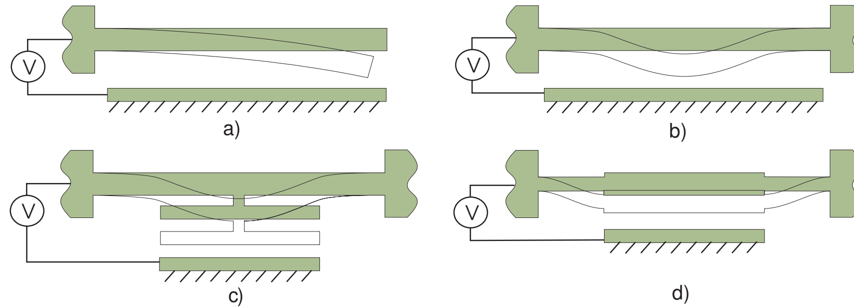

Figure 1.2: Basic MEMS capacitor configurations a) Free-end beam. The gap, and consequently the force, is not uniform. Maximum bending at the end of the beam. b) Clamped-clamped beam. The beam bends forming a not uniform gap. The force is variable depending on position. Maximum bending at the center of the beam. c) Clamped-clamped beam. A parallel plate is added to maintain the capacitor gap uniform. Maximum bending is at the center which defines the capacitor gap. d) Guided-end beam. Gap and force are uniform. Maximum bending at the extremum of both suspension-beams.

The voltage applied between the capacitor plates will depend on the application where the actuator is used. When the goal is positioning the beam, a constant electric load is applied to the electrodes. Depending on the DC polarization, a permanent displacement of the beam is achieved. Positioning optical switches, adjusting elements or acting micro-grippers are typical applications.

When the objective is closing the gap between the capacitor plates, as in relays, micro-switches or valves; DC polarization is, also, usually applied. In these cases, full displacement of the electrode is sought.

Finally, when permanent oscillation is necessary for the application, DC polarization is complemented with an AC signal to excite harmonic motion. This is the case of resonant pressure sensors, accelerometers or gyroscopes.

The same configurations can be used to sense the plate movement. If a constant voltage load is applied between the capacitor plates, the movement of the plate translates to capacitance variation. This capacitance variation can be sensed as a current moving through the capacitor [200].

1.2.2 Simplified actuator model

To study the behavior of the devices, a simplified lumped mass-spring system model of a MEMS device with a parallel plate actuator can be used (Figure 1.3). Using this model, the energy of the electro-mechanical system is

$$T = \frac{1}{2}\mathrm{M}\ \dot{\hat{w}}^2;\ U_k = \frac{1}{2}\mathrm{K}\ \hat{w}^2;\ U_e = -\frac{1}{2}\frac{\varepsilon_0\,\mathrm{A}_c}{(\mathrm{g}_0 - \hat{w})}V^2 \tag{1.1}$$

$$E = T + U_k + U_e \tag{1.2}$$

where $\hat{w}$ is the displacement of the moving plate from its initial equilibrium, T is the kinetic energy of the plate, U_k is the potential energy stored in the spring, U_e is the potential energy stored in the parallel-plate capacitor, and E is the energy of the whole system. And from electrostatics, ε_0 is the dielectric constant, g_0 is the designed static gap between the plates, A_c is the area of the plates and V is the applied voltage between the electrodes

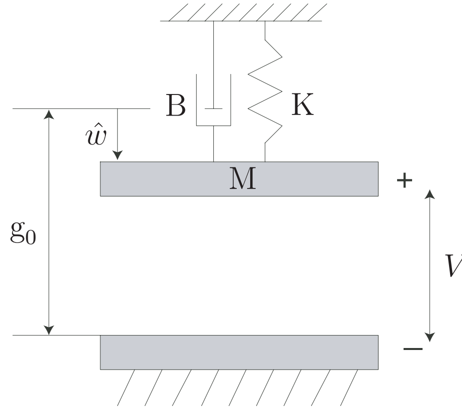

Figure 1.3: Scheme of a parallel plate actuator coupled to a mass-spring-damper system.

The dynamics of the system is derived using Lagrange's formulation, being $L = T - U_k - U_e$ the Lagrangian of the system, and introducing the damping force, $F_d = -\mathrm{B}\ \dot{\hat{w}}$ as the only contributing force to the work (W) of the system

$$\mathrm{M}\ \ddot{\hat{w}} + \mathrm{K}\ \hat{w} - \frac{1}{2}\frac{\varepsilon_0\,\mathrm{A}_c}{(\mathrm{g}_0 - \hat{w})^2}V^2 = -\mathrm{B}\ \dot{\hat{w}}. \tag{1.3}$$

This equation is the usual mass-spring-damper equation of dynamics, with an electrostatic force.

1.2.3 The pull-in limitation

The use of a parallel-plate electrostatic actuator with voltage control impose some limitations to the actuation of the device. From equation (1.3) it can be observed that the force generated between the parallel plates takes the following form

$$F_e = \frac{1}{2} \frac{\varepsilon_0 \, \mathrm{A}_c}{(\mathrm{g}_0 - \hat{w})^2} V^2. \tag{1.4}$$

This implies that the electrostatic force is inversely proportional to the gap between the plates of the actuator. As the gap decreases, the generated attractive force increases quadratically. The only opposing force to the electrostatic loading is the mechanical restoring force (K).

Consequently, if the voltage is increased, the gap decreases generating an incremented force. At some point the mechanical forces defined by the spring cannot balance this force anymore. Once reached this state, the electrodes will snap one against the other, and in most cases, the system would be permanently disabled.

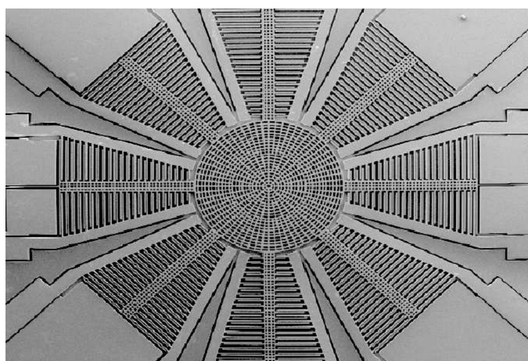

Figure 1.4: Angle gyro designed and patented by the Microsystems Lab, University of California, Irvine [147]. Due to its design, only parallel-plate electrostatic actuation and sensing can be used to drive the system to resonance and detecting the precession of the oscillation.

The electrostatic loading has an upper limit beyond which the mechanical force can no longer resist the opposing electrostatic force, thereby leading to the collapse of the structure. This actuation instability phenomenon is known as pull-in, and the associated critical voltage is called the *Pull-in Voltage*.

In positioning applications, reaching to the *Pull-in Voltage* must be avoided. In switching applications, the *Pull-in Voltage* must be reached in order to force the change of state.

The problem associated with the pull-in phenomena is the limitation of the region between

the plates that can be reached without leading to snapping of the device. In positioning applications, it implies that the device can only be moved up to 1/3 of the gap [96].
And in oscillating devices, as it would be a resonant angle-gyroscope as the one in Figure 1.4, the amplitude of oscillation is also limited, imposing restrictions on the sensor output and sensitivity.

1.3 Research objective

The main objective of the dissertation is to understand the behavior of electrostatically actuated MEMS resonators to develop a control algorithm that would overcome the nonlinearity of parallel-plate electrostatic actuation to achieve the most energy efficient sinus-like performance.
Due to their intrinsic nonlinearities, the use of the parallel-plate electrostatic actuators is usually restricted to low amplitudes. However, MEMS resonators need large robust sinus-like oscillations to reach high grade applications. Improvements on the actual behavior would foster the desired expansion of its use in MEMS resonators.
To reach this objective, the first step is the characterization of parallel-plate electrostatically actuated MEMS, including dynamic pull-in analysis and steady-state oscillatory motion.
Several issues exist in MEMS resonators and must be characterized. In oscillating applications regions of instability appear. They define the maximum combination of DC and AC voltages that can be used, and limit the maximum amplitude of oscillation that can be reached.
Oscillations are greatly influenced by MEMS fabrication imperfections, affecting their robustness. And the nonlinear forces generate oscillations of the MEMS resonator that are not purely sinusoidal what can interfere with the output of the system or excite undesirable modes.
All these problems lead to the necessity of applying control techniques to reach high performance in electrostatically actuated MEMS resonators. But the chosen technique must be energy efficient in order to be readily implementable in real MEMS devices.
This sets four main goals that must be accomplished by the new control algorithm:

1. Stable oscillation with large amplitudes of motion.

2. Robust oscillation independently of MEMS imperfections.

3. Pure sinus-like oscillation.

4. Low energy consumption.

1.4 Dissertation outline

The first part of the Dissertation studies the characterization of parallel-plate electrostatically actuated MEMS resonators, including steady-state characterization of oscillatory motion and dynamic pull-in analysis. This characterization is used to define the control specifications for oscillatory motion.

In Chapter 2, the modeling of the electromechanical lumped system is analyzed beginning with the distributed parameters. This model includes the main characteristics that can be found in a large number of MEMS devices which rely on electrostatic actuation. Complete formulation of the electrostatically actuated MEMS resonator is presented. After that, analysis of the approaches to simplify the ideal model are presented. This leads to formulate the concentrated parameters simplification that will be used all through the dissertation.

In Chapter 3, energy-based analysis of the pull-in instability is performed. The classic approach is revisited to extend the results to the model with nonlinear springs. Analysis of the effect of dynamics is studied as an important factor affecting the stability of the system. From this study, the *Resonant Pull-in Condition* for electrostatically actuated MEMS resonators is defined and experimentally validated.

In Chapter 4, the dynamic analysis of the system is extended in order to characterize the main behaviors that intervene in the steady-state oscillations of an electrostatically actuated MEMS resonator. This analysis is the basis of the election of Harmonic Balance as a tool to characterize the steady-state oscillation of the MEMS resonators. Harmonic Balance characterization leads to the understanding of the key factors that determine a stable and large oscillation of the MEMS resonator. Based on these results, the desired controller specifications are defined.

The second part of the Dissertation concentrates on control design. Once, the desired performance has been selected, control strategy selection, design and verification are developed.

In Chapter 5, a survey of prior work on MEMS control confirms that existing control approaches cannot provide the desired performance. Consequently, in order to satisfy

the performance goals and obtain the desired oscillation with the expected stability and energy efficiency, a three-stage controller is proposed.

In Chapter 6, the proposed controller is analytically designed and its parameters tuned. The controller has three different loops: a robust control loop, a resonant control loop and an extremum seeking control loop. Each controller loop is designed, analyzed and verified individually in order to obtain the desired performance.

In Chapter 7, the verification of the complete controller is accomplished. In the first part, simulation tests of the complete set-up are presented, and its stability, robustness and performance analyzed. In the second part, the needed steps for a real implementation are analyzed. First of all, design modifications are presented to overcome possible implementation difficulties. A two-sided actuation for full-range amplitude and bias oscillation selection is presented. And a modification of standard Electromechanical Amplitude Modulation is analyzed and validated for position feedback implementation. Finally, a MEMS resonator with the desired specifications for testing the proposed control is designed for fabrication. Based on this design, testing procedure is discussed.

And in Chapter 8, the Conclusions are presented, as well as, the Future work, including the experimentation that has not been performed.

Chapter 2

Electrostatically actuated MEMS resonator model

In this Chapter the complete model of an electrostatically actuated beam is presented. This model includes the main characteristics that can be found in a large number of MEMS devices which rely on electrostatic actuation.
The analysis of the different participating terms is presented separately, to understand each aspect of the dynamics. Once each part is understood, the complete formulation is presented.
The Chapter finishes with an analysis of the approaches to simplify the ideal model. This leads to formulate the concentrated parameters simplification that will be used all through the dissertation.

2.1 Distributed parameters model formulation

To perform the analysis of a system, the first step is to obtain an accurate model of the system which must include all the relevant characteristics. This section presents the distributed parameters model of any resonant MEMS device electrostatically actuated.

2.1.1 Mechanical model

In MEMS devices, we have a basic structure: the *beam*. This mechanical component, and its extension, the *plate*, generate the majority of MEMS sensors and actuators. Consequently, the first step to analyze the behavior of any device is to understand and model the dynamic characteristics of a beam.
The deformation of a beam (Figure 2.1), using the Euler-Bernoulli theory of thin beams [163] is composed of two basic terms [170], the potential energy generated due to the

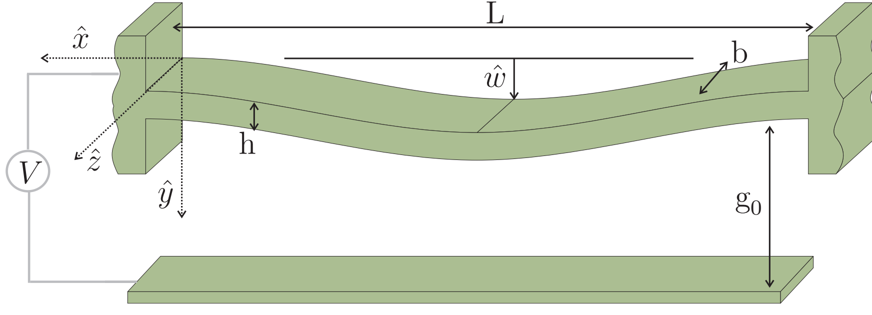

Figure 2.1: Basic scheme of a deflected beam

deformation of the beam

$$U_{def} = \frac{\mathrm{EI}}{2} \int_0^{\mathrm{L}} \left(\frac{\partial^2 \hat{w}}{\partial \hat{x}^2} \right)^2 \mathrm{d}\hat{x} \tag{2.1}$$

that it's proportional to its curvature, $\frac{\partial^2 \hat{w}}{\partial \hat{x}^2}$, and the kinetic energy due to its movement

$$T = \frac{\rho \mathrm{A}}{2} \int_0^{\mathrm{L}} \left(\frac{\partial \hat{w}}{\partial \hat{t}} \right)^2 \mathrm{d}\hat{x} \tag{2.2}$$

where $\hat{w}$ is the oscillation amplitude, ρ is the density of the beam, A is the area of the cross-section of the beam ($\mathrm{A} = \mathrm{b} \cdot \mathrm{h}$, b and h are the width and height of the section of the beam), L is the longitude of the beam, E is the Young Modulus and I is the moment of inertia of the cross-section ($\mathrm{I} = \mathrm{bh}^3/12$).

Typically in MEMS, a beam can also be externally stretched by an axial force $\hat{N}(\hat{t})$ (Figure 2.2). This force could be generated by different sources: thermal load, fabrication stresses, external beam tuning, etc. In this case, another energy term appears that englobes the deformation generated by the external force

$$U_N = \frac{\hat{N}(\hat{t})}{2} \int_0^{\mathrm{L}} \left(\frac{\partial \hat{w}}{\partial \hat{x}} \right)^2 \mathrm{d}\hat{x}. \tag{2.3}$$

As can be observed, the deformation is proportional to the axial force.

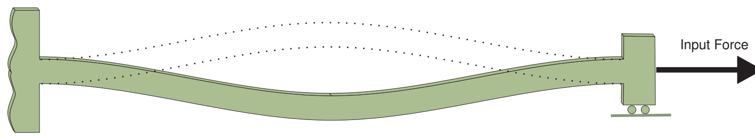

Figure 2.2: Vibrating beam oscillating under the influence of an axial force

Finally, in the case of large oscillations, the beam movement generates self-stretching forces that actuate as structural damping. This effect can be accounted assuming that an internal force, F_{int}, is producing an elongation of the beam. This force would have the

following form [162], [222]

$$F_{int} = \frac{\mathrm{EA}}{4\mathrm{L}} \int_0^{\mathrm{L}} \left(\frac{\partial \hat{w}}{\partial \hat{x}}\right)^2 \mathrm{d}\hat{x} \tag{2.4}$$

and, substituting this force in (2.3), we obtain the energy of deformation due to self-stretching

$$U_{int} = \frac{\mathrm{EA}}{8\mathrm{L}} \left[\int_0^{\mathrm{L}} \left(\frac{\partial \hat{w}}{\partial \hat{x}}\right)^2 \mathrm{d}\hat{x}\right]^2 \tag{2.5}$$

The dynamic equation of the free deflection of an homogeneous beam undergoing bending can be obtained using the Lagrange equations, from the Lagrangian

$$L = T - U_{def} - U_N - U_{int} \tag{2.6}$$

and it is written as follows

$$\mathrm{E'I}\frac{\partial^4 \hat{w}}{\partial \hat{x}^4} + \rho\mathrm{A}\frac{\partial^2 \hat{w}}{\partial \hat{t}^2} - \left[\hat{N}(\hat{t}) + \frac{\mathrm{E'A}}{2\mathrm{L}} \int_0^{\mathrm{L}} \left(\frac{\partial \hat{w}}{\partial \hat{x}}\right)^2 \mathrm{d}\hat{x}\right] \frac{\partial^2 \hat{w}}{\partial \hat{x}^2} = 0 \tag{2.7}$$

where A is the area of the section of the beam, and in this case, the extended Young Modulus, $\mathrm{E'} = \mathrm{E}/(1-\nu^2)$, is introduced to account for a wide microbeam (plate) where ν is the Poisson ratio. For a narrow beam $\mathrm{E'} = \mathrm{E}$.

As can be observed, the microbeam dynamics is composed of four terms: the beam resistance to bending, the inertia due to movement, the beam stiffness due to the externally applied axial load and mid-plane stretching due to elongation of the beam. The first three components are treated as linear terms in the equation of motion, whereas the third component is represented by a nonlinear term in the equation of motion.

For convenience, and uniformity with other formulations [222] , we introduce the following nondimensional variables

$$w = \frac{\hat{w}}{\mathrm{g}_0},\ x = \frac{\hat{x}}{\mathrm{L}},\ t = \frac{\hat{t}}{\mathrm{T}} \tag{2.8}$$

where T is a time-scale defined as $\mathrm{T} = (\rho\mathrm{AL}^4/(\mathrm{E'I}))^{1/2}$. Writing down the equation in the non-dimensional variables

$$\frac{\partial^4 w}{\partial x^4} + \frac{\partial^2 w}{\partial t^2} - [\alpha_\mathrm{f}\Gamma(w,w) + N]\frac{\partial^2 w}{\partial x^2} = 0. \tag{2.9}$$

The parameters appearing in equation (2.9) can be defined as follows

$$\alpha_\mathrm{f} = 6\left(\frac{\mathrm{g}_0}{\mathrm{h}}\right)^2,\ N = \frac{\hat{N}\mathrm{L}^2}{\mathrm{E'I}} \tag{2.10}$$

and the operator Γ is defined as

$$\Gamma(f_1(x,t), f_2(x,t)) = \int_0^1 \frac{\partial f_1}{\partial x}\frac{\partial f_2}{\partial x}\,\mathrm{d}x$$

being f_1 and f_2 any two functions of x and t.

2.1.2 Electrostatic actuation

In MEMS, the basic electrostatic system is a parallel-plates capacitor (Figure 2.3). In this case, electrostatic forces are generated between two conducting elements separated a distance g_0 by a dielectric element. In MEMS, the dielectric is usually air. And an usual assumption is that the distance is differentially uniform between the two plates.

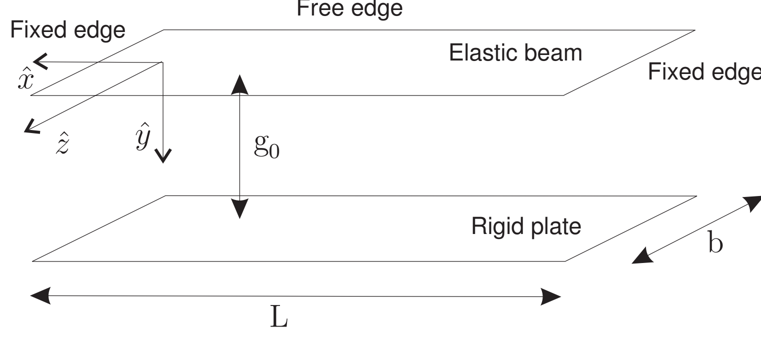

Figure 2.3: Geometry of the idealized capacitor [157]

Having these assumptions in mind, there exists an electrostatic potential, $\hat{\psi}$, associated to each point of the plates of the capacitor, Figure 2.3, that satisfies

$$\nabla^2 \hat{\psi} = 0, \tag{2.11}$$

$$\hat{\psi}(\hat{x}, g_0, \hat{z}) = 0, \quad \hat{x}\epsilon[-L/2, L/2], \quad \hat{z}\epsilon[-b/2, b/2] \tag{2.12}$$

$$\hat{\psi}(\hat{x}, \hat{w}, \hat{z}) = V \cdot f(\hat{w}/g_0), \quad \hat{x}\epsilon[-L/2, L/2], \quad \hat{z}\epsilon[-b/2, b/2] \tag{2.13}$$

where $\nabla^2 \equiv \frac{\partial}{\partial \hat{x}} + \frac{\partial}{\partial \hat{y}} + \frac{\partial}{\partial \hat{z}}$ stands for the Laplacian operator, $\hat{w}$ is the displacement of each point of the beam from $\hat{z} = 0$, V is the applied voltage, and the dimensionless function f is used to represent the fact that the voltage drop between the two plates may depend upon $\hat{w}$ [157]. It is of special importance to remember that $\hat{w}$ should satisfy equation (2.7).

If nondimensional variables are introduced as in (2.8),

$$\psi = \frac{\hat{\psi}}{V}, \; w = \frac{\hat{w}}{g_0}, \; x = \frac{\hat{x}}{L}, \; y = \frac{\hat{y}}{g_0}, \; z = \frac{\hat{z}}{b} \tag{2.14}$$

and substituted in equations (2.11)-(2.13), this yields

$$\epsilon^2 \left(\frac{\partial^2 \psi}{\partial x^2} + a_b^2 \frac{\partial^2 \psi}{\partial z^2} \right) + \frac{\partial^2 \psi}{\partial y^2} = 0, \tag{2.15}$$

$$\psi(x, 1, z) = 0, \quad x\epsilon[-1/2, 1/2], \quad z\epsilon[-1/2, 1/2] \tag{2.16}$$

$$\psi(x, w, z) = f(w), \quad x\epsilon[-1/2, 1/2], \quad z\epsilon[-1/2, 1/2] \tag{2.17}$$

where $\epsilon = \frac{\mathrm{g}_0}{\mathrm{L}}$ is an aspect ratio comparing the gap size to beam length and $\mathrm{a}_b = \frac{\mathrm{L}}{\mathrm{b}}$ is an aspect ratio of the beam design, comparing its length and width. Usually, in most applications the potential difference, V, is fixed and then $f(w) = 1$.

Using basic electrostatics equations, the *Potential Energy* stored in the *Electric Field* created between the capacitor plates is defined as [153]

$$U_e(\hat{x}, \hat{y}, \hat{z}) = \frac{\varepsilon}{2} \int_v |\hat{\mathbf{e}}|^2 \mathrm{d}v \tag{2.18}$$

where ε is the permittivity constant of the dielectric element between the plates (Free-space permittivity is $\varepsilon_0 = 8.854 \cdot 10^{-12} F/m$), $\int_v$ stands for the volume integral, $|\ |$ stands for a 2-norm of a vector, and given that the *Electrostatic field* $\hat{\mathbf{e}}$ is defined as

$$\hat{\mathbf{e}} = -\nabla \hat{\psi} \tag{2.19}$$

where ∇ is the gradient operator.

For consistency, we can use normalized variables, then

$$\mathbf{e} = \frac{\hat{\mathbf{e}}}{V} \ ; \ \mathbf{e} = -\nabla \psi \tag{2.20}$$

and consequently,

$$U_e(x, y, z) = -\frac{\varepsilon V^2}{2} \int_v |\nabla \psi|^2 \mathrm{d}v. \tag{2.21}$$

As the electrostatic force generated by the conservative electrostatic potential field in vacuum can be calculated as the gradient of the potential energy, using equation (2.21) we can obtain

$$F = -\nabla U_e = -\frac{\varepsilon_0 V^2}{2} |\nabla \psi|^2. \tag{2.22}$$

Consequently, the key problem to define the electrostatic force is solving the equation (2.15) for the electrostatic potential ψ.

Numerically, the potential can be calculated using finite elements [157]. However, approximations can be done in order to develop the formulation.

The typical approximation is to consider that the plate width and longitude are considerably large against the gap between the plates, what implies that the force lines are basically parallel and the fringing fields are negligible. In this case, ϵ^2 in equation (2.15) is small, and the terms that are multiplied by this term can be ignored, resulting in equation

$$\frac{\partial^2 \psi}{\partial y^2} = 0. \tag{2.23}$$

Then, solving this equation for the potential ψ, it can be found that

$$\psi = \frac{f(w)(1-y)}{(1-w)} \tag{2.24}$$

and the differential force generated by this potential is

$$F_e(x,z) = -\frac{\varepsilon_0 V^2}{2\mathrm{g}_0^2(1-w)^2}. \tag{2.25}$$

As can be observed, this approximation gives way to the expression of the force mostly used to calculate the electrostatic force between two parallel plates

$$F_e = -\frac{1}{2}\frac{\varepsilon_0 \mathrm{A}_c V^2}{\mathrm{g}_0^2(1-w)^2} \tag{2.26}$$

where A_c is the area of the capacitor plate. This formulation is only valid if the force contribution by the fringing fields that appear at the ends of the parallel plates can be assumed small compared to the total force.

This approximation is shown to be valid for the small aspect ratio devices. In [157] and [154] comparison between both approaches are presented and justifications of the validity of the approximation stated.

Another option to overcome the fringing fields is presented by [139]. In this case, knowing that the charge distribution is not even and taking into account the effect of the fringing fields, a capacitance correction C_n is derived that includes this effects. Given a parallel plate capacitor, the *capacitance* C is defined as the proportionality constant between the charge (Q) and the applied voltage

$$\mathrm{C} = \frac{\varepsilon \mathrm{A}_c}{\mathrm{g}} \quad ; \quad Q = \mathrm{C}V. \tag{2.27}$$

Then the *fringing-field corrected capacitance* $\tilde{\mathrm{C}}$ is defined as

$$\tilde{\mathrm{C}} = \mathrm{C}\mathrm{C}_n \tag{2.28}$$

where

$$\mathrm{C}_n = 1 + 4.246\vartheta, \qquad 0 \leq \vartheta < 0.005 \tag{2.29}$$

$$\mathrm{C}_n = 1 + \sqrt{11.0872\vartheta^2 + 0.001097}, \quad 0.005 \leq \vartheta < 0.05 \tag{2.30}$$

$$\mathrm{C}_n = 1 + 1.9861\vartheta^{0.8258}, \qquad 0.05 \leq \vartheta \tag{2.31}$$

given that $\vartheta = \mathrm{g}_0/\mathrm{b}$ is the aspect ratio of the gap against the width of the beam. The constants are derived applying regression analysis to numerically obtained data. The

model has been validated to measured data [139]. Other authors have obtained equivalent results with different fitting formulas, An example is the [84] derivation,

$$\mathrm{C}_n = 1 + 0.65\frac{\mathrm{g}_0}{\mathrm{b}}.$$

Consequently, with these approximations, the force can be computed with

$$U = \frac{1}{2}\tilde{\mathrm{C}}V^2 = \frac{1}{2}\mathrm{C}_n\mathrm{C}V^2 = \frac{1}{2}\mathrm{C}_n\frac{\varepsilon_0\mathrm{A}_c}{\mathrm{g}_0}V^2 \tag{2.32}$$

$$F = -\nabla U = \frac{1}{2}\mathrm{C}_n\frac{\varepsilon_0\mathrm{A}_cV^2}{\mathrm{g}_0^2(1-w)^2}. \tag{2.33}$$

The derived expressions can be extended to non-uniform gap capacitors using sum of elementary capacitors [126].

2.1.3 Damping in MEMS

In MEMS, there are two basic sources of damping forces: structural damping and viscous damping (or aerodynamic damping).

The structural damping is generated by the molecular interaction in the material due to deformations. It happens in the moving parts and at the anchoring points [57]. The main contribution has already been introduced in the mechanical model with the term including internal forces due to stretching. If the amplitude of oscillation of the beam is small, the values of these forces in materials like the polysilicon are negligible compared to the viscous damping effects.

The viscous damping effects appear due to the fluid that surrounds the MEMS device. The generated forces can be specially large if the fluid is air. For this reason, most devices are packaged in vacuum environments.

Two different types of viscous damping can be usually identified in micromachined moving structures: *couette flow damping* and *squeeze film damping*.

To analyze the generated forces, one can turn to classical fluid mechanics and use the Navier-Stokes equations, which are composed of the continuity equation

$$\frac{d\rho_m}{d\hat{t}} + \rho_m\nabla\hat{\mathbf{v}} = 0 \tag{2.34}$$

and the motion equation

$$\rho_m\frac{d\hat{\mathbf{v}}}{d\hat{t}} = -\nabla P + \rho_m\mathrm{g} + \eta\nabla^2\hat{\mathbf{v}} + \frac{\eta}{3}\nabla(\nabla\cdot\hat{\mathbf{v}}) \tag{2.35}$$

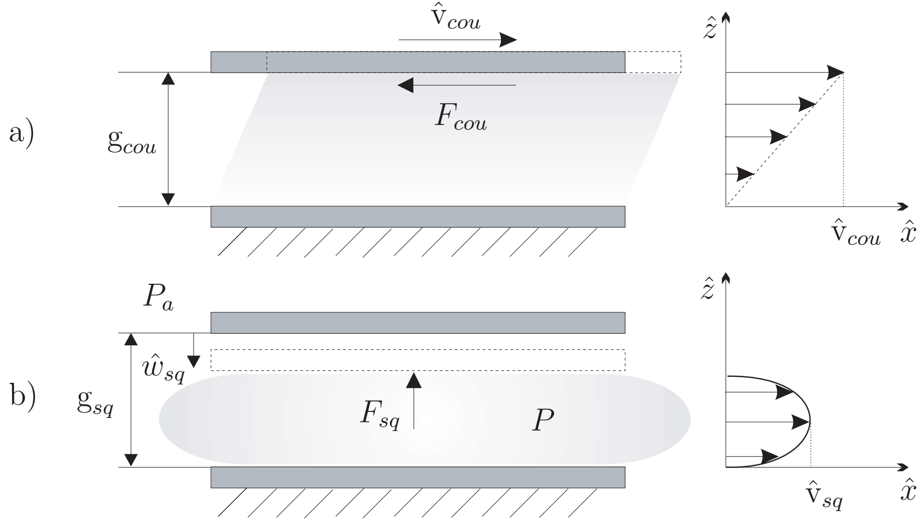

Figure 2.4: a) Couette flow damping between two plates that move parallel one to the other and its velocity profile; b) Squeeze film damping between two plates that move one against the other and its velocity profile.

where ρ_m is the mass-density of the fluid, η is the viscosity (assumed to be constant), g is the acceleration of gravity, P is the pressure of the fluid, $\hat{\mathbf{v}}$ is the velocity of the fluid and $\frac{d}{d\hat{t}}$ stands as the time-derivative of a vector [153].

2.1.3.1 Couette flow damping

In the *couette flow* case, the damping force appears between two plates that move parallel one to the other and are separated by a Newtonian fluid (Figure 2.4a) [44]. As the distance between the plates is considered constant, the working regime is under incompressible flow, meaning that the rate of change of density $\frac{d\rho_m}{d\hat{t}}$ is negligible. Under this circumstances, the continuity equation (2.34) becomes

$$\nabla \hat{\mathbf{v}}_{cou} = 0 \tag{2.36}$$

and the Navier-Stokes equation of motion (2.35) reduces to

$$\rho_m \frac{d\hat{\mathbf{v}}_{cou}}{d\hat{t}} = -\nabla P + \rho_m \mathrm{g} + \eta \nabla^2 \hat{\mathbf{v}}_{cou} \tag{2.37}$$

for incompressible flow. Here the velocity, $\hat{\mathbf{v}}_{cou}$, is constrained in the x-direction.

The pressure and gravity body-force terms can be combined introducing a position vector $\hat{\mathbf{r}}$, and defining

$$P^* = P - \rho_m \mathrm{g}\,\hat{\mathbf{r}}.$$

Using this definition, the Navier-Stokes equation reduces to the following steady-flow equation

$$\rho_m \frac{d\hat{\mathbf{v}}_{cou}}{d\hat{t}} = \eta \nabla^2 \hat{\mathbf{v}}_{cou} - \nabla P^*. \quad (2.38)$$

From Figure 2.4a, it can be seen that the flow becomes perfectly one-dimensional away from the edges. This aspect linked to condition (2.36) delimits that the velocity profile is composed of streamlines, so

$$\hat{\mathbf{v}}_{cou} = \begin{pmatrix} \hat{v}_{cou,\hat{x}}(\hat{y}) \\ 0 \end{pmatrix}. \quad (2.39)$$

Under these steady-flow conditions,

$$\frac{d\hat{\mathbf{v}}_{cou}}{d\hat{t}} = 0 \quad (2.40)$$

and considering that no pressure gradient is generated by the moving plate, the Navier-Stokes equation reduces to

$$\frac{\partial^2 \hat{v}_{cou,\hat{x}}}{\partial \hat{y}^2} = 0 \quad (2.41)$$

giving a linear velocity profile as a solution.

If the fluid is liquid or gas, and the structures are relatively large (see [207] for correction in case of gas rarefication), one can apply the usual no-slip boundary condition, to the profile in Figure 2.4a. Then the velocity is

$$\hat{v}_{cou,\hat{x}} = \frac{\hat{y}}{\mathrm{g}_{cou}} \hat{\mathrm{v}}_{cou} \quad (2.42)$$

and the shear stress, using the Newtonian fluid condition, on the moving plate is

$$\tau = -\eta \frac{\partial \hat{v}_{cou,\hat{x}}}{\partial \hat{y}} |_{\hat{y}=\mathrm{g}_{cou}} = \begin{pmatrix} -\eta \frac{\hat{\mathrm{v}}_{cou}}{\mathrm{g}_{cou}} \\ 0 \end{pmatrix}. \quad (2.43)$$

Finally, having the shear stress, the *couette damping force* in the direction of the movement of the whole structure can be calculated as

$$F_{cou} = \tau \mathrm{A}_{cou} = -\eta \frac{\mathrm{A}_{cou}}{\mathrm{g}_{cou}} \hat{\mathrm{v}}_{cou} = \hat{c}_{cou} \hat{\mathrm{v}}_{cou} \quad (2.44)$$

where the force is directly proportional to the velocity of the structure, $\hat{\mathrm{v}}_{cou}$, and A_{cou} is the area of overlapping between the structures.

It is important to analyze in what direction the system induces the *couette damping force* to maintain the consistency of the formulation. This will depend on the system configuration. In most cases, the system moves over the substrate and the *couette damping force* is generated between the moving structure and the substrate, in this case, $\hat{\mathrm{v}}_{cou} = \dot{\hat{w}}$.

2.1.3.2 Squeeze film damping

However, in MEMS actuated with parallel plate capacitors, the main source of damping is the *Squeeze film force*. In parallel-plate capacitor designs, an articulated plate moves towards a fixed plate (Figure 2.4b). During this movement, when the plates approach each other the pressure of the trapped fluid increases, and the fluid is squeezed out through the edges of the plates. When the plates separate, a sucking drag is generated due to the fluid filling back the gap.

To solve this case, we must return to the Navier-Stokes equation (2.35), but this time we need the full compressible fluid equation. Consequently, to handle the analytical derivation, several assumptions must be done in our system:

- The aspect ratio is large, meaning that the gap is smaller than the plates extent.
- The motion is slow, meaning that the inertial term can be neglected in front of the viscous one, and the fluid works under Stokes flow.
- The pressure between the plates is homogeneous.
- The fluid flow at the edges of the plates follows a parabolic profile, defined by a Pousille-like equation (Figure 2.4b).
- The gas behaves under the ideal gas law.
- The system is isothermal.

Under these assumptions, the Navier-Stokes equations can be simplified, and the behavior of the fluid is governed by the Reynolds equation [78]

$$12\eta_{eff}\frac{\partial P\hat{g}_{sq}}{\partial t} = \nabla[\hat{g}_{sq}^3 P\nabla P] \tag{2.45}$$

where $P(\hat{x},\hat{y},t)$ is the pressure between the plates, $\hat{g}_{sq}(\hat{x},\hat{y},t)$ is the distance between the parallel plates, and η_{eff} is the corrected viscosity of the fluid, accounting for the rarefication effects due to low pressure [206]

$$\eta_{eff} = \frac{\eta}{1 + 9.638\mathrm{K}_n^{1.159}} \tag{2.46}$$

where $\mathrm{K}_n = \lambda/\mathrm{g}_{sq}$ is the Knudsen number, which compares the mean free path of a fluid molecule (λ) against the static gap distance (g_{sq}). The constant is experimentally

obtained. In a typical MEMS example, where λ is approximately 0.1 microns, the air is at atmospheric pressure and the gap is of 2 microns, the value of K_n would be 0.05. The mean free path is inversely proportional to fluid pressure.

Solution of equation (2.45) on P will lead to derivation of the *squeeze film forces*.

$$F_{sq} = (P - P_a) \cdot \mathrm{A}_{sq} \tag{2.47}$$

where P_a is the static pressure force and A_{sq} the area of overlapping of the capacitor plates. As can be observed, the *squeeze forces* calculation is coupled to the mechanical deflection of the beam [132].

To approximate the damping forces, one must linearize equation (2.45) assuming small amplitude motions. This way the gap distance and the pressure of the gap can be expressed as follows

$$\hat{g}_{sq}(\hat{x}, \hat{y}, t) = \mathrm{g}_{sq} - \hat{w}_{sq}(\hat{x}, \hat{y}, t) \ ; \ P(\hat{x}, \hat{y}, t) = P_a + \bar{P}(\hat{x}, \hat{y}, t) \tag{2.48}$$

where $\hat{w}_{sq}$ is the gap reduction (usually, oscillation of the device) and $\bar{P}$ the pressure variations from the static pressure. Substitution in (2.45) leads to

$$\frac{12\eta_{eff}}{P_a \mathrm{g}_{sq}^3}\left(\mathrm{g}_{sq}\frac{\partial \bar{P}}{\partial t} - P_a \frac{\partial \hat{w}_{sq}}{\partial t}\right) = \nabla^2 \bar{P} = \frac{\partial^2 \bar{P}}{\partial \hat{x}^2} + \frac{\partial^2 \bar{P}}{\partial \hat{y}^2}. \tag{2.49}$$

From this equation, in [132] they show that numerical coupled perturbation methods can predict experimental damping forces accurately.

If we add the assumption that the capacitor plates are long and narrow (a beam), the equation can be much reduced due to the fact that the fluid movement is only in one direction (y-direction in our device)

$$\frac{\partial \bar{P}}{\partial t} = \frac{P_a \mathrm{g}_{sq}^2}{12\eta_{eff}}\frac{\partial^2 \bar{P}}{\partial \hat{y}^2} + \frac{P_a}{\mathrm{g}_{sq}}\frac{\partial \hat{w}_{sq}}{\partial t}. \tag{2.50}$$

From this equation, one can solve for $\bar{P}$, obtaining the following force on the capacitors [183], using Laplace transformation

$$F_{sq}(s) = \left[\frac{96\eta_{eff}\mathrm{L}\mathrm{b}^3}{\pi^4 \mathrm{g}_{sq}^3}\sum_{n_{odd}}\frac{1}{n^4}\frac{1}{1+\frac{s}{\alpha_n}}\right] s\hat{y}(s) \tag{2.51}$$

where

$$\alpha_n = \frac{\mathrm{g}_{sq}^2 P_a n^2 \pi^2}{12\eta_{eff}\mathrm{b}^2} \tag{2.52}$$

given that $\hat{y}(s)$ is the input displacement, in Laplace formulation. As we are assuming small amplitudes, the first term of the expansion is a good approximation of the force

$$F_{sq}(s) = \left[\frac{96\eta_{eff}\mathrm{L}\mathrm{b}^3}{\pi^4 \mathrm{g}_{sq}^3} \frac{1}{1 + \frac{s}{\omega_{sq}}} \right] s\hat{y}(s). \tag{2.53}$$

From this derivation two important parameters arise, the *cut-off frequency*, ω_{sq},

$$\omega_{sq} = \frac{\pi^2 \mathrm{g}_{sq}^2 P_a}{12\eta_{eff}\mathrm{b}^2} \tag{2.54}$$

that indicates the bandwidth of the squeeze-film force, and the *squeeze number*, σ_{sq},

$$\sigma_{sq} = \frac{\pi^2 \omega}{\omega_{sq}} = \frac{12\eta_{eff}\mathrm{b}^2}{\mathrm{g}_{sq}^2 P_a}\omega. \tag{2.55}$$

The squeeze number allows to analyze the behavior of the squeeze film damping forces. When the squeeze number decreases, due to low pressure or low frequencies of oscillation, the fluid force becomes a pure damping force. However, at high frequencies or high squeeze number, a spring force component appears and becomes dominant with the damping force still present. Example of the contributions of each force can be found in [183]. Similar analysis and discussions are shown by [11] and [206] using the force decomposition derived in [24].

Consequently, the squeeze film damping force can be reduced to

$$F_{sq} = c_{sq}(\hat{w}_{sq}, \sigma_{sq}) \frac{\partial \hat{w}_{sq}}{\partial t} \tag{2.56}$$

with damping and spring effects depending on σ_{sq} [212].

Again, it is important to analyze in what direction the system induces the *squeeze film damping force* to maintain the consistency of the formulation. In most cases, the *squeeze film damping force* is generated between the moving plate and the fix plate, and in this case, the force direction is opposed to the amplitude of oscillation of the device, $\hat{w}_{sq} = \hat{w}$.

2.1.3.3 Total damping forces

Finally, the fluid damping effects in the model are the combination of squeeze film and couette film damping, giving a final force

$$F_d = F_{cou} + F_{sq} = -\eta \frac{\mathrm{A}_{cou}}{\mathrm{g}_{cou}} \hat{\mathrm{v}}_{cou} + (P - P_a) \cdot \mathrm{A}_{sq}. \tag{2.57}$$

Using the assumptions previously stated, $\mathrm{v}_{cou} = \dot{\hat{w}}$ and $\hat{w}_{sq} = \hat{w}$, the damping forces can be represented as

$$F_d = (c_{sq} + c_{cou}) \frac{d\hat{w}}{d\hat{t}} = \hat{c}_d \frac{d\hat{w}}{d\hat{t}}. \tag{2.58}$$

2.1.4 Lumped system

The complete set of equations defining the behavior of the system can be obtained linking the different energies and non-conservative forces acting in the system.

The kinetic energy is defined in (2.2)

$$T = \frac{\rho \mathrm{A}}{2} \int_0^{\mathrm{L}} \left(\frac{\partial \hat{w}}{\partial \hat{t}}\right)^2 \mathrm{d}\hat{x}. \tag{2.59}$$

The potential energy is composed of mechanical (2.1),(2.3),(2.5) and electrostatic terms (2.18)

$$U = \frac{\mathrm{EI}}{2} \int_0^{\mathrm{L}} \left(\frac{\partial^2 \hat{w}}{\partial \hat{x}^2}\right)^2 \mathrm{d}\hat{x} + \frac{\hat{N}(\hat{t})}{2} \int_0^{\mathrm{L}} \left(\frac{\partial \hat{w}}{\partial \hat{x}}\right)^2 \mathrm{d}\hat{x} + \frac{\mathrm{EA}}{8\mathrm{L}} \left[\int_0^{\mathrm{L}} \left(\frac{\partial \hat{w}}{\partial \hat{x}}\right)^2 \mathrm{d}\hat{x}\right]^2 + \frac{\varepsilon V^2}{2} \int_v |\nabla \psi|^2 \mathrm{d}v. \tag{2.60}$$

The fluid damping is the only non-conservative force (2.57)

$$F_d = -\eta \frac{A_{ov}}{\mathrm{g}_0} U + (P - P_a) \cdot \mathrm{A}_c. \tag{2.61}$$

Consequently, using Lagrange formulation and non-dimensional variables, the dynamics of the system is as follows:

$$\frac{\partial^4 w}{\partial x^4} + \frac{\partial^2 w}{\partial t^2} - [\alpha_{\mathrm{f}} \Gamma(w, w) + N] \frac{\partial^2 w}{\partial x^2} = \gamma V^2 |\nabla \psi|^2 - \frac{12\mathrm{L}^4}{\mathrm{E' \, h^3 T}} \left[-\eta \frac{A_{ov}}{\mathrm{g}} U + (P - P_a) \cdot \mathrm{A}_c\right] \tag{2.62}$$

given that the electrostatic potential and the fluid pressure satisfy the following conditions

$$\epsilon^2 \left(\frac{\partial^2 \psi}{\partial x^2} + \mathrm{a}_b^2 \frac{\partial^2 \psi}{\partial y^2}\right) + \frac{\partial^2 \psi}{\partial z^2} = 0 \tag{2.63}$$

$$12\eta_{eff} \frac{\partial P d}{\partial t} = \nabla [d^3 P \nabla P]. \tag{2.64}$$

Linking the different formulations previously derived, the dynamics of the system can be reduced to [1]:

$$\frac{\partial^2 w}{\partial t^2} + c \frac{\partial w}{\partial t} + \frac{\partial^4 w}{\partial x^4} - [\alpha_{\mathrm{f}} \Gamma(w, w) + N] \frac{\partial^2 w}{\partial x^2} = \gamma V^2 |\nabla \psi|^2 \tag{2.65}$$

$$w(0, t) = w(1, t) = 0, \quad w'(0, t) = w'(1, t) = 0.$$

And the parameters appearing in equation (2.65) can be defined as follows

$$c = \frac{\hat{c}_d \, \mathrm{L}^4}{\mathrm{E' \, I \, T}}, \quad N = \frac{\hat{N} \mathrm{L}^2}{\mathrm{E'I}}$$

$$\alpha_{\mathrm{f}} = 6 \left(\frac{g}{h}\right)^2, \quad \gamma = \frac{6 \varepsilon_0 \mathrm{L}^4}{\mathrm{E' \, h^3 g}}. \tag{2.66}$$

Equation (2.65) translates to the following formulation once the electrostatic force is approximated

$$\frac{\partial^2 w}{\partial t^2} + c\frac{\partial w}{\partial t} + \frac{\partial^4 w}{\partial x^4} - [\alpha_{\mathrm{f}}\Gamma(w,w) + N]\frac{\partial^2 w}{\partial x^2} = \Upsilon\frac{V^2}{(1-w)^2} \tag{2.67}$$

where $\Upsilon = \frac{6\mathrm{C}_n\varepsilon_0\mathrm{L}^4}{\mathrm{E'}\,\mathrm{h}^3\mathrm{g}^3}$, using fringing fields correction in the capacitance term.

2.2 Evolution in MEMS modeling

The general equations of the system (2.62), as defined in the previous section, are difficult to handle, and investigators have tried to approach the analysis of the system using simplified models, leaving the complete equations to finite-elements analysis applications and numerical solution approaches. The problem with the simplified solutions is their closeness to reality. Table 2.1 presents a summary of the different approaches and the goals that have been analyzed with each one.

The earliest study of the parallel-plate electrostatic actuation of a beam may be found in the pioneering work of Nathanson et al. [131] [137]. In their study of a resonant gate transistor, they constructed and analyzed a mass-spring model with electrostatic actuation. They predicted and offered the first theoretical explanation of the so-called pull-in instability.

For its simplicity, the mass-spring-damper system has been extensively used in order to simulate and design MEMS devices. The model has been used to predict static displacements and to study the main behaviors of the system. For instance, the equations allow to analytically determine the static pull-in and the maximum travel range in the static case, which is one-third of the initial gap [183]. In [77], they expand this analysis to predict pull-in times and derive the *Dynamic Pull-in Voltage* (DPV) which indicates the maximum voltage that can be applied as a step-function to the system without producing snapping in vacuum environment [38]. A extended discussion on energy-dependence of the *Dynamic Pull-in Voltage* can be found in [204] and [61].

Analysis involving theoretical squeeze film equations can be found in [125], which are applicable for large displacement simulation. The simulated and experimental results were compared, and they have good agreement.

The model is less accurate when oscillations are introduced, as these kind of models cannot accurately predict the inherent nonlinearities of the electrostatic force and the

	Differential Equations	Numerical Solution	Simple Model	Parametric excitation	Modal/Energy Analysis
Static Solution	[2], [155] [156], [68]	[9], [59] [10]	[179], [88] [45]		[197] [88]
Dynamic Solution	[2], [224], [1] [68], [215]	[10]	[179], [39], [221] [88], [77]	[33], [127] [130]	[197], [218] [88], [170]
Static Pull-in	[2], [155] [156], [68]	[10] [59]	[179], [166] [45]		[197] [83]
Dynamic Pull-in	[2], [224] [68]	[10]	[77], [166] [39]		[197]
Spring softening	[222]	[10]			[197] [170]
AC actuation	[2], [101] [222]		[180]		[197] [170]
Large amplitude	[2] [222]			[130] [231]	[197] [170]
Tension sensitivity	[2] [222]				[197] [170]
Control	[156]		[39], [192] [221]	[127]	
Stability	[156], [224] [68]		[153]	[33] [127]	[88]
Damping		[219]	[45] [77]	[231]	[218]
Comparison to reality	[2]	[10]	[45]	[130], [231] [127]	[197] [83]
Model comparison		[9]			[88] [83]

Table 2.1: Comparison of the different analysis approaches in the literature

beam deformation [45], [39]. The model assumes a linear spring, thus neglects midplane stretching effects. However, the model can be used to extract the expression for the fundamental natural frequency as a function of the DC polarization voltage, as the experiments show [182], [191]. A way to expand the model to oscillation applications is to restrict the amplitude of oscillation [208], [166].

Even with its limitations, the model includes most of the main nonlinear characteristics, as it has been shown by several authors. In [180] and [63] they showed that resonant pull-in can be predicted in electrostatically actuated oscillators and experimental results are presented to validate the concept.

Further analysis of the nonlinear behavior based on the mass-spring-damper model have been carried on in [213] and [110], which show that period doubling and chaos can appear in parallel-plate electrostatically actuated MEMS.

The mass-spring-damper linear model is specially used when applications have to be demonstrated. For example, in microrelay applications, where pull-in or gap-closing is the objective [77], [166]. Or for device definition, no matter if they are resonant accelerometers [192], gyroscopes [148] or micromirrors [233].

In order to present control strategies, this model has been mainly used [182], [178].

To improve the accuracy of the analysis, some authors have tried finite-elements modeling, using the simplified equations. Or have tried to expand the one-degree of freedom system to three-degree of freedom analysis. Software as MEMCAD [184] has been designed using these approaches.

In [10], the method of linear normal mode summation is utilized to construct reduced order macromodels to perform the nonlinear dynamic analysis. Using the reduced order macromodel, it is possible to observe nonlinear effects such as the frequency shift due to a DC bias voltage, and the amplitude-dependence of resonance frequency. In [74], the models are expanded to simulate the pull-in voltage, the resonance frequency, the quality factor, the switching time and the electrostatic spring softening of the microrelay. However computation times can be quite demanding in the case of non-linear coupling.

In [86], it is shown that a way of solving the simulation of the system is rewriting the solution as a sum of orthogonal basis functions, that correspond to the oscillation modes. They show the feasibility using an initial model with internal tension and damping. The obtained low-order models are quicker for numerical modeling. The model is extended in [123] introducing stress stiffening.

Another approach is numerical simulation of the dynamics of MEMS carried out by a hybrid BEM/FEM (Boundary Element and Finite Element Method) method, FEM for the structure and BEM for the electrostatic analysis. In [185] several numerical techniques are proposed for time-integration in order to obtain the non-linear dynamic response of a MEMS microtweezer. Study of this model helps to understand some of the complex non-linear responses of the microtweezer.

In [236], a numerical code is proposed that associates the finite element methods for deformation, the moment method for electrostatic fields and the arc-length control approach in the quantitative calculations. And general numerical solutions using finite elements with reduced-order energy equations are presented in [59] using relaxation techniques. FEM solutions allow to handle the complete deformation of the device, without just focusing on the maximum amplitude, but large computational time is needed. Similar analysis are done in [95], and using BEM and FEM techniques, the pull-in is characterized using homothopy parameters. The transient analysis time is calculated in [79], using mass-spring-damper models linked to FEM analysis.

All these finite-element approaches are good to determine precise deformations of the system or natural frequencies, but lack the simplicity needed to expand the method to complex analysis or control strategies.

On the other hand, the fact of having the power of numerical computation at hand has lead to improvement on the equations that are used. It would be ideal to work with the complete set of nonlinear equations, and some authors have tried this approach.

Some elaborated solutions and behavior analysis are derived in [21] and [157] directly form the differential equations. To obtain the solutions, a simplified membrane model is used where the plate inertial and bending effects are neglected. However, numerical implicit formula solution is also needed to evaluate the static solution. Nevertheless, this analysis allows to define stability conditions based on implicit eigenvalue equations.

In [68], they expand the solutions of the system including the viscous regime. Their simplified mathematical model allows to study a parabolic equation of reaction-diffusion type. A central result of the paper is that when the applied voltage is beyond the critical voltage where steady-state solutions cease to exist, the solution touches down in finite time. Bounds on the touchdown time are computed and the structure of solutions near touchdown is investigated.

Complete analysis based on the theoretical framework are presented in [2], [1]. Shooting

methods combined with nonlinear boundary-value problem are used to solve the existing eigenvalue problem. The vibrations around the deflected position of the microbeam are solved numerically for various parameters to obtain the natural frequencies and mode shapes. This approach allows to numerically calculate the exact Static Pull-in Voltage using the same numerical method. The results are compared with experimental results available in the literature with good agreement. Their analysis shows that neglecting the nonlinear effects leads to underestimating the stability limits of the system. The travel range taking into account the nonlinearities can be doubled.

The complete simulation of the system is presented in [132], where the modeling and simulation under the effect of squeeze-film damping is analyzed. They use the compressible Reynolds equation coupled with the equation governing the plate deflection. The model accounts for the electrostatic forcing of the capacitor air-gap, the restoring force of the microplate and the applied in-plane loads. Perturbation methods are used to derive an analytical expression for the pressure distribution. This expression is then substituted into the plate equation, which is solved in turn using a finite-element method for the structural mode shapes, the pressure distributions, the natural frequencies and the quality factors.

Following the same study, in [224] they present a methodology to simulate the transient and steady-state dynamics of microbeams undergoing small or large motions actuated by combined DC and AC loads. They use the model to produce results showing the effect of varying the DC bias, the damping, and the AC excitation amplitude on the frequency-response curves. In their analysis they detect the existence of dynamic effects that can produce pull-in with electric loads much lower than that predicted based on static analysis.

Since then, theoretical and simulation analysis of the nonlinear oscillation behavior and the study of the mechanisms that lead to dynamic pull-in have been presented in [134] for primary-resonance excitation and in [133] for subharmonic and superharmonic excitation.

Forced oscillations under superharmonic excitations are presented in [52]. Presence of symmetry-breaking by increases of DC and AC voltages are presented as well as period doubling and chaotic transitions. The significance of the mechanical and the fluidic nonlinearities is also studied.

Similar results have also been obtained by converting the system equations to Mathieu equations. This can be done by expanding the electrostatic force as Taylor series and using only the first and second term. In [129] and [128] experimental results confirm the validity of the model, and in particular, illustrate that parametric resonance phenomena

occur in capacitively actuated micro-cantilevers.

In [164], analysis of the complex dynamics is presented, where the device's nonlinear frequency response is found to be qualitatively dependent on the systems AC excitation amplitude.

Parametric excitation is used in [100] as a way of stabilizing the actuation voltage beyond the pull-in value. The parametric stabilization of a cantilever beam is demonstrated experimentally.

However, while trying to obtain good models to work with, the better method is to convert the partial differential equations to a concentrated-parameters model. To do so, different approaches are used, but all of them rely on the decomposition of the response of the system on its harmonics.

The first approach to analyze the response of a microbeam to a generalized transverse excitation and axial force was based on using Rayleigh's energy method to approximate the fundamental natural frequency of the straight, undeflected beam [88]. Later, they solved the same static problem using the Rayleigh-Ritz method assuming a combination of trial functions [197]. They used this formulation to generate an analytical expression for the pull-in voltage, based on energy methods. Even with the needed approximations to solve the equations, the calculated values of the pull-in voltage were in good agreement with the results of experiments they conducted on MEMS resonators of various lengths. The system approximation generates good results while large amplitudes are not taken into account.

Similar approaches are used in [75] to theoretically and experimentally analyze the nonlinearities and hysteresis effects of electrostatically activated voltage-driven resonant microbridges.

Energy methods are used in [109] to analyze the transient behavior between pull-in and release states. The concept of dynamic pull-in is studied as well as hysteresis phenomena. No evolution analysis are performed. In [171], the energy method allows to develop an analytical model for the deflection of clamped-clamped multilayer beams as a function of applied voltage.

Using energy analysis, in [136] an analytical expression to calculate the *Static Pull-in* as a function of the nonlinear spring is presented. Following similar analysis, the formulation is extended to the *Dynamic Pull-in* case in [62]

However, the most usual way to obtained a concentrated-parameters model is to use the

Galerkin procedure to decouple the partial differential equations into a set of nonlinear ordinary differential equations for each modal shape and each modal frequency.

Using this method, the behavior of the beam can be approximated to that of a non-linear spring for a given deformation mode, and approximations can also be obtained for the electrostatic force and damping, giving way to a mass-spring-damper model that englobes all the nonlinearities. This model can characterize axial forces on the structure and beam stiffening due to large deformations [170].

Without taking the damping into account, [215] uses the invariant manifold method to obtain the associated nonlinear modal shapes, and modal motion governing equations. The model allows to examine the nonlinearities and the pull-in phenomena. Similar results using shooting methods combined with nonlinear boundary-value problem where presented in [2].

In [83], Galerkin method allows to obtain the mechanical model considering complicated geometry and the residual stress effect, and to predict the effective stiffness constant and critical collapse voltage of the bridge for several typical bridge geometries.

In [100] and [101] they develop a model using the Galerkin procedure with normal modes as a basis. It accounts for the distributed nonlinear electrostatic forces, nonlinear squeezed film damping, and rotational inertia of a mass carried by the beam. Special attention is paid to the dynamics of the beam near instability points. The results generated by the model, and confirmed experimentally, show that nonlinear damping leads to shrinkage of the spatial region where stable motion is realizable. With this modeling, in [194] they show AC actuation sensitivity to design parameters.

The usefulness of these models is clear. In [99], stability analysis of a beam actuated by one and two electrodes is performed by evaluating the largest Lyapunov exponent on the reduced order models. Based on the Lyapunov exponent criterion, the influence of various parameters on the beam dynamic stability is investigated. And in [135], they study the dynamic pull-in, and formulate safety criteria for the design of MEMS resonant sensors and filters excited near one of their natural frequencies.

And in [62], it is shown that Galerkin method allows to expand the mass-spring-damper formulation to include the large amplitude stresses, making the resulting models useful for control analysis.

2.3 Concentrated parameters model formulation

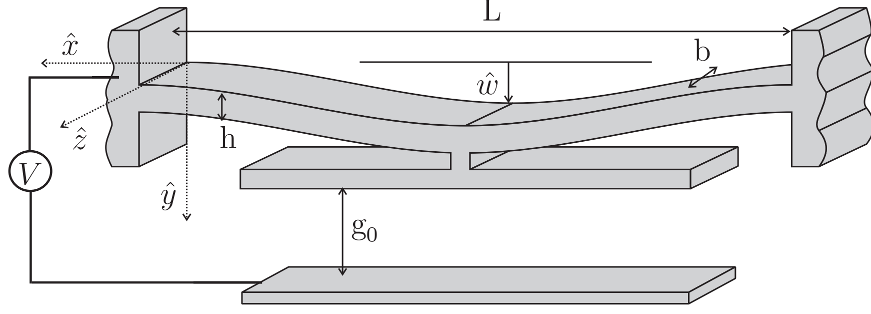

Figure 2.5: Basic scheme of a deflected beam with electrostatic parallel-plate actuation, as the ones used for testing.

As indicated, a concentrated parameters model is needed in order to analyze the system and apply control strategies. The full distributed model is too difficult to handle, and in some cases, the increased difficulty does not offer significantly better results.

Parting from the complete derivation previously presented, the Galerkin method can be used to simplify the partial differential equations into single-degree of freedom ordinary differential equations. The approach is based on decomposition of the beam vibration for each mode of oscillation, resulting on an ordinary differential equation for each mode.

On the first place, the beam response is assumed to be composed of an infinite number of oscillation modes, and consequently, the displacement $\hat{w}$ can be decomposed in

$$\hat{w}(\hat{x},\hat{t}) = \sum_i \hat{q}_i(\hat{t})\hat{\phi}_i(\hat{x}) \tag{2.68}$$

where $\hat{q}_i(\hat{t})$ is the time-dependent modal displacement for the oscillation mode i and $\hat{\phi}_i(\hat{x})$ is the position-dependent modal shape.

Equation (2.68) can be substituted in the Lagrangian formulation of the homogeneous beam developed in (2.6) to obtain a Lagrangian for each vibration mode of the beam [170]

$$\begin{gathered} L_i = T_i - U_{def,i} - U_{N,i} - U_{int,i} = \\ \frac{\rho \mathrm{A}}{2}\int_0^{\mathrm{L}} \hat{\phi}_i^2 \mathrm{d}\hat{x}\ \dot{\hat{q}}_i^2 - \left[\frac{\mathrm{EI}}{2}\int_0^{\mathrm{L}}\left(\frac{\partial^2\hat{\phi}_i}{\partial\hat{x}^2}\right)^2\mathrm{d}\hat{x} + \frac{\hat{N}(\hat{t})}{2}\int_0^{\mathrm{L}}\left(\frac{\partial\hat{\phi}_i}{\partial\hat{x}}\right)^2\mathrm{d}\hat{x}\right]\hat{q}_i^2 - \frac{\mathrm{EA}}{8\mathrm{L}}\left[\int_0^{\mathrm{L}}\left(\frac{\partial\hat{\phi}_i}{\partial\hat{x}}\right)^2\mathrm{d}\hat{x}\right]^2\hat{q}_i^4 = \\ \frac{1}{2}M_{eff,i}\cdot\dot{\hat{q}}_i^2 - \frac{1}{2}K_{eff,i}\cdot\hat{q}_i^2 - \frac{1}{4}K_{3,eff,i}\cdot\hat{q}_i^4. \end{gathered} \tag{2.69}$$

Once substituted, the terms can be rearranged, in order to obtain the appropriate configuration. In the derivation, $(\dot{\ })$ denotes time-derivative.

Consequently, using Lagrange formulation (2.7), the dynamics of each of the infinite modes of the beam is governed by

$$M_{eff,i} \cdot \ddot{\hat{q}}_i + K_{eff,i} \cdot \hat{q}_i + K_{3,eff,i} \cdot \hat{q}_i^3 = 0 \tag{2.70}$$

where

$$M_{eff,i} = \rho \mathrm{A} \int_0^{\mathrm{L}} \hat{\phi}_i^2 \mathrm{d}\hat{x} \tag{2.71}$$

$$K_{eff,i} = \mathrm{EI} \int_0^{\mathrm{L}} \left(\frac{\partial^2 \hat{\phi}_i}{\partial \hat{x}^2}\right)^2 \mathrm{d}\hat{x} + \hat{N}(\hat{t}) \int_0^{\mathrm{L}} \left(\frac{\partial \hat{\phi}_i}{\partial \hat{x}}\right)^2 \mathrm{d}\hat{x} \tag{2.72}$$

$$K_{3,eff,i} = \frac{\mathrm{EA}}{2\mathrm{L}} \left[\int_0^{\mathrm{L}} \left(\frac{\partial \hat{\phi}_i}{\partial \hat{x}}\right)^2 \mathrm{d}\hat{x}\right]^2 . \tag{2.73}$$

And the behavior of the beam, for a given mode of vibration, can be approximated by a mass-spring model, allowing to use known analysis techniques.
At this point, two important considerations must be done. Firstly, the beam, in all cases, is supposed to be oscillated at its first vibration mode, as shown in Figure 2.5. The equation of the first modal vibration of a clamped-clamped beam is as follows

$$\hat{\phi}_1(\hat{x}/L) = \gamma \left(\sinh(\beta\hat{x}/L) - \sin(\beta\hat{x}/L) + \alpha(\cosh(\beta\hat{x}/L) - \cos(\beta\hat{x}/L))\right) \tag{2.74}$$

where $\alpha = -1.018$, $\beta = 4.730$ and $\gamma = -0.618$ [170]. Using this definition, $\phi_1(\hat{x}/(2L)) = 1$, and this is convenient because it implies that $\hat{w}(L/2, \hat{t}) = \hat{q}_1(t)$, or what its the same, $\hat{q}_1(t)$ is the position of the center of the beam.
Secondly, and associated to the actual design of each device, in most cases, as in Figure 2.5, the beam can have an actuator attached to its center point. In that case, the mass formulation must be corrected to capture all dynamic effects [170]. The corrected equivalent mass is as follows

$$\mathrm{M}_{eff,i} = \rho \mathrm{A} \int_0^{\mathrm{L}} \phi_i^2 \mathrm{d}\hat{x} + m_p \phi_i(\hat{x}_p)^2 , \tag{2.75}$$

where m_p is the added actuator mass and $\hat{x}_p$ is the position of the geometric center of the beam.
At the same time, the electrostatic potential energy associated with the actuator capacitor is defined as follows assuming a concentrated parameters formulation

$$U_e = -\frac{1}{2} \frac{\mathrm{C}}{(1 - \frac{\hat{q}_1(t)}{\mathrm{g}_0})} V^2 , \tag{2.76}$$

where

$$\mathrm{C} = \frac{\varepsilon_0\,\mathrm{A}_c}{\mathrm{g}_0}\left(1 + 0.65\frac{\mathrm{g}_0}{\mathrm{b}}\right)$$

is the capacitance at rest using a first-order fringing field correction [84], ε_0 is the dielectric constant, g_0 is the initial gap between the plates, b is the device thickness, A_c is the area of the plates, and V is the applied voltage between the electrodes.

Using the previous definitions, the dynamics of the whole system can be computed. Assuming, as usual, that the system behavior is sufficiently captured by the first mode of oscillation, the dynamic response of the beam in Figure 2.5 can be modeled by the lumped mass-spring-damper in Figure 2.6, given that $\hat{q}_1(t) \simeq \hat{y}(t)$, $\mathrm{M}_{eff,1} \simeq \mathrm{M}$, $\mathrm{K}_{eff,1} \simeq \mathrm{K}$ and $\mathrm{K}_{3,eff,i} \simeq \mathrm{K}_3$. The consideration of higher order modes would improve the accuracy of the model, as shown in [223], but at expense of the mathematical tools to be used.

Consequently, the dynamics of the system is derived using Lagrange's formulation, introducing the damping force [84], $\mathrm{F}_d = -\mathrm{B}\ \dot{\hat{y}}$ as the only non-conservative force contributing to the work (W) of the system

$$\mathrm{M}\ \ddot{\hat{y}} + \mathrm{K}\ \hat{y} + \mathrm{K}_3\ \hat{y}^3 - \frac{1}{2}\frac{\mathrm{C}_0}{\mathrm{g}_0(1-\frac{\hat{y}}{\mathrm{g}_0})^2}V^2 = -\mathrm{B}\ \dot{\hat{y}} \tag{2.77}$$

This is the dynamics equation of a concentrated-parameters mass-spring-damper with parallel-plate electrostatic actuation and a nonlinear spring (Figure 2.6).

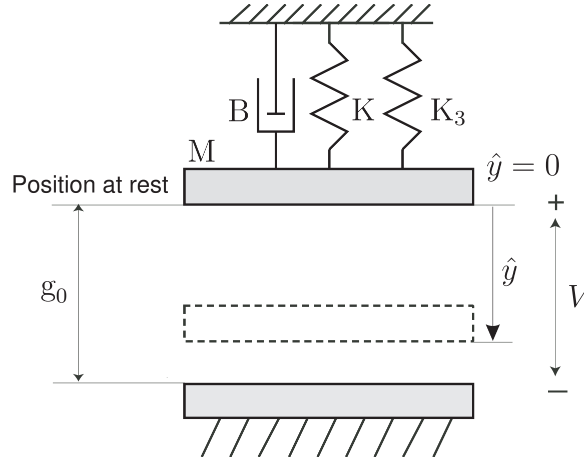

Figure 2.6: Schematics of an electromechanical system with parallel-plate actuation. It includes a linear spring, a nonlinear spring and linear velocity damping.

Normalizing the displacement $y = \hat{y}/\mathrm{g}_0$, the system behavior is defined by

$$\frac{d^2y}{dt^2} + \frac{\omega_\mathrm{n}}{\mathrm{Q}}\frac{dy}{dt} + \omega_\mathrm{n}^2 y + \kappa y^3 = \mathrm{f}_k\mathrm{g}_k\frac{V^2}{(1-y)^2} \tag{2.78}$$

where $\mathrm{C_0} = \frac{\epsilon \mathrm{A_c}}{\mathrm{g_0}}$, $\mathrm{f}_k = \frac{\mathrm{C_0}}{2\mathrm{g_0}}$, $\mathrm{g}_k = \frac{1}{\mathrm{g_0 M}}$, $\frac{\mathrm{B}}{\mathrm{M}} = \frac{\omega_\mathrm{n}}{\mathrm{Q}}$, $\frac{\mathrm{K}}{\mathrm{M}} = \omega_\mathrm{n}^2$ and $\kappa = \frac{\mathrm{K_3 g_0^2}}{\mathrm{M}}$, being ω_n the natural frequency of the system, $\mathrm{Q} = \frac{1}{2\zeta}$ the quality factor and ζ the damping of the system.
Finally, in some analysis, it is better to work with the resulting normalized actuation gap (g), in that case, the variable change is $g = 1-y$ and once introduced into equation (2.78) gives

$$-\frac{d^2g}{dt^2} - \frac{\omega_\mathrm{n}}{\mathrm{Q}}\frac{dg}{dt} + \omega_\mathrm{n}^2(1-g) + \kappa(1-g)^3 = \mathrm{f}_k\mathrm{g}_k\frac{V^2}{g^2} \tag{2.79}$$

Rearranging terms:

$$\left(-\frac{d^2g}{dt^2} - \frac{\omega_\mathrm{n}}{\mathrm{Q}}\frac{dg}{dt} + \omega_\mathrm{n}^2 + \kappa - \omega_\mathrm{n}^2 g - 3\kappa g + 3\kappa g^2 - \kappa g^3\right)g^2 = \mathrm{f}_k\mathrm{g}_kV^2 \tag{2.80}$$

or

$$-\frac{d^2g}{dt^2}g^2 - \frac{\omega_\mathrm{n}}{\mathrm{Q}}\frac{dg}{dt}g^2 + (\omega_\mathrm{n}^2+\kappa)g^2 - (\omega_\mathrm{n}^2+3\kappa)g^3 + 3\kappa g^4 - \kappa g^5 = \mathrm{f}_k\mathrm{g}_kV^2 \tag{2.81}$$

To simplify the complexity, a final rearrangement can be done

$$\Big(-\big(\frac{d^2g}{dt^2} + \frac{\omega_\mathrm{n}}{\mathrm{Q}}\frac{dg}{dt} + \omega_\mathrm{n}^2 g + \kappa g^3\big) + \omega_\mathrm{n}^2 + \kappa - 3\kappa g + 3\kappa g^2\Big)g^2 = \mathrm{f}_k\mathrm{g}_kV^2 \tag{2.82}$$

and finally, the equation converts to

$$-H(g)g^2 + \Big((\omega_\mathrm{n}^2+\kappa)g^2 - 3\kappa g^3 + 3\kappa g^4\Big) = \mathrm{f}_k\mathrm{g}_kV^2 \tag{2.83}$$

where we define $H(g)$ as

$$H(g) = \frac{d^2g}{dt^2} + \frac{\omega_\mathrm{n}}{\mathrm{Q}}\frac{dg}{dt} + \omega_\mathrm{n}^2 g + \kappa g^3 \tag{2.84}$$

englobing the standard nonlinear equation of a mechanical system.

2.4 Conclusions

Correct modeling of parallel-plate electrostatic actuation of MEMS is an important step to design better MEMS devices. It has been shown that different approaches can be taken to try to capture the behavior of the devices, but lots of issues are yet to be solved.
This work has tried to compile the main approaches in the literature in order to analyze the advantages of each one. The main conclusion achieved is that depending on the goal while designing MEMS actuators, the complexity of the model has to be evaluated. Complete models involved time-consuming calculations while reduced models imply reduced accuracy.

Table 2.1 shows a summarized classification of the different approaches in the literature and the analyzed phenomena.

A concentrated parameters model has been developed, based on the dissertation needs. It is a good compromise between complexity and accuracy, and it will allow to perform the needed analysis.

Chapter 3

Pull-in analysis in MEMS resonators

3.1 Introduction

Consider the lumped model (2.77) derived in the previous Chapter. With the usual assumption of voltage-controlled actuation, the pull-in instability is the main limitation to the position of the capacitor plates in the gap. As shown in Figure 3.1, in the linear spring case ($K_3 = 0$), the static pull-in occurs when the distance between plates is 2/3 of the initial gap. What means that most of the gap cannot be used.

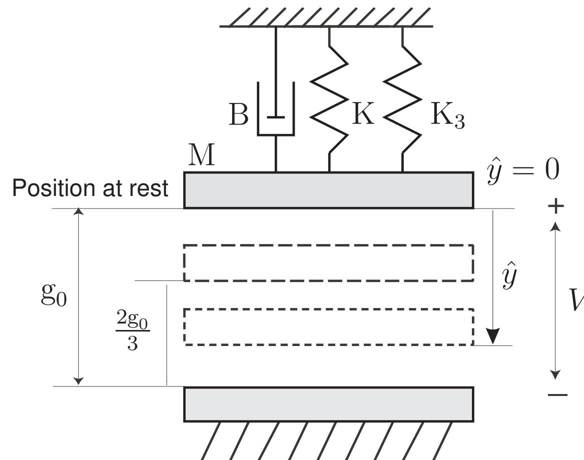

Figure 3.1: Schematics of an electromechanical system with parallel-plate actuation and nonlinear mechanical spring.

This Chapter uses the analysis of the evolution of the total energy of the system based on equation (2.77)

$$E = \frac{1}{2}\mathrm{M}\,\dot{\hat{y}}^2 + \frac{1}{2}\mathrm{K}\,\hat{y}^2 + \frac{1}{4}\mathrm{K}_3\,\hat{y}^4 - \frac{1}{2}\frac{\mathrm{C}_0}{(1-\frac{\hat{y}}{\mathrm{g}_0})}V^2 \tag{3.1}$$

to determine the equilibrium positions of the device, as well as, the regions of instability. Dynamics is studied as an important factor affecting the stability of the system.

3.2 Static Pull-in case

In static equilibrium, $\ddot{\hat{y}} = \dot{\hat{y}} = 0$, the energy of the system (3.1) consists only of potential energy terms:

$$E = \frac{1}{2}\mathrm{K}\ \hat{y}^2 + \frac{1}{4}\mathrm{K}_3\ \hat{y}^4 - \frac{1}{2}\frac{\mathrm{C}_0}{(1-\frac{\hat{y}}{\mathrm{g}_0})}V^2 \tag{3.2}$$

As a result, the distribution of the system energy along the gap between the electrodes is constant and unique for each voltage applied, as can be observed in Figure 3.2.

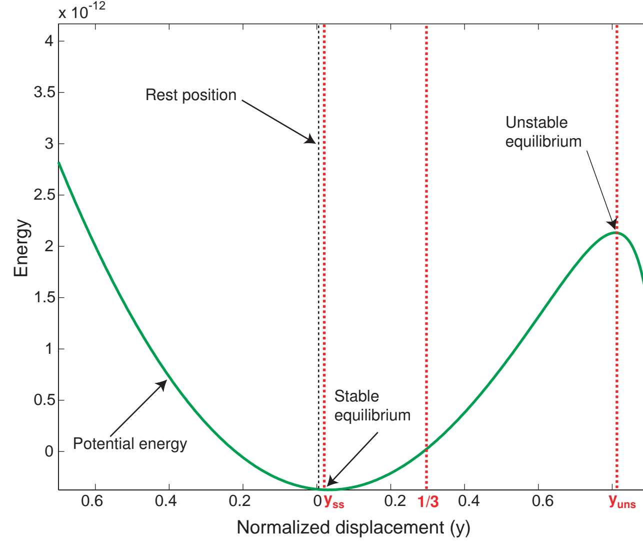

Figure 3.2: Typical potential energy profile of the system for a given voltage.

For low voltages, the energy profile is composed of a stable equilibrium position near the initial position of the system and an unstable equilibrium position near the opposing capacitor plate (Figure 3.2). As the voltage increases, both equilibrium positions migrate (e.g. 10 V to 50 V in Figure 3.3) until they merge into an inflection point of the energy curve (e.g. 91.69 V in Figure 3.3). Once this voltage limit is reached, no equilibrium positions exist. The limiting condition for existence of a stable equilibrium is the presence of an inflection point in (3.2) defined by $\frac{d^2E}{d\hat{y}^2} = 0$. This condition provides the analytical value for the maximum static stable displacement from the initial equilibrium ($\hat{y}_{spv}$) and the voltage needed to reach this position. This voltage limit is the *Static Pull-in Voltage* (SPV). The values can be obtained analytically using the following formulas [136]

$$\hat{y}_{spv} = \frac{\mathrm{g}_0}{5} + \mathrm{g}_0\left[\frac{5\beta+1}{125} + \frac{\sqrt{5\beta^3 - 2\beta^2 + \beta}}{25}\right]^{\frac{1}{3}} \tag{3.3}$$

$$- \mathrm{g}_0\frac{5\beta-1}{25}\left[\frac{5\beta+1}{125} + \frac{\sqrt{5\beta^3 - 2\beta^2 + \beta}}{25}\right]^{-\frac{1}{3}} \tag{3.4}$$

$$SPV = \sqrt{\frac{2\,\mathrm{K}\,\mathrm{g}_0^2}{\mathrm{C}_0}\,\frac{\hat{y}_{spv}}{\mathrm{g}_0}\left(1+\frac{\hat{y}_{spv}^2}{\beta \mathrm{g}_0^2}\right)\left(1-\frac{\hat{y}_{spv}}{\mathrm{g}_0}\right)^2}. \tag{3.5}$$

In this expression, the nonlinear spring factor of a beam is introduced, $\beta = \mathrm{K}/(\mathrm{K}_3\,\mathrm{g}_0^2)$. The β-factor indicates the significance of the nonlinear spring in front of the linear one. The importance of taking into account the nonlinear spring (K_3) can be observed in Figure 3.3, where the potential energy curves using a linear stiffness model and nonlinear stiffness model are plotted. For small displacements from the rest position the influence is negligible, but as the displacement is increased, the effect becomes important. In the example, pull-in instability occurs when the moving plate reaches to 47% of the total gap displacement, farther than the usual 1/3 value.

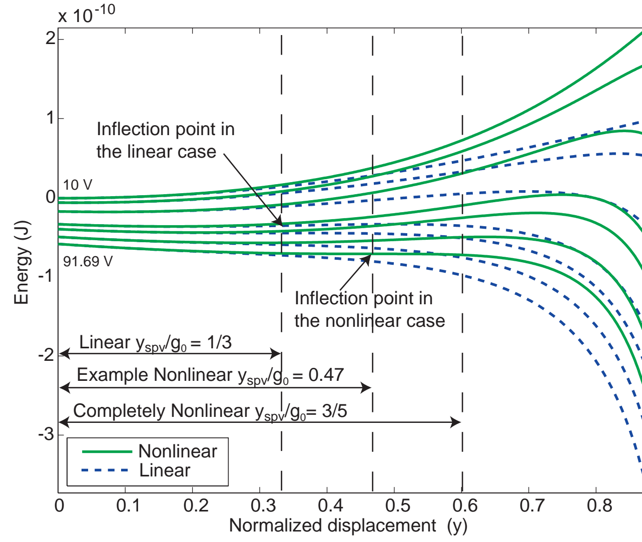

Figure 3.3: Potential energy of the system versus normalized displacement for different applied voltages are displayed (10 V, 30 V ,50 V, 69.45 V, 75.61 V, 84.41 V, 91.69 V), including the *Static Pull-in Voltage* and the *Dynamic Pull-in Voltage* of the example for the linear case (75.61 V and 69.45 V) and nonlinear case (91.69 V and 84.41 V).

For the case of linear spring assumption ($\mathrm{K}_3 = 0$), the resulting value is the classical *Static Pull-in Voltage* and its corresponding displacement:

$$\mathrm{SPV} = \sqrt{\frac{8}{27}\frac{\mathrm{K}\,\mathrm{g}_0^2}{\mathrm{C}_0}}\ ;\ \hat{y}_{spv} = \frac{\mathrm{g}_0}{3}. \tag{3.6}$$

The study of (3.3) and (3.5) reveals that the maximum displacement is obtained when the spring is completely nonlinear ($\mathrm{K} = 0$), and this maximum displacement is 3/5 of the initial gap [136]. This can be observed in Figure 3.4, where it is shown that the nonlinearity is important for values of β smaller than 20, and when β is smaller than

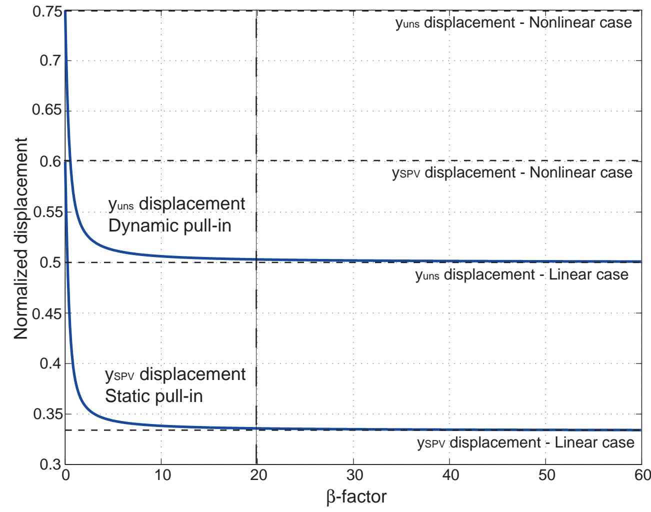

Figure 3.4: Influence of β-factor on the value of the *Static Pull-in displacement* and the *Dynamic Pull-in displacement*.

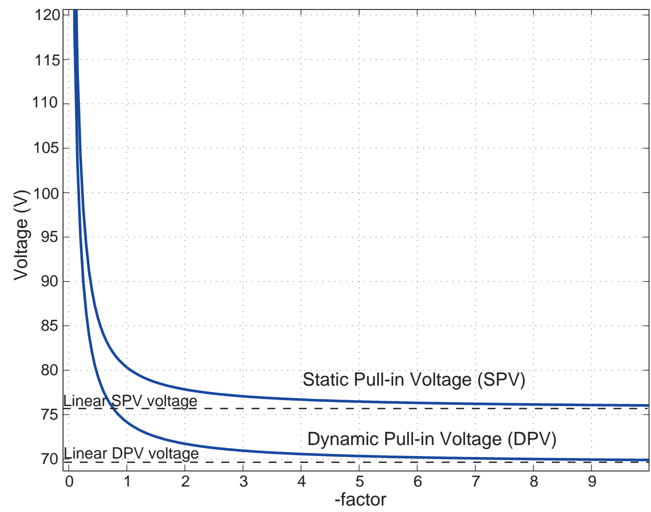

Figure 3.5: Influence of β-factor on the value of the *Static Pull-in Voltage* and the *Dynamic Pull-in Voltage* for one of the fabricated MEMS resonators. To calculate the values, the linear parameters are used, and the nonlinear spring is increased to observe the effect on the pull-in voltages.

2 it cannot be neglected. The same evolution appears for the SPV values, as shown in Figure 3.5. Increasing the nonlinearity in the mechanical spring increases the *Static Pull-in Voltage*.

3.3 Dynamic Pull-in case

The derivations for the static case neglect the transient effects that occur in the system when the voltage is applied. In some cases such approximation is correct, for example, if the voltage is slowly applied or the system is highly-damped. However, for low damping, e. g. in a vacuum environment, the transient dynamics must be taken into account.
The energy analysis can be expanded to account for the transient dynamics of the system when an actuation voltage is applied.
The time derivative of the system energy as defined in (3.1) is

$$\frac{dE}{dt}(t) = \left(\mathrm{M}\ \ddot{\hat{y}}(t) + \mathrm{K}\ \hat{y}(t) + \mathrm{K}_3\ \hat{y}(t)^3 - \frac{1}{2}\frac{\mathrm{C}_0}{\mathrm{g}_0(1-\frac{\hat{y}(t)}{\mathrm{g}_0})^2}\ V^2 \right)\ \dot{\hat{y}}(t) \tag{3.7}$$

and using the dynamic equation of the system equivalence (2.77),

$$\mathrm{M}\ \ddot{\hat{y}}(t) + \mathrm{K}\ \hat{y}(t) + \mathrm{K}_3\ \hat{y}(t)^3 - \frac{1}{2}\frac{\mathrm{C}_0}{\mathrm{g}_0(1-\frac{\hat{y}(t)}{\mathrm{g}_0})^2}\ V(t)^2 = -\mathrm{B}\ \dot{\hat{y}}(t)$$

the resulting equation is

$$\frac{dE}{dt}(t) = -\mathrm{B}\ \dot{\hat{y}}(t)^2 \tag{3.8}$$

indicating that, unless energy is continuously pumped into the system, the energy decreases with time from its initial energy value until it reaches an equilibrium state, $\frac{dE}{dt} = 0$. According to the model, the only factor that defines the pattern of the energy decay is the damping, B, of the system.
As can be observed in Figure 3.6, the initial energy corresponds to the potential energy (mechanical and electrostatic). When the motion begins, the potential energy is converted to kinetic energy and dissipation due to damping forces. The energy of the system is dissipated until the stable equilibrium position is reached.
The maximum amplitude of displacement of the moving plate is limited by the potential energy bound. If the voltage is increased, at some point the initial energy of the system and the energy at the unstable peak have the same magnitude (Figure 3.7). Assuming that the system has no damping, the total energy of the system remains constant, which

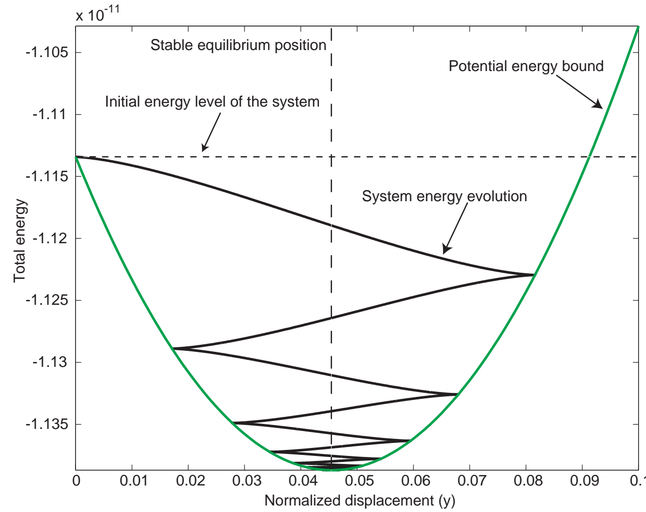

Figure 3.6: Evolution of system's energy when a 40 V step-function is applied. In the example the Quality Factor is 7.

implies that when applying a higher voltage the system will move until it overshoots the unstable equilibrium ($\hat{y}_{uns}$), and the electrodes will collide. This voltage limit is called *Dynamic Pull-in Voltage* (DPV). Any voltage lower than DPV magnitude cannot produce snapping.

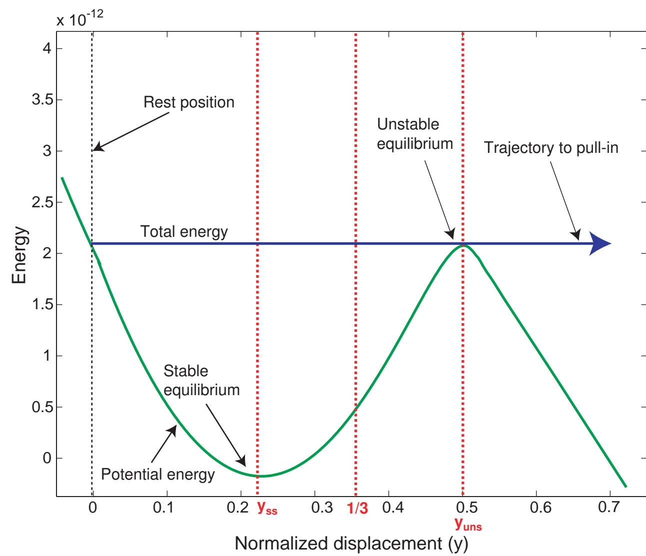

Figure 3.7: Evolution of system's energy when the *Dynamic Pull-in Voltage* is applied and no damping term exists

In order to obtain the *Dynamic Pull-in Voltage (DPV)*, the potential energy at rest must be equated to the energy at the unstable equilibrium. This will give the maximum amplitude that can be reached during the step evolution ($\hat{y}_{uns}$) and the maximum voltage that can be applied (DPV). Using the same terminology as in (3.3), the displacement

expression is

$$\hat{y}_{uns} = \frac{g_0}{4} + g_0 \left[\frac{8\beta + 1}{64} + \frac{\sqrt{768\beta^3 - 108\beta^2 + 162\beta}}{144} \right]^{\frac{1}{3}} - g_0 \frac{16\beta - 3}{48} \left[\frac{8\beta + 1}{64} + \frac{\sqrt{768\beta^3 - 108\beta^2 + 162\beta}}{144} \right]^{-\frac{1}{3}} \tag{3.9}$$

and the corresponding *Dynamic Pull-in Voltage* is

$$DPV = \sqrt{\frac{2Kg_0^2 - 16K\hat{y}_{uns}^2 + 20K\hat{y}_{uns}g_0 + 3K_3\hat{y}_{uns}^2 g_0^2}{32\,C_0}}. \tag{3.10}$$

Again, if a linear spring is used, the analytical expression has a simplified form. In this case, the voltage limit has always the unstable equilibrium at the center of the gap and is described by the following expression [76]

$$\hat{y}_{uns} = \frac{g_0}{2}\ ;\ DPV = \sqrt{\frac{1}{4}\frac{K\,g_0^2}{C_0}}. \tag{3.11}$$

As can be observed, the expressions have some similarities with the static case. Figures 3.4 and 3.5 show the evolution of the *Static and Dynamic Pull-in* parameters with the variation of the nonlinear factor (β). Static and Dynamic parameters behave in the same manner. Values of β higher than 20 indicate the suitability of a linear model. Values of β smaller than 2 indicate that the nonlinearities are predominant. In the case of the *Dynamic Pull-in displacement*, the maximum displacement during the evolution reaches up to 3/4 of the gap in the case of a completely nonlinear spring.

Consequently, equations (3.9) and (3.10) expand prior *Dynamic Pull-in Voltage* formulations to the whole range of values of nonlinear springs.

Another important aspect is the relationship between the *Static* and *Dynamic Pull-in Voltage*. Figure 3.8 shows the simulation analysis of the pull-in voltage as a function of the damping of the system (ζ) and the nonlinear factor (β). The Quality Factor, $Q = \frac{\sqrt{MK}}{B} = \frac{1}{2\zeta}$, is introduced as a usual parameter to evaluate the damping. As can be observed, in highly-damped systems ($Q \approx 0$) the voltage needed to produce snapping corresponds to the *Static Pull-in Voltage*. As the Quality Factor increases, the voltage value decreases until it settles at the *Dynamic Pull-in Voltage*. This happens for the whole range of spring values, from the linear case to the completely nonlinear case, and with the same pattern.

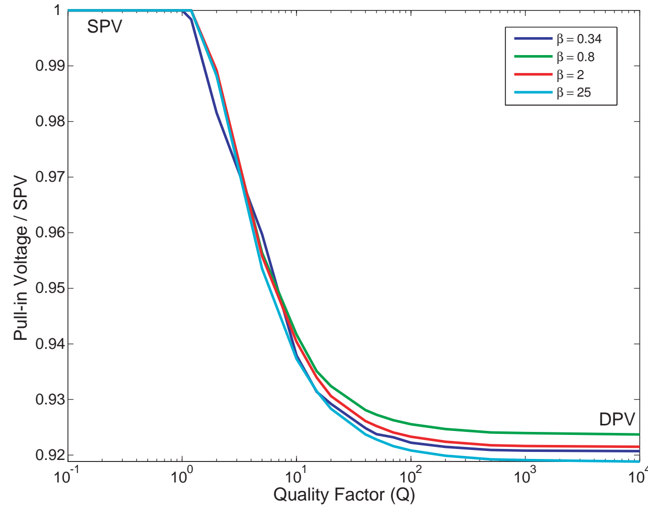

Figure 3.8: Comparison of the evolution of the pull-in voltage as a function of the Quality Factor, depending on the nonlinear factor (β). Simulation is carried out to determine the exact Pull-in Voltage at which snapping is produced when a voltage step is applied. The values are normalized for better comparison, by dividing the calculated Pull-in Voltage by the SPV.

3.4 Oscillatory Pull-in case

In those cases where the system is dynamically actuated to resonance, as in oscillators, accelerometers or gyroscopes, the stability analysis becomes more difficult.

Under forced oscillation, the voltage varies with time, $V(t) = \mathrm{V_{DC}} + V_{\mathrm{AC}}(t)$, meaning that the energy equilibrium points given by $\frac{dE}{dy}$ are changing continuously

$$\frac{dE}{d\hat{y}}(t) = \mathrm{K} \cdot \hat{y}(t) + \mathrm{K_3} \cdot \hat{y}(t)^3 - \frac{1}{2}\frac{\mathrm{C_0}}{\mathrm{g_0}(1 - \frac{\hat{y}(t)}{\mathrm{g_0}})^2} V(t)^2 = 0 \tag{3.12}$$

As will be shown in Chapter 4, the oscillatory behavior becomes more complex, and phase-plane analysis is needed to predict the regions of stability.

However, a special case can be analyzed that gives insight in the underlying phenomena and allows to predict the limiting actuation voltages. This is the actuation of the system at resonant-like frequency with a square voltage function. This case can be analytically treated, due to the piece-wise characteristics of the actuation, and allows to define the *Resonant Pull-in Condition.*

3.4.1 Resonant Pull-in case

If the alternating voltage $V_{\mathrm{AC}}(t)$ is considered to be a square-function, at each half period the system behaves like in the dynamic case when a constant load is applied. When the voltage changes, the energy of the system jumps to the other energy region (Figure 3.9).

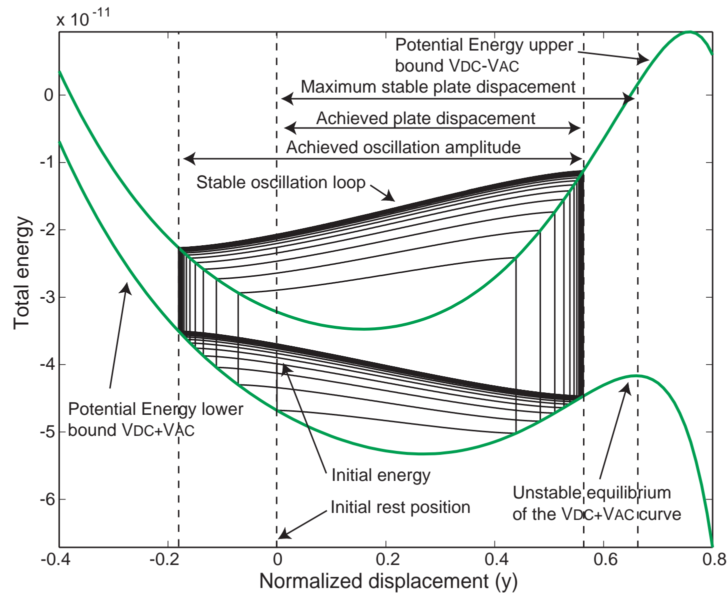

a)

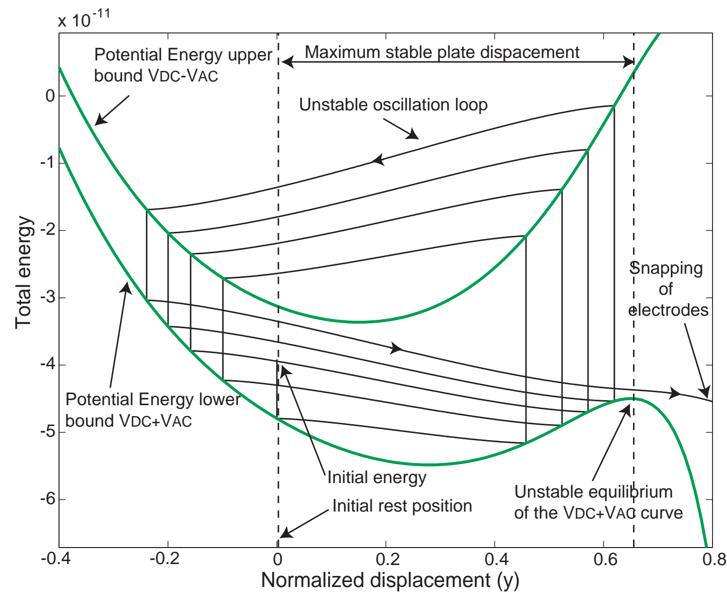

b)

Figure 3.9: a) Energy loop showing a stable oscillation with 75 V_{DC} bias voltage and a 7 V_{AC} amplitude. b) Energy loop showing an unstable oscillation with 75 V_{DC} and 8 V_{AC}.

Consequently, as in the dynamic case, the potential energy curves bound the evolution of the total energy of the system and their analysis allow to determine the maximum amplitude of oscillation that can be achieved without reaching the pull-in zone. Figure 3.9a shows an stable oscillation loop with the energy bounded, while Figure 3.9b shows another example where the amplitude of oscillation increases until it reaches the unstable equilibrium point at $\mathrm{V_{DC}} + \mathrm{V_{AC}}$, resulting in snapping.

Equation (3.12) provides the condition for the extreme points of the energy function. Solving the equation for $V(t) = \mathrm{V_{DC}} + \mathrm{V_{AC}}$, and discriminating maximum and minimum points using the second derivative, we can define $\hat{y}_{uns}$ as the unstable equilibrium (maximum) of the $\mathrm{V_{DC}} + \mathrm{V_{AC}}$ potential energy curve. Oscillations smaller than $\hat{y}_{uns}$ are stable, while larger oscillations lead to pull-in [64].

In the resonant case, energy is continuously pumped into the system trying to reach the resonant frequency. Then, conceptually, stable actuation occurs while the energy of the system is confined in the valley of the potential energy.

As shown in Figure 3.10, using the *Resonant Pull-in Algorithm* [64] an oscillating loop in the energy domain close to the maximum amplitude can be generated to analyze the stability of the oscillation. For a complete driving voltage time-period, an oscillating loop is constructed, estimating the energy decay from the value of the Quality Factor of the system. When the loop is closed, amplitude increase determines that the system is unstable, while amplitude decrease indicates that the system is stable.

3.4.2 Resonant Pull-in Condition

Using the energy evolution in an steady-state oscillation loop presented in the previous section, under the square-function driving voltage assumption, the *Resonant Pull-in Condition* can be derived.

The energy decay during the oscillation is controlled by the damping constant (B). Assuming that the oscillation is sinusoidal, $\hat{y}(t) = \hat{Y}_1 \sin(\omega t)$, the value of the energy losses due to damping forces at each half period can be estimated as

$$E_{lost} = -\mathrm{B}\hat{\mathrm{Y}}_1^2 \omega \frac{\pi}{2} \tag{3.13}$$

where $\hat{Y}_1$ is the amplitude of oscillation and ω is the resonant frequency of oscillation of the system. The resonant frequency is usually different from the natural frequency of the mechanical system, $\omega_{\mathrm{n}} = \sqrt{\frac{\mathrm{K}}{\mathrm{M}}}$.

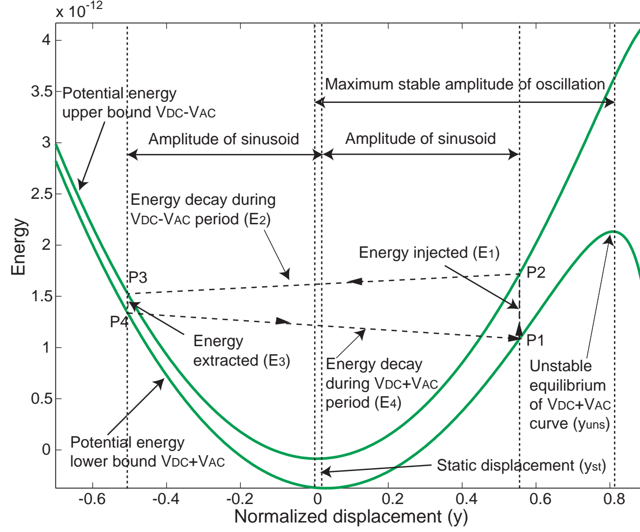

Figure 3.10: *Resonant Pull-in Algorithm.* The energy evolution presented for the actuation voltage is stable as it generates a closed loop. The energy injected by the actuation is balanced with the damping losses.

Consequently, the stability of oscillation will depend on the energy balance between the energy gained due to $V(t) = \mathrm{V_{DC}} + V_{\mathrm{AC}}(t)$ actuation and the energy lost due to damping [180].

In an energy oscillation loop, four energy terms are considered: E_1, E_2, E_3, E_4 (Figure 3.10). The initially gained energy (E_1), when moving from $\mathrm{V_{DC}}+\mathrm{V_{AC}}$ curve to $\mathrm{V_{DC}}-\mathrm{V_{AC}}$ curve is

$$
\begin{aligned}
E_1 =& \left[\frac{1}{2}\mathrm{K}\ (\hat{y}_{st}+\hat{Y}_1)^2 + \frac{1}{4}\mathrm{K}_3\ (\hat{y}_{st}+\hat{Y}_1)^4 - \frac{1}{2}\frac{\mathrm{C}_0(\mathrm{V_{DC}}-\mathrm{V_{AC}})^2}{(1-(\hat{y}_{st}+\hat{Y}_1)/\mathrm{g}_0)}\right] \\
&- \left[\frac{1}{2}\mathrm{K}\ (\hat{y}_{st}+\hat{Y}_1)^2 + \frac{1}{4}\mathrm{K}_3\ (\hat{y}_{st}+\hat{Y}_1)^4 - \frac{1}{2}\frac{\mathrm{C}_0(\mathrm{V_{DC}}+\mathrm{V_{AC}})^2}{(1-(\hat{y}_{st}+\hat{Y}_1)/\mathrm{g}_0)}\right] \\
=& \frac{2\,\mathrm{C}_0\mathrm{V_{DC}}\,\mathrm{V_{AC}}}{(1-(\hat{y}_{st}+\hat{Y}_1)/\mathrm{g}_0)}
\end{aligned}
\tag{3.14}
$$

where $\hat{y}_{st}$ is the position displacement of the electrode due to the $\mathrm{V_{DC}}$ bias. In this expression, $\hat{y}_{st}+\hat{Y}_1$ represents the effective maximum position in the gap.

The energy losses due to damping during the $\mathrm{V_{DC}}-\mathrm{V_{AC}}$ half-period (E_2) are

$$
E_2 = -\mathrm{B}\hat{Y}_1^2\omega\frac{\pi}{2}. \tag{3.15}
$$

The energy reduction when moving from $\mathrm{V_{DC}}-\mathrm{V_{AC}}$ curve to $\mathrm{V_{DC}}+\mathrm{V_{AC}}$ curve, obtained in a similar way as in (3.14) is

$$
E_3 = -\frac{2\,\mathrm{C}_0\,\mathrm{V_{DC}}\,\mathrm{V_{AC}}}{(1-(\hat{y}_{st}-\hat{Y}_1)/\mathrm{g}_0)} \tag{3.16}
$$

where $\hat{y}_{st} - \hat{Y}_1$ represents the effective minimum amplitude position in the gap.

And finally, the energy losses due to damping during the $\mathrm{V_{DC}} + \mathrm{V_{AC}}$ half-period (E_4) are

$$E_4 = -\mathrm{B}\hat{Y}_1^2 \omega \frac{\pi}{2}. \tag{3.17}$$

If the system is actuated at a stable resonant-like frequency, there must exist an amplitude of oscillation where the energy balance of the loop is zero. Consequently, the following equation has to be satisfied

$$E_1 + E_2 + E_3 + E_4 = \frac{4\,\mathrm{C_0 g_0}\,\mathrm{V_{DC}}\,\mathrm{V_{AC}}\,\hat{Y}_1}{(\mathrm{g_0} - \hat{y}_{st})^2 - \hat{Y}_1^2} - \mathrm{B}\hat{Y}_1^2 \omega \pi = 0. \tag{3.18}$$

Rearranging terms in (3.18), the amplitude of oscillation of the stable loop, $\hat{Y}_1$, can be obtained from the following equation

$$\hat{Y}_1^3 - (\mathrm{g_0} - \hat{y}_{st})^2\,\hat{Y}_1 + \frac{4\,\mathrm{C_0}\,\mathrm{g_0}\,\mathrm{V_{DC}}\,\mathrm{V_{AC}}}{\mathrm{B}\omega\pi} = 0. \tag{3.19}$$

The equation can be solved analytically. However, to predict the existence of stable oscillation, we only need to know the type of solutions of equation (3.19). This analysis can be done through the third order polynomial discriminant, D, of the equation

$$D = -\frac{1}{27}(\mathrm{g_0} - \hat{y}_{st})^6 + \frac{4\,\mathrm{C_0^2}\,\mathrm{g_0^2}\,\mathrm{V_{DC}^2}\,\mathrm{V_{AC}^2}}{\mathrm{B}^2\omega^2\pi^2}. \tag{3.20}$$

In a cubic polynomial, $D = 0$ identifies the transition between all-real solutions and the existence of complex solutions. Applied to the parallel-plate system, this equation leads to the *Resonant Pull-in Condition (RPC)*

$$RPC = \mathrm{V_{DC}}\,\mathrm{V_{AC}} = \frac{\mathrm{B}\,\omega\,\pi\,(\mathrm{g_0} - \hat{y}_{st})^3}{6\sqrt{3}\,\mathrm{C_0}\,\mathrm{g_0}} \tag{3.21}$$

that provides the maximum value of the product $\mathrm{V_{DC}}\,\mathrm{V_{AC}}$ producing stable oscillation. Once the $\mathrm{V_{DC}}$ load applied to the system is defined, the static displacement ($\hat{y}_{st}$) can be calculated, and accordingly, the real resonant frequency (ω) can be estimated, for example, using the voltage-corrected frequency

$$\omega_e = \sqrt{\frac{\mathrm{K} - \frac{\mathrm{C_0 V_{DC}^2}}{\mathrm{g_0^2}}}{\mathrm{M}}}. \tag{3.22}$$

Consequently, the *Resonant Pull-in Condition* defines a constructive domain of $\mathrm{V_{DC}}$ and $\mathrm{V_{AC}}$ actuation voltages versus Quality factor preserving stability of the parallel-plate actuation.

As can be observed, the introduction of the nonlinear spring in the model does not change the *Resonant Pull-in Condition*, which is equal to that derived in the linear spring case [63].

In case of only V_{AC} actuation, two-sided push-pull actuation is needed with square-function voltages, and equation (3.21) transforms to

$$RPC = V_{AC} = \sqrt{\frac{B\,\omega\,\pi\,g_0^2}{\sqrt{27}\,C_0}} \tag{3.23}$$

as presented in [180]. Again the derivation holds even considering large amplitudes and nonlinear spring behavior.

It is important to notice that at resonant frequency the maximum amplitude of oscillation is limited. In [180] it was indicated that in two-sided actuation the maximum amplitude of oscillation is

$$\hat{Y}_1 = \frac{g_0}{\sqrt{3}}, \tag{3.24}$$

that corresponds to the maximum displacement in the gap.

In the case of $V_{DC} + V_{AC}$ actuation, this limitation translates to

$$\hat{Y}_1 = \frac{g_0 - \hat{y}_{st}}{\sqrt{3}}, \tag{3.25}$$

obtained by substitution of the *Resonant Pull-in Condition* in equation (3.19). Consequently, the maximum displacement in the capacitive gap is

$$\hat{y}_{max} = \hat{y}_{st} + \frac{g_0 - \hat{y}_{st}}{\sqrt{3}}. \tag{3.26}$$

3.4.3 Experimental validation

A family of Silicon-On-Insulator (SOI) MEMS resonators were fabricated (Figure 1.1), in order to experimentally validate the *Resonant Pull-in Condition*. The structures were fabricated in the *Centro Nacional de Microelectrònica - Barcelona* using a one mask bulk-micromachining process, based on deep-reactive ion etching (DRIE) through the 15 to 70 μm device layer of silicon-on-insulator wafers [4]. In Table 3.1 the main parameters of two of the MEMS resonators used for experiments are summarized. The parameters have been obtained from the initial fabrication designs and corrected taking into account the observed fabrication imperfections.

In the case of the *1500-Model* (Table 3.1), the classical pull-in analysis defines that the static instability (3.6) occurs at 75.61 V, when the gap becomes approximately 7.6 μm.

	1500-Model	2500-Model
Stiffness K	$2.066\ N/m$	$1.766\ N/m$
Nonlinear Stiffness K_3	$4.678 \cdot 10^{10}\ N/m^3$	$4.463 \cdot 10^{10}\ N/m^3$
Mass M	$6.753 \cdot 10^{-10}\ Kg$	$3.830 \cdot 10^{-9}\ Kg$
Initial gap g_0	$11.4\ \mu m$	$11.3\ \mu m$
Parallel-plate actuator A_c	$800 \cdot 15\ \mu m^2$	$800 \cdot 75\ \mu m^2$
Beam length L	$1500\ \mu$	$2500\ \mu$
Beam width h	$5.6\ \mu$	$5.3\ \mu$
Device thickness b	$15\ \mu$	$70\ \mu$
Nominal frequency f_n	$8.804\ kHz$	$3.41\ kHz$
β-factor	0.34	0.31

Table 3.1: Structural parameters of the fabricated devices

Introduction of the existing nonlinear effects allows to conclude that the allowed driving voltage (3.5) is in fact larger, 91.69 V, and the final remaining gap much smaller, 6.01 μm (3.3).

If the dynamics of the system is taking in consideration, the classical *Dynamic Pull-in Voltage* formulation (3.11) gives 69.45 V, as the minimum voltage that can produce dynamic snapping. It has been shown that the introduction of the nonlinear spring constant has its effect on the *Dynamic Pull-in Voltage*. Using (3.10) it can be observed that the *Dynamic Pull-in Voltage* increases up to 84.41 V due to the nonlinear forces. In this case, the minimum gap during the evolution would be 4.15 μm from (3.9). The snapping for voltages higher than this value will depend on the damping of the system, which is directly proportional to the air pressure of packaged micro-devices. For low pressure or vacuum conditions, voltages higher than DPV would imply snapping (Figure 3.8).

As can be observed, calculation of *Static Pull-in Voltage* and *Dynamic Pull-in Voltage* are very much dependent on the nonlinearities of the system (Figure 3.4 and Figure 3.5). In the MEMS resonator considered in this example, the β-factor is 0.34, what translates to increases of the needed voltage by 20%. This conclusion is important as it extends the stable range for non-snapping applications. On the contrary, it is a drawback for applications where pull-in is desired, showing that higher voltages are needed than those classically predicted.

These results show the importance of dynamics and nonlinearities when studying the stability of MEMS devices. They play an important role when the structure is dynamically actuated to its resonant frequency. In resonant devices, the instability (or snapping)

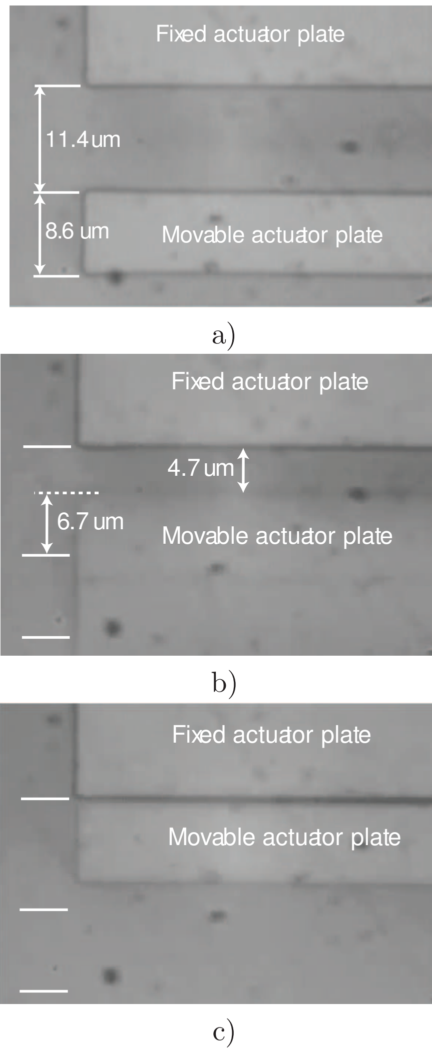

Figure 3.11: The set of pictures presents evolution of the amplitude of oscillation of the MEMS resonator in Figure 1.1 due to changes of AC-DC driving voltages. The pictures show a close-up of the parallel-plate electrodes. a) Beam at rest. b) Beam oscillating with 75 V_{DC} and 6.8 V_{AC}. c) Beam snapped after applying a combination of 75 V_{DC} and 6.9 V_{AC} drive voltages.

occurs at much smaller voltages. In the example presented in Figure 3.11, snapping occurred with 75 V DC-bias and 6.9 V AC peak-amplitude (The sum of the voltages is smaller than DPV = 84.41 V). During oscillation large stable amplitudes have been reached, or equivalently smaller gaps, approximately 4.7 μm in our case (60 % gap reduction). As can be observed, significantly larger amplitude of actuation can be achieved when dynamic actuation is used. The 'overshoot' effect of the static equilibrium is explained by the gained kinetic energy of the system which allows it to return to the stable region of actuation.

This dynamic behavior can be predicted using the *Resonant Pull-in Condition*. With resonant devices, it plays the same role as the *Static Pull-in Voltage* in positioning

applications or the *Dynamic Pull-in Voltage* in switching applications.

The experimental snapping values obtained for the *1500-Model* in air are presented in Figure 3.12. In the same plot, calculations of the *Resonant Pull-in Condition* are used to produce the combination of maximum allowed V_{DC} and V_{AC} voltages for values of the Quality Factor ranging from 4 to 6, which correspond to the range of Q of the device in air. As can be observed, experimental data is consistent with the analytically derived regions of instability.

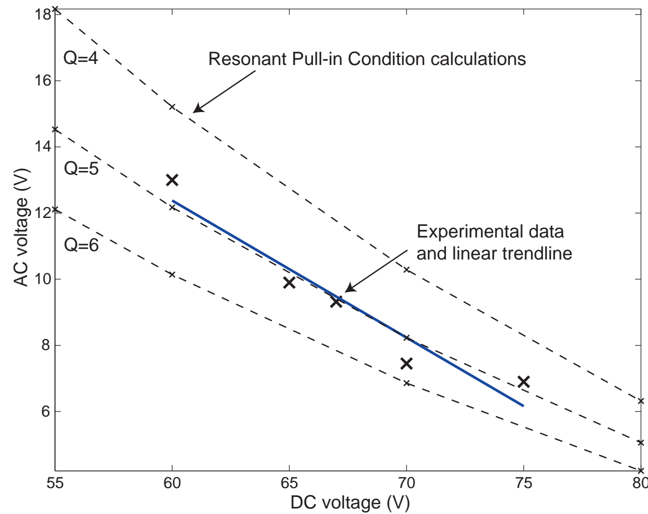

Figure 3.12: Maximum combinations of V_{DC} and V_{AC} voltages for the different values of the Quality Factor (Q) for the *1500-Model*. Values estimated with the *Resonant Pull-in Condition* are presented with the experimental data in air.

Furthermore, the same experimental testing was done for the *2500-Model* (Figure 3.13). In this comparison, results of *Resonant Pull-in Condition* obtained via direct time-integration of the system equations (2.77) at the testing environment conditions ($Q = 2$ for the *2500-Model*) are also provided. As can be observed, *Resonant Pull-in Condition* predictions show good agreement with experimental data.

The results in Figure 3.13 also show that *Resonant Pull-in Condition* predictions are close to the values obtained via numerical time-integration of the system equations (2.77). This is important because within the *Resonant Pull-in Condition* calculation, the resonant frequency is approximated by the voltage-corrected frequency (3.22). Figure 3.13 illustrates that this approximation has a small effect (5% error) in predicting the snapping values.

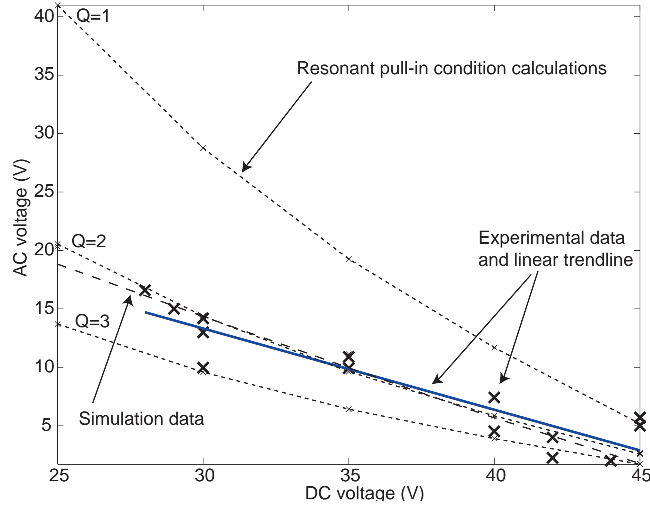

Figure 3.13: Maximum combinations of V_{DC} and V_{AC} voltages for the different values of the Quality Factor (Q) for the *2500-Model*. *Resonant Pull-in Condition* values are presented together with experimental data obtained in air, and data from the numerical time-integration of system equations for $Q = 2$.

3.5 Conclusions

Operation of electrostatically actuated MEMS with amplitudes much higher than 1/3 of the initial actuation gap can be achieved with appropriate selection of actuation voltages. The kinetic energy of the system gained during actuation allows the system to travel beyond the static equilibrium, reaching large amplitudes of oscillation without snapping.

Energy analysis has been used to define an unified framework to analyze pull-in voltages introducing nonlinear mechanical springs. Form this analysis, it has been derived the *Resonant Pull-in Condition* which provides the combination of maximum V_{DC} and V_{AC} voltages that can be used to actuate the system without producing snapping at resonance frequency.

Resonant Pull-in Condition (RPC) has been shown to predict snapping in fabricated MEMS devices at resonant actuation. However, it is known that transient effects can affect the nonlinear dynamic behavior of the system and lead the system to pull-in at lower voltages [134].

RPC can be a useful tool to design dynamic MEMS, along with the estimation of the *Static Pull-in Voltage* and the *Dynamic Pull-in Voltage*. The derived stability limits represent upper limits to the dynamic pull-in, beyond which no stable motion can exist.

Resonant Pull-in Condition can also be used as the first order solution for iterative

numerical simulation analysis or for prototyping.

It has also been shown that the *Resonant Pull-in Condition* can deal with nonlinear spring models, expanding the previously reported formulations.

Not only that, the importance of the derivation of the *RPC* is that it can be extended to different system configurations. In [36], the condition has been extended to include the quadratic springs that appear in prebuckled beams. In this case, as the goal is bistable switching, the *RPC* provides the voltages needed for resonant switching.

Chapter 4

Oscillation characterization of MEMS resonators

4.1 Introduction

This chapter studies the oscillations of electrostatically actuated MEMS resonators, taking special attention on the reachable stationary trajectories and the required input voltage. Combined analytic and numeric analysis on electrostatically actuated MEMS resonators is presented. The main behaviors are characterized.

The analytic analysis is based on Harmonic Balance. This approach is shown to capture in great measure the stable stationary trajectories. Consequently, harmonic balance is applied to determine stable actuation voltages, stability zones and minimum energy feasible actuation schemes.

4.2 Simulation characterization

In order to study the system behavior, long time simulation is used on the concentrated-parameters system equations (2.80). Matlab® Simulink® has been selected to perform the numerical simulations. This scheme allows to analyze the system from transient to steady-state regimes and study frequency spectrum of the position output.

The only drawback in the proposed simulation scheme is the convergence problems that can be observed when approaching unstable regime (bifurcation points or pull-in) or when the domain of attraction is too small [8]. Consequently, the simulation step must be correctly chosen to deal with these situations.

The simulations have been selected to study the steady-state and transient response of the system for sinusoidal voltage inputs with frequencies ranging from $0.4\omega_{\mathrm{n}}$ to $2\omega_{\mathrm{n}}$ (being

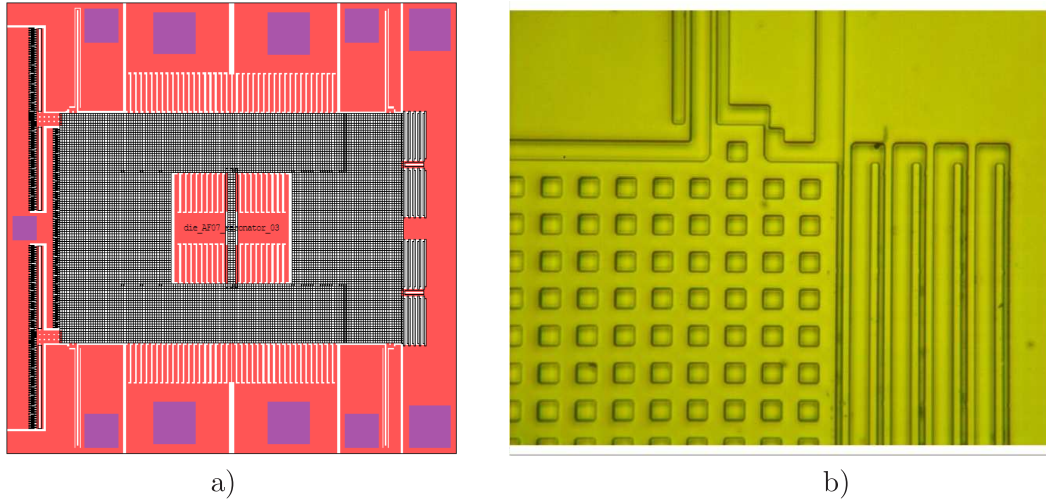

a) b)

Figure 4.1: a) Design of a fabricated MEMS resonator. This is a capture of the L-Edit® fabrication design program with the complete system. b) Close-up of the upper-right part of the real fabricated device, showing the suspension and the parallel-plate capacitor fingers. The devices were fabricated on polysilicon wafers in the University of California, Irvine. (Mask 9. AF07_resonator3 design. UCI 2007).

ω_n the natural frequency of the mechanical system) and damping conditions ranging from Q = 1 to Q = 1000 or higher.

To summarize, the analyzed cases are:

- Analysis of the variations on the AC-voltage load.
- Analysis of the variations on the damping.
- Analysis of the effect of the way the input load is applied.
- Analysis of presence of subharmonic oscillations.
- Analysis of presence of superharmonic oscillations.
- Comparison between linear spring and nonlinear spring models.
- Effect of shocks in the evolution of the system and its stability
- Resonant pull-in analysis.

All these cases are studied from four points of view:

- System position time response.
- Phase-plot and energy evolution.

- Frequency spectrum analysis.
- Stability and pull-in.

The results are particularized with values of a fabricated device, Figure 4.1. The system parameters are shown in Table 4.1. It can be observed that the MEMS resonator has a β-factor value in the transition between linear and nonlinear behavior, as presented in Chapter 3.

Parameter	Value
K	13.406 N/m
K_3	$3.768 \cdot 10^{10}\ N/m^3$
M	$5.6 \cdot 10^{-7}$ Kg
g_0	$5 \cdot 10^{-6}$ m
A_c	$3.86 \cdot 10^{-7}\ m^2$
ε	$8.85 \cdot 10^{-10}$
C_0	$6.83 \cdot 10^{-13}$ F
ω_n	4892 rad/s
f_n	0.78 kHz
$\beta - factor = K/(K_3\, g_0^2)$	14.23

Table 4.1: MEMS Resonator parameters of the fabricated design, used for simulations (AF07_resonator3 fabricated design).

4.2.1 Time response of the system

Analysis of the time response of the system is performed under different input and environmental conditions. This analysis presents the general characteristics of the steady-state oscillations, transient trajectories and instabilities under the parameters that can be usually modified.

As expected in an oscillating system, the input voltage magnitude and frequency have an important effect on the output of the system. Figure 4.2 shows the variations of the amplitude while varying the AC-component of the input voltage for a fixed DC-voltage of $5V$ and a Quality factor of 100. Examples are presented at natural frequency and at a frequency close to the frequency of resonance.

The normalized frequency is introduced

$$w_k = \frac{\omega}{\omega_n} = \frac{f}{f_n} \tag{4.1}$$

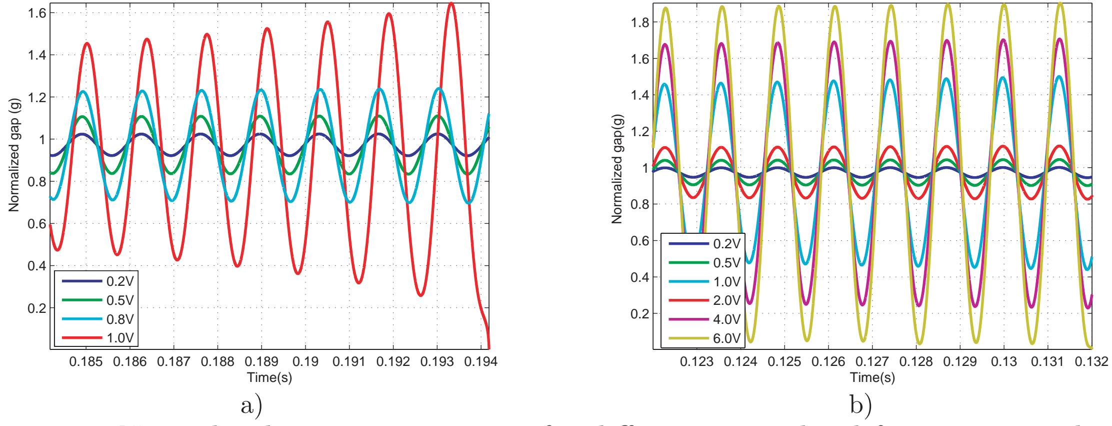

Figure 4.2: Normalized gap time response for different normalized frequencies and input voltages. a) $w_k = 0.95$, $\mathrm{V_{DC}} = 5V$ and $\mathrm{V_{AC}} = 0.2, 0.5, 0.8, 1\ V$. b) $w_k = 1$, $\mathrm{V_{DC}} = 5V$ and $\mathrm{V_{AC}} = 0.2, 0.5, 1, 3, 4, 6\ V$.

as a means to identify how close a chosen driving frequency is to the natural mechanical frequency.

The importance of the frequency of the input can be observed when compared both results. In the first case, with very low AC-voltage ($\mathrm{V_{AC}} = 1V$) snapping of the device occurs, while in the second case voltages as large as $\mathrm{V_{AC}} = 4V$ can be used without risk of snapping. Moreover, large amplitudes of oscillation can be obtained outside of the frequency of resonance without snapping, but at expense of larger voltage load. Amplitudes as large as 80% of the gap can be obtained.

Another important effect on the behavior of the system is produced by the damping (see Chapter 3). Figure 4.3 shows the effect of damping on the time response. Amplitude of the response is extremely affected when changing the environmental conditions of the system from overdamped (Q = 1) to underdamped (Q = 1000). Consequently, the damping is a parameter that must be under control because influences the needed voltage load and the stability of the system. Uncontrolled changes on the damping can lead to unpredictable behavior.

Figure 4.4 shows the transient evolution of the system for an applied voltage input. Four scenarios are compared, depending on how is the voltage applied to the system. In all four cases, the final generated input consists of a $5V$ DC-bias and a $3V$ AC-component. In the first case, the signal is directly applied. In the other cases, the AC-voltage is applied as an increasing ramp. As can be observed, the response can change from unstable (Case 1) to stable depending on how the voltage is applied. Consequently, to analyze the feasibility of steady-state oscillation under a defined voltage load, this input must be applied as a

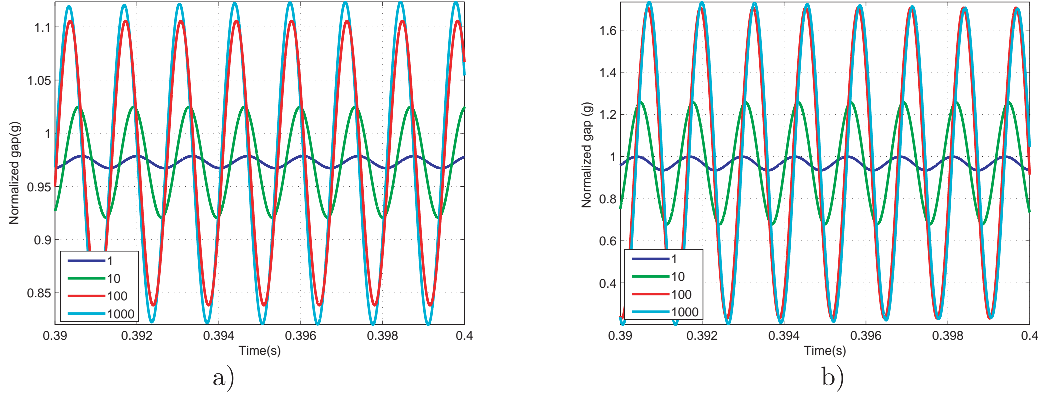

a) b)

Figure 4.3: Normalized gap time response for different frequencies and damping (Q = 1, 10, 100 and 1000). Fixed DC-voltage at $5V$ for both cases. a) Fixed AC-component of the input voltage at $0.5V$ and $w_k = 0.95$. b) Fixed AC-component of the input voltage at $3V$ and $w_k = 1$.

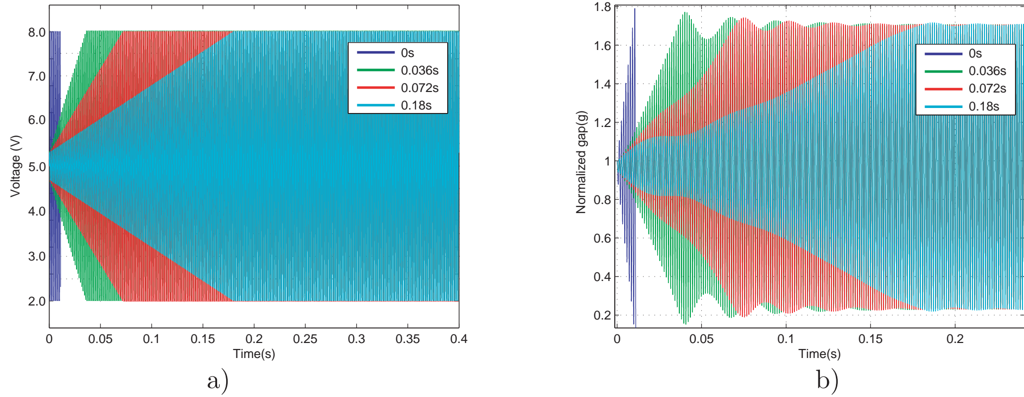

a) b)

Figure 4.4: a) Four different voltage inputs used to test the transient effects on the system. In all four cases, the final input generated consists of a $5V$ DC-bias and a $3V$ AC-component. In the first case the voltage is applied directly and in the rest of the cases the voltage load is applied as an increasing ramp with different time constants (0.036s, 0.072s, 0.18s). b) Normalized gap time response for the different input voltages of a). The first response reaches pull-in.

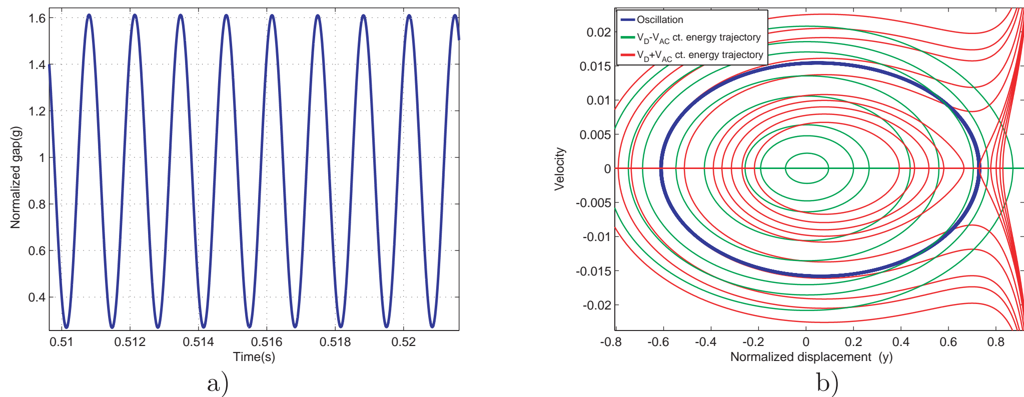

a) b)

Figure 4.5: a) Normalized gap time response and b) Normalized displacement and velocity phaseplot showing the subharmonic oscillation for an input voltage of frequency $1.92\omega_n$, $V_{AC} = 2V$ and $V_{DC} = 5V$. In the phaseplot, curves of constant energy are plotted for the maximum ($V_{AC} + V_{DC}$) and minimum ($V_{AC} + V_{DC}$) applied voltages.

slow ramp (Case 4) to avoid transient effects.

Finally, an important fact is that the system can develop subharmonic and superharmonic oscillations. Figure 4.5 shows the subharmonic oscillation of the system for $\mathrm{V_{AC}} = 2V$ and $\mathrm{V_{DC}} = 5V$ when the input frequency is $1.92\omega_\mathrm{n}$. At this frequency, the observed oscillation is close to pure sinusoidal, as can be observed in the time response and the phaseplot. When moving outside of the subharmonic frequency, the mix of amplitudes between the driving frequency and subharmonic oscillation is more clear. In the phaseplot, the constant energy trajectories for the maximum ($\mathrm{V_{AC}}+\mathrm{V_{DC}}$) and minimum ($\mathrm{V_{AC}}+\mathrm{V_{DC}}$) applied voltage are presented. They allow to delimit the feasibility of oscillation and its stability.

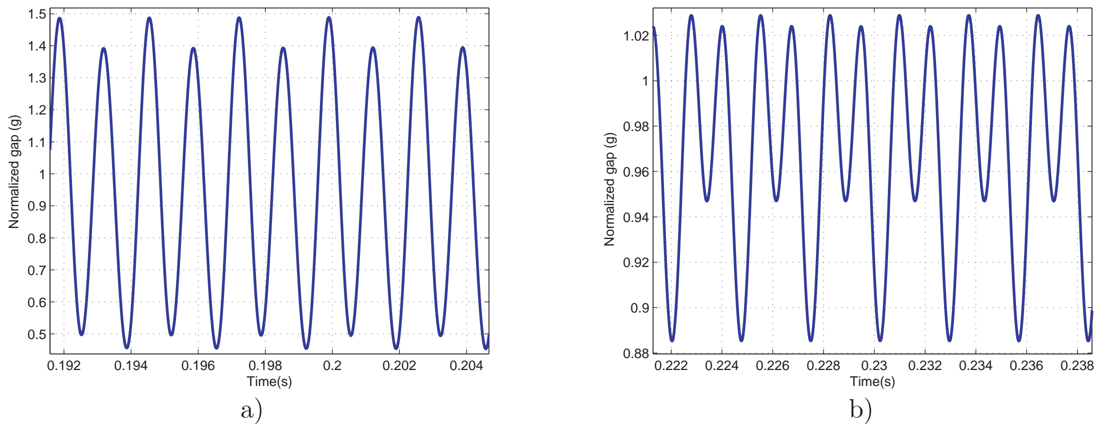

Figure 4.6: Normalized gap position in superharmonic oscillation. In both cases $\mathrm{V_{DC}} = 5$. a) Input frequency of $0.48\omega_\mathrm{n}$ and $\mathrm{V_{AC}} = 3V$. b) Input frequency of $0.47\omega_\mathrm{n}$ and $\mathrm{V_{AC}} = 2V$.

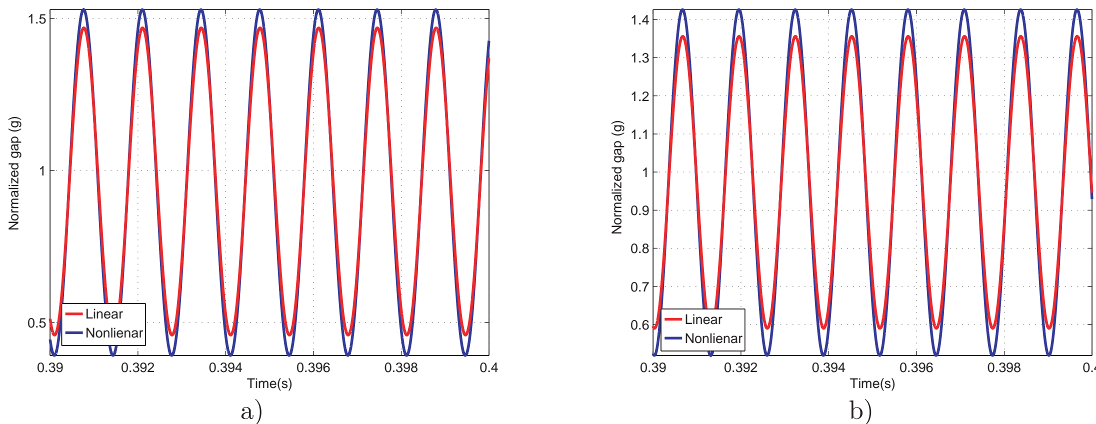

Figure 4.7: Normalized gap time response for different frequencies, comparing linear (red) and cubic nonlinear (blue) spring models. a) Fixed DC-voltage is $5V$, fixed AC-component is $0.5V$ and $w_k = 0.95$. b) Fixed DC-voltage is $5V$, fixed AC-component is $3V$ and $w_k = 1$.

Figure 4.6 shows the superharmonic oscillation of the system for two different input frequencies ($0.48\omega_\mathrm{n}$ and $0.47\omega_\mathrm{n}$). In the first case, large amplitudes are achieved with an input voltage composed of an AC-component of $3V$ and a DC-voltage of $5V$. In this case, all the input energy transfers to the superharmonic oscillation. However, when the input frequency is changed to $0.47\omega_\mathrm{n}$, the oscillation is more asymmetric and the same voltages levels drive the system to pull-in. In the example, AC-component has been reduced to $2V$ to avoid pull-in, and the time response is shown.

Figure 4.7 shows the comparison between the output of the linear and nonlinear spring-model. Again natural frequency and resonance-like frequency are used. As can be observed, in all cases, the nonlinear spring model obtains larger amplitudes of oscillation than the linear spring model. This again has influence on the stability analysis of the system.

4.2.2 Phase-plot and energy evolution

As the system has an oscillatory behavior, the best approach to observe its oscillation pattern is the use of the phase-plane. The effect of the nonlinearity on the oscillations can be clearly observed as amplitude increases and trajectories get close to the saddle point. To observe the saddle point, the constant energy trajectories for the maximum ($\mathrm{V_{AC}} + \mathrm{V_{DC}}$) and minimum ($\mathrm{V_{AC}} + \mathrm{V_{DC}}$) applied voltage are presented in the phaseplots. They allow to delimit the feasibility of oscillation and its stability. Moreover, pull-in occurs when the system has enough energy to overshoot the maximum of the potential energy curve (saddle point on the phase-plane).

Figure 4.8 shows the variations on the phase-plot and energy profile of the system evolution while varying the AC-component of the input voltage for a fixed DC-voltage of $5V$. Examples are presented again at a frequency close the frequency of resonance and at natural frequency.

The energy plots allow to observe the evolution of the energy during the oscillation loops. As discussed in Chapter 3, the energy of the system is confined between the potential energy curves. However, as the input voltage is sinusoidal, this effect is less evident as the value of the input voltage changes continuously. In Figure 4.8d the transition to pull-in is presented for the $1V$ input voltage case. The maximum of the potential energy is surpassed and pull-in occurs.

Figure 4.9 shows the effect of damping in the steady-state response of the system for

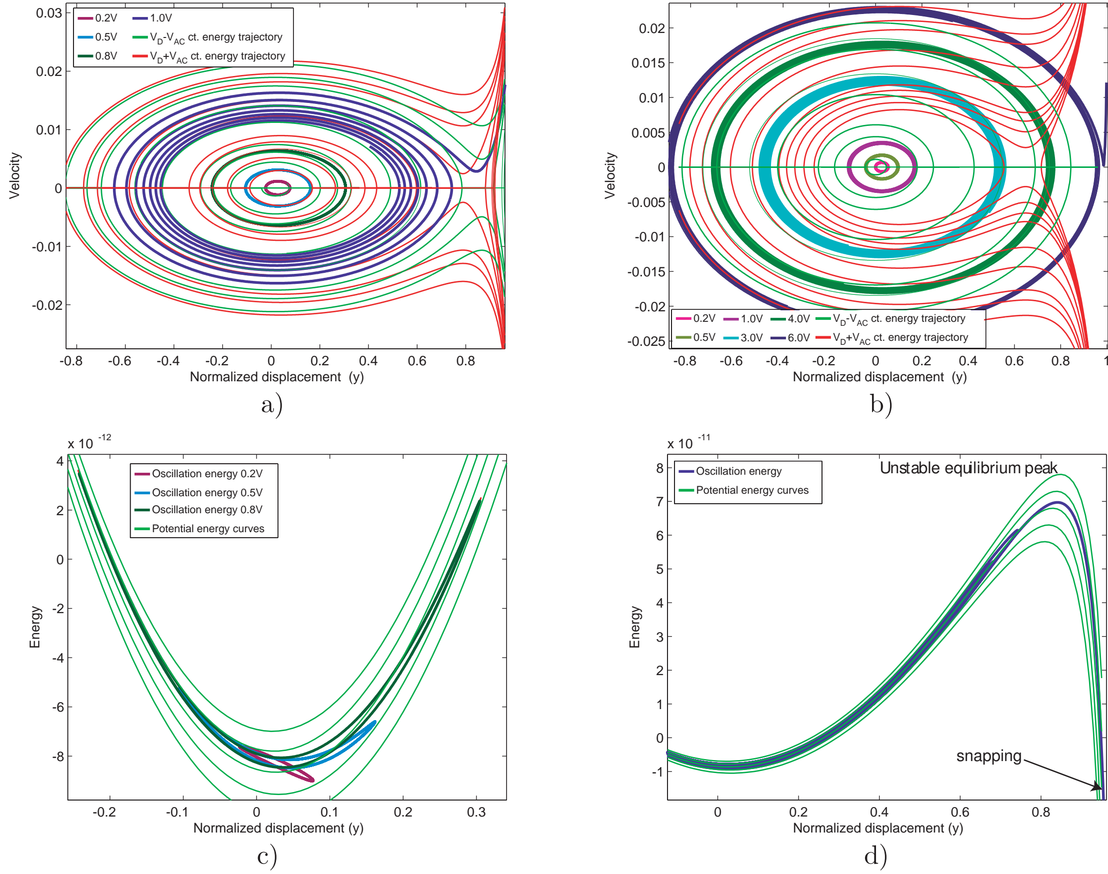

Figure 4.8: Normalized displacement and velocity phase-plots for different frequencies and input voltages. a) Normalized frequency is $w_k = 0.96$, $\mathrm{V_{DC}} = 5V$ and $\mathrm{V_{AC}} = 0.2, 0.5, 0.8, 1V$ b) Normalized frequency is $w_k = 1$, $\mathrm{V_{DC}} = 5V$ and $\mathrm{V_{AC}} = 0.2, 0.5, 1, 3, 4, 6V$. c) Same evolutions than a) are presented in the energy plots. In this case, energy loops are presented for $\mathrm{V_{AC}} = 0.2, 0.5, 0.8V$ at $0.96\omega_\mathrm{n}$. d) Energy loop for $\mathrm{V_{AC}} = 1V$ $(0.96\omega_\mathrm{n})$ showing pull-in.

---

the whole spectrum of damping conditions (from overdamped ($\mathrm{Q} = 1$) to underdamped ($\mathrm{Q} = 1000$). During simulations the DC-voltage is fixed at $5V$ and the frequencies are the same as before. In both cases, energy levels increase when damping is reduced because the amplitude of oscillation increases. The used AC-voltages are limited by resonant snapping.

Figure 4.10 shows the phase-plots of the subharmonic oscillation of the system for frequencies ranging from $1.91\omega_\mathrm{n}$ to $1.96\omega_\mathrm{n}$. In Figure 4.10a, the phase plot trajectories for each frequency are compared. In Figure 4.10b, a close-up of the phase-plot for an input frequency of $1.96\omega_\mathrm{n}$ is shown. As can be observed, at this frequency the subharmonic oscillation amplitude is low, what leads to mixing of the subharmonic and driving frequencies to a non-sinusoidal oscillation. For the simulated parameters, pure subharmonic oscillation occurs at $1.92\omega_\mathrm{n}$ (Figure 4.5).

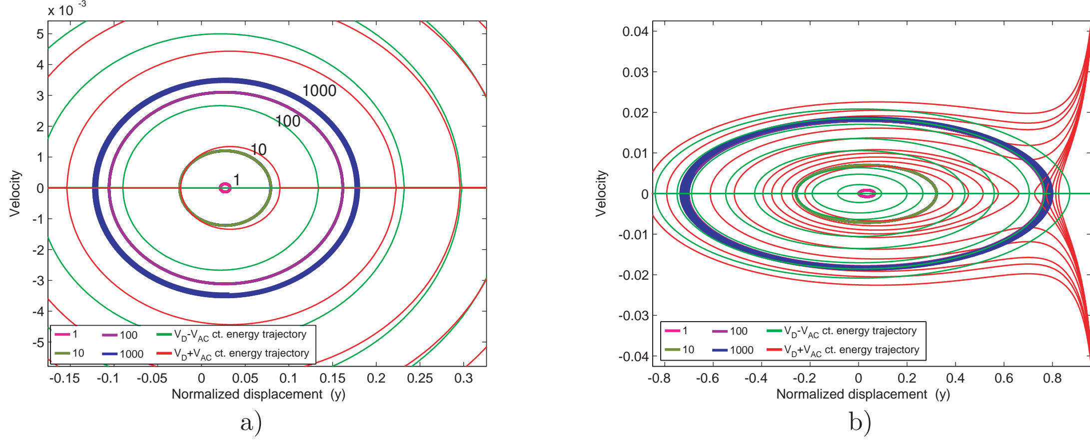

Figure 4.9: Normalized displacement and velocity phase-plots for different frequencies and damping (Q $= 1, 10, 100$ and 1000). Fixed DC-voltage at $5V$. a) Fixed AC-component of the input voltage at $0.5V$ and $w_k = 0.95$. b) Fixed AC-component of the input voltage at $3V$ and $w_k = 1$.

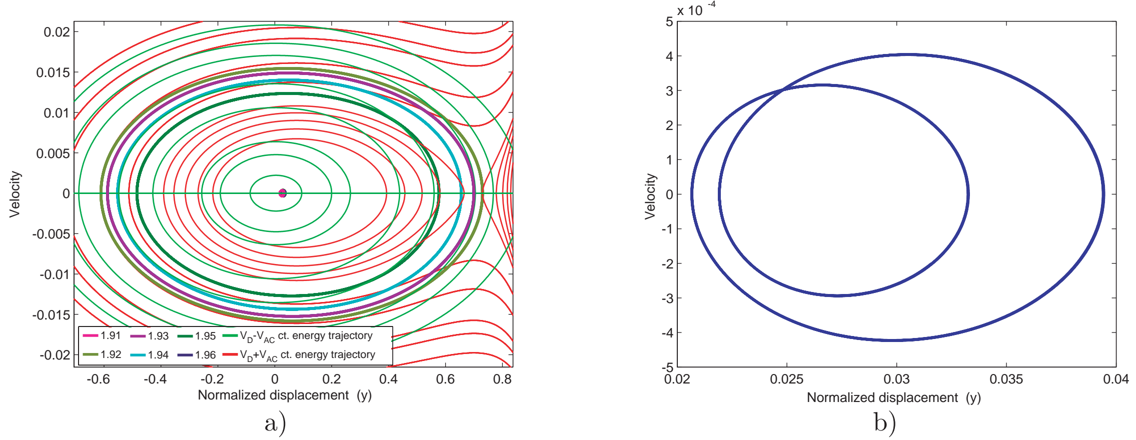

Figure 4.10: Normalized gap subharmonic oscillation response with fixed DC-voltage at $5V$ and AC-component at $3V$. a) Oscillation loops for frequencies of the input voltage ranging from $1.91\omega_{\mathrm{n}}$ to $1.96\omega_{\mathrm{n}}$. b) Detailed phase-plot for $1.96\omega_{\mathrm{n}}$.

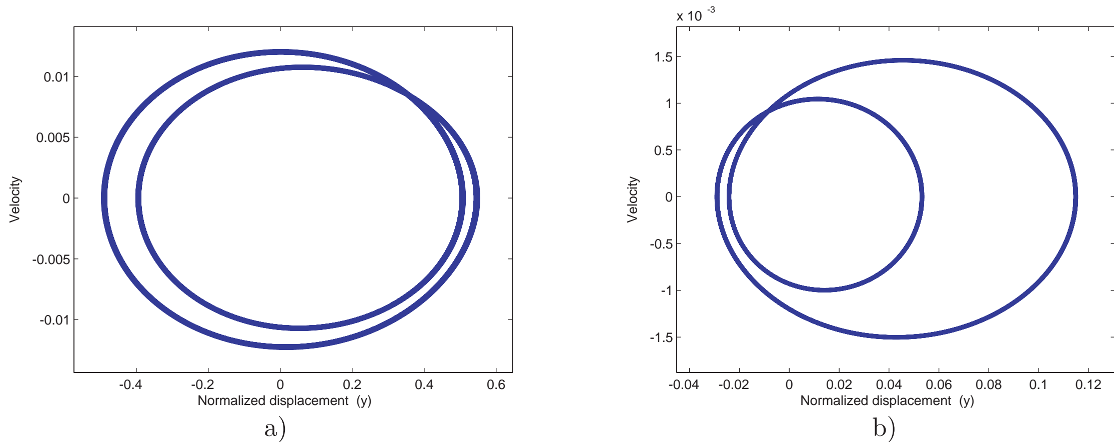

Figure 4.11: Normalized gap superharmonic oscillation response with fixed DC-voltage at $5V$. The phase-plots show that oscillation is composed of a mix between oscillation at driving frequency and oscillation at superharmonic frequency. a) Fixed AC-component at $3V$ and frequency at $0.48\omega_{\mathrm{n}}$. b) Fixed AC-component at $2V$ and frequency at $0.47\omega_{\mathrm{n}}$.

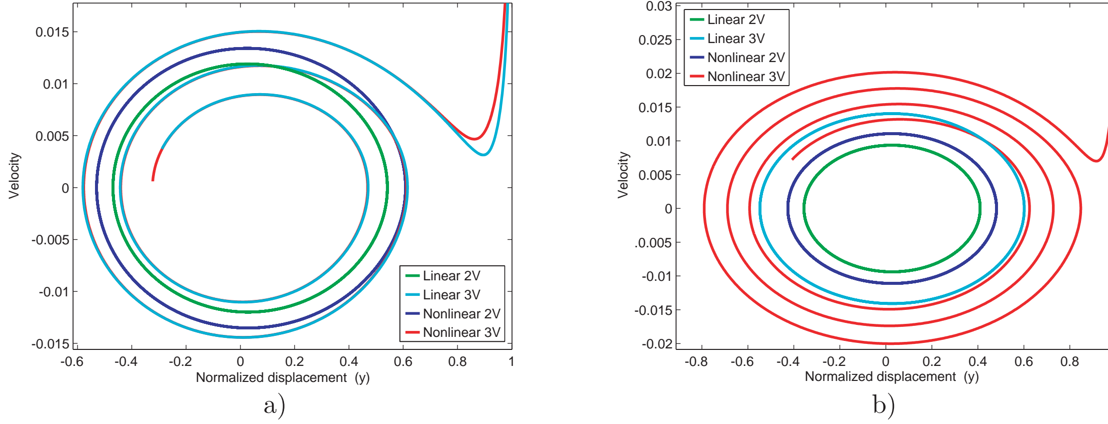

Figure 4.12: Normalized displacement and velocity phase-plots for linear spring and nonlinear cubic spring models. Comparison for $V_{DC} = 5V$ and $V_{AC} = 2V$ and $3V$. a) Frequency is $0.96\omega_n$. b) Natural mechanical frequency is used.

Figure 4.11 shows the phase-plots of the superharmonic oscillation of the system for the same cases as in Figure 4.6. When the frequency is $0.48\omega_n$, the system oscillates with an almost-sinusoidal large amplitude. However, when closer to frequency $0.47\omega_n$, the oscillation losses its sinus-like form. In this second case, interaction between both harmonics lead the system to snapping if the voltage is increased to $3V$. For this reason, AC-component has been reduced to $2V$ to avoid snapping.

Figure 4.12 shows the comparison of phase-plots between a linear and nonlinear spring model for both frequency cases. In the first case, close to resonant frequency, both simulations lead to pull-in when changing the AC-component from $2V$ to $3V$. In the second case, only the cubic spring model leads the system to pull-in with the same change. Nonlinear spring model produce snapping for $V_{AC} = 3V$.

4.2.3 Frequency response

Another important information is the frequency components of the MEMS oscillation, in order to understand at which frequencies the energy is transferred between voltage driving input and position output. Most analysis assume that the MEMS resonator oscillates as a pure sinusoidal, but this is not true in most cases. For low input voltages, higher harmonics are negligible, but when the input voltage is increased second order harmonic gains significance. And if the input voltage is not directly a pure sinusoidal, higher harmonics can easily appear.

In the simulations, the frequency spectrum is calculated using the Power Spectral Density estimation obtained with Matlab© Fast-Fourier Transform function. The results show

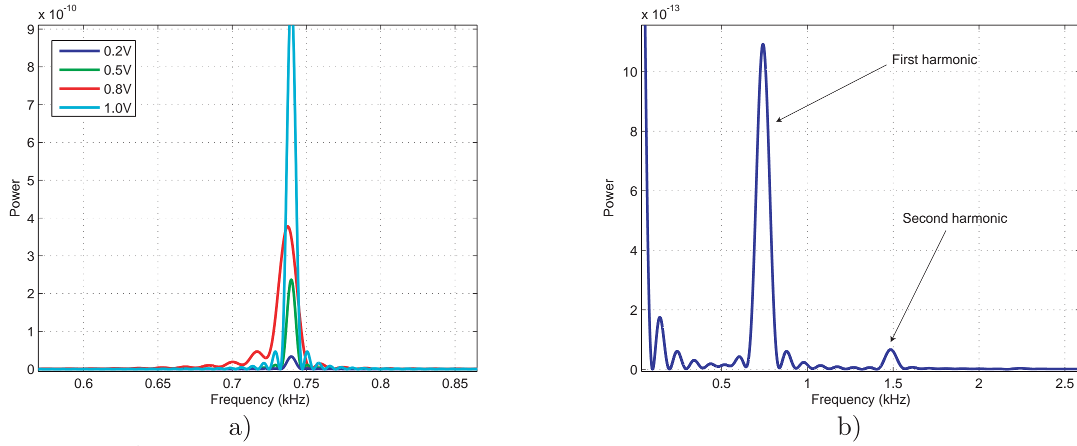

Figure 4.13: a) Frequency analysis of the response with frequency of the input at $0.95\omega_n$, and input voltages $V_{DC} = 5V$, $V_{AC} = 0.2, 0.5, 0.8, 1V$ and $Q = 100$. b) Frequency analysis of the response with frequency of the input at $0.95\omega_n$, input voltage $V_{DC} = 5V$ and $V_{AC} = 15V$ and $Q = 1$.

that usually the oscillation concentrates on the first harmonic frequency of the driving voltage, except during subharmonic and superharmonic oscillations.

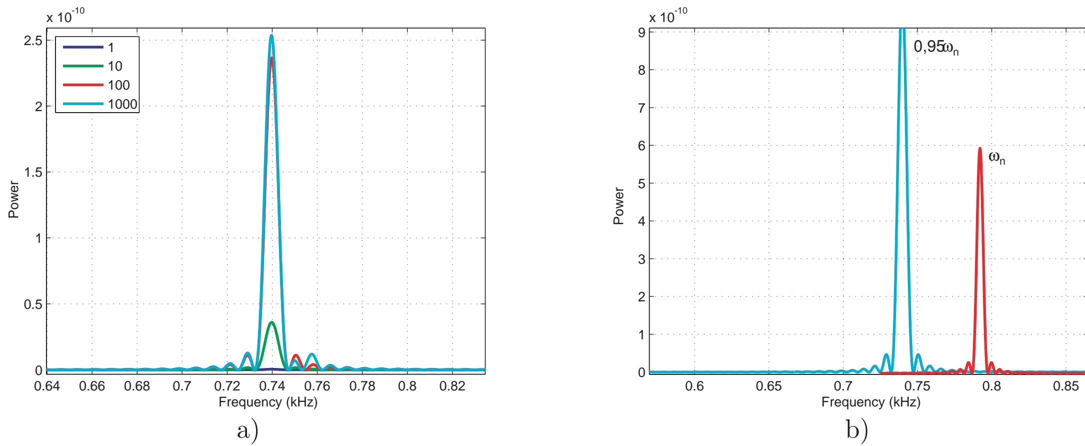

Figure 4.14: a) Frequency power spectrum of the response with input at frequency $0.95\omega_n$, fixed DC-voltage at $5V$ an AC-component at $0.5V$. Damping is changed from $Q = 1$ to $Q = 1000$. b) Frequency power spectrum of the response with input at frequency $0.95\omega_n$ and at ω_n. Fixed DC-voltage at $5V$, AC-component at $1V$ and damping at $Q = 100$.

Figure 4.13a shows the frequency response of the oscillation of the MEMS resonator for different driving voltages. Given a Quality factor of 100, a frequency of $0.95\omega_n$ and a fixed DC input bias of $5V$, the AC-component is changed from $V_{AC} = 0.2V$ to $V_{AC} = 1V$. The oscillation amplitude increases with the AC voltage, as expected. Only first harmonic is detected in the output spectrum, due to the low voltages. In Figure 4.13b, the input voltage is increased, because the example is overdamped ($Q = 1$), and in this case with same input frequency ($0.95\omega_n$) and DC bias ($5V$), the AC-component is $15V$, and second

harmonic appears in the frequency power spectrum.

Figure 4.14a shows the effect of damping in the frequency power spectrum of the output response. Conditions are changed from overdamped (Q = 1) to underdamped (Q = 1000). The output frequency bands remain fixed, as damping has no effect on the frequency, only on the amplitude of oscillation.

Figure 4.14b shows the effect known as spring softening. The frequency power spectrum shows the response of the system at two different frequencies, one is the mechanical natural frequency ω_{n} and the other slightly lower, $0.95\omega_{\mathrm{n}}$. The input has a fixed DC-bias of $5V$, an AC-component of $1V$, while the damping is fixed at Q = 100. As can be observed, the amplitude of oscillation of the system, with identical voltages at the input is higher at a frequency lower than the mechanical natural frequency. The effect is called *spring softening* because the electrostatic force can be approximated to a negative spring proportional to the input voltage, what generates resonant frequency shifting due to reduction of the effective spring constant of the system [183]. For this reason, resonance of the electrostatically actuated MEMS resonators is at lower frequencies than natural frequency.

Figure 4.15 analyzes the effect of the nonlinear spring in the frequency spectrum of the oscillation of the system. No effect on the frequency of oscillation is observed, as both examples suffer the same amount of resonance frequency softening. But as previously identified, amplitudes of nonlinear model are larger.

Figure 4.16 shows two cases of subharmonic oscillation with fixed AC-component of the input voltage at $2V$ and fixed DC-voltage at $5V$. In the first case, the frequency response of the output oscillation is at $0.96\omega_{\mathrm{n}}$ ($0.7477\ kHz$) while the driving frequency is at $1.92\omega_{\mathrm{n}}$. All the energy of the system is almost completely transferred from input driving frequency to the subharmonic oscillation frequency (half input frequency), as no frequency component is observed in the driving frequency. This observation is in line with those presented in the previous sections. In the second case, the subharmonic frequency response of the output oscillation is at $0.98\omega_{\mathrm{n}}$ ($0.7631\ kHz$) while the driving frequency is at $1.96\omega_{\mathrm{n}}$. In this case, the energy is not completely transferred, and most energy still remains at driving frequency.

Similarly, Figure 4.17 shows two cases of superharmonic oscillation with fixed AC-component of the input voltage at $2V$ and fixed DC-voltage at $5V$. In the first case, the frequency response of the output oscillation is at $0.96\omega_{\mathrm{n}}$ ($0.7477\ kHz$) while the driving

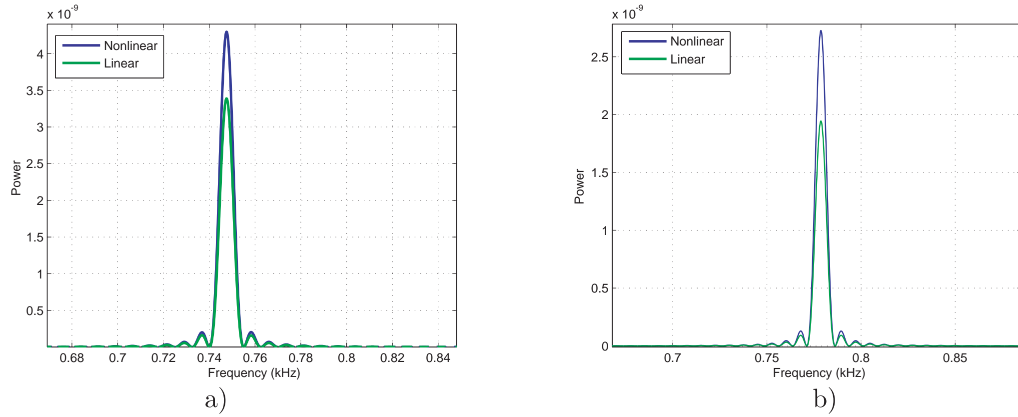

Figure 4.15: Frequency response comparing linear and nonlinear spring models. Fixed DC-voltage at $5V$. a) At frequency $0.96\omega_n$ with AC-component of the input voltage at $0.5V$. b) At frequency ω_n with AC-component of the input voltage at $2V$.

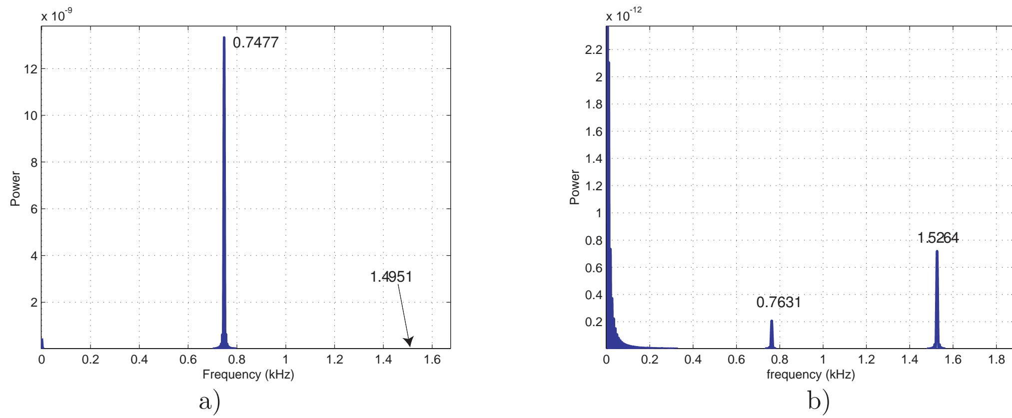

Figure 4.16: Subharmonic frequency response with input drive with $2V$ AC-component and $5V$ DC-bias. a) Frequency response occurs at half the driving frequency, $0.96\omega_n$, while driving frequency is at $1.92\omega_n$. b) Subharmonic response appears at $0.98\omega_n$ while driving frequency is at $1.96\omega_n$.

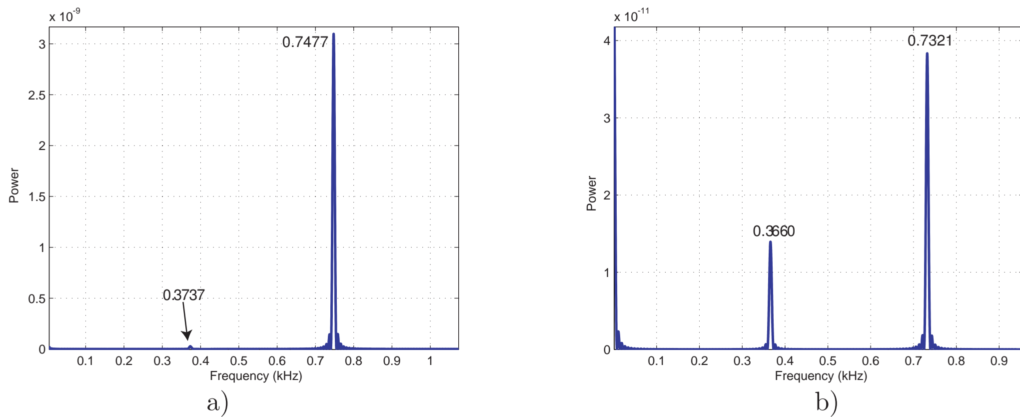

Figure 4.17: Superharmonic frequency response with input drive with $2V$ AC-component and $5V$ DC-bias. a) Frequency response occurs at $0.96\omega_n$ while driving frequency is at $0.48\omega_n$. b) Superharmonic response appears at $0.94\omega_n$ while driving frequency is at $0.47\omega_n$.

---

frequency is at half that value, $0.48\omega_{\rm n}$. In this case, most of the energy of the system is transferred to the superharmonic frequency, as only a slight oscillation is observed in the driving frequency. However, transfer of energy is not completed, for this reason the phase-plot in Figure 4.11 is not completely elliptic. In the second case, the frequency response of the output oscillation is at $0.47\omega_{\rm n}$ ($0.3660\ kHz$) while the driving frequency is at $0.47\omega_{\rm n}$. In this case, the energy is not completely transferred, and the magnitude of the oscillation at the driving frequency is half that of the superharmonic frequency.

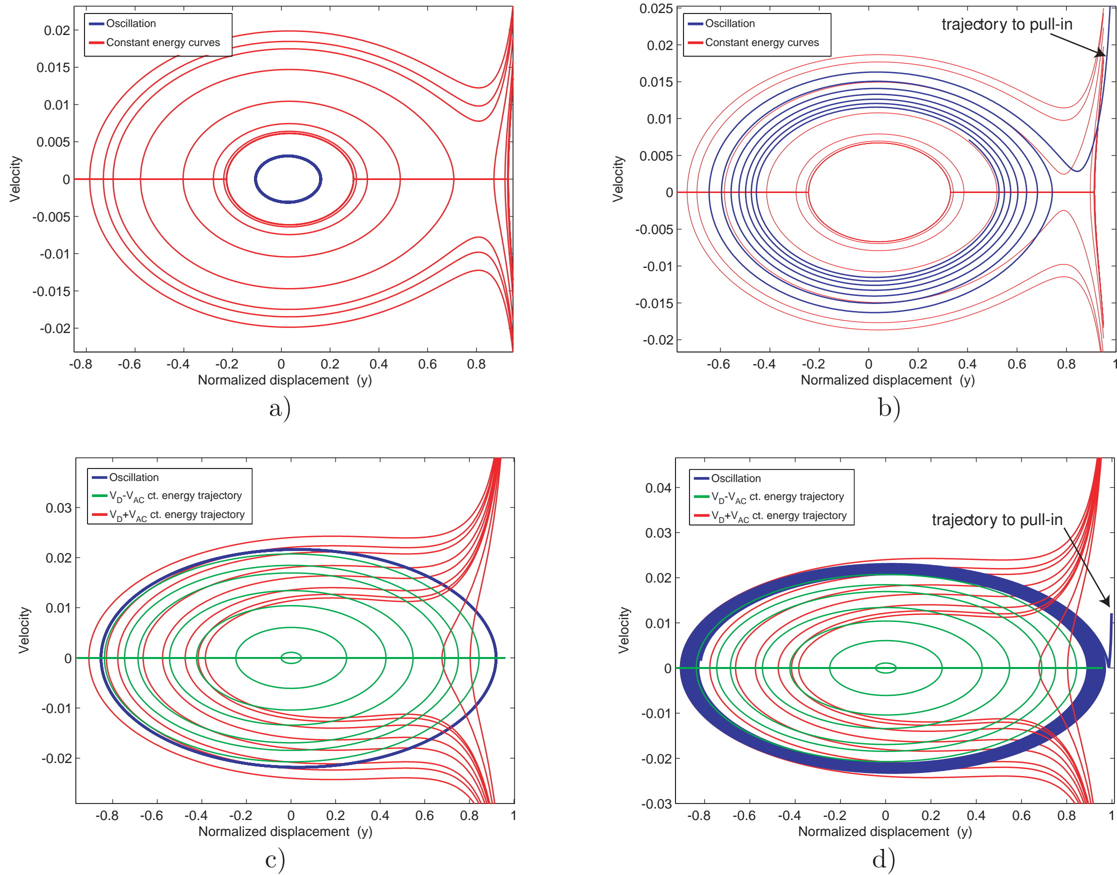

Figure 4.18: Phase-plot response of the system for a fixed DC-voltage of $5V$. a) Frequency is $0.96\omega_{\rm n}$ and AC voltage is $V_{AC} = 0.5V$. b) Frequency is $0.96\omega_{\rm n}$ and AC voltage is $V_{AC} = 1V$. c) Frequency is $\omega_{\rm n}$ and AC voltage is $V_{AC} = 4V$. d) Frequency is $\omega_{\rm n}$ and AC voltage is $V_{AC} = 6V$.

4.2.4 Stability and Pull-in analysis

In order to design new devices, it is important to understand the factors that define the stability of the trajectories and how this stability can be lost. Unstable trajectories lead to pull-in and this can cause permanent failure of the device.

As it is shown in the simulations, multiple factors influence the stability of the device and

they must be taken into account in order to guarantee stable oscillation of the system.

Figure 4.18 shows the variations in the phase plane evolution when the AC-component of the input voltage is changed for a fixed DC-voltage of $5V$. Examples are presented at two different frequencies and at two different voltages. In both cases, the change in the AC-voltage leads the system to loose its stable oscillation and snapping occurs when the amplitude of oscillation reaches out of the stable basin of attraction.

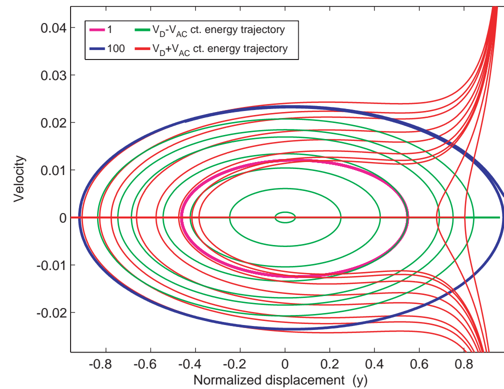

Figure 4.19: Phase-plot of the evolution of the system oscillated with a fixed AC-component of $5V$, a fixed DC-voltage of $5V$ and at natural frequency. Curves shown for Q $= 1$ and Q $= 100$.

Figure 4.19 shows the effect of damping in the steady-state response of the system. Again, the change from damped (Q $= 10$) to slightly underdamped (Q $= 100$) conditions can produce the system to loose its stability and to lead its oscillation to snapping. In the example, this occurs for Q $= 100$.

Apart from the factors that are directly chosen, as the voltage or the damping, external factors can force the system to loose its stability. An usual problem is the reaction of the system to an external shock. The shock introduces a disruption in the trajectory of the system, that can help the system to reach out its safe basin of attraction and lead its trajectory to pull-in.

Figure 4.20 compares the stability of oscillations when a disruption on its trajectory by a value of ten-percent of the gap is applied. In the first case the input voltage has an AC-component of $2V$ and oscillates at natural frequency. The trajectory in this case remains stable and it is able to return to its steady-state oscillation. In the second case, the input voltage has an AC-component of $3V$, and this time, as the trajectory is more energetic and has a larger amplitude, the disruption is more harmful, and the system

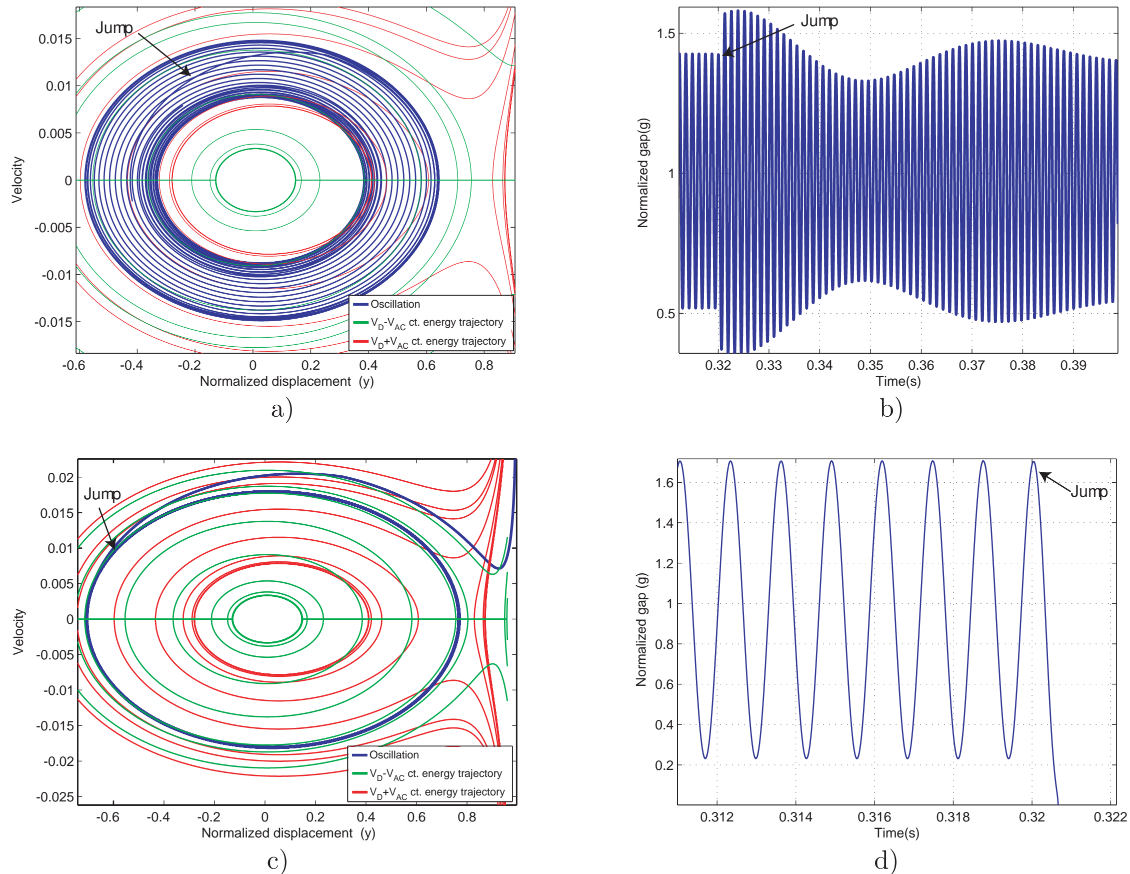

Figure 4.20: Phase-plot and time-response of the system when a jump of ten-percent of the gap is suddenly applied. Fixed DC-voltage of $5V$ and oscillation at natural frequency with Q = 100 a) Fixed AC-voltage of $2V$ b) Fixed AC-voltage of $3V$. In this case the system becomes unstable.

---

becomes unstable and leads to pull-in.

Moreover, Figure 4.21 shows that the damping has a dramatic effect on the stability of the system when it undergoes an impulse response against an external shock of ten-percent of the maximum gap of oscillation. Changes from overdamped (Q = 1) to underdamped (Q = 1000) conditions are presented in the example. In the first case, the shock modifies the trajectory, but it recovers immediately due to its high damping. In the second case, the low damping of the systems helps the trajectory to become seriously distorted.

Figure 4.22 shows again the transient evolution of the system for four different kind of actuation inputs. Using the same example previously presented, this time the phase-plot can be analyzed to observe how the response changes from stable to unstable oscillation. In the case of directly applying the voltage, oscillation builds up reaching out of the safe basin of oscillation. The other driving voltage alternatives are capable of oscillating the system without reaching pull-in. The transients are different but the steady-state is equal

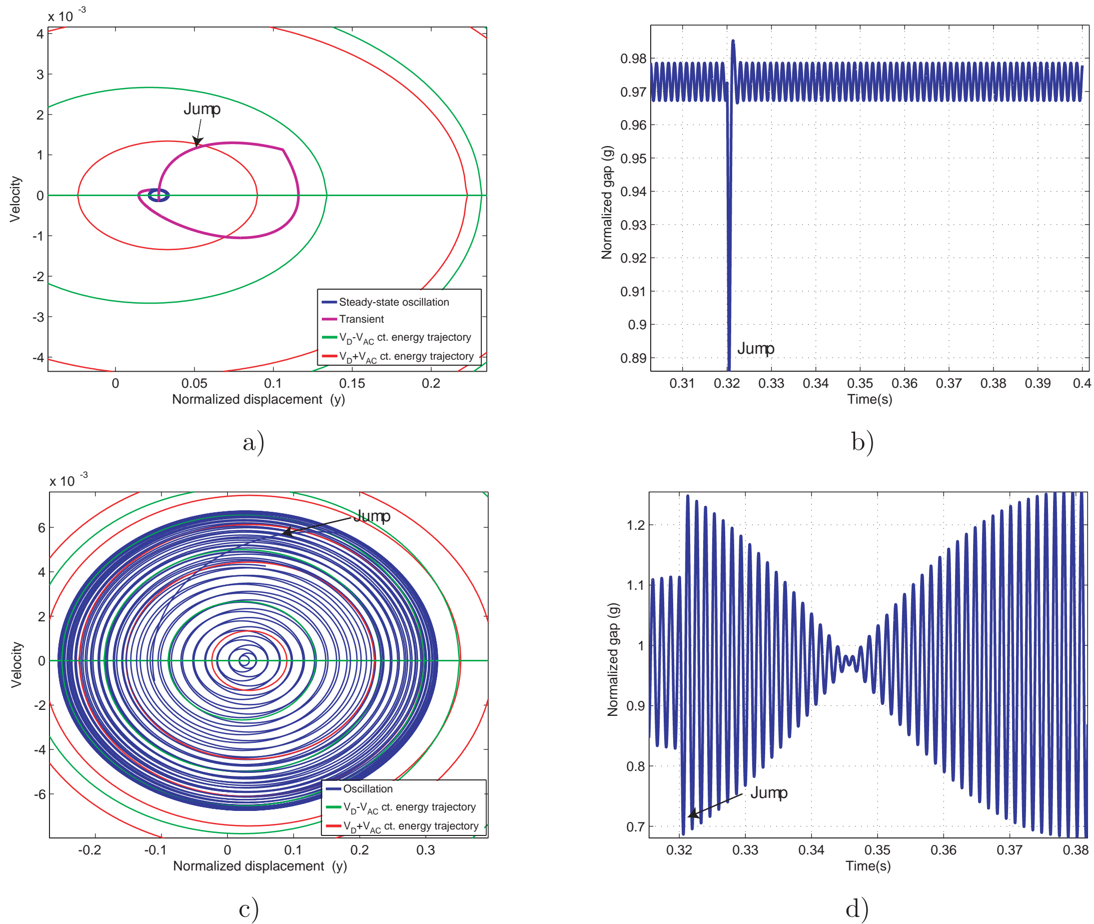

Figure 4.21: Phase-plot and time-response of the system when a jump of ten-percent of the gap is suddenly applied. Fixed AC-component of the input voltage at $0.5V$, fixed DC-voltage at $5V$ and frequency at $0.96\omega_{\text{n}}$. a) and b) Phase-plot and time response of the system under Q = 1. c) and d) Phase-plot and time response of the system under Q = 1000.

for the three stable cases.

Figure 4.23 shows that subharmonic oscillation must be taken into account while designing the system, if one can predict that its frequency can be reached. In the case that is shown, with a frequency of $1.93\omega_{\text{n}}$, a DC-component of $5V$ and an AC-component of $2V$, the system is stable. However, if the AC-component is raised to $2.5V$, the system becomes unstable and leads to pull-in.

Figure 4.24 shows that the same reasoning applied to subharmonic oscillation must be analyzed for superharmonic oscillations. Moreover, in this case, higher attention must be paid, as lower frequencies are more easily excited during the life of a design. In the example, superharmonic oscillations are presented for a frequency of $0.47\omega_{\text{n}}$, $5V$ DC-component and $3V$ AC-component. It has been previously presented, in Figure 4.6, that the system with an input of frequency of $0.47\omega_{\text{n}}$ and $2V$ of AC-component can oscillate

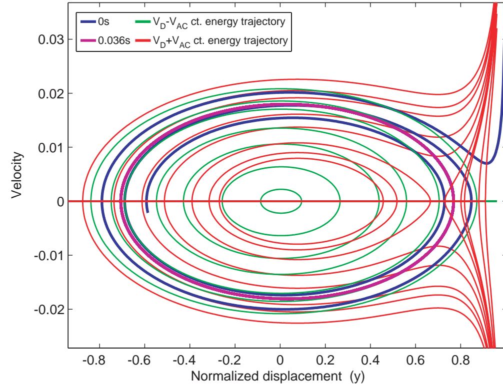

Figure 4.22: Phase-plot of the evolution of the system with a fixed AC-component of the input voltage at $3V$, fixed DC-voltage at $5V$ and natural frequency for the direct input and the input with a ramp of $0.036s$ in Figure 4.4.

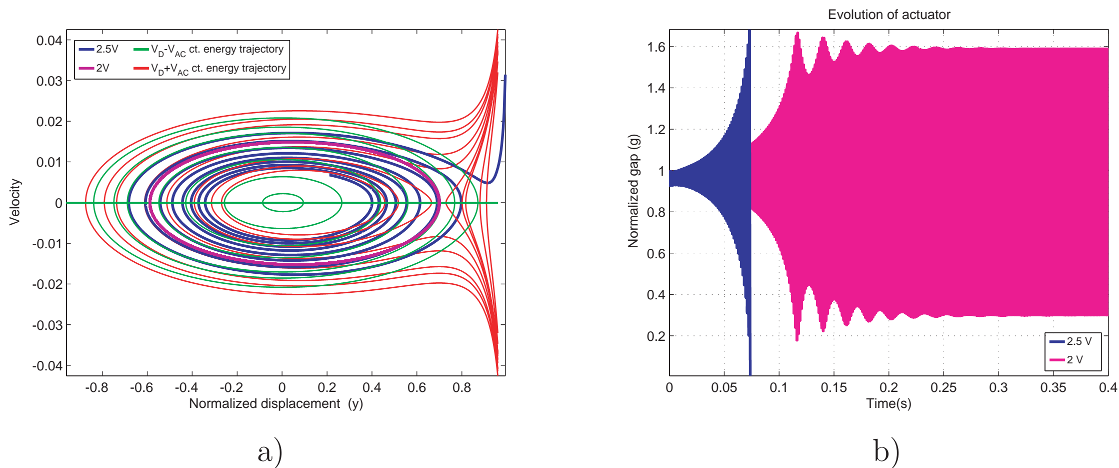

a) b)

Figure 4.23: Comparison of the evolution of the normalized gap subharmonic oscillations ($w_k = 1.93$) of the system with a fixed DC-voltage of $5V$ and an AC-component of $\mathrm{V_{AC}} = 2V$ and $\mathrm{V_{AC}} = 2.5V$. a) Phase-plot. b) Time response.

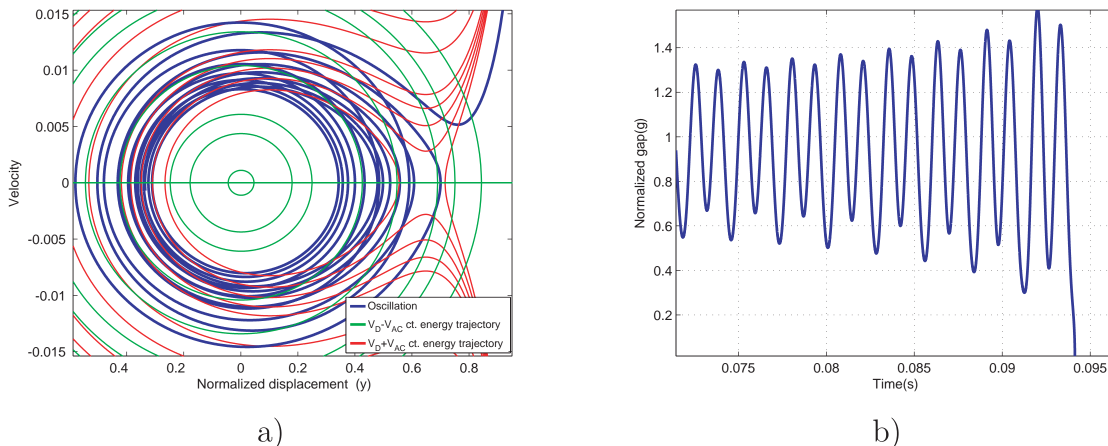

a) b)

Figure 4.24: Unstable evolution of the superharmonic normalized gap oscillations ($w_k = 0.47$) of the system with a fixed DC-voltage of $5V$ and an AC-component $\mathrm{V_{AC}} = 3V$. a) Phase-plot. b) Time response.

in a stable fashion. In the current example, increasing the AC-component to $3V$ has led the system to snapping.

Given the importance of the pull-in voltage of the system, Figure 4.25 shows the *AC-DC pull-in curves* for different voltages, frequencies and damping. The plot covers from superharmonic to subharmonic frequencies. The three resonant peaks are clearly visible and their evolution is quite similar, except for the subharmonic oscillation in underdamped conditions (Q = 10), where instability is clearly reduced. It is also visible the frequency shift associated with the value of the AC-component, usually known as spring-softening. Damping has an effect in frequency because it delimits the maximum voltage that can be applied. As it changes between Q-factor 10 and 20 there is a major change in the system behavior. After that initial jump, changes are at small steps.

Figure 4.26 shows the comparison between the AC-pull-in curves of a linear spring model and a nonlinear cubic spring model, obtained via simulation. First of all, it can be observed that both models behave in a similar way, showing in both cases the three resonant peaks (superharmonic, resonance, subharmonic). The most interesting information that can be extracted from the plot is the fact that the cubic spring model reaches pull-in at lower voltages than the linear spring model. One can remember that in the Static Pull-in case, the linear spring model produces snapping more easily than the cubic spring model because the cubic spring increases the restoring force of the system. However, in the AC-pull-in case, the interaction between the different harmonics in the cubic spring model helps to increase the oscillation amplitude, what leads the system to pull-in more easily.

4.2.5 Analysis conclusions

The oscillation of a parallel-plate electrostatically actuated MEMS resonator is extremely rich in behaviors. Different factors have been shown that interact in the final oscillation of the devices. A pure sinusoidal oscillation is not directly obtained in most cases when the system is excited with a sinusoidal input, specially when large voltages are applied to obtain large amplitudes. Moreover, stability issues appear when the amplitudes of oscillation increase.

Consequently, tools to predict the performance and stability of a MEMS resonator when actuated with electrostatic parallel-plates actuators are necessary. These tools could be used to design better MEMS resonators and improve their overall performance.

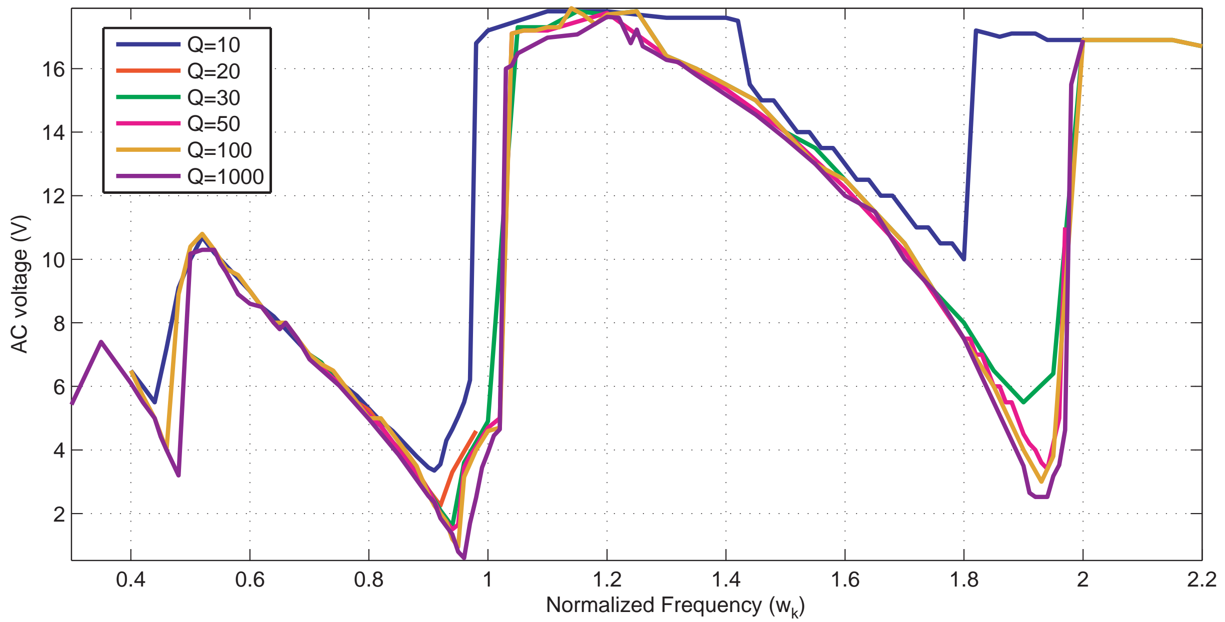

Figure 4.25: Analysis of the *AC-DC pull-in curves* as a function of the damping of the system (Q $= 10 \div 1000$). Fixed DC component is $5V$. In the X-axis appears the normalized frequency ($f = w_k \cdot f_n$).

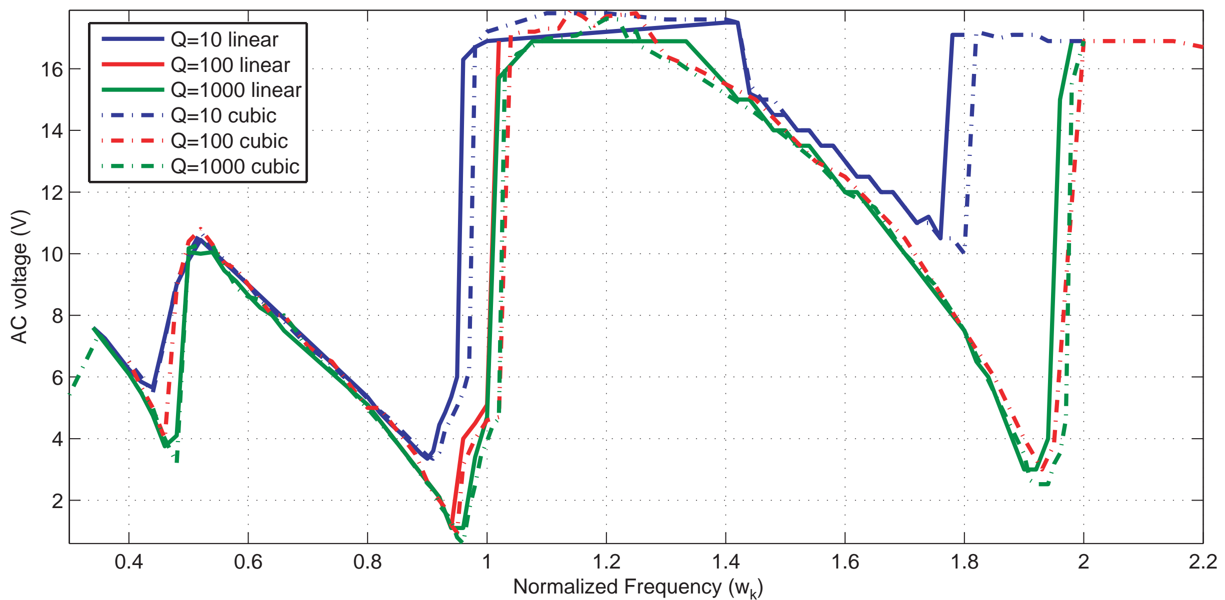

Figure 4.26: Analysis of the *AC-DC pull-in curves* as a function of the damping of the system (Q $= 10 \div 1000$) comparing the results for a model with cubic and linear spring and a model with only linear spring. Fixed DC component is $5V$. In the X-axis appears the normalized frequency.

4.3 Harmonic Balance characterization

There is a need for a formulation able to capture the main behaviors that exist in the electrostatically actuated MEMS resonator system. In this section, Harmonic balance characterization is shown to be able to do it in an appropriate way.

4.3.1 Series expansion of system equations

To use Harmonic Balance analysis some assumptions must be done. First of all, the interest is fixed in studying the steady-state oscillations of the system, and these oscillations are assumed to be always periodic. Secondly, the voltage input to the system is assumed to be also periodic.

Consequently, all the system variables can be expanded using Fourier series in order to use Harmonic Balance analysis.

4.3.1.1 Series expansion of system variables

The system to be analyzed is based on equation (2.79). In this equation, the output of the system is the actual gap distance ($g(t)$), that can be approximated, using Fourier series as follows

$$g(t) = \sum_{n=0}^{\infty} G_n \sin(n\,\omega\,t + \phi_n) \tag{4.2}$$

where $G_n \in \mathbb{R}$ is the amplitude of each harmonic and ω is the first harmonic oscillation frequency. For simplicity, the exponential series is preferred, then

$$g(t) = \sum_{n=-\infty}^{\infty} \breve{G}_n e^{j\,n\,\omega\,t} \tag{4.3}$$

where $\breve{G}_n \in \mathbb{C}$ is the amplitude of the harmonic oscillation in exponential form. The correspondence is as follows:

$$\breve{G}_0 = G_0 \tag{4.4}$$

$$\breve{G}_n = \frac{G_n}{2j}\, e^{j\,n\,\phi_n} \qquad n = 1..\infty \tag{4.5}$$

$$\breve{G}_{-n} = -\frac{G_n}{2j}\, e^{-j\,n\,\phi_n} \quad n = 1..\infty \tag{4.6}$$

Parting from equation (4.3), we can obtain the different needed formulations. The velocity and acceleration of the gap change take the following form

$$\frac{dg(t)}{dt} = \sum_{n=-\infty}^{\infty} j\,n\,\omega\,\breve{G}_n\, e^{j\,n\,\omega t} \;;\; \frac{d^2g(t)}{dt^2} = \sum_{n=-\infty}^{\infty} -n^2\,\omega^2\,\breve{G}_n\, e^{j\,n\,\omega\,t} \tag{4.7}$$

and all the higher order terms are expressed as follow

$$g(t)^2 = \sum_{n=-\infty}^{\infty} \left(\sum_{p=-\infty}^{\infty} \breve{G}_{n-p}\, \breve{G}_p \right) e^{j\,n\,\omega\,t} = \sum_{n=-\infty}^{\infty} \alpha_n\, e^{j\,n\,\omega\,t} \quad \text{where} \;\; \alpha_n = \sum_{p=-\infty}^{\infty} \breve{G}_{n-p}\, \breve{G}_p \tag{4.8}$$

$$g(t)^3 = \sum_{n=-\infty}^{\infty} \tau_n\, e^{j\,n\,\omega\,t} \quad \text{where} \;\; \tau_n = \sum_{r=-\infty}^{\infty} \breve{G}_{n-r}\, \alpha_r \tag{4.9}$$

$$g(t)^4 = \sum_{n=-\infty}^{\infty} \delta_n\, e^{j\,n\,\omega\,t} \quad \text{where} \;\; \delta_n = \sum_{q=-\infty}^{\infty} \alpha_{n-q}\, \alpha_q \tag{4.10}$$

At the same time, as previously stated, the input voltage is assumed to be periodic

$$V(t) = \sum_{n=-\infty}^{\infty} \breve{V}_n\, e^{j\,n\,\omega\,t} \tag{4.11}$$

being $\breve{V}_n$ the n-th harmonic amplitude of the voltage in exponential form. This implies that the square of the input takes the following form

$$V(t)^2 = \sum_{n=-\infty}^{\infty} \left(\sum_{p=-\infty}^{\infty} \breve{V}_{n-p}\, \breve{V}_p \right) e^{j\,n\,\omega\,t} = \sum_{n=-\infty}^{\infty} \beta_n\, e^{j\,n\,\omega\,t} \quad \text{where} \;\; \beta_n = \sum_{p=-\infty}^{\infty} \breve{V}_{n-p}\, \breve{V}_p \tag{4.12}$$

being β_n the amplitude of each harmonic of the square of the voltage in exponential form. Finally, the $H(g)$ term, previously defined (2.84), becomes

$$\begin{aligned} H(g) &= \sum_{n=-\infty}^{\infty} -n^2\omega^2\breve{G}_n e^{jn\omega t} + \frac{\omega_\mathrm{n}}{\mathrm{Q}} \sum_{n=-\infty}^{\infty} jn\omega\breve{G}_n e^{jn\omega t} + \omega_\mathrm{n}^2 \sum_{n=-\infty}^{\infty} \breve{G}_n e^{jn\omega t} + \kappa \sum_{n=-\infty}^{\infty} \tau_n e^{jn\omega t} \\ &= \sum_{n=-\infty}^{\infty} \Big((-\omega^2\, n^2 + j\,\frac{\omega_\mathrm{n}}{\mathrm{Q}}\,\omega\; n + \omega_\mathrm{n}^2)\, \breve{G}_n + \kappa\tau_n \Big) e^{jn\omega t} \\ &= \sum_{n=-\infty}^{\infty} \Lambda_n e^{jn\omega t} \end{aligned} \tag{4.13}$$

$$\text{where } \Lambda_n = \Lambda_{l,n} + \Lambda_{nl,n} = (-\omega^2\, n^2 + j\,\frac{\omega_\mathrm{n}}{\mathrm{Q}}\,\omega\; n + \omega_\mathrm{n}^2)\, \breve{G}_n + \kappa\tau_n$$

where $\Lambda_{l,n}$ is the linear system component and $\Lambda_{nl,n}$ the nonlinear part.

4.3.1.2 General set of equations

Using these definitions on equation (2.83), the complete system dynamics can be represented as follows

$$-\sum_{n=-\infty}^{\infty} \Lambda_n e^{jn\omega t} \sum_{n=-\infty}^{\infty} \alpha_n e^{jn\omega t} \;+ \sum_{n=-\infty}^{\infty} \Big((\omega_\mathrm{n}^2 + \kappa)\alpha_n - 3\kappa\tau_n + 3\kappa\delta_n \Big) e^{jn\omega t} = \mathrm{f}_k \mathrm{g}_k \sum_{n=-\infty}^{\infty} \beta_n e^{jn\omega t}$$

Or equivalently

$$-\sum_{n=-\infty}^{\infty} \sum_{q=-\infty}^{\infty} \Lambda_q \alpha_{n-q} e^{jn\omega t} \;+ \sum_{n=-\infty}^{\infty} \Big((\omega_\mathrm{n}^2 + \kappa)\alpha_n - 3\kappa\tau_n + 3\kappa\delta_n \Big) e^{jn\omega t} = \mathrm{f}_k \mathrm{g}_k \sum_{n=-\infty}^{\infty} \beta_n e^{jn\omega t}$$

Rearranging terms, the equation can be rewritten as

$$\sum_{n=-\infty}^{\infty}\left(-\sum_{q=-\infty}^{\infty}\Lambda_q\,\alpha_{n-q}+(\omega_{\mathrm{n}}^2+\kappa)\alpha_n-3\kappa\tau_n+3\kappa\delta_n-\mathrm{f}_k\mathrm{g}_k\beta_n\right)e^{jn\omega t}=0 \tag{4.14}$$

giving place to the following set of equations to be solved for each harmonic:

$$-\sum_{q=-\infty}^{\infty}\Lambda_q\,\alpha_{-q}+(\omega_{\mathrm{n}}^2+\kappa)\alpha_0-3\kappa\tau_0+3\kappa\delta_0-\mathrm{f}_k\mathrm{g}_k\beta_0=0\,;\ \mathrm{n=0} \tag{4.15}$$

$$-\sum_{q=-\infty}^{\infty}\Lambda_q\,\alpha_{1-q}+(\omega_{\mathrm{n}}^2+\kappa)\alpha_1-3\kappa\tau_1+3\kappa\delta_1-\mathrm{f}_k\mathrm{g}_k\beta_1=0\,;\ \mathrm{n=1} \tag{4.16}$$

$$-\sum_{q=-\infty}^{\infty}\Lambda_q\,\alpha_{-1-q}+(\omega_{\mathrm{n}}^2+\kappa)\alpha_{-1}-3\kappa\tau_{-1}+3\kappa\delta_{-1}-\mathrm{f}_k\mathrm{g}_k\beta_{-1}=0\,;\ \mathrm{n=-1} \tag{4.17}$$

$$-\sum_{q=-\infty}^{\infty}\Lambda_q\,\alpha_{2-q}+(\omega_{\mathrm{n}}^2+\kappa)\alpha_2-3\kappa\tau_2+3\kappa\delta_2-\mathrm{f}_k\mathrm{g}_k\beta_2=0\,;\ \mathrm{n=2} \tag{4.18}$$

$$-\sum_{q=-\infty}^{\infty}\Lambda_q\,\alpha_{-2-q}+(\omega_{\mathrm{n}}^2+\kappa)\alpha_{-2}-3\kappa\tau_{-2}+3\kappa\delta_{-2}-\mathrm{f}_k\mathrm{g}_k\beta_{-2}=0\,;\ \mathrm{n=-2} \tag{4.19}$$

$$\ldots\quad \text{for n}$$

4.3.2 Cases of study

Solving the set of equations (4.15)-(4.19) can be complex. However, analytical or numerical solutions can be obtained if assumptions on the characteristics of the response of the system are defined.

Due to the nature of the studied system, six different cases are considered, in increasing order of difficulty. Firstly, linear and nonlinear spring models are taken into consideration, in order to evaluate the effectiveness of the approach with both cases. And secondly, the output of the system is considered to have one, two or three harmonics, in order to evaluate the effect on driving voltages.

In conclusion, the following cases are studied:

1. Linear spring model (no K_3 term) : Assuming only first harmonic oscillation; first and second harmonic oscillation; and first, second and third harmonic oscillation.

2. Nonlinear spring model: Assuming only first harmonic oscillation; first and second harmonic oscillation; and first, second and third harmonic oscillation.

4.3.2.1 Linear spring case

In a first approach, if the amplitude of oscillation is not large, the nonlinear spring can be considered negligible, $K_3 = 0$. This is a usual simplification in MEMS devices. In that case the nonlinear spring term vanishes ($\kappa = 0$), and the set of equations (4.14) reduces to

$$\sum_{n=-\infty}^{\infty}\left(\sum_{q=-\infty}^{\infty}\Lambda_{l,q}\,\alpha_{n-q}+\omega_{\mathrm{n}}^2\alpha_n-\mathrm{f}_k\mathrm{g}_k\beta_n\right)e^{jn\omega t}=0 \tag{4.20}$$

which can be developed in n equations as follows:

$$\sum_{q=-\infty}^{\infty}(\omega^2\,q^2-j\,\frac{\omega_{\mathrm{n}}}{\mathrm{Q}}\,\omega\;q-\omega_{\mathrm{n}}^2)\breve{G}_q\,\alpha_{-q}+\omega_{\mathrm{n}}^2\alpha_0-\mathrm{f}_k\mathrm{g}_k\beta_0=0\,;\;\mathrm{n{=}0}$$

$$\sum_{q=-\infty}^{\infty}(\omega^2\,q^2-j\,\frac{\omega_{\mathrm{n}}}{\mathrm{Q}}\,\omega\;q-\omega_{\mathrm{n}}^2)\breve{G}_q\,\alpha_{1-q}+\omega_{\mathrm{n}}^2\alpha_1-\mathrm{f}_k\mathrm{g}_k\beta_1=0\,;\;\mathrm{n{=}1}$$

$$\sum_{q=-\infty}^{\infty}(\omega^2\,q^2-j\,\frac{\omega_{\mathrm{n}}}{\mathrm{Q}}\,\omega\;q-\omega_{\mathrm{n}}^2)\breve{G}_q\,\alpha_{-1-q}+\omega_{\mathrm{n}}^2\alpha_{-1}-\mathrm{f}_k\mathrm{g}_k\beta_{-1}=0\,;\;\mathrm{n{=}{-1}}$$

$$\sum_{q=-\infty}^{\infty}(\omega^2\,q^2-j\,\frac{\omega_{\mathrm{n}}}{\mathrm{Q}}\,\omega\;q-\omega_{\mathrm{n}}^2)\breve{G}_q\,\alpha_{2-q}+\omega_{\mathrm{n}}^2\alpha_2-\mathrm{f}_k\mathrm{g}_k\beta_2=0\,;\;\mathrm{n{=}2}$$

$$\sum_{q=-\infty}^{\infty}(\omega^2\,q^2-j\,\frac{\omega_{\mathrm{n}}}{\mathrm{Q}}\,\omega\;q-\omega_{\mathrm{n}}^2)\breve{G}_q\,\alpha_{-2-q}+\omega_{\mathrm{n}}^2\alpha_{-2}-\mathrm{f}_k\mathrm{g}_k\beta_{-2}=0\,;\;\mathrm{n{=}{-2}}$$

$$\ldots\quad\text{for n}$$

First harmonic approximation

Once simplified the system with the linear spring assumption, the next step is to define the expected output characteristics.

Assuming that the system evolution is a pure sinusoidal, the gap distance (g) reduces to

$$g(t)=G_0+G_1\sin(\omega\,t+\phi_1)=\breve{G}_0+\breve{G}_1e^{j\,\omega\,t}+\breve{G}_{-1}e^{-j\,\omega\,t} \tag{4.21}$$

where $\breve{G}_0=G_0$, $\breve{G}_1=\frac{G_1}{2j}\,e^{j\,\phi_1}$ and $\breve{G}_{-1}=\overline{\breve{G}_1}$ is the conjugate of $\breve{G}_1$.

Consequently, the complete set of equations is reduced to the following equations:

$$\beta_0=\frac{1}{\mathrm{f}_k\mathrm{g}_k}\Big(-\omega_{\mathrm{n}}^2\breve{G}_0^3+\omega_{\mathrm{n}}^2\breve{G}_0^2+\big(4\omega^2-6\omega_{\mathrm{n}}^2\big)|\breve{G}_1|^2\breve{G}_0+2\omega_{\mathrm{n}}^2|\breve{G}_1|^2\Big)$$

$$\beta_1=\frac{1}{\mathrm{f}_k\mathrm{g}_k}\Big(\big(3\omega^2-j\frac{\omega_{\mathrm{n}}}{\mathrm{Q}}\omega-3\omega_{\mathrm{n}}^2\big)|\breve{G}_1|^2+\big(\omega^2-j\frac{\omega_{\mathrm{n}}}{\mathrm{Q}}\omega-3\omega_{\mathrm{n}}^2\big)\breve{G}_0^2+2\omega_{\mathrm{n}}^2\breve{G}_0\Big)\breve{G}_1$$

$$\beta_2=\frac{1}{\mathrm{f}_k\mathrm{g}_k}\Big(\big(2\omega^2-2j\frac{\omega_{\mathrm{n}}}{\mathrm{Q}}\omega-3\omega_{\mathrm{n}}^2\big)\breve{G}_0+\omega_{\mathrm{n}}^2\Big)\breve{G}_1^2$$

$$\beta_3=\frac{1}{\mathrm{f}_k\mathrm{g}_k}\big(\omega^2-j\frac{\omega_{\mathrm{n}}}{\mathrm{Q}}\omega-\omega_{\mathrm{n}}^2\big)\breve{G}_1^3$$

where $|\breve{G}_n|$ is the absolute value of $\breve{G}_n$. Only β_i terms are presented, as $\beta_{-i} = \overline{\beta_i}$.

For a chosen oscillation amplitude, G_0 and G_1, these equations provide the needed input control action β_i.

Similar sets of equations can be obtained for the second and third harmonic formulations. In Appendix A, the second harmonic complete formulation is presented, as its equations can be useful to understand the effect of each harmonic in the final voltage.

4.3.2.2 Nonlinear spring case

In the more general case, the nonlinear spring term cannot be neglected and the complete set of equations (4.14) must be used.

As can be observed in the following equations, each input control action, β_i, appears affected by the nonlinear spring term, κ.

First harmonic approximation

Assuming, again, pure sinusoidal output oscillations

$$g(t) = \breve{G}_0 + \breve{G}_1 e^{j\omega t} + \breve{G}_{-1} e^{-j\omega t}$$

the complete set of equations is reduced to the following equations:

$$\begin{aligned}
\beta_0 =& \frac{1}{\mathrm{f}_k \mathrm{g}_k}\Big(-\omega_\mathrm{n}^2 \breve{G}_0^3 + \omega_\mathrm{n}^2 \breve{G}_0^2 + \big(4\omega^2 - 6\omega_\mathrm{n}^2\big)|\breve{G}_1|^2 \breve{G}_0 + 2\omega_\mathrm{n}^2 |\breve{G}_1|^2\Big) \\
&+ \frac{\kappa}{\mathrm{f}_k \mathrm{g}_k}\big(-\breve{G}_0^5 + 3\breve{G}_0^4 - 3\breve{G}_0^3 + \breve{G}_0^2\big) \\
&+ \frac{\kappa}{\mathrm{f}_k \mathrm{g}_k}\Big(-30|\breve{G}_1|^4 \breve{G}_0 - 20|\breve{G}_1|^2 \breve{G}_0^3 + 36|\breve{G}_1|^2 \breve{G}_0^2 + 18|\breve{G}_1|^4 - 18|\breve{G}_1|^2 \breve{G}_0 + 2|\breve{G}_1|^2\Big) \\
\beta_1 =& \frac{1}{\mathrm{f}_k \mathrm{g}_k}\Big(\big(3\omega^2 - j\frac{\omega_\mathrm{n}}{\mathrm{Q}}\omega - 3\omega_\mathrm{n}^2\big)|\breve{G}_1|^2 + \big(\omega^2 - j\frac{\omega_\mathrm{n}}{\mathrm{Q}}\omega - 3\omega_\mathrm{n}^2\big)\breve{G}_0^2 + 2\omega_\mathrm{n}^2 \breve{G}_0\Big)\breve{G}_1 \\
&+ \frac{\kappa}{\mathrm{f}_k \mathrm{g}_k}\Big(-10|\breve{G}_1|^4 - 30|\breve{G}_1|^2 \breve{G}_0^2 - 5\breve{G}_0^4 + 36|\breve{G}_1|^2 \breve{G}_0 + 12\breve{G}_0^3 - 9|\breve{G}_1|^2 - 9\breve{G}_0^2 + 2\breve{G}_0\Big)\breve{G}_1 \\
\beta_2 =& \frac{1}{\mathrm{f}_k \mathrm{g}_k}\Big(\big(2\omega^2 - 2j\frac{\omega_\mathrm{n}}{\mathrm{Q}}\omega - 3\omega_\mathrm{n}^2\big)\breve{G}_0 + \omega_\mathrm{n}^2\Big)\breve{G}_1^2 \\
&+ \frac{\kappa}{\mathrm{f}_k \mathrm{g}_k}\Big(-20|\breve{G}_1|^2 \breve{G}_0 - 10\breve{G}_0^3 + 12|\breve{G}_1|^2 + 18\breve{G}_0^2 - 9\breve{G}_0 + 1\Big)\breve{G}_1^2 \\
\beta_3 =& \frac{1}{\mathrm{f}_k \mathrm{g}_k}\big(\omega^2 - j\frac{\omega_\mathrm{n}}{\mathrm{Q}}\omega - \omega_\mathrm{n}^2\big)\breve{G}_1^3 + \frac{\kappa}{\mathrm{f}_k \mathrm{g}_k}\big(-5|\breve{G}_1|^2 - 10\breve{G}_0^2 + 12\breve{G}_0 - 3\big)\breve{G}_1^3 \\
\beta_4 =& \frac{\kappa}{\mathrm{f}_k \mathrm{g}_k}\big(-5\breve{G}_0 + 3\big)\breve{G}_1^4 \\
\beta_5 =& -\frac{\kappa}{\mathrm{f}_k \mathrm{g}_k}\breve{G}_1^5
\end{aligned}$$

where $|\breve{G}_n|$ is the absolute value of $\breve{G}_n$. Only β_i terms are presented, as $\beta_{-i} = \overline{\beta_i}$.

Again, for a chosen oscillation amplitude, G_0 and G_1, these equations provide the needed input control action β_i.

Similar sets of equations can be obtained for the second and third harmonic formulations. As in the linear spring case, in Appendix A, the second harmonic complete formulation is presented, as its equations can be useful to understand the effect of each harmonic in the final voltage.

4.3.2.3 Comparison of approaches

Depending on the selected approach, the difficulty to obtain an analytical or numerical solution is challenging. The complexity of the different approaches can be summarized in Table 4.2.

Case	Number of equations	Needed terms
Linear spring - 1 harmonic	4 $\mathbb{R}$-equations	β_0 to β_3
Linear spring - 2 harmonics	7 $\mathbb{R}$-equations	β_0 to β_6
Linear spring - 3 harmonics	10 $\mathbb{R}$-equations	β_0 to β_9
Nonlinear spring - 1 harmonic	6 $\mathbb{R}$-equations	β_0 to β_5
Nonlinear spring - 2 harmonics	11 $\mathbb{R}$-equations	β_0 to β_{10}
Nonlinear spring - 3 harmonics	16 $\mathbb{R}$-equations	β_0 to β_{15}

Table 4.2: Summary of approaches

As can be observed, a minimum of four real-valued equations must be solved in order to obtain a solution of the system and a maximum of sixteen is needed to evaluate the system using a nonlinear spring and evaluating up to three harmonics in the output response.

Consequently, it is important to obtain a clear idea of which are the advantages and disadvantages of each approach, and to choose the correct approximation for each application.

4.3.3 Approach validation

Given the six proposed cases, comparison of the solution of the system presented in Section 4.2 using long-time numerical simulations and the harmonic balance solutions are presented.

The following questions are analyzed:

- Comparison of Harmonic Balance solution in the linear and non-linear case.

- Comparison of Harmonic Balance solution with one, two or three harmonics.
- Comparison of Harmonic Balance solution with the Numerical solution.

The calculated solutions are based on the fabricated device presented in Figure 4.1. The parameters of the device are shown in Table 4.1. The numerical solution of the implicit harmonic balance equations is obtained with Maple®.

4.3.3.1 Linear vs nonlinear spring model in Harmonic Balance calculations

As have been extendedly reported in the literature, large differences can be obtained in the response of the system when using linear or nonlinear spring models when analyzing MEMS devices.

In the examples, comparison between the linear and the nonlinear spring case are presented for two different frequencies and voltage loads. Each example compares the solution obtained by resolving the corresponding implicit equation with one, two or three harmonics.

As can be observed in Figure 4.27, the pure sinusoidal output formulation is more sensitive to the presence of the nonlinear spring term. All solutions are unstable with the nonlinear spring model (amplitude of the gap smaller than zero means snapping of the capacitor). However, for the linear spring model, oscillation is possible under certain voltage loads, as presented in Figure 4.27b.

The system, when using two or three harmonics in the equations (Figure 4.28 and 4.29) behave similarly under the presence or not of the nonlinear spring term. Depending on the input load, amplitudes change considerably if compared the linear and nonlinear spring models, as expected. The magnitude of the amplitude difference between both models can lead the system to pull-in when oscillation is close to the unstable transition.

Consequently, as identified at the beginning of the Chapter, the nonlinear term must be taken into consideration when it is large enough as its influence in the amplitude of the system is not negligible. The Harmonic Balance is able to capture this effect, and it is clear in all the example, and specially in the pure sinusoidal case.

4.3.3.2 Number of harmonics in Harmonic Balance calculations

When analyzing a system using Harmonic Balance, it is well known that an increase in the number of harmonics usually leads to an increase in the precision of the obtained

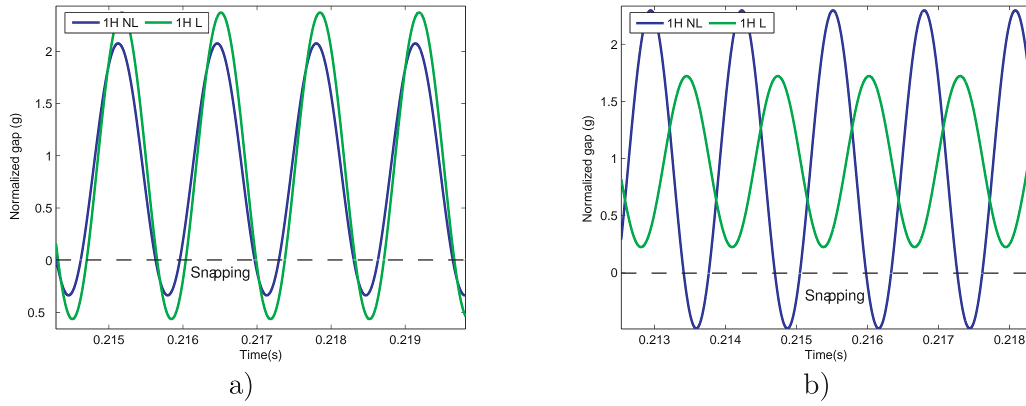

Figure 4.27: Harmonic Balance solutions with only 1 harmonic at the output. Comparison of linear (1H L) and nonlinear (1H NL) spring model. a) $\mathrm{V_{DC}} = 5V$, $\mathrm{V_{AC}} = 3V$, $\mathrm{Q} = 100$, $w_k = 0.96$. b) $\mathrm{V_{DC}} = 5V$, $\mathrm{V_{AC}} = 4V$, $\mathrm{Q} = 100$, $w_k = 1$.

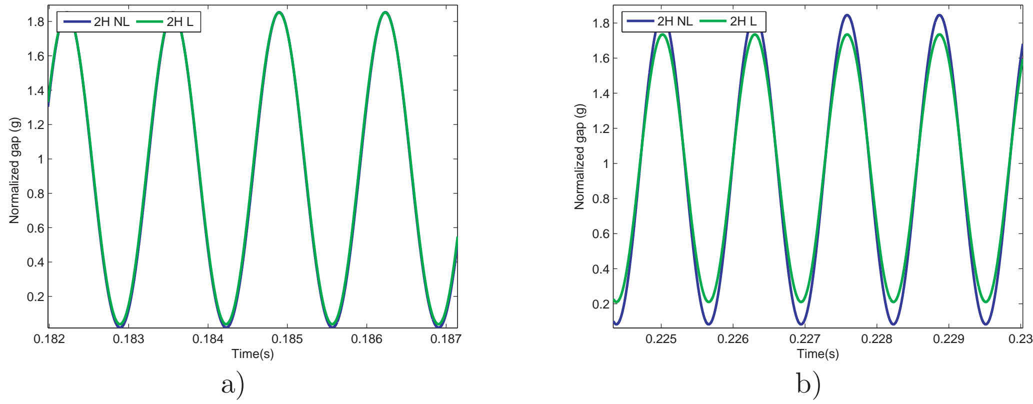

Figure 4.28: Harmonic Balance solutions with 2 harmonics at the output. Comparison of linear (2H L) and nonlinear (2H NL) spring model. a) $\mathrm{V_{DC}} = 5V$, $\mathrm{V_{AC}} = 3V$, $\mathrm{Q} = 100$, $w_k = 0.96$. b) $\mathrm{V_{DC}} = 5V$, $\mathrm{V_{AC}} = 4V$, $\mathrm{Q} = 100$, $w_k = 1$.

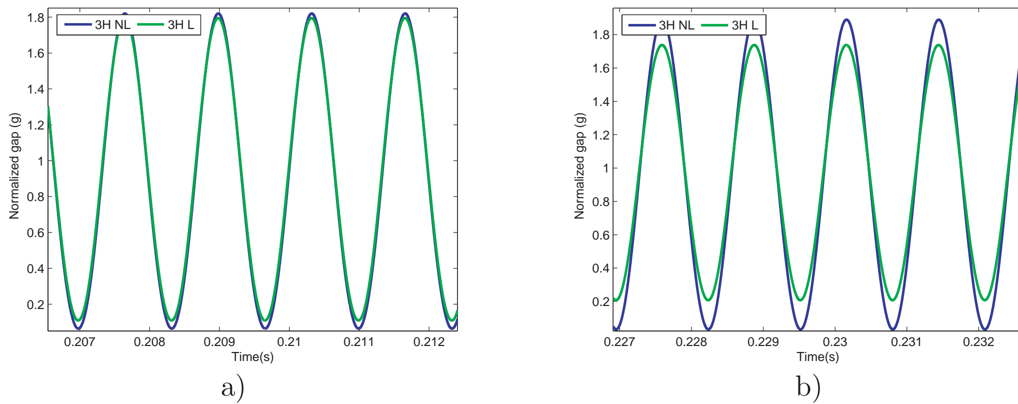

Figure 4.29: Harmonic Balance solutions with 3 harmonics at the output. Comparison of linear (3H L) and nonlinear (3H NL) spring model. a) $\mathrm{V_{DC}} = 5V$, $\mathrm{V_{AC}} = 3V$, $\mathrm{Q} = 100$, $w_k = 0.96$. b) $\mathrm{V_{DC}} = 5V$, $\mathrm{V_{AC}} = 4V$, $\mathrm{Q} = 100$, $w_k = 1$.

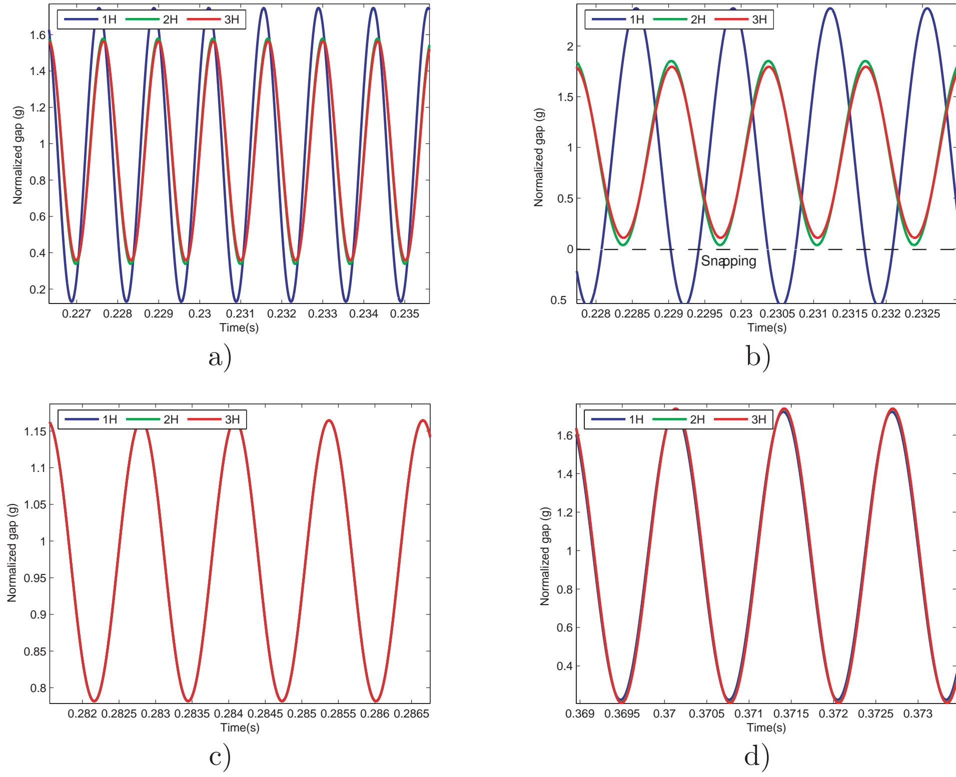

Figure 4.30: Comparison of the calculated position oscillation depending on the number of harmonics in the solution (1H, 2H, 3H) using the linear spring model. Different voltage loads and frequencies. Q = 100. $V_{DC} = 5V$. a) $V_{AC} = 1V$, $w_k = 0.96$. b) $V_{AC} = 3V$, $w_k = 0.96$. c) $V_{AC} = 1V$, $w_k = 1$. d) $V_{AC} = 4V$, $w_k = 1$.

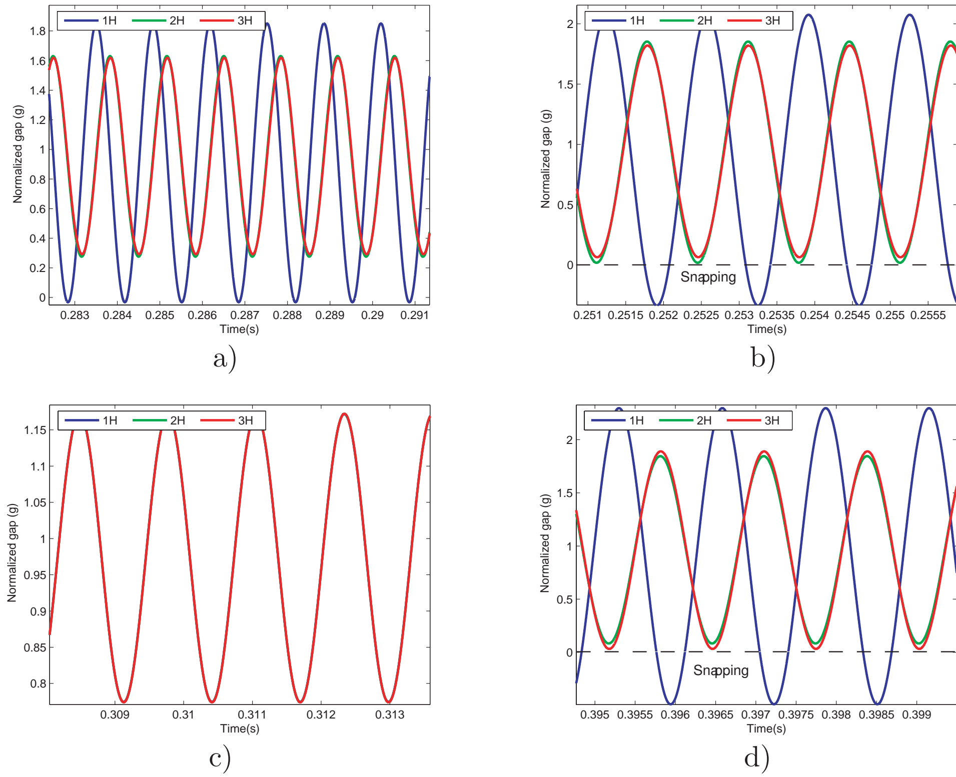

Figure 4.31: Comparison of the calculated position oscillation depending on the number of harmonics in the solution (1H, 2H, 3H) using the linear spring model. Different voltage loads and frequencies. Q = 100. $V_{DC} = 5V$. a) $V_{AC} = 1V$, $w_k = 0.96$. b) $V_{AC} = 3V$, $w_k = 0.96$. c) $V_{AC} = 1V$, $w_k = 1$. d) $V_{AC} = 4V$, $w_k = 1$.

response solution. However, increasing the number of harmonics always inevitably leads to an increase of the complexity of the system equations, what could imply impossibility to reach a computed solution. It is then important to guarantee that the number of harmonics used are the minimum really needed to accomplish the solution goals.

As can be seen in Figures 4.30 and 4.31, the one-harmonic solution differs from the two and three harmonics solutions except in the small amplitude cases. This is true for both the linear and nonlinear sprig models. Consequently, this approach only holds for small amplitude analysis, and cannot be used to predict snapping transition, as it always predicts pull-in well in advance than the higher harmonics solutions.

On the other hand, when comparing the two and three harmonics approximations, they have similar behaviors with both spring models. The two-harmonics approximations tend to predict slightly larger amplitudes, but no pattern have been detected. Both solutions can be similarly valid based on this analysis.

4.3.3.3 Comparison of Harmonic Balance and simulated solutions

As has been detected in the previous section, two and three harmonics harmonic balance solutions differences are small. Consequently, there is a need to decide which of the two models is better when compared to the long-time numerical simulation behavior.

The use of a linear spring model when solving the Harmonic balance equations is analyzed in Figure 4.32. As can be seen, as the simulated real system has a nonlinear spring component, harmonic balance approximation with a linear spring model clearly fails to achieve a decent approximation, as it should be expected. Only in the case of small amplitudes, the approximation can be taken into account to define the evolution of the system, but always with extreme caution.

However, when a nonlinear spring model is used, a good fit is achieved with the two and three harmonics approximation, as can be seen in Figure 4.33. In some cases the two-harmonics approximation behaves better and in other cases the three-harmonics approximation obtains a better fit, so two harmonics approximation could be used in most cases, without losing the main information of the system behavior.

In consequence, Harmonic Balance is able to capture most of the steady-state behavior of the system, and can be used to analyze it.

The Harmonic Balance approximations only have a drawback: the impossibility to predict the pull-in in a confident way. In some cases, the lack of existence of a solution to the

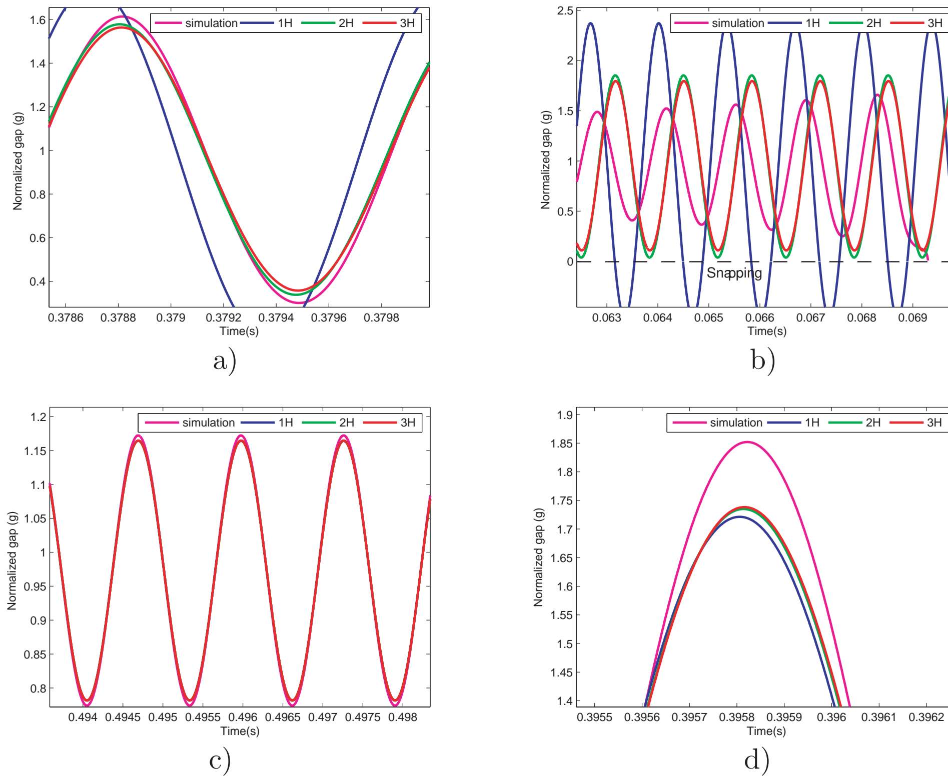

Figure 4.32: Simulated behavior of a real system compared to harmonic balance solution using a linear spring model. a) Detail for $\mathrm{V_{DC}} = 5V$, $\mathrm{V_{AC}} = 1V$, Q = 100, $w_k = 0.96$. b)$\mathrm{V_{DC}} = 5V$, $\mathrm{V_{AC}} = 3V$, Q = 100, $w_k = 0.96$. c) $\mathrm{V_{DC}} = 5V$, $\mathrm{V_{AC}} = 1V$, Q = 100, $w_k = 1$. d) Detail for $\mathrm{V_{DC}} = 5V$, $\mathrm{V_{AC}} = 4V$, Q = 100, $w_k = 1$.

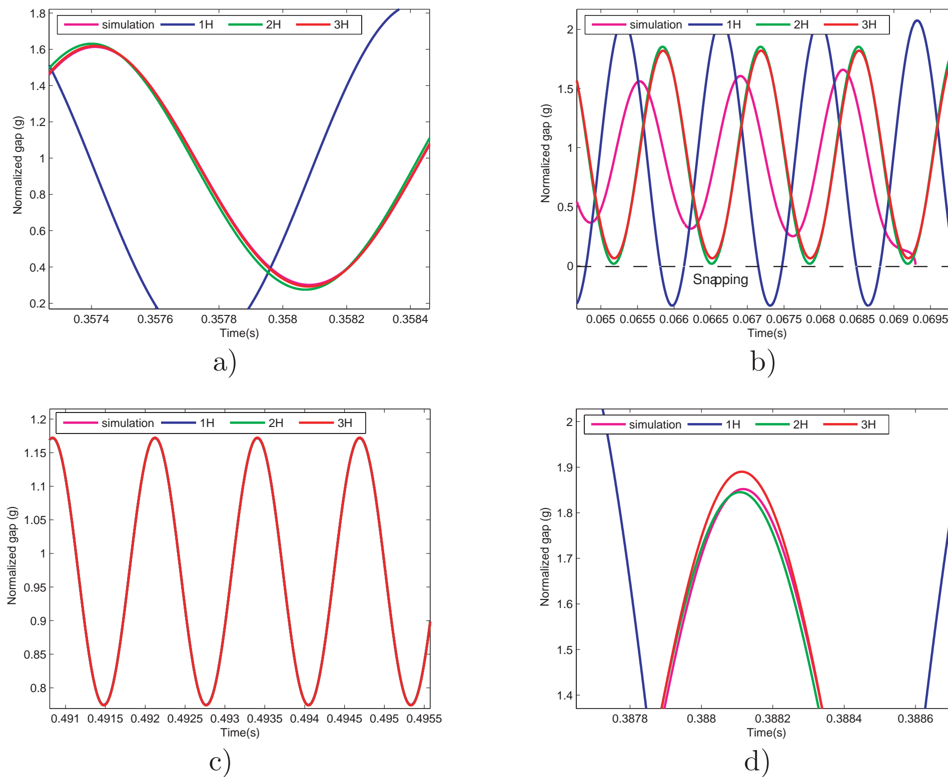

Figure 4.33: Simulated behavior of a real system compared to harmonic balance solution using a nonlinear spring model. a) Detail for $\mathrm{V_{DC}} = 5V$, $\mathrm{V_{AC}} = 1V$, Q = 100, $w_k = 0.96$. b)$\mathrm{V_{DC}} = 5V$, $\mathrm{V_{AC}} = 3V$, Q = 100, $w_k = 0.96$. c) $\mathrm{V_{DC}} = 5V$, $\mathrm{V_{AC}} = 1V$, Q = 100, $w_k = 1$. d) Detail for $\mathrm{V_{DC}} = 5V$, $\mathrm{V_{AC}} = 4V$, Q = 100, $w_k = 1$.

harmonic balance equations predicts the instability of the solution. However, existence of the solution cannot be used to predict that the oscillation is feasible. An example is shown in Figure 4.33b, where the simulation predicts snapping, while the harmonic balance approximations with two and three harmonics predict feasible oscillations. However, Harmonic Balance solutions have amplitudes that cover up to 95% of the gap, what is highly unrealistic and not advisable, as any transient behavior would lead the system to pull-in. Consequently, harmonic balance approximations can only be used if we guarantee that the pull-in breakdown cannot be reached. This means that when predicted oscillations cover more than 80% of the gap, more analysis must be done to guarantee that pull-in doesn't occur.

4.4 Driving voltage characterization

The previous section has identified that at least two harmonics have to be taken into account in the output of the system when analyzing the characteristics of the oscillations when a pure sinusoidal input is used. This result is directly related to the characteristics of the electrostatic actuator.
A deeper insight on the influence of the input load of the system is needed, as its selection would define the characteristics of the oscillation.

4.4.1 Voltage types

Two different cases of driving input voltages are analyzed: one-harmonic sinusoidal actuation and multiple-harmonics sinusoidal actuation.

4.4.1.1 One-harmonic sinusoidal actuation

It is usual, in MEMS driving schemes, to use a single harmonic to excite the system. Using this scheme, three different cases can be analyzed:

- Pure sinusoidal actuation
- Subharmonic sinusoidal actuation
- Superharmonic sinusoidal actuation

Pure sinusoidal actuation

The system can be oscillated at the desired frequency of oscillation with a single harmonic at this frequency, this is what we call a pure sinusoidal actuation.
A pure sinusoidal driving voltage takes the following form

$$V(t) = \mathrm{V_{DC}} + \mathrm{V_{AC}}\,\sin(\omega\,t + \phi) \tag{4.22}$$

what translates to

$$V(t) = \breve{V}_0 + \breve{V}_1\,e^{j\,\omega\,t} + \breve{V}_{-1}\,e^{-j\,\omega\,t} \tag{4.23}$$

where $\breve{V}_0 = \mathrm{V_{DC}}$, $\breve{V}_1 = -j\,\frac{\mathrm{V_{AC}}}{2}\,e^{j\,\phi}$ and $\breve{V}_{-1} = j\,\frac{\mathrm{V_{AC}}}{2}\,e^{-j\,\phi}$.
Consequently, the Fourier expansion of the square of the voltage, using equation (4.12), is as follows

$$\begin{aligned} V(t)^2 =& \breve{V}_0^2 + 2\,\breve{V}_1\,\breve{V}_{-1} + 2\,\breve{V}_0\,\breve{V}_1\,e^{j\,\omega\,t} + 2\,\breve{V}_0\,\breve{V}_{-1}\,e^{-j\,\omega\,t} + \breve{V}_1^2\,e^{2\,j\,\omega\,t} + \breve{V}_{-1}^2\,e^{-2\,j\,\omega\,t} \\ =& \left(\mathrm{V_{DC}^2} + \frac{\mathrm{V_{AC}^2}}{2}\right) - j\,\mathrm{V_{DC}}\,\mathrm{V_{AC}}\,e^{j\phi}\,e^{j\,\omega\,t} + j\,\mathrm{V_{DC}}\mathrm{V_{AC}}\,e^{-j\,\phi}\,e^{-j\,\omega\,t} \\ & - \frac{\mathrm{V_{AC}^2}}{4}\,e^{2\,j\,\phi}\,e^{2\,j\,\omega\,t} - \frac{\mathrm{V_{AC}^2}}{4}\,e^{-2\,j\,\phi}e^{-2\,j\,\omega\,t} \\ =& \beta_0 + \beta_1\,e^{j\omega t} + \beta_{-1}\,e^{-j\omega t} + \beta_2\,e^{2j\omega t} + \beta_{-2}\,e^{-2j\omega t} \end{aligned} \tag{4.24}$$

and the β-terms are

$$\beta_0 = \mathrm{V_{DC}^2} + \frac{\mathrm{V_{AC}^2}}{2} \tag{4.25}$$

$$\beta_1 = -j\,\mathrm{V_{DC}}\,\mathrm{V_{AC}}\,e^{j\,\phi} \tag{4.26}$$

$$\beta_2 = -\frac{\mathrm{V_{AC}^2}}{4}\,e^{2\,j\,\phi} \tag{4.27}$$

$$\beta_i = 0 \;\text{ for } i \geq 3 \tag{4.28}$$

As can be observed, no β_3 component can be produced with this kind of actuation, what implies that the solution of the system is not well defined for any of the cases in Table 4.2.
In particular, it is important to note that with a pure sinusoidal actuation voltage, the system output can never be a pure sinusoidal at the input frequency, because the driving voltage always generates a second harmonic excitation that cannot be compensated.

Subharmonic sinusoidal actuation

The system can be oscillated with only the second harmonic of the desired oscillation frequency, in order to excite subharmonic oscillations at the first harmonic.
In that case, the system input driving voltage takes the following form

$$V(t) = \mathrm{V_{DC}} + \mathrm{V_{AC}}\,\sin(2\,\omega\,t + \phi) \tag{4.29}$$

what translates to

$$V(t) = \breve{V}_0 + \breve{V}_2\,e^{\,2\,j\,\omega t} + \breve{V}_{-2}\,e^{\,-2\,j\,\omega\,t} \tag{4.30}$$

where $\breve{V}_0 = \mathrm{V_{DC}}$, $\breve{V}_1 = \breve{V}_{-1} = 0$, $\breve{V}_2 = -\,j\,\frac{\mathrm{V_{AC}}}{2}\,e^{j\,\phi}$ and $\breve{V}_{-2} = j\,\frac{\mathrm{V_{AC}}}{2}\,e^{-j\,\phi}$.
Consequently, the Fourier expansion of the square of the voltage is as follows

$$\begin{aligned}
V(t)^2 =& \breve{V}_0^2 + 2\,\breve{V}_1\,\breve{V}_{-1} + 2\,\breve{V}_2\,\breve{V}_{-2} + (2\,\breve{V}_0\,\breve{V}_1 + 2\,\breve{V}_2\,\breve{V}_{-1})\,e^{j\,\omega\,t} + (2\,\breve{V}_0\,\breve{V}_{-1} + 2\,\breve{V}_1\,\breve{V}_{-2})\,e^{-j\,\omega\,t} \\
&+ (\breve{V}_1^2 + 2\,\breve{V}_0\,\breve{V}_2)\,e^{2\,j\,\omega\,t} + (\breve{V}_{-1}^2 + 2\,\breve{V}_0\,\breve{V}_{-2})\,e^{-2\,j\,\omega\,t} + 2\,\breve{V}_1\,\breve{V}_2\,e^{3\,j\,\omega\,t} + 2\,\breve{V}_{-1}\,\breve{V}_{-2}\,e^{-3\,j\,\omega\,t} \\
&+ \breve{V}_2^2\,e^{\,j\,\omega\,t} + \breve{V}_{-2}^2\,e^{-4\,j\,\omega\,t} \\
=& \left(\mathrm{V_{DC}^2} + \frac{\mathrm{V_{AC}^2}}{2}\right) - j\,\mathrm{V_{DC}}\,\mathrm{V_{AC}}\,e^{j\,\phi}\,e^{2\,j\,\omega\,t} + j\,\mathrm{V_{DC}}\,\mathrm{V_{AC}}\,e^{-j\,\phi}\,e^{-2\,j\,\omega\,t} \\
&- \frac{\mathrm{V_{AC}^2}}{4}\,e^{2\,j\,\phi}\,e^{4\,j\,\omega\,t} - \frac{\mathrm{V_{AC}^2}}{4}\,e^{-2\,j\,\phi}\,e^{-4\,j\,\omega\,t} \\
=& \beta_0 + \beta_1\,e^{j\,\omega\,t} + \beta_{-1}\,e^{-j\,\omega\,t} + \beta_2\,e^{2\,j\,\omega\,t} + \beta_{-2}\,e^{-2\,j\,\omega\,t} \\
&+ \beta_3\,e^{3\,j\,\omega\,t} + \beta_{-3}\,e^{-3\,j\,\omega\,t} + \beta_4\,e^{4\,j\,\omega\,t} + \beta_{-4}\,e^{-4\,j\,\omega\,t}
\end{aligned} \tag{4.31}$$

and the β-terms are

$$\beta_0 = \mathrm{V_{DC}^2} + \frac{\mathrm{V_{AC}^2}}{2} \tag{4.32}$$

$$\beta_1 = 0 \tag{4.33}$$

$$\beta_2 = -j\,\mathrm{V_{DC}}\,\mathrm{V_{AC}}\,e^{\,j\,\phi} \tag{4.34}$$

$$\beta_3 = 0 \tag{4.35}$$

$$\beta_4 = -\frac{\mathrm{V_{AC}^2}}{4}\,e^{\,2\,j\,\phi} \tag{4.36}$$

$$\beta_i = 0 \;\; \text{for } i \geq 5 \tag{4.37}$$

As can be observed, β_4 component exists, but not the β_5 component, what implies again that the solution of the system is not well defined for any of the cases in Table 4.2.
Again, it is impossible to obtain oscillation only in the first harmonic, as there is always excitation in the second harmonic, and cannot be compensated.

Superharmonic sinusoidal actuation

Finally, the system can be oscillated with only the first harmonic of the frequency, but with the goal to excite superharmonic oscillations at the second harmonic frequency.

In this case, the formulation is identical to the pure sinusoidal case, equation (4.22).

As previously stated, the existing β terms don't allow to solve the equations correctly. And although the second harmonic can be excited and the amplitude selected, there will be always an oscillation in the first harmonic, as the excitation cannot be suppressed.

4.4.1.2 Multiple-harmonics sinusoidal actuation

Actuation schemes that include only a single harmonic have clear limitations on the selection of the desired output. This is clear when the produced β_i terms are compared to the needed β_i provided by Harmonic Balance equations. Moreover, due to the nature of the physical properties associated with the parallel-plate electrostatic actuator, the β_i terms are obtained by squaring the applied voltage, what limits the achievable values that can be generated.

To understand the limitations in the generation of the input voltage a general case is analyzed including a large number of harmonics in the input voltage. We assume, as example, an actuation voltage composed of five harmonics. In this case, the input voltage would be of the following form

$$\begin{aligned} V(t) &= V_0 + V_1 \sin(\omega\, t + \phi_1) + V_2 \sin(2\,\omega t + \phi_2) \\ &\quad + V_3 \sin(3\,\omega t + \phi_3) + V_4 \sin(4\,\omega t + \phi_4) + V_5 \sin(5\,\omega t + \phi_5) \end{aligned} \tag{4.38}$$

what translates using exponential form to

$$\begin{aligned} V(t) &= \breve{V}_0 + \breve{V}_1\, e^{j\,\omega t} + \breve{V}_{-1}\, e^{-j\,\omega t} + \breve{V}_2\, e^{2\,j\,\omega t} + \breve{V}_{-2}\, e^{-2\,j\,\omega t} + \breve{V}_3\, e^{3\,j\,\omega t} \\ &\quad + \breve{V}_{-3}\, e^{-3\,j\,\omega t} + \breve{V}_4\, e^{4\,j\,\omega t} + \breve{V}_{-4}\, e^{-4\,j\,\omega t} + \breve{V}_5\, e^{5\,j\,\omega t} + \breve{V}_{-5}\, e^{-5\,j\,\omega t} \end{aligned} \tag{4.39}$$

where $\breve{V}_0 = V_0$ and $\breve{V}_i = -j\,\frac{V_i}{2}\, e^{j\,\phi_i}$ and $\breve{V}_{-i} = j\,\frac{V_i}{2}\, e^{-j\,\phi_i}$.

Using these parameters definitions and the equation (4.12) previously derived, the β-terms

are calculated as follows

$$
\begin{aligned}
\beta_0 &= V_0^2 + \frac{V_1^2}{2} + \frac{V_2^2}{2} + \frac{V_3^2}{2} + \frac{V_4^2}{2} + \frac{V_5^2}{2} \\
\beta_1 &= -jV_0V_1e^{j\phi_1} + \frac{V_1V_2}{2}e^{j(\phi_2-\phi_1)} + \frac{V_2V_3}{2}e^{j(\phi_3-\phi_2)} + \frac{V_3V_4}{2}e^{j(\phi_4-\phi_3)} + \frac{V_4V_5}{2}e^{j(\phi_5-\phi_4)} \\
\beta_2 &= -\frac{V_1^2}{4}\,e^{2j\phi_1} - jV_0V_2\,e^{j\phi_2} + \frac{V_1V_3}{2}\,e^{j(\phi_3-\phi_1)} + \frac{V_2V_4}{2}\,e^{j(\phi_4-\phi_2)} + \frac{V_3V_5}{2}\,e^{j(\phi_5-\phi_3)} \\
\beta_3 &= -\frac{V_1V_2}{2}\,e^{j(\phi_2+\phi_1)} - jV_0V_3\,e^{j\phi_3} + \frac{V_1V_4}{2}\,e^{j(\phi_4-\phi_1)} + \frac{V_2V_5}{2}\,e^{j(\phi_5-\phi_2)} \\
\beta_4 &= -\frac{V_2^2}{4}\,e^{2j\phi_2} - \frac{V_1V_3}{2}\,e^{j(\phi_3+\phi_1)} - jV_0V_4\,e^{j\phi_4} + \frac{V_1V_5}{2}\,e^{j(\phi_5-\phi_1)} \\
\beta_5 &= -\frac{V_2V_3}{2}\,e^{j(\phi_3+\phi_2)} - \frac{V_1V_4}{2}e^{j(\phi_4+\phi_1)} - jV_0V_5\,e^{j\phi_5} \\
\beta_6 &= -\frac{V_3^2}{4}\,e^{2j\phi_3} - \frac{V_2V_4}{2}\,e^{j(\phi_4+\phi_2)} - \frac{V_1V_5}{2}\,e^{j(\phi_5+\phi_1)} \\
\beta_7 &= -\frac{V_2V_5}{2}\,e^{j(\phi_5+\phi_2)} - \frac{V_3V_4}{2}\,e^{j(\phi_4+\phi_3)} \\
\beta_8 &= -\frac{V_4^2}{4}\,e^{2j\phi_4} - \frac{V_3V_5}{2}\,e^{j(\phi_5+\phi_3)} \\
\beta_9 &= -\frac{V_4V_5}{2}\,e^{j(\phi_5+\phi_4)} \\
\beta_{10} &= -\frac{V_5^2}{4}\,e^{2j\phi_5} \\
\beta_i &= 0 \;\text{ for } i \geq 11 \quad \textit{and} \quad \beta_{-i} = \overline{\beta_i} \;\text{ for } i
\end{aligned}
$$

where $\overline{\beta_i}$ stands for the complex conjugate of the number.

Looking at the obtained equations, we realize that using only the first harmonic frequency in the input voltage, V_1, we generate up to the β_2 term. If we use an input voltage with second harmonic terms, V_2, we generate up to the β_4 term. And if we use an input voltage with fifth harmonic terms, V_5, we generate up to the β_{10} term. This can be extended to any input harmonic frequency. Then, using these equations and comparing the results with the number of harmonics needed for the solution of the Harmonic Balance equations, it can be analyzed what approaches in Table 4.2 can be correctly solved.

It is important to notice that only the sets of equations of the Linear and Non-linear harmonic balance approximations with 2 harmonics in the output are completely well-defined with the voltage control. In these cases, we are able to produce the needed β_i, for the whole set of equations. In the linear case, we need up to the third harmonic in the input voltage, V_3, and in the nonlinear case, we need up to the fifth harmonic in the input voltage, V_5. See Table 4.3.

In the rest of the cases, it is not possible to generate the right β_i to fit the set of equations.

Case	Num. equations	Terms	Needed actuation voltages
Linear spring- 1 harm	4 equations	β_0 to β_3	not well-defined
Linear spring- 2 harm	7 equations	β_0 to β_6	V_0, V_1, V_2, V_3
Linear spring- 3 harm	10 equations	β_0 to β_9	not well-defined
Nonlinear spring- 1 harm	6 equations	β_0 to β_5	not well-defined
Nonlinear spring- 2 harm	11 equations	β_0 to β_{10}	$V_0, V_1, V_2, V_3, V_4, V_5$
Nonlinear spring- 3 harm	16 equations	β_0 to β_{15}	not well-defined

Table 4.3: Summary of approaches

4.4.2 Actuation error

In the thesis, the goal is to obtain a pure sinusoidal oscillation as an output of the system. As presented in Section 4.3.2, the Harmonic Balance equations allow to calculate the needed actuation voltage for a desired output oscillation. If this voltage is applied to the system, the desired oscillation is achieved.

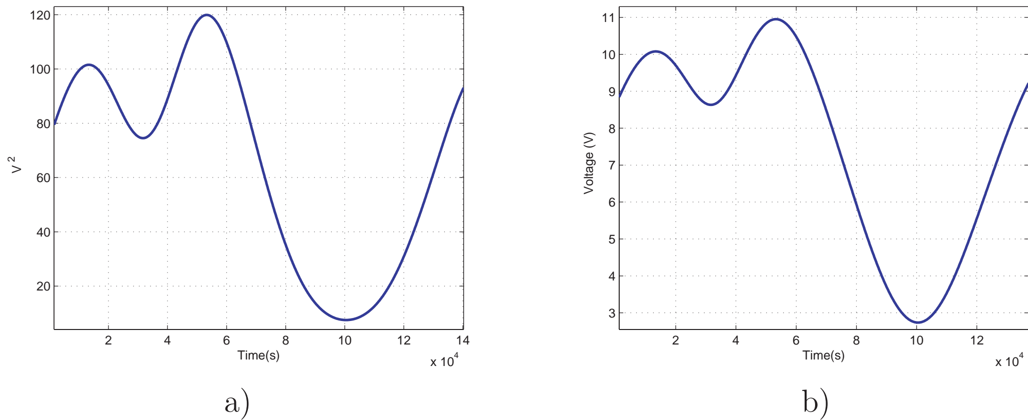

Figure 4.34: Input voltage needed for an oscillation with damping Q = 100 and frequency of $w_k = 0.96$, to obtain a static gap position of $G_0 = 0.9$ and an amplitude of oscillation of $G_1 = 0.7$. a) The square of input voltage (V^2) directly obtained from the β_i. b) The real input voltage (V) needed.

Using the equations for a nonlinear spring model and assuming pure sinusoidal oscillation, an example of the needed actuation voltage, defined by the β_i, is shown in Figure 4.34. In the presented example, an static gap displacement of $G_0 = 0.9$ is desired, as well as, an amplitude of oscillation of $G_1 = 0.7$. This features are imposed for a frequency close to resonance, $w_k = 0.96$, and medium damping conditions Q = 100. The simulated output when applying the calculated input voltage is presented in Figure 4.36, where oscillation is shown to satisfy the desired static and oscillation amplitudes.

One of the main results obtained by the Harmonic Balance analysis is that depending on

the desired oscillation, the actuation voltages that are calculated from the β-equations cannot always be reproduced as the square of a sinusoidal signal. As can be seen in Figure 4.35, Harmonic Balance indicates that V^2 must have negative values, what is completely impossible using only V as driving voltage. This leads to impossibility to reach the desired oscillation with a one-sided voltage driving scheme. However, there are implementation improvements that can lead to full Harmonic Balance applicability, and they are presented in Chapter 7.

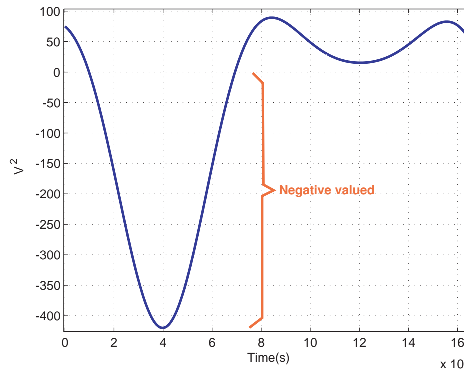

Figure 4.35: Square of input voltage (V^2) needed for an oscillation with medium damping Q = 100 and low frequency, $w_k = 0.8$. It is desired to obtain a static gap position of $G_0 = 0.9$ and an amplitude of oscillation of $G_1 = 0.7$. This voltage is directly obtained from the β_i of the Harmonic Balance.

Apart from the necessity of a positive valued solution in order to be able to generate the driving voltage, V, the calculated solutions can also be difficult to reproduce. There is not a closed form that allows to obtain the voltage input once calculated the β_i of the square of the input voltage. Consequently, the input voltage must be calculated numerically in order to apply it to the system. As can be observed in Figure 4.36, in the example at least a five harmonics fit is needed to produce the calculated input voltage. However, the positive conclusion is that if the reproduction obtained with the fit is fine, the desired output can be perfectly achieved, as observed in Figure 4.36b.

To have better insight in the difficulties to produce the needed input voltage, Table 4.4 presents the obtained harmonic components. Matlab®'s *fit()* function is used with the method of *Nonlinear Least Squares* and a maximum of 1000 iterations. The sum of squares due to the error (*sse*) and the coefficient of determination (*rsquare*) are used to define the precision of the fit. As can be observed, discrepancies between the five harmonics and ten harmonics solutions are slight, but give differences in the final solution error. If an

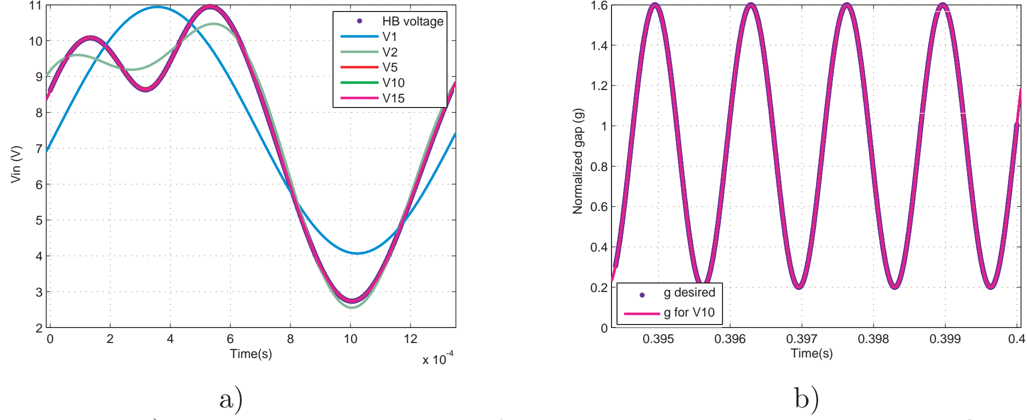

a) b)

Figure 4.36: a) Input voltage needed for an oscillation with damping Q = 100, a normalized frequency of $w_k = 0.96$, a static gap position of $G_0 = 0.9$ and an amplitude of oscillation of $G_1 = 0.7$. The fitted solutions (1 to 15 Harmonics) for the calculated input voltage (HB voltage) are compared. b) Simulated oscillation obtained with the voltage input constructed with the ten harmonics fit (V10) in a).

---

rsquare value of 1 is fixed as a goal, the ten-harmonics fit is the first one to obtain it.

The generation of the desired input voltage could not be always possible, as a ten harmonics input voltage is not straightforward for most applications. Consequently, the actuation error must be analyzed. Figure 4.37 shows the evolution of the output when the input voltage is truncated at a desired number of harmonics. In this particular case, a truncation of five harmonics is able to produce a solution without significant error. However, shorter truncations generate solutions that underscore or overscore the desired amplitude of oscillation.

From the Harmonic Balance analysis an important conclusion can be extracted: for a pure sinusoidal oscillation output, the first harmonic is always necessary in the input voltage. Consequently, it is not possible to design an input voltage without first harmonic component that could oscillate the system as a pure sinusoidal at that frequency. This translates also to the fact that the use of subharmonic or superharmonic oscillation always leads to the existence of first and second harmonic component in the output. Amplitudes of this oscillation may vary, and driving frequency output could be negligible, but the output is never a perfect sinusoid. That could be enough for most applications, but must be taken in consideration when applying these actuation schemes.

And the most important conclusion: if the Harmonic Balance calculated voltage can be generated, the desired oscillation can be achieved.

	1 H	**2 H**	**5 H**	**10 H**	**15 H**
sse	1844,3	119,58	0,17156	0,000025162	0,0000029298
rsquare	0,81009	0,98769	0,99998	1	1
	V_0 = 7.504	V_0 = 7.541	V_0= 7.502	V_0 = 7.502	V_0= 7.502
	V_1 = 3.437	V_1 = 3.37	V_1 = 3.37	V_1 = 3.429	V_1 = 3.43
	ϕ_1 = -0.1122	ϕ_1 = 0.02342	ϕ_1 = -0.09609	ϕ_1 = -0.09697	ϕ_1=-0.09705
	ω_1 = 4719	V_2 = -1.643	V_2 = -1.6	V_2 = -1.6	V_2 = -1.6
		ϕ_2 = -1.223	ϕ_2= -1.454	ϕ_2= -1.456	ϕ_2= -1.456
		ω_1 = 4568	V_3 = 0.3969	V_3 = 0.3974	V_3 = 0.3975
			ϕ_3= 0.1009	ϕ_3= 0.1006	ϕ_3= 0.1005
			V_4 = 0.192	V_4 = -0.1918	V_4 = -0.1918
			ϕ_4= -1.486	ϕ_4 = 1.656	ϕ_4= 1.657
			V_5 = -0.04469	V_5 = -0.04427	V_5 = -0.04424
			ϕ_5 = 0.1945	ϕ_5 = 0.1937	ϕ_5 = 0.1936
			ω_1= 4696	V_6 = -0.01463	V_6 = -0.01462
				ϕ_6 = 4.971	ϕ_6 = -1.314
				V_7= 0.006008	V_7 = 0.00603
				ϕ_7= -6.006	ϕ_7= 0.2765
				V_8= 0.002402	V_8 = 0.002406
				ϕ_8 = -1.249	ϕ_8 = -1.241
				V_9 = -0.0009948	V_9 = -0.000978
				ϕ_9= -5.9	ϕ_9= 0.3874
				V_{10}= 0.000421	V_{10} = -0.0004156
				ϕ_{10}= -4.243	ϕ_{10}= -1.136
				ω_1= 4697	V_{11} = -0.0001597
					ϕ_{11}= -2.622
					V_{12}= -7.852e-005
					ϕ_{12}= 2.09
					V_{13} = -3.571e-005
					ϕ_{13}= 0.5667
					V_{14}= -1.611e-005
					ϕ_{14}= -0.9077
					V_{15} = -6.566e-006
					ϕ_{15}= -2.419
					ω_1= 4697

Table 4.4: Input voltage needed for an oscillation with medium damping Q = 100 and a frequency close to resonance, $w_k = 0.96$. It is desired to obtain a static gap position of $G_0 = 0.9$ and an amplitude of oscillation of $G_1 = 0.7$. Harmonic fits are presented with 1 to 15 harmonics.

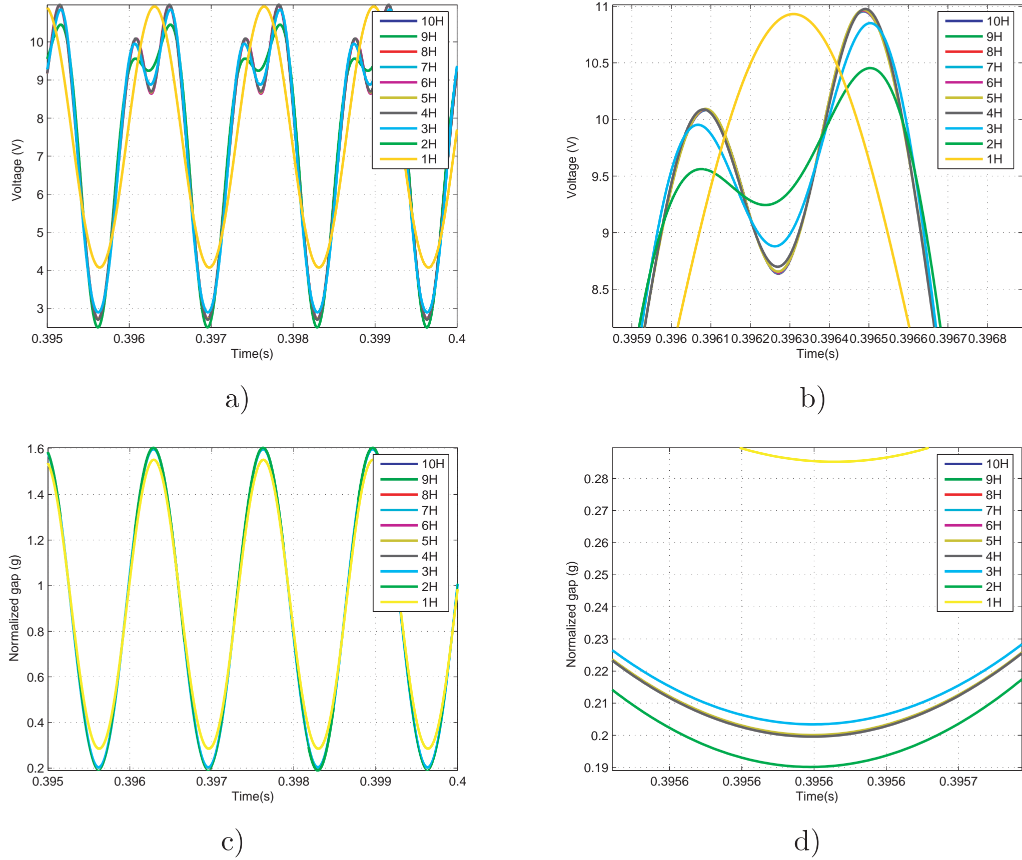

Figure 4.37: Analysis of reproduction of the Harmonic Balance voltage to obtain a static gap position of $G_0 = 0.9$ and an amplitude of oscillation of $G_1 = 0.7$, with damping Q = 100 and a frequency of $w_k = 0.96$. a) Ten harmonics approximation of the input voltage needed for actuation and the truncated options. b) Close-up of the voltages. c) Simulated oscillation obtained with the voltage input constructed with the ten harmonics fit and the truncated ones. d) Close-up of the oscillations.

4.5 Driving voltage analysis

In the previous sections, the natural behavior of the system has been studied. In this section, it will be analyzed how to actuate the system to obtain a desired performance.

In the design of vibratory devices, it is an usual goal to have a stable and pure sinusoidal oscillation. If this aim is achieved, the device would perform at its best. As the system is inherently nonlinear, as has been previously shown, the election of the input actuation must be accurate to obtain the desired sinusoidal oscillation. Consequently, an analysis of the needed characteristics of the control action is performed, using Harmonic Balance as the election tool.

4.5.1 Number of harmonics

The number of harmonics needed to accurately reproduce the calculated input voltage to obtain a pure sinusoidal solution is analyzed in this subsection, based on Harmonic Balance solution.

Iterative solutions of the Harmonic Balance equations have been calculated for different system parameters. The presented examples are based on the device parameters on Table 4.1. At each step, the needed input voltage is approximated using Matlab®'s *fit()* command to determine the minimum number of harmonics needed to obtain an *rsquare*-error of unity. The results are calculated on a square grid with 2 degrees of freedom: X-axis corresponds to the static displacement (G_0) ranging from 0.7 to 1 and the Y-axis corresponds to the oscillation amplitude (G_1) ranging from 0.05 to 0.9.

Figures 4.38-4.41 show the number of harmonics needed to produce an input voltage that obtain the desired oscillation given by the X(G_0)-Y(G_1) axis. The plots are obtained for four different frequencies ($0.8\omega_\mathrm{n}$, $0.9\omega_\mathrm{n}$, $0.96\omega_\mathrm{n}$, ω_n) and three different damping conditions (Q = 10, 100 and 1000). The plots show that the variations in the damping and chosen frequency have an effect on the desired input voltage and the number of harmonics needed to reproduce it.

To understand the plots, it is important to note that the region on the right of the plots (*red zone*) indicates that the voltage solution calculated by the harmonic balance approximation is not completely real-valued, and consequently, impossible to be achieved directly as input voltage (see Figure 4.35 in the previous section as example and Chapter 7 solution). The region on top (*brown zone*) is the area that cannot be achieved by physical limitations, as it implies that the total amplitude is greater than the physical gap. And the orange zone indicates that with 10 harmonics the calculated input voltage is not satisfactorily generated (the *rsquare*-error of the fitted solution is lower than 1).

The small orange dots in the large blue area indicate poor fitting results, but they can be due to not a good enough initial condition in the iterative analysis procedure, consequently, no special conclusions can be drawn from them. The same analysis can be done with the large *orange area*. As has been commented in the previous section, small errors in the fitting doesn't necessarily imply large errors in the desired output. It only indicates a working zone where the voltage election is more demanding.

The analysis of the plots show that in the frequencies closer to resonance (w_k = 0.96

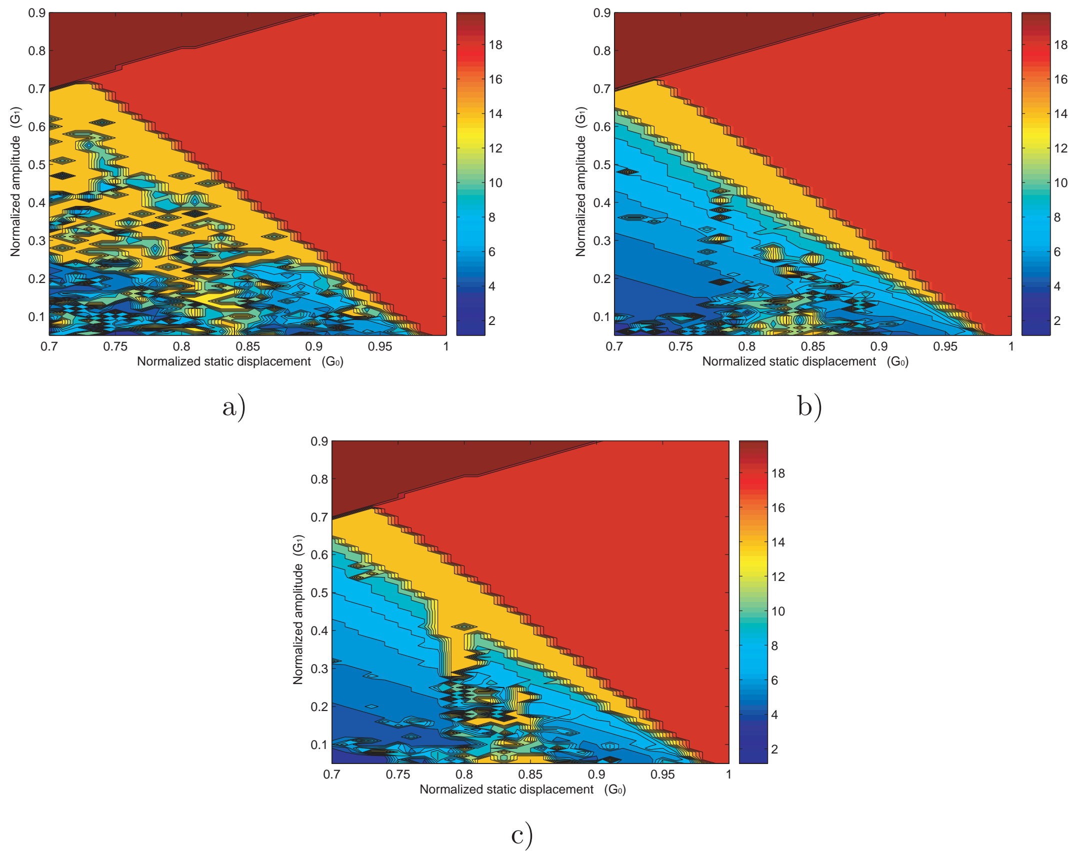

Figure 4.38: Number of harmonics needed to reproduce the harmonic balance voltage using a nonlinear spring model. $w_k = 0.8$ a) Q = 10 b) Q = 100 c) Q = 1000.

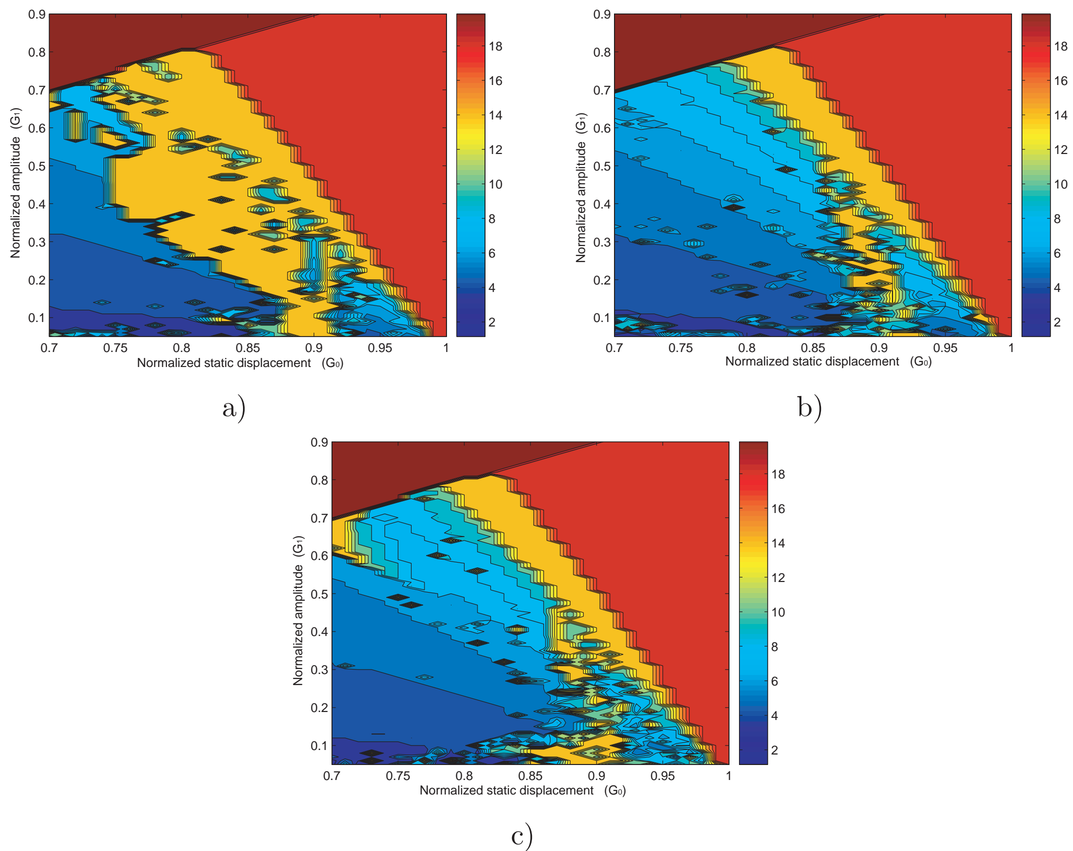

Figure 4.39: Number of harmonics needed to reproduce the harmonic balance voltage using a nonlinear spring model. $w_k = 0.9$ a) Q = 10 b) Q = 100 c) Q = 1000.

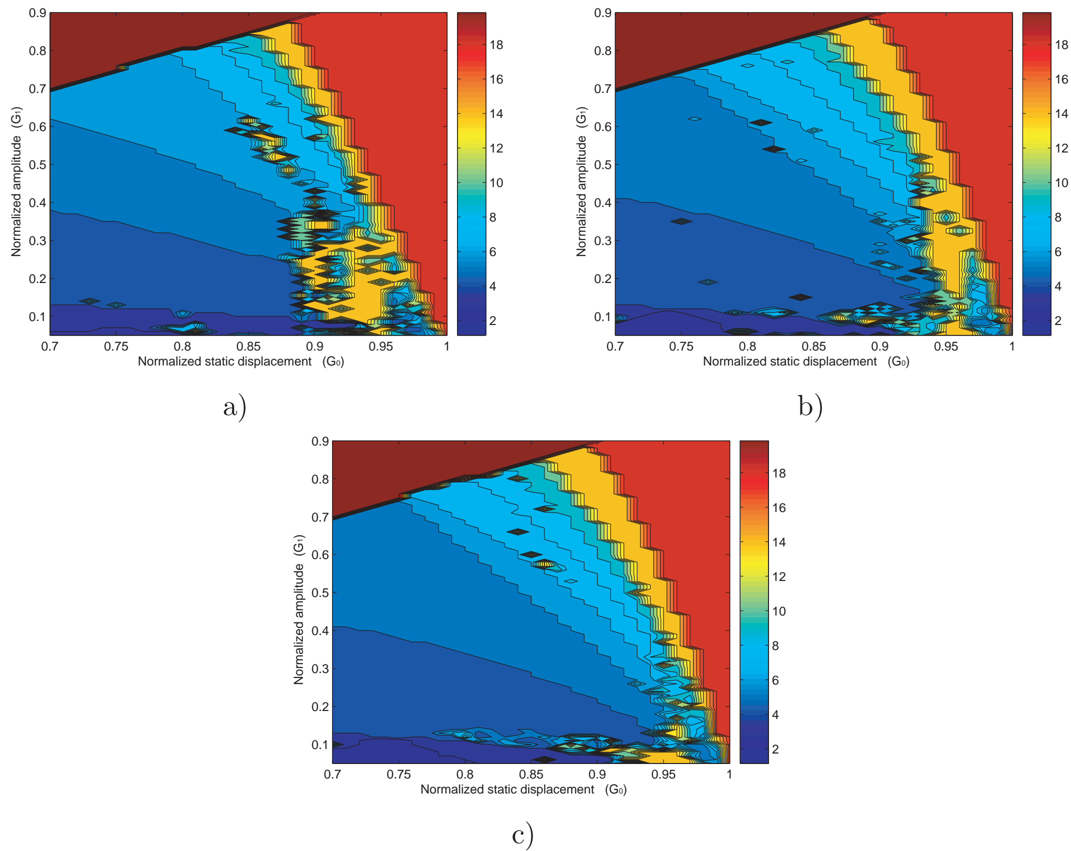

Figure 4.40: Number of harmonics needed to reproduce the harmonic balance voltage using a nonlinear spring model. $w_k = 0.96$ a) Q = 10 b) Q = 100 c) Q = 1000.

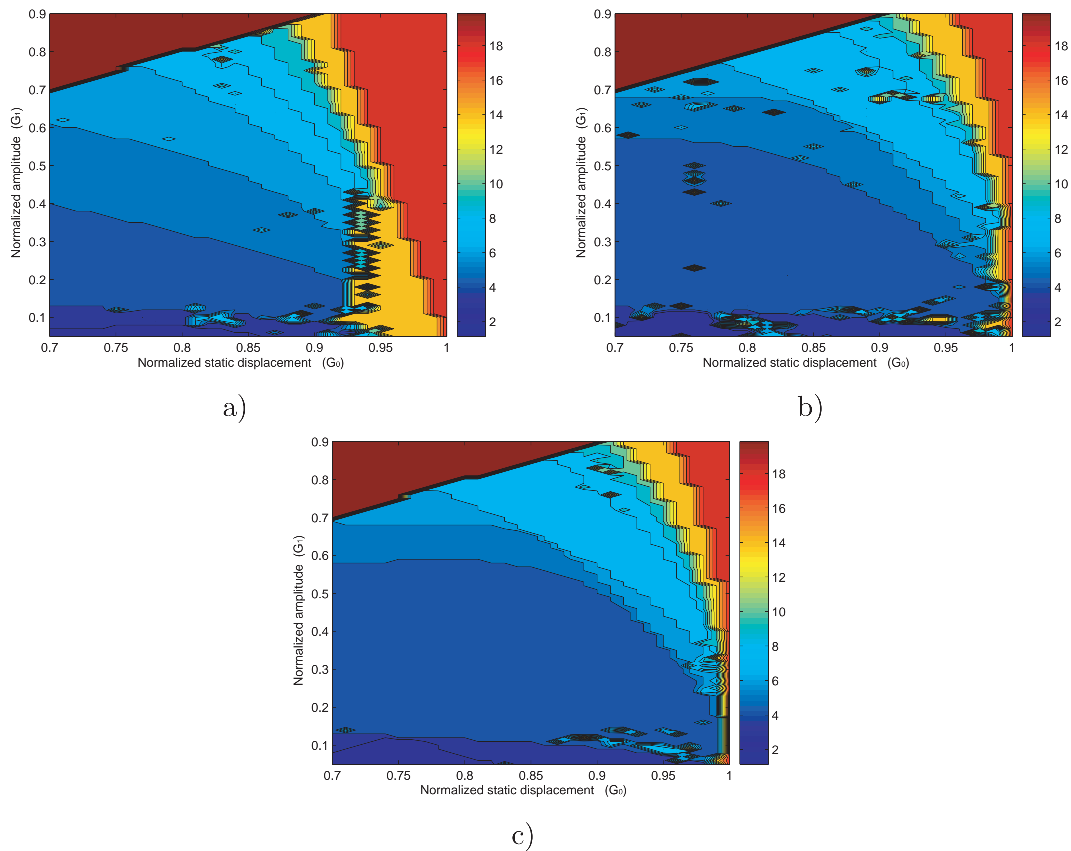

Figure 4.41: Number of harmonics needed to reproduce the harmonic balance voltage using a nonlinear spring model. $w_k = 1$ a) Q = 10 b) Q = 100 c) Q = 1000.

and $w_k = 1$), it is easier to obtain a pure sinusoidal oscillation: the range of obtainable oscillations is wider, and large amplitudes can be achieved with few harmonics in the input. When the desired frequencies are further away ($w_k = 0.9$ and $w_k = 0.8$), the range of obtainable oscillations diminishes and the difficulty to calculate the input voltage increases, as observed by the increase of the *orange zones*.

The increase of the Quality factor has some impact in the reachable area when it is increased from 10 to 100, as observed in Figure 4.41. In this example, the calculated input voltage is feasible for $G_0 = 0.95$ and $G_1 = 0.9$ when Q = 100 but not in the Q = 10 case. However, increases in the Quality factor from 100 to 1000 have no significant effect. At the same time, the number of harmonics needed, based on harmonic balance approximation, has similar behavior in all cases. With five or six harmonics, most of the range can be accessed, but higher harmonics are needed to reach to the upper limit. The increase in the Quality factor has impact when changing from 10 to 100, reducing its impact in the 100 to 1000 increase.

It is interesting to note that the Quality factor increase is especially noted by the range of oscillations where five and six harmonics input approximations can be used. That area is widely increased with the increase of the Quality factor from 10 to 100, depending on the example. At the same time, the area where input approximations with three and four harmonics are enough has no significant variation, and the effect on the higher harmonics approximations is also limited.

4.5.2 Voltage magnitude

In parallel with the number of harmonics, there are magnitude related aspects of the input voltage that have effect on the behavior of the system. It is important to know the maximum voltage that is applied, or the peak-to-peak magnitude. This analysis is performed in this section.

All the results are generated on the basis of the input voltage calculated using Harmonic Balance approximation. Calculations have been done based on the parameters of Table 4.1, and the nonlinear spring model. The *dark blue zones* of the figures indicate that the combination of static bias and amplitude of oscillation is not feasible in that area. The *right-side blue zone* is not feasible due to not directly reproducible voltage results. The *top blue zone* is not feasible because the amplitude combination would be larger than the physical gap.

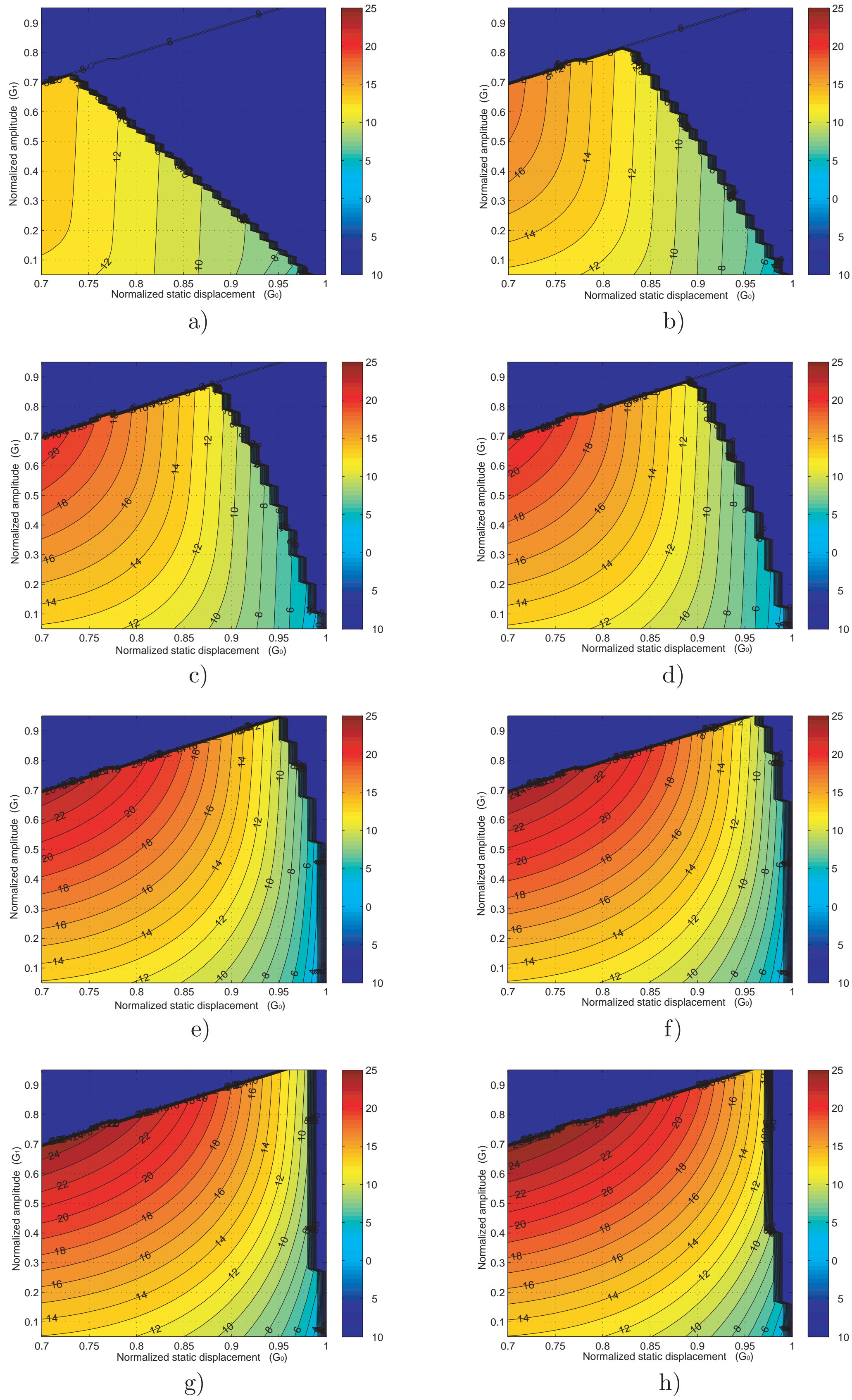

Figure 4.42: Analysis of the peak value of the input voltage (V_{peak}) depending on the desired oscillation bias and amplitude. Fixed damping at Q = 100, and different frequencies. a) $w_k = 0.80$. b) $w_k = 0.90$. c) $w_k = 0.95$. d) $w_k = 0.96$ e) $w_k = 1.00$. f) $w_k = 1.01$. g) $w_k = 1.02$. h)$w_k = 1.03$.

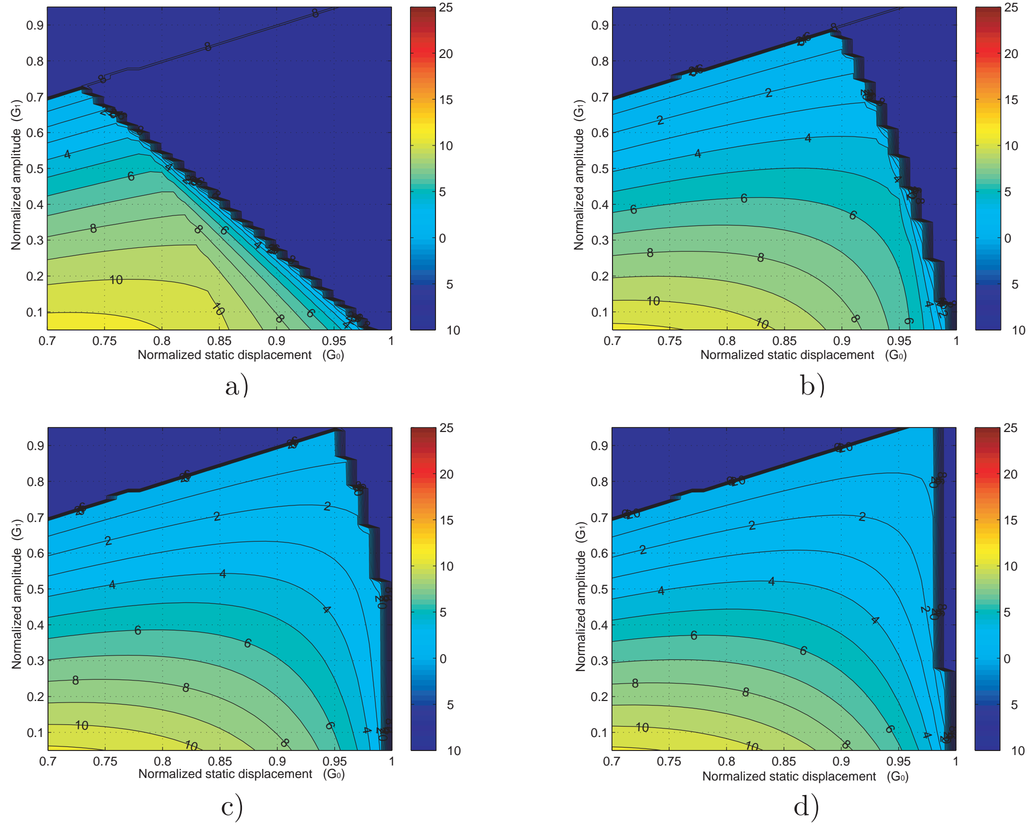

Figure 4.43: Analysis of the minimum applied voltage value (V_{min}), depending on the desired oscillation bias and amplitude. Fixed damping at Q = 100, and different frequencies. a) $w_k = 0.80$. b) $w_k = 0.96$. c) $w_k = 1$. d) $w_k = 1.02$.

As a first approach, the needed voltage peak of the input voltage is used to identify the difficulty to generate the desired output, as it is related to the maximum power demand and device insulation. Moreover, as previously stated in Chapter 3, the oscillation in the energy domain is limited by the potential energy curves of the maximum and minimum voltages applied to the device. Consequently, the voltage peak gives insight on the possible failure of the device due to snapping.

Figure 4.42 shows the voltage peak of the calculated input voltages. An extended range of frequencies is presented, from $w_k = 0.8$ up to $w_k = 1.03$. The evolution of the reachable area with one-sided actuation is interesting, as it increases up to $w_k = 1.02$ and then it begins to be reduced. An unexpected result also appears. Based on the Harmonic Balance calculations, in order to obtain a pure sinusoidal output, the maximum reachable amplitude with the lower voltage peak is obtained around natural frequency ($w_k = 1$). For each selected amplitude (G_1), around natural frequency the system can be oscillated with less voltage peak amplitude. Not only that, the static displacement (G_0) is around the initial position of the gap, what is in general desirable.

This result is important because changes expected placement of the resonance frequency

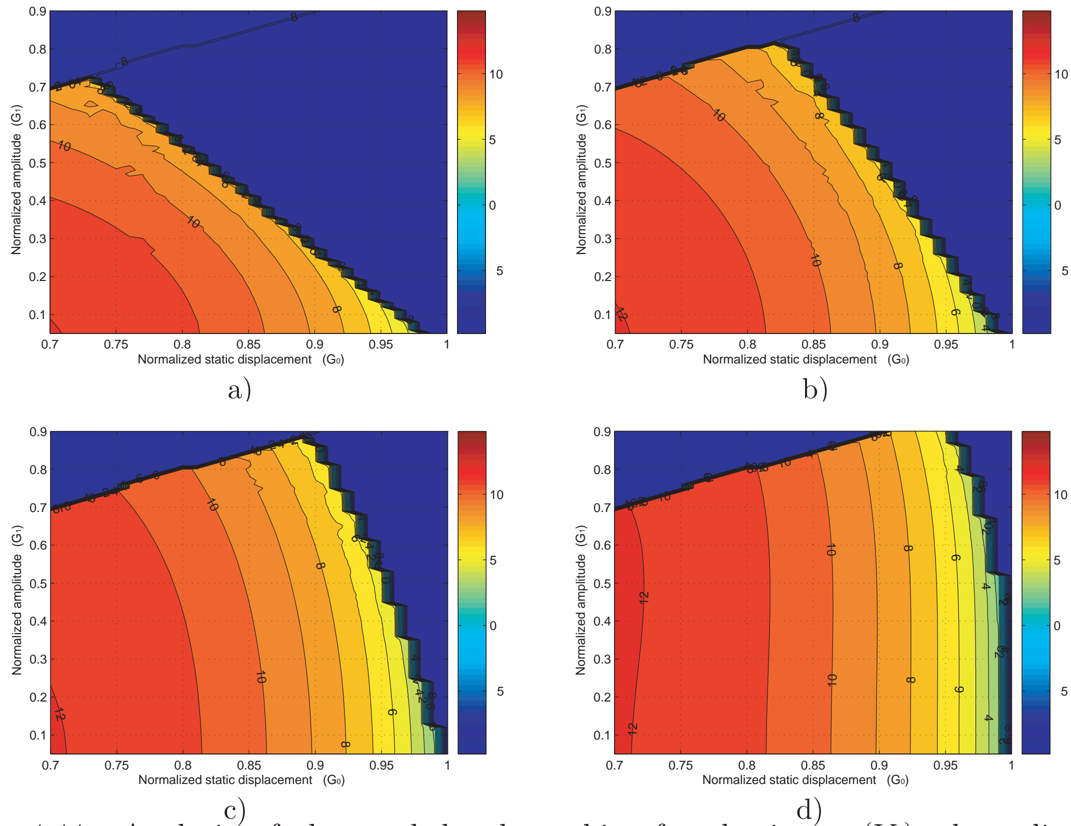

Figure 4.44: Analysis of the needed voltage bias for the input (V_0), depending on the desired oscillation bias and amplitude. Fixed damping at Q = 100, and different frequencies. a) $w_k = 0.80$. b) $w_k = 0.90$. c) $w_k = 0.96$. d) $w_k = 1$.

compared to the AC-DC pull-in curves, in Figure 4.25. In order to obtain the maximum amplitude at the minimum voltage, voltage sweeps are usually carried out. However, that approach fixes the DC-voltage and correspondingly the frequency shift due to softening. The AC-DC pull-in curves in Figure 4.25 are based on a fixed DC bias of $5V$ and oscillated with only the first harmonic at the driving voltage, giving a resonance peak around $w_k = 0.95$ without control of harmonics at the output. Using the Harmonic Balance approach, we concentrate on obtaining a pure sinusoidal output and use an input voltage with up to ten harmonics, and consequently, the system changes its resonant behavior.

Based on Harmonic Balance approach, with frequency at $w_k = 0.95$, the maximum achievable amplitude is $G_1 = 0.87$ with a bias of $G_0 = 0.88$, obtained with a peak of $11.83V$. However, with driving frequency at natural frequency, $w_k = 1$, the maximum achievable amplitude is $G_1 = 0.90$ with a bias of $G_0 = 0.94$, obtained with a peak of $11.5V$. In both cases, reachability is not guaranteed.

The minimum voltage level indicates the minimum energy that the system keeps during the oscillation. Again, this value gives insight on the lower limit of the oscillation trajectory and can give information of the possible failure of the device due to snapping.

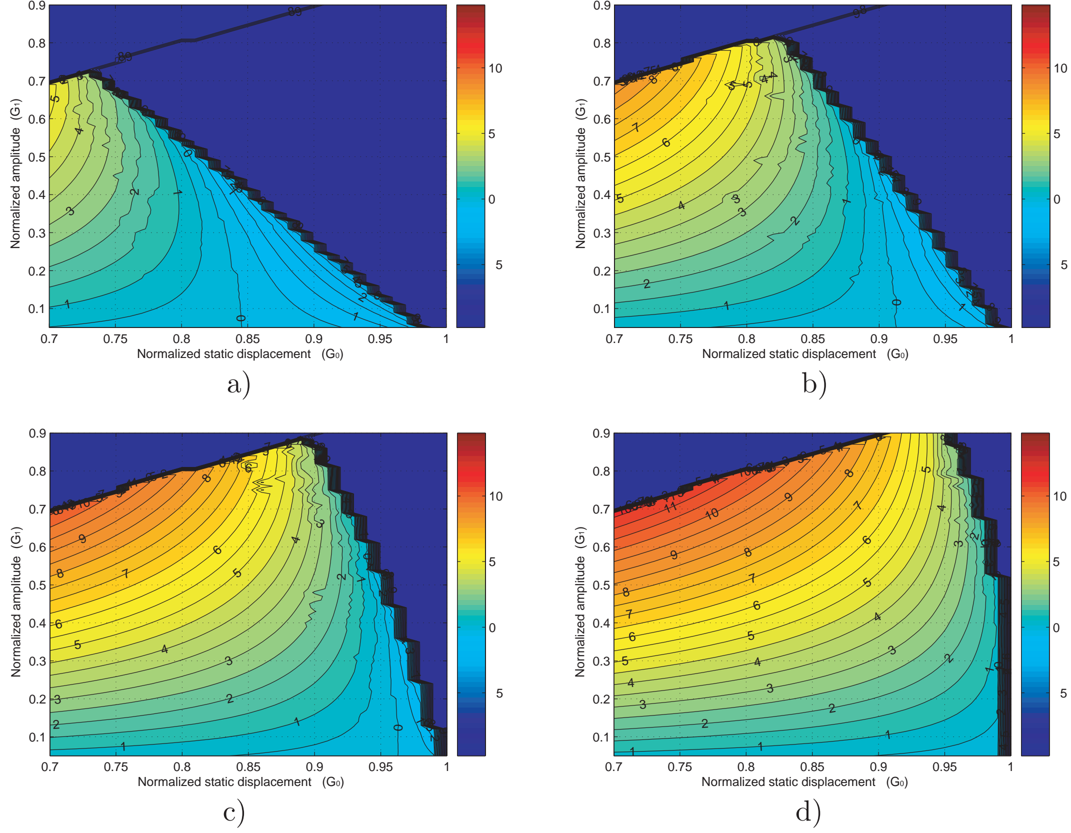

Figure 4.45: Analysis of the needed amplitude of the first harmonic of the input (V_1), depending on the desired oscillation bias and amplitude. Fixed damping at Q = 100, and different frequencies. a) $w_k = 0.80$. b) $w_k = 0.90$. c) $w_k = 0.96$. d) $w_k = 1$.

Figure 4.43 presents the results of the simulation for the example. All plots are similar without special differences between them.

Finally, analysis of the evolution of the static voltage load (V_0) that is needed and the magnitude of the first harmonic component (V_1) based on Harmonic Balance calculations are presented in Figure 4.44 and Figure 4.45. In the case of DC-bias, as expected, the DC voltage is related to the final position bias (G_0), with similar plots for $w_k = 0.96$ and $w_k = 1$. And in the case of the first harmonic, it is related to the final amplitude (G_1).

4.5.3 Energy consumption

The voltage magnitudes of previous section give an indication of the maximum load that must be applied, but they provide no insight on the energy consumption generated by the Harmonic Balance input voltage. Moreover, as has been shown in the examples, the needed voltage pattern can be really complex, and in those cases, the voltage magnitudes only capture the range of fluctuation of the signal but not the complexity of it.

The goal is to obtain the cheapest oscillation in energy consumption terms. In order to

evaluate the Harmonic Balance driving voltage energy consumption, the actual voltage driving scheme including the voltage source must be analyzed. Figure 4.46 shows the electrical equivalent schematic of the system including the voltage source. In this scheme, the voltage source charges and discharges the driving capacitor (electrostatic transducer) with a series resistance, which is coupled to a mechanical load that moves due to the generated force by the electrostatic transducer [183]. In the example, the mechanical system is converted to its electrical equivalent.

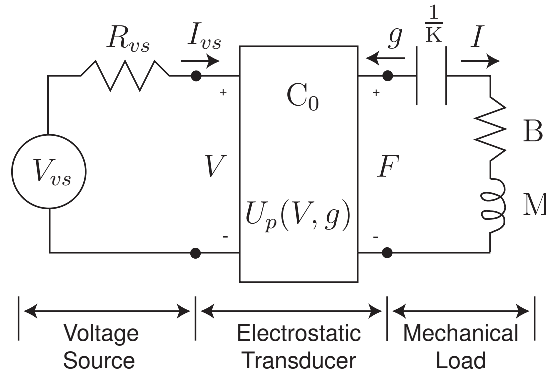

Figure 4.46: Electrical port-model of the electromechanical system including the voltage source, based on [183].

The energy introduced in the system by the voltage source is transformed to capacitor electrostatic potential energy, and this energy is converted to kinetic energy and mechanical potential energy during the oscillation. In the ideal case of having an ideal voltage source and a system without dissipation, if the MEMS resonator is excited at resonance, it would continue oscillating without need of more energy. However, this is not true in most cases. In real applications, the voltage source is not ideal, compensates the damping losses and forces the oscillation at the driving frequency. Consequently, continuous energy supply exists, and the goal is to minimize it.

To analyze the energy consumption, we must turn back to the energy equation (3.1) from Chapter 3, now assuming that the voltage is a function of time

$$E(t) = \frac{1}{2}\mathrm{M}\ \dot{\hat{y}}(t)^2 + \frac{1}{2}\mathrm{K}\ \hat{y}(t)^2 + \frac{1}{4}\mathrm{K}_3\ \hat{y}(t)^4 - \frac{1}{2}\frac{\mathrm{C}_0}{(1-\frac{\hat{y}(y)}{\mathrm{g}_0})}V(t)^2 \tag{4.40}$$

and remembering that $\hat{y}(t) = \mathrm{g}_0 - \hat{g}(t)$. We want to analyze how the energy is exchanged

in the system, what implies studying the energy variation

$$\frac{d}{dt}E(t) = \mathrm{M}\ \ddot{\hat{y}}(t)\ \dot{\hat{y}}(t) + \mathrm{K}\ \hat{y}(t)\ \dot{\hat{y}}(t) + \mathrm{K}_3\ \hat{y}(t)^3\ \dot{\hat{y}}(t) - \frac{1}{2}\frac{\mathrm{C}_0}{\mathrm{g}_0(1-\frac{\hat{y}(t)}{\mathrm{g}_0})^2}\ V(t)^2\ \dot{\hat{y}}(t) - \frac{\mathrm{C}_0}{(1-\frac{\hat{y}(t)}{\mathrm{g}_0})}\ V(t)\ \dot{V}(t) \tag{4.41}$$

where $\dot{V}(t)$ is the time derivative of the input voltage. Rearranging terms

$$\frac{d}{dt}E(t) = \left(\mathrm{M}\ \ddot{\hat{y}}(t) + \mathrm{K}\ \hat{y}(t) + \mathrm{K}_3\ \hat{y}(t)^3 - \frac{1}{2}\frac{\mathrm{C}_0}{\mathrm{g}_0(1-\frac{\hat{y}(t)}{\mathrm{g}_0})^2}\ V(t)^2\right)\ \dot{\hat{y}}(t) - \frac{\mathrm{C}_0}{(1-\frac{\hat{y}(t)}{\mathrm{g}_0})}\ V(t)\ \dot{V}(t) \tag{4.42}$$

and using the dynamic equation of the system equivalence (2.77)

$$\mathrm{M}\ \ddot{\hat{y}}(t) + \mathrm{K}\ \hat{y}(t) + \mathrm{K}_3\ \hat{y}(t)^3 - \frac{1}{2}\frac{\mathrm{C}_0}{\mathrm{g}_0(1-\frac{\hat{y}(t)}{\mathrm{g}_0})^2}\ V(t)^2 = -\mathrm{B}\ \dot{\hat{y}}(t)$$

the resulting equation is

$$\frac{d}{dt}E(t) = -\mathrm{B}\ \dot{\hat{y}}(t)^2 - \frac{\mathrm{C}_0}{(1-\frac{\hat{y}(t)}{\mathrm{g}_0})}\ V(t)\ \dot{V}(t) \tag{4.43}$$

meaning that the energy variation has a part that corresponds to the energy mechanically dissipated in the damper and another part that corresponds to the energy exchanged between the voltage source and the electrostatic actuator.

At this point, it is necessary to introduce the source as an active part in the circuit, as indicated in Figure 4.46. Introducing the source voltage, $V_{vs}(t)$, and the source current, $I_{vs}(t)$, the voltage applied to the actuator is

$$V(t) = V_{vs}(t) + \mathrm{R}_{vs}\ I_{vs}(t) \tag{4.44}$$

$$\dot{V}(t) = I_{vs}(t) \tag{4.45}$$

where the positive sign in the voltage is due to the different direction between position and current, Figure 4.46, to guarantee sign consistency. R_{vs} is the resistance associated with the internal resistance of the voltage source, and also aggregates the rest of resistances associated with the wiring and the electronics from the voltage source up to the capacitor. Then, equation (4.43) can be rewritten as

$$\frac{d}{dt}E(t) = -\mathrm{B}\ \dot{\hat{y}}(t)^2 - \frac{\mathrm{C}_0}{(1-\frac{\hat{y}(t)}{\mathrm{g}_0})}\ \left(V_{vs}(t)\ I_{vs}(t) + \mathrm{R}_{vs}\ I_{vs}(t)^2\right). \tag{4.46}$$

Assuming steady-state oscillation, the energy balance in one oscillation cycle must be zero, then from equation (4.46), we obtain

$$\int_0^{\frac{2\pi}{\omega}} \frac{d}{dt}E(t)dt = -\int_0^{\frac{2\pi}{\omega}} \mathrm{B}\ \dot{\hat{y}}(t)^2 dt - \int_0^{\frac{2\pi}{\omega}} \frac{\mathrm{C}_0}{(1-\frac{\hat{y}(t)}{\mathrm{g}_0})}\ \left(V_{vs}(t)\ I_{vs}(t) + \mathrm{R}_{vs}\ I_{vs}(t)^2\right) dt = 0 \tag{4.47}$$

and from this equation, the energy provided by the voltage source can be isolated as

$$\int_0^{\frac{2\pi}{\omega}} V_{vs}(t)\ I_{vs}(t)dt = -\int_0^{\frac{2\pi}{\omega}} \frac{\mathrm{B}}{\mathrm{C}_0}\ \dot{\hat{y}}^2\ \left(1-\frac{\hat{y}}{\mathrm{g}_0}\right) dt - \int_0^{\frac{2\pi}{\omega}} \mathrm{R}_{vs}\ I_{vs}(t)^2 dt \tag{4.48}$$

meaning that the voltage source is used to compensate two energy losses: the damping of the system and the source/circuitry losses. If we could assume that the source is ideal, all the losses would be due to the damping of the MEMS resonator. And if the MEMS resonator could have no damping, the voltage source would have zero energy balance, as the current delivered during the charging of the capacitor would be returned during discharging.

However, in real applications the losses exist, and as we want to optimize the energy consumption for sinusoidal oscillation, we need to calculate the actual energy losses in an oscillation cycle. If the oscillation is fixed to be a perfect sinusoidal

$$\hat{y}(t) = \hat{Y}_1 \sin(\omega t) \tag{4.49}$$

$$\dot{\hat{y}}(t) = \hat{Y}_1 \omega \cos(\omega t) \tag{4.50}$$

the consumed electrical energy by the voltage source is given by (4.48), where the mechanical part can be solved leaving

$$E_{losses} = \int_0^{\frac{2\pi}{\omega}} V_{vs}(t)\ I_{vs}(t)dt = -\frac{\mathrm{B}\,\pi}{\mathrm{C}_0}\,\hat{Y}_1^2\,\omega - \mathrm{R}_{vs}\int_0^{\frac{2\pi}{\omega}} I_{vs}(t)^2 dt. \tag{4.51}$$

Consequently, the consumed energy has two terms. The first term is proportional to the oscillation frequency, amplitude of oscillation and damping of the system and inversely proportional to capacitance. And the other one is proportional to the resistance of the power source and the circuitry, and also proportional to the integration of the square of the current needed to drive the system.

As Harmonic Balance calculates the voltage input, $V(t)$, the estimated energy consumption for each driving scheme can be calculated and compared. If we analyze the magnitude of the two terms, even in the case of having a low-loss voltage supply,

the electrical term is several times larger than the damping term. Figure 4.47a shows the value of the damping losses for the simulated example. The range of frequencies goes from $w_k = 0.8$ to $w_k = 1.2$ and Quality-factor ranges from 10 to 100000. For a given Quality factor, the frequency and amplitude of oscillation have little influence on the final losses. Figure 4.47b shows together for the same range the electrical and damping losses. In the case of electrical losses, the source and circuitry resistance is assumed to be as low as 1 Ω. As can be observed, the damping value and its variation is negligible in front of the electrical losses (the four plots are one in top of the other).

Figure 4.47b also introduces an interesting result. The electrical losses have less influence than expected from the Quality-factor when a desired pure-sinusoidal oscillation is fixed. There is a jump from Q = 10 to Q = 100, but then the difference is negligible. In the plot, the three graphs (Q = 100, 1000, 100000) are one on top of the other.

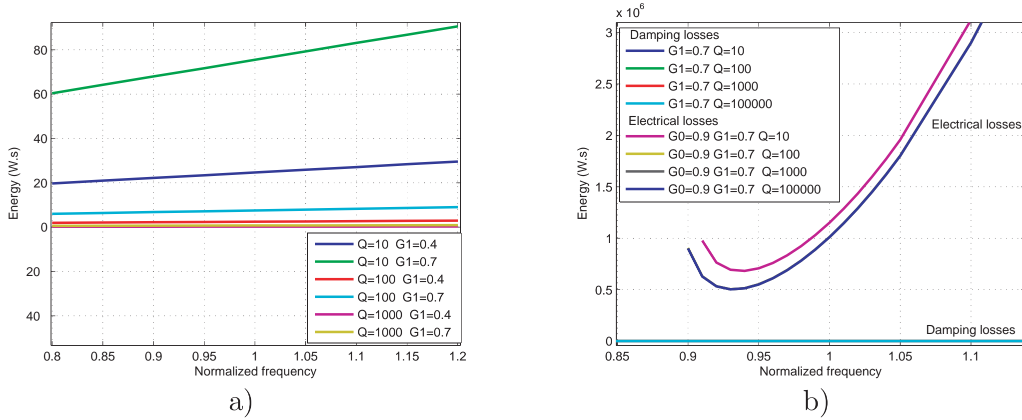

Figure 4.47: a) Energy losses due to mechanical system damping for three different Quality-factors and two different oscillation amplitudes, for the MEMS resonator values in Table 4.1. b) Comparison of the magnitude of the electrical losses and the damping losses, shown in a), for the same range of amplitudes, frequencies and Quality factor.

Figure 4.48 shows the energy consumption calculation for amplitudes of $0.4g_0$ and $0.7g_0$, for an oscillation with a Quality factor of 100. Given a desired gap bias, ranging from 0.9 to 0.99, the energy plots show that for each bias a different minimum energy frequency exists. There is a limitation, the curves show that as the bias is close to unity, the range of feasible frequencies gets reduced, what implies difficulty of using that combination with one-sided actuation. In special, Figure 4.48b doesn't present a curve for bias 0.99, as all Harmonic Balance voltage predictions have negative-valued V^2.

Another interesting result can be extracted of the plots. As the oscillation bias is close to unity, the lowest energy frequency moves to natural frequency ($w_k = 1$) or even

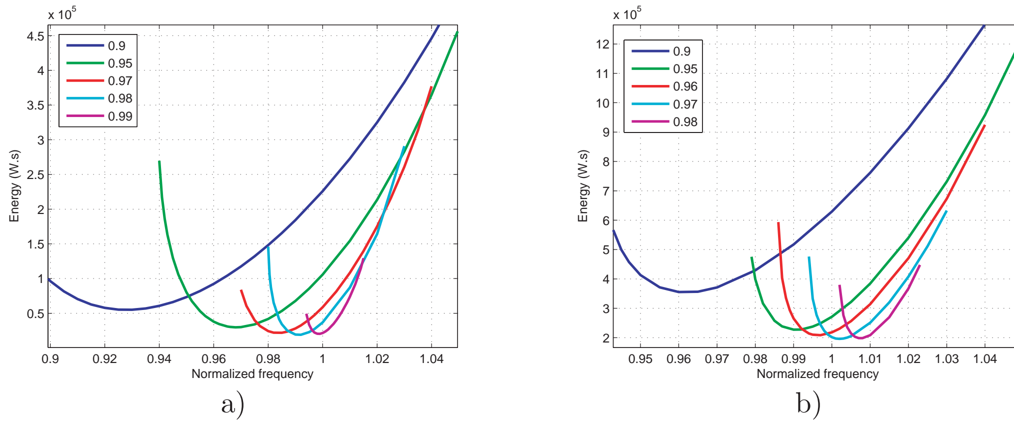

Figure 4.48: Steady-state energy consumption curve based on the calculated Harmonic balance voltage for fixed damping at Q = 100. The curves are shown for different gap bias, and with normalized frequency in the x-axis. a) Amplitude of desired oscillation $0.4g_0$. b) Amplitude of desired oscillation $0.7g_0$.

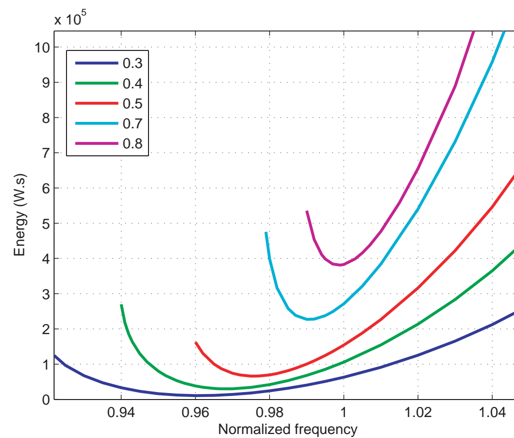

Figure 4.49: Steady-state energy consumption curves based on the Harmonic balance voltage for a fixed damping of Q = 100 and a fixed gap bias of 0.95. The curves compare the energy consumption depending on the amplitude of the oscillation.

higher frequencies. This frequency displacement is coherent with results of the maximum voltage peak. But leads to an unexpected conclusion, in some cases, for large amplitudes, frequencies higher than natural frequency can lead to more energy efficient system driving.

The same conclusion is extracted if the desired bias is fixed, as shown in Figure 4.49. As the goal is large amplitudes, Harmonic Balance also allows to analyze the effect of increasing the oscillation amplitude for a given gap bias. As amplitude increases, energy consumption increases, as expected. But at the same time, the frequency range decreases and the minimum oscillation frequency shifts to natural frequency.

As a conclusion, Harmonic Balance allows to choose the minimum energy consumption frequency of oscillation depending on the desired oscillation. And as can be seen in

the plots, the difference in energy consumption can be important. Moreover, Harmonic Balance energy analysis is critical, as depending on the desired oscillation amplitude can lead to unexpected range of efficient frequencies.

4.5.4 Stability

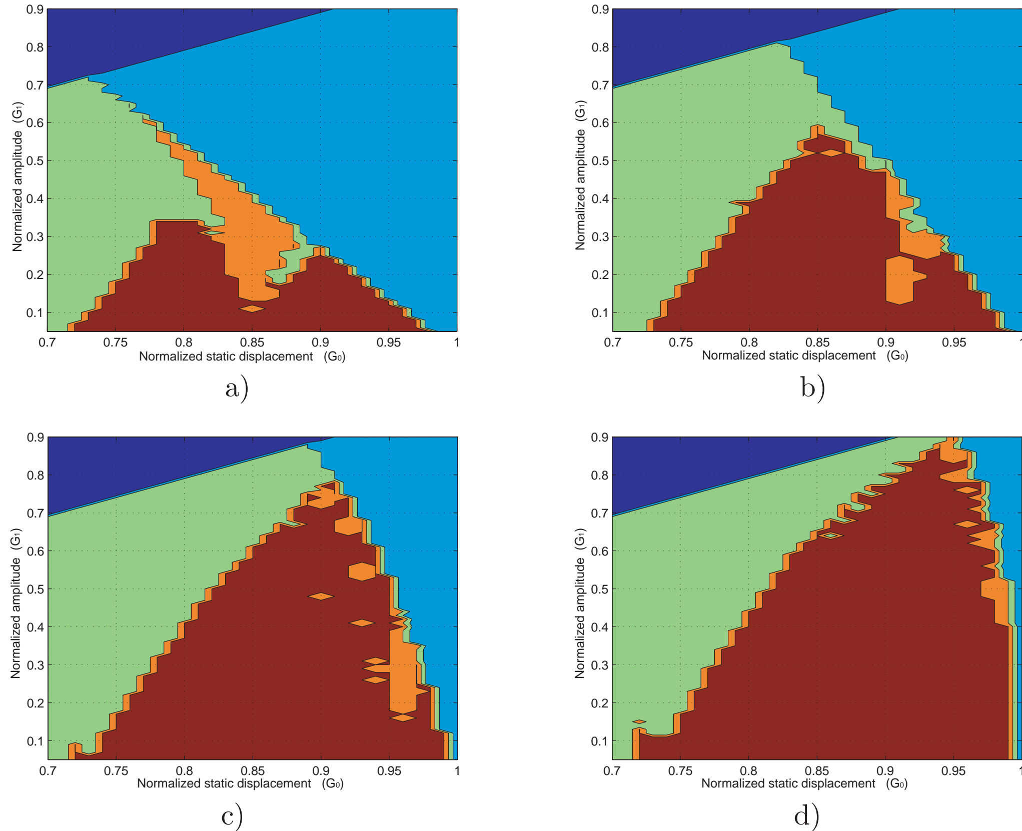

Figure 4.50: The stability of the solutions is analyzed with long-time numerical simulations, applying the Harmonic Balance driving voltage in open-loop. Fixed damping at Q = 100 and different input frequencies. a) $w_k = 0.80$. b) $w_k = 0.90$. c) $w_k = 0.96$. d) $w_k = 1$.

The Harmonic Balance solutions predict the range of feasible oscillations in open-loop driving, but they don't guarantee the stability of the solutions. Analysis of the stability of the predicted solution is carried out using long-time numerical simulations. To do so, the simulations are run on the system using the fitted voltage obtained by Harmonic Balance for the desired combination of static displacement and oscillation amplitude. To emulate the steady-state response predicted by Harmonic Balance, the voltage is applied in open-loop to the MEMS resonator with a very slow increasing ramp to avoid transients in the simulations.

As expected, the stable outcome is more restrictive than the Harmonic Balance prediction,

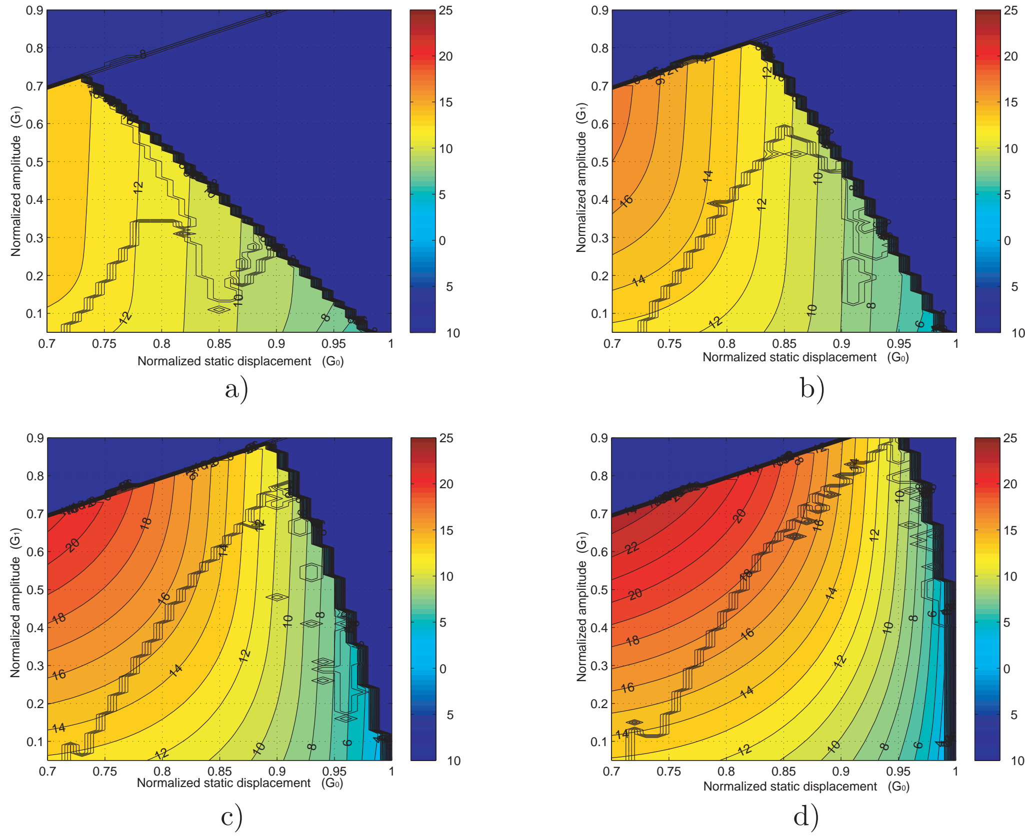

Figure 4.51: The stability of the solutions of the previous figure is compared to the input voltage peak (V_{max}). a) $w_k = 0.80$. b) $w_k = 0.90$. c) $w_k = 0.96$. d) $w_k = 1$.

Figure 4.50. The plots show that the stable (*brown area*) area is much reduced than the feasible one (*green area*). Not only that, there is a stable zone where the desired oscillation output is not satisfied (*orange area*). In this area, the difference between the desired output and the simulated output is larger than a 5%.

The analysis shows that, as frequency differs from resonance (e. g. $w_k = 0.8$), the Harmonic Balance calculations of pure sinusoidal oscillation fail more often. This is related to the difficulty to fit a correct voltage to that one obtained using the Harmonic Balance equations. Moreover, the results rely on open-loop driving and how the voltage is applied. Improvements should be expected including closed-loop schemes.

These results turn out the question of the possibilities to predict the goodness of Harmonic Balance solution. To try to obtain an insight on the question, the stability curves has been compared to the input voltage peak curves, Figure 4.51. Analysis of the plots show that no clear correspondence between the peak voltage and the stability can be drawn.

4.6 Conclusions

This Chapter highlights the following points:

- The use of a sinusoidal input signal with only first harmonic always generates outputs with at least first and second harmonic component, due to the nature of the parallel plate actuator. The existence of the V^2 term leads to a nonlinear response, with the possibility of non-pure-sinusoidal responses. Moreover, we cannot choose the desired static bias and oscillation amplitude, as this is determined by the magnitude of the input voltage. This has been confirmed numerically using long-time simulation and analytically using harmonic balance analysis. The use of a sinusoidal input signal with only first harmonic always generates outputs with at least first and second harmonic component, due to the nature of the parallel plate actuator. The existence of the V^2 term leads to a nonlinear response, with the possibility of non-pure-sinusoidal responses. Moreover, we cannot choose the desired static bias and oscillation amplitude, as this is determined by the magnitude of the input voltage. This has been confirmed numerically using long-time simulation and analytically using harmonic balance analysis.

- A perfect sinusoidal output can only be achieved with an input signal with the appropriate form and number of harmonics. As desired amplitude increases, also increase the number of needed harmonics. Although a closed-form analytical solution cannot be obtained, the combination of Harmonic balance calculations and the use of numerical fitting allows to choose the right input signal to reach the desired oscillation in most of the available oscillation range. Examples show the viability under changes of damping and frequency of oscillation.

- The use of Harmonic Balance calculations to choose the desired oscillation amplitude breaks the usual concept of resonant frequency associated with a fixed sinusoidal driving with a DC load plus and AC load. Any combination of oscillation and frequency is possible. And for each amplitude of oscillation a minimum energy frequency can be chosen. The only constrain is the ability to apply the calculated voltage, and the impossibility to generate some voltages with one-sided actuation.

- The range of reachable amplitudes is large, and the stability and feasibility has been

shown using long-time numerical simulation. Based on Harmonic Balance, stability predictions are not precise and still relay on time-demanding simulations.

Consequently, the analysis gives the needed insight to propose a control strategy that must be able to guarantee a perfect sinusoidal oscillation of the MEMS resonator. The controller must be able to produce the desired frequency components for the input voltage, adapting them to the desired amplitude and bias, and ensuring the stability of the oscillation at minimum energy consumption.

Chapter 5

Control of electrostatically actuated MEMS

5.1 A survey of prior work on MEMS control

In order to improve the performance of the system, two main approaches exist in MEMS. The first approach is based on modifying the design of the electromechanical system, either by introducing mechanical nonlinear leverages [85], or changing the profile of the electrostatic forces by modifying the design of the capacitor plates [172], [32].

The second approach is based on control strategies. Multiple control techniques have been used in the literature. Table 5.1 tries to summarize some of the different approaches that exist, the purpose of each of the approaches, and the device or the model in which are based. Recent control approaches are each time more complex and in some cases a mixture of different methodologies.

The majority of the approaches choose as a control variable the driving voltage, specially in the fabricated devices. Current drive [39], [37] and charge drive [181], [117] are studied and tested, but no commercial devices use the approach to our knowledge.

The major part of the control analysis and simulations are based on the mass-spring-damper model, and only in some studies other nonlinearities are treated. In resonators only a few examples analyze the non-linear cubic spring [107], [22]. However, in gyroscopes the quadrature errors are more generalized [91], [187].

5.1.1 MEMS oriented control strategies

Due to its electronics-derived fabrication techniques, most of the initial control schemes in MEMS have been adapted from standard electronic devices, for example, clock-oscillators or RF-antennas.

	Position Control	Oscillation control	Resonators - Accelerometers	Gyroscopes	Mirrors - Switches
Voltage drive	[113], [99] [176], [244] [29], [22] [239], [53] [39] [100] [165] [161] [237], [238] [47], [140] [35] [182] [40]	[233] [107] [211]	[210] [175] [112] [214] [6] [80] [31] [93] [191] [232] [169]	[91] [94] [105] , [167] [19], [67] [72], [48] [148] [160] [187] [121] [106], [193] [150] [3], [142] [180]	[220] [209] [42] [46] [177] [209] [28] [234]
Current drive	[37] [39]	[16] [110]			
Charge drive	[238], [117] [116] [157] [189] [115] [181]	[23]			
Theoretical	[115], [99] [140] [238] [239] [53] [117] [116], [176] [244], [237] [22] [182] [29] [157]	[107] [233]	[93] [232]	[121], [48] [160], [105] [3], [106] [19], [67] [242], [243] [150], [187] [148] [91] [94] [111] [158]	
MEMS applied control	[39] [40] [182] [35]	[226]	[169], [217] [112] [175] [31] [6]	[41], [3], [97] [168], [48] [180], [142] [102] , [91] [241] , [121]	[209]
Classical control	[29] [47]		[210] [93]	[160], [193]	[42] [234] [28]
Non-linear Control	[161] [239] [22], [53] [100], [165] [237], [238] [244] [186] [240]	[107] [110] [16]	[214] [191] [80]	[106], [150] [105], [151] [19], [94] [72], [193] [160] [152] [187], [121] [148], [67] [120]	[220] [177] [46]
Energy control	[116] [176], [140] [117] [115]		[232]	[160], [148] [121]	
Chaos	[100]	[23] [211] [16] [110] [233]		[158]	
Experimental	[181] [161] [35] [100], [165] [47] [29] [113]	[211]	[80] [31] [214] [6] [175] [112] [169] [193] [191]	[150], [97] [120], [48] [168] [142], [121] [160] [152] [111]	[28] [42] [178] [177] [234]

Table 5.1: Classification of the different control approaches in the literature

Initially, the introduction of control has been linked to positioning applications and the necessity of extending the travel range, which is limited by the pull-in instability. In [182] they showed that the pull-in instability can be avoided by the simple addition of a series capacitance, externally or on-chip. Similar approach was presented in [40]. Later, the study was complemented introducing a charge control technique, that clearly improves the travel range (83% of the gap), and defined the Charge Pull-in that appears instead, due to charge accumulations [181]. Similar results were presented in [37] with charge drive and a pulsed current source delivering the needed amount of charge to the actuator. The case is analyzed theoretically with an ideal model in [157], showing that the embedding of a device into a control circuit gives rise to a nonlinear and nonlocal elliptic problem. Various capacitive control schemes are shown to give rise to variations in the bifurcation diagram and changes in the pull-in voltage and pull-in distance.

Other approaches to increase the travel range in MEMS positioning rely on high speed switching. In [189] bidirectional driving is possible using high-speed switching and charge control. In [35], what they call resonant drive technique is used, based on placing an inductor in series with the actuator capacitor and operating the circuit at its electrical resonance frequency with the help of an oscillator loop. In [165], voltage switching with position feedback is used to extend the travel range up to 70% of the gap. Operation is limited only by the position jitter due to the time delay introduced by the readout circuits. This approaches are in line with the technique used in [51], where pre-shaping of the input voltages is used to obtain larger plate movements.

Another field of study has been microswitches and their switching time. In [39] they found that the value of the source resistance of the voltage drive used for switching has a profound effect on both switching speed and energy requirements, and tuned its value to optimize switching applications.

Finally, an important field for control is the inertial sensors applications. Concerning to the control part, they can be differentiated between static applications and oscillatory applications.

We refer as static applications those were the inertia proof mass remains static in the sensing direction, and the force that is applied to maintain the mass static gives the value of the sensed variable. This procedure is known as Force-Balancing technique. It can be extensively found in accelerometers ([114], [112], [175]) where the generated force balances the inertial force created by the acceleration of the mass. Or in gyroscope applications [91],

where is used to extract the Coriolis force. The fact that the generated force is directly the sensed variable, added to the static behavior of the mass, makes this approach very popular.

More elaborated approaches, based on sigma-delta digital to analog modulation have been developed, making use of the existing knowledge of the IC technology. Explanation of the capabilities and the limitations of the sigma-delta force-feedback loops are presented in [80] and [214]. Applications to vibratory gyroscopes can be found in [97] and [168]. All of them emphasize the increase in the dynamic range and reduction of susceptibility to environmental parameters. Nowadays they are still a typical approach, even in commercial devices, when accuracy in the modulation is needed [41] [55]

In oscillatory applications, one can basically find vibrating accelerometers and gyroscopes. At the beginning, oscillation was usually obtained by implementing a positive feedback loop with a transresistance amplifier between the output and input of the device, using an inverting amplifier to produce a 90-degree phase-shift and drive the system to resonance [169], [48]. This basic approach was improved using standard oscillatory circuits, widely known from quartz technology, as Phase-Locked Loop (PLL) drive and Automatic Gain Control (AGC) [48] (Figure 5.1).

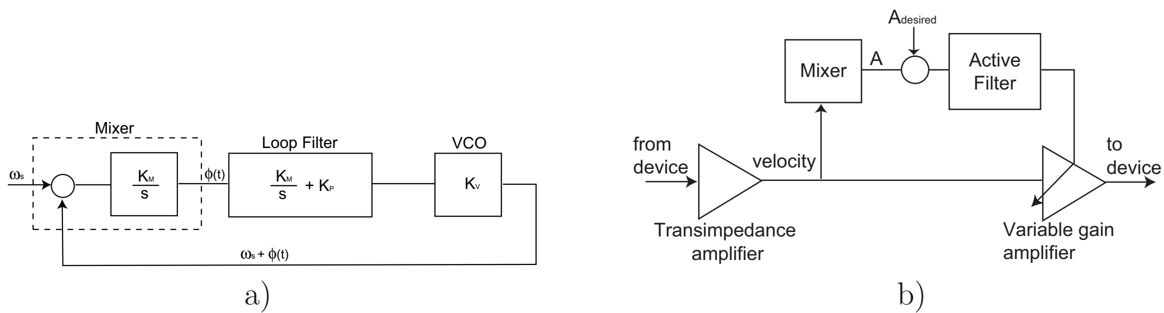

Figure 5.1: Example of a) a linear PLL and b) AGC control loops [48]

Phase-locked loop circuits allow to extract with precision the frequency of a signal, and this is used to generate the feedback signal that drives the resonator to its resonant frequency. An example of a phase-locked loop driven accelerometer consisting of a doubly clamped beam coupled to a seismic mass can be find in [6]. In [111], a PLL-based control system was designed, analyzed and implemented in a vibrating cylinder gyroscope. The control system drives the resonator at resonance with a constant amplitude and nulls the rotation-induced vibrations.

Another example can be found in [209], where the phase-locked loop control method is specially designed for operation of MEMS actuators at their resonant frequency.

Improvements in the use of PLL in MEMS control are still under way, as they are used in most commercial resonators and gyroscopes. An example can be found in [102] where PLL is used in parallel with other feedback loops. And in [217], an all digital PLL control for tuning-fork resonator is shown with fixed amplitude control.

As the device is driven to resonance, and is very dependent on damping conditions, amplitude control is needed to guarantee the needed amplitude of vibration. The IC approach to ensure that oscillations are at a fixed amplitude is Automatic Gain Control (AGC). A basic AGC design consists of a transimpedance amplifier loop with the gain adjusted to cancel out the damping of the system, Figure 5.1. An example of an accelerometer with electrothermal excitation can be found in [31]. Example and design of the loop for vibrating mass gyroscopes can be found in [48].

Tuning of the nonlinear loop defined by the AGC is presented in [122], [121] for the Jet Propulsion Laboratory vibratory gyroscope. Analytical and experimental results are presented for a significant range of controller parameters. Example of a proposed implementation for a dual-mass gyroscope is also presented in [3]. In [142] a discrete AGC control is proposed for a z-axis MEMS vibrational gyroscope. And in [199] implementation in DSP board is presented, connected to resonant frequency tracking with EAM demodulation to avoid parasitics.

Automatic Gain Control is still a hot topic, as multiple approaches to fix the variable gain are present in literature. In [41] an automatic gain control (AGC) circuit without a PI is presented for the drive mode, combined with sigma-delta force feedback control loop. In [226], application of AGC is presented in RF-MEMS oscillators. And in [241], a modified AGC approach is presented, with parallel amplitude gain and phase controllers for gyroscopes.

All these approaches have been complemented with introduction of parametric excitation of MEMS devices. Oscillatory loops are maintained, but the frequencies of the driving voltage exploit the parametric resonance of the device. Examples are found in [100] and [72]. They show that parametric excitation can have an stabilizing effect and resolution enhancement.

In commercial devices, they often use a mixture the presented approaches, as in the case of the Northrop Grumman control approach [201] where in a digital board four primary

servo loops are implemented for gyroscopes: drive amplitude, drive frequency PLL, sense Coriolis force rebalance and sense quadrature.

5.1.2 Classical control strategies

In order to improve the performance of the devices, classical control strategies have also been implemented. Proportional-Integral-Derivative (PID) controllers, pole-placement or feedforward approaches have been proposed as the main control, or as a part of the complete control strategy.

Classical control is a good approach for positioning applications. In [47], they proposed a position feedback controller to stabilize a electrostatic microgripper, and analyzed the differences between open-loop and closed-loop actuation. In [113], voltage control is used to extend the travel range of a parallel-plate electrostatic microactuator beyond the pull-in limit. A classical controller is designed over the linearized plant for each working point.

In microswitches, switching motion is regulated by feedback approaches. In [29], a comparison of pre-shaped open-loop driving against a feed-forward and feedback proportional-derivative loop are presented for an optical switch. Their conclusion is that in MEMS devices open-loop can be easily implemented and with good performance, however closed-loop is more robust but of difficult implementation.

In [42], feedback control using a linear voltage control law enables operation of electrostatic micromirrors beyond the pull-in angle. Experimental measurements show that tilt angles beyond the pull-in point can be achieved. In [234], a multi-loop digital PID control method is proposed to significantly improve the positioning performance of a dual-axis micromirror.

For accelerometers and gyroscopes, PID techniques are usually too limited to handle the complete dynamics, and PID control is usually a part of one of the control loops. As example, in [142] a PI controller drives the error of the AGC loop to zero. An interesting direct application of a basic PID control is shown in [210]. Optical position sensing of the oscillation is implemented and used to feed the value in the controller to sustain the oscillation of the resonator. However, these are experimental controllers without formal validation.

5.1.3 Classical nonlinear control strategies

The nonlinear nature of the MEMS electrostatically actuated devices is usually too strong to achieve good performances with a PID control. Consequently, nonlinear control strategies have also been studied to overcome linear control limitations.

For positioning applications, much effort has been devoted to feedback and feedforward techniques, combined with Lyapunov analysis. In [46], full-state feedback control with current estimation and feedforward is applied to an electrostatically actuated double-gimbaled MEMS mirror. In [53], different methods for improving position control of electrostatic MEMS actuators are analyzed, including switching control and two methods of feedback linearization. And in [238], charge-position control is improved by a combination of trajectory planning and nonlinear control with Lyapunov analysis. The results show stabilization of the system at any point in the gap while ensuring desired performances. And in [5], combination of feedback linearization and trajectory planning show the capability to extend stable operation range and enhance system's performance.

When it comes to oscillation control, a full range of elaborated approaches are present. In [22], oscillations of a fixed amplitude in a nanoelectromechanical devices are sustained with nonlinear state feedback. And describing function is used in [191] to define a nonlinear feedback loop for a resonant accelerometer, Analog Devices ACRC-RXL. The nonlinearity is implemented in analog electronics and tested.

Sliding mode approaches are also proposed for different devices. In [178], [220], [177], a sliding mode control algorithm for a two-axis gimbaled MEMS micromirror with a first-order sliding function is shown to yield a fast and robust switching performance over a range of system parameters, in simulation as well as experimentation. Or in [19], sliding-mode control is proposed for a vibrating gyroscope. They show that a sliding-mode controller for the vibration of the proof mass generates a better estimate of the unknown angular velocity than that of a model reference adaptive feedback controller, resulting in improved performance.

Different sliding-mode approaches are still under test. In [174], sliding mode observer, as well as, a robust control scheme is used to improve performance in gyroscopes. In [65], a sliding mode control for a vibratory gyroscope with adaptation is presented. And in [58], a model-based and a non-model-based sliding model control approaches are presented to improve tracking control of the drive and sense modes of an uncertain vibratory gyroscope.

Optimal control is used in [107] to deal with the problem of controlling the nonlinear dynamics of electrically actuated microbeams. A theoretical study using Melkinov analysis and derivation of the optimal excitation is presented. Its use shifts the erosion of the safe basin in the phase plane, which is the event that triggers the pull-in. They highlight good performances of the simulated control method beyond theoretical expectations.

This optimal control study is linked to research works that analyze the possibility of chaotic behavior in the actuation of the electrostatic devices. The works conclude that chaotic behavior is possible [110], [213], [23], [233], including period doubling and strange attractors, and experimental data confirm this analysis. In order to prevent chaotic behavior, in [16] they compute the Melkinov function in terms of the parameters of a PD controller, and using this relation conclude that is possible to design controllers that will remove the possibility of chaos. On the other hand, some researchers exploit the possibility of chaos to select high amplitudes of oscillation [92].

Moreover, due to its fabrication process, MEMS devices have plenty of imperfections. For this reason, several authors have proposed control techniques to compensate for them.

Multiple H_∞ controllers have been proposed for the different kinds of applications. In [244], a robust model-based controller coupled to a feed-forward compensator is designed to setpoint regulation maneuvers of an electrostatic actuator. Linearized models of the nonlinear system are considered at multiple operating points for short-range maneuvers, while the feedforward compensator provides the nominal voltage. The robust controller, designed via H_∞ loop-shaping, handles any perturbations around these points. H_∞ loop-shaping for a tunneling accelerometer is reported in [93], where the control shapes the loop to achieve high disturbance rejection, noise attenuation, and robustness to parameter variations. In [193], an H_∞ feedback controller for a MEMS gyroscope is presented and experimentally tested with the closed-loop fabricated using discrete analog circuits. Performance is compared to a PID controller, showing its robustness over unmodeled dynamics. Another approach is designing a robust controller using input-to-state stability combined with backstepping [240]. Or designing an H_∞ controller complemented with linear parameter variation, as in is [186], for general electrostatic actuators.

A recent example of a resonant gas sensor with Amplitude Feedback Control using H_∞ loop shaping is presented in [81].

The other approach that has been extensively proposed to improve the performance of the MEMS devices against uncertainties is adaptive control, linked to any of the other control

techniques. A good general formulation of adaptive controller strategy for sinusoidal disturbances rejection, with stability discussion of general plants is presented in [159].

Adaptive control is specially proposed in gyroscopes, due to its necessity of high performance. But other applications as MEMS microactuators have also been studied [161].

In [187], they analyze the dynamics of ideal and non-ideal vibrating gyroscopes, and suggested an approach that uses nonlinear feedback control to drive the system and compensate for errors. Both non-adaptive and adaptive strategies are presented. Extending this approach, adaptive add-on control algorithms for the conventional mode of operation of MEMS z-axis gyroscopes is presented in [149], [150]. This scheme is realized by adding an outer loop to a conventional force-balancing scheme that includes a parameter estimation algorithm. The parameter adaptation algorithm estimates the angular rate, identifies and compensates the quadrature error, and may permit on-line automatic mode tuning. A discrete time version of the observer-based adaptive control was presented in [152], and implemented using digital processors.

In [105], an adaptive controller is used to tune the frequency of the drive axis of a vibrational gyroscope. This is an attractive alternative to a standard PLL approaches, since it introduces feedback, which can reduce the effects of imprecise fabrication. An extension with force-to-rebalance is proposed in [106]. Two adaptive controllers are described to tune the drive axis frequency to a preselected frequency, regulate the amplitude of the vibration, cancel out quadrature error due to stiffness coupling, and drive the sense axis vibration to zero. The first controller is based on an averaged, low frequency model, and the second is based on the full gyroscope model.

Similar approaches are presented in [94] or [67], with an adaptive control to guarantee the stability of the gyroscope. Or in [91], where an adaptive force-balancing control scheme is presented for a MEMS Z-axis gyroscope. The proposed scheme controls the vibratory modes of the proof mass while ensuring that the control input satisfies the magnitude constraints. The performance of the gyroscope is enhanced even in the presence of fabrication uncertainties.

In [90], the optical position feedback presented in [210] is used for an adaptive control approach that handles the uncertainties and faulty conditions.

5.1.4 New nonlinear control strategies

The evolution of control techniques has lead to design of controllers that can specifically solve some of the particularities of the parallel-plate electrostatically actuated MEMS.

In [237], improvement of the performance of a parallel-plate electrostatic micro-actuator is shown using three different approaches: differential flatness, Lyapunov functions, and backstepping. The simulation results demonstrate the efficiency of the considered control schemes and provide some comparisons on their performance. Extension of the work, including uncertainties is presented in [239], with two control schemes, both based on input-to-state stabilization (ISS) and robust backstepping.

In [190], an interesting approach to solve the robust output regulation problem of the oscillatory one-degree-of-freedom electrostatic actuator is presented. They show that it can be converted into a robust regulation problem with output constrained by internal model design. The problem is analyzed and a controller designed using a Lyapunov function technique. The final design of the output-error-constrained tracking control law ensures that, in the presence of large parameter variations, the harmonic displacement of the parallel-plate electrostatic actuator can be beyond the pull-in position and up to the full gap without contact between the movable and fixed plate during the transient period.

Using the specific characteristics of MEMS electrostatic devices, passivity and energy-shaping approaches have been presented to solve the problem from the energy point of view. In [145], the approach is tested with a reduced-order model of a MEMS device, allowing to design controllers that adjust the energy transfer in a desired manner.

Passivity-based strategies have also been analyzed for positioning applications. In [118] and [116] they showed that input-output linearization, passivity-based design, and the theory of port-controlled Hamiltonian systems lead naturally to static output feedback of device charge. Using this analysis, they implement an output-feedback control using a reduced-order nonlinear observer of the electrode velocity. Simulations predict greatly improved transient behavior, and large reductions in control voltage. A model improvement and generalization of the approach is presented in [115] and actuation under presence of parasitics is analyzed in [117]. No extension of the approach to oscillating devices have been presented.

Other energy approaches are averaged potential function shaping, as is used in [140] to stabilize and extend the operation range of a parallel plate actuator bi-directionally.

An oscillatory stabilizing control law is designed by parametrically shaping the averaged potential. The performance of the controlled system is shown to be robust with respect to disturbances. Or the design of nonlinear controllers based on energy-control, as in [176], that are used to stabilize all equilibria of an electrostatically controlled actuator, while guaranteeing that pull-in does not occur. The approach guarantees stability and performance, against other approaches in the literature.

In gyroscopes, energy control is used as a means of controlling the axis of oscillation [187]. In [148] they showed that a dual stage control architecture with self-calibration and feedback capabilities is needed to control a MEMS angle-gyro. The self-calibrating portion of the control identifies and electronically trims large imperfections, while the feedback energy control compensates for remaining small nonidealities and in-operation perturbations.

Similar approach is presented in [160], where a nonlinear feedback control system that compensates for dissipative forces, mismatched springs and cross-axis stiffness ensures that the mass continues to behave as a freely vibrating structure. Theoretical analysis and simulation results presented in the paper show that the gyroscope can accurately measure both angle and angular rate for low-bandwidth applications.

5.2 Thesis proposed strategies

As has been presented in the previous Section, multiple approaches have already been applied to MEMS electrostatically actuated resonators. However, after analyzing the existing control strategies, none of them specifically copes with the thesis desired goals.

In Chapter 4, the behavior of parallel-plate electrostatically actuated MEMS resonators has been studied. From that analysis, four main goals for the new controller can be defined:

- Stability of the oscillation for large amplitudes.
- Robustness of the oscillation against inherent MEMS fabrication uncertainties.
- Perfect sinus-like oscillation for high precision applications.
- Minimum energy consumption to sustain the oscillation.

In detail, the first goal is straightforward, as any control strategy aims to guarantee the stability of the system and tracking of the desired set-point.

The second goal is of great importance in MEMS devices. Batch in-die fabrication techniques produce device imperfections. This drawback is inherent to MEMS devices. Combined with imperfect parameter characterization and degradation over time, it leads to control strategies capable of absorbing these imperfections and uncertainties.

The third goal is associated to system performance. As explained in Chapter 4, when a MEMS Resonator has to be used as a high performance sensor device, the existence of non-desired harmonics in the oscillation can interfere with the precision of the sensed output. MEMS Resonant Gyroscopes are good examples of devices where the purity of the harmonic oscillation is crucial [187]. For this reason, the Parallel-Plate Electrostatic Actuators are often avoided, because they are extremely nonlinear and introduce a second order harmonic in the oscillation of the device [183]. Electrostatic Comb Actuators are used in this case, however, in some devices Comb Actuators cannot be used [146]. As stated in Chapter 4, a pure harmonic oscillation can be achieved, if the right control action is provided.

Finally, MEMS resonators are often connected to low energy sources. Consequently, an energy efficient control law must be provided.

5.2.1 Proposed controller

In order to satisfy the four goals and obtain the desired oscillation with the expected stability and performance, a three-stage controller is proposed. Figure 5.2 describes the architecture of the controller.

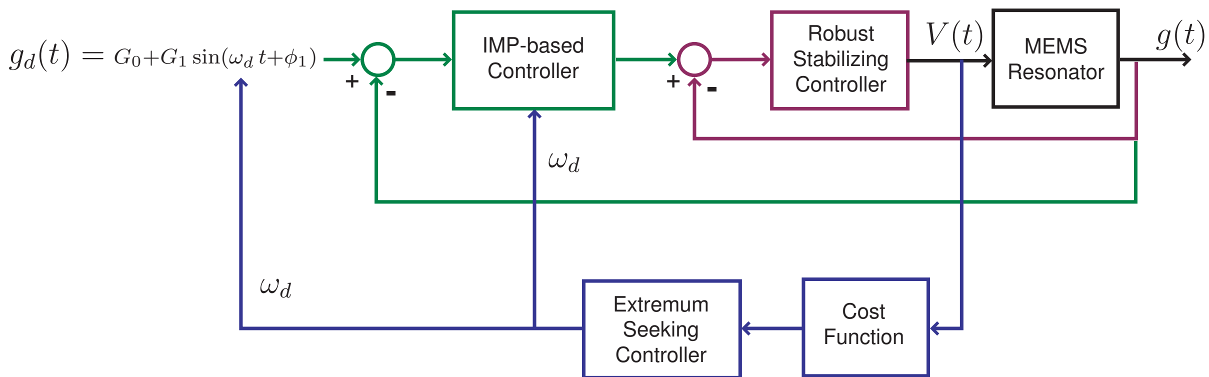

Figure 5.2: Control architecture. A three-stage controller is proposed for control of the system. First stage is a Robust Stabilizing Controller. The second stage is an IMP-based Controller. The third stage is a low energy Extremum Seeking Controller.

On the first stage, a Robust Stabilizing Controller is used to improve the stability and

robustness of the system. On the second stage, an Internal Model Principle (IMP) based Controller [69] is used to generate the desired control action to obtain a pure-sinusoidal oscillation and reject any harmonic or oscillation perturbation. On the third stage, an Extremum Seeking Controller reduces the energy consumption by selecting an appropriate oscillation frequency for the desired oscillation amplitude and static displacement. The selected *cost function* is based on the energy content of the input to the MEMS Resonator. In the rest of the Section, the three stages are discussed and justified based on literature references. In Chapter 6, the controller is designed and in Chapter 7 its performance is tested in simulations.

5.2.2 Robust control strategy

The previously presented literature review shows that robust control strategies, Figure 5.3, can deal with MEMS resonators imperfections [244], and successful approaches has been presented [93], [193], [240], [186], [81].

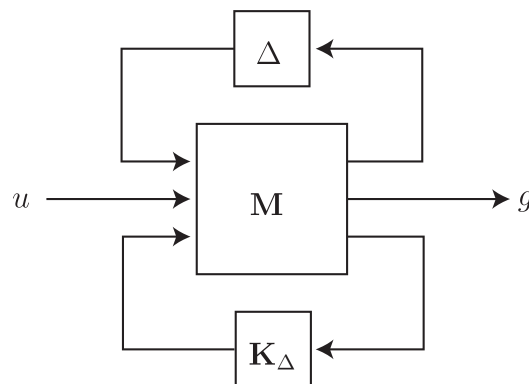

Figure 5.3: Robust control system framework

However, none of the literature examples treat the non-linearity of the spring into account. This approach increases the uncertainty, and would be a clear extension some of the existing approaches. Moreover, the fact that the output must be a perfect sinusoid at with minimum energy consumption adds constrains to the robust controller, as it must not interfere with the rest of the loop.

5.2.3 Internal-Model-Principle based control strategy

The Internal Model Principle states that a controller must incorporate a model of the disturbance or reference dynamics to have perfect disturbance rejection or signal tracking [69].

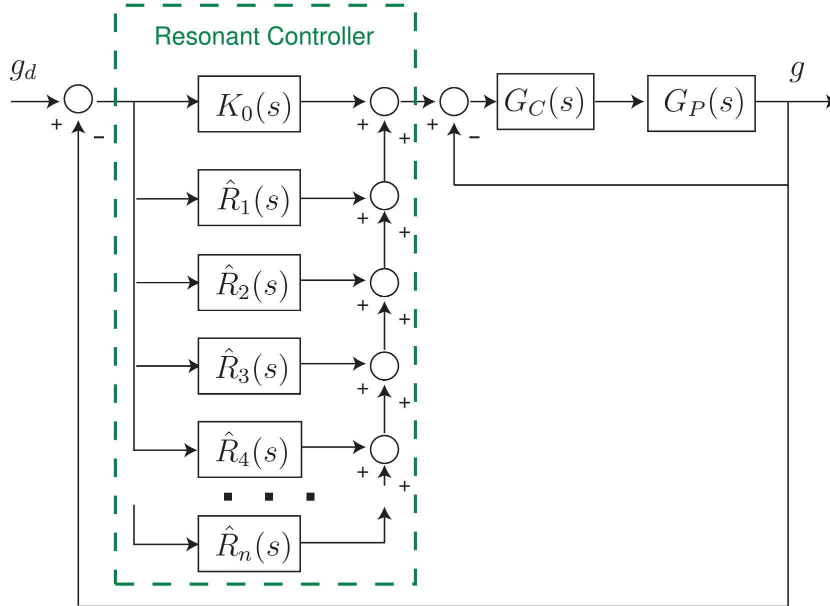

Figure 5.4: Control loop using a Resonant Controller with n resonators.

Several approaches to the Internal Model Principle exist, as can be seen in [25]. Moreover, IMP based approaches are equivalent to adaptive feed-forward control [124] [20] [26], and its associated theory applies. In [50], examples of IMP based controller implementation and their capabilities are presented, with clear explanation of the approaches.

Literature shows that IMP Resonant controllers, Figure 5.4, or IMP Repetitive controllers, Figure 5.5, can handle the issues involved in the control of parallel-plate electrostatically actuated oscillatory MEMS devices, specially when dealing with the goal of obtaining a perfect sinusoidal. Most applications of existing controllers are related to the control of sinusoidal voltage sources, as in voltage rectifiers [49] or voltage inverters [119]. In these examples, the controller is designed and its performance analyzed to obtain perfect sinusoidal rejection of undesired harmonics.

Resonant controllers are based in the concept of introducing an infinite gain at a selected oscillation frequency, in order to eliminate the steady-state errors in that frequency, Figure 5.4. It applies directly to oscillatory MEMS applications and allows to choose the final shape of the response. It has the advantage that the specific signals and harmonics that

are desired to be canceled/tracked can be selected. Different types of implementations can be found and for many devices. In [196], different applications are shown and analyzed in voltage-source converters. Application to disturbance rejection in smart structures, with Integral Resonant Controller is presented in [7], [14], [144]. Disturbance rejection in a rotary fast tool servo machine is presented in [34]. And the rejection capability is tested in [104] against non-linear triangular disturbances.

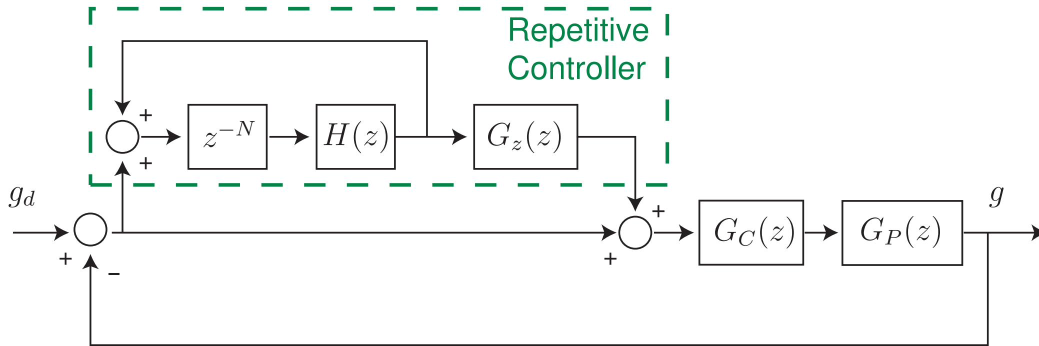

Figure 5.5: Control loop using a Repetitive Controller.

Using similar approach, Repetitive controllers force the inclusion of the modes of the disturbance/tracking signal in the feedback loop. They are equivalent to include infinite resonators in the control loop, but they are automatically generated by the repetitive controller, Figure 5.5. It has two main characteristics: the closed-loop system asymptotically tracks the reference periodic signal, and this property holds for small variations of plant parameters (robust tracking property) [82], [108]. This technique has been extensively used in different engineering areas, such as CD and hard-disk arm actuators [43], robotics [60], electronic rectifiers, current harmonics active filters [245] and small actuators [89]. It can be implemented in analogical or digital form [216]. Analysis of robustness, performance and trade-offs is discussed in [103]. And interestingly, in [203], a repetitive controller with time period adaptation is presented, showing good performance, what validates one of the approaches that can be needed.

Both IMP based controllers could be ideal in oscillatory MEMS applications, in order to obtain a perfect sinusoidal oscillation with rejection of all the existing harmonics due to nonlinearities of the system and uncertainties. And none of the capabilities of Internal Model Principle Resonant Controllers or Repetitive Controllers have been applied to the oscillation of parallel-plate electrostatically actuated MEMS to present day.

5.2.4 Extremum seeking control strategy

As a final strategy, energy minimization is introduced. This involves selection of a Cost Function and optimization of the control action. If the Cost Function is explicitly known, optimal control strategies can be applied, but as this is not the case with the MEMS resonators, other approaches must be used.

Extremum Seeking Controllers are a known approach that has been lately recovered in the literature due to its capability to drive complex systems to desired cost function goals without need of complex strategies or mathematical manipulations, Figure 5.6. Extensive survey is presented in [56] and detailed application in [15].

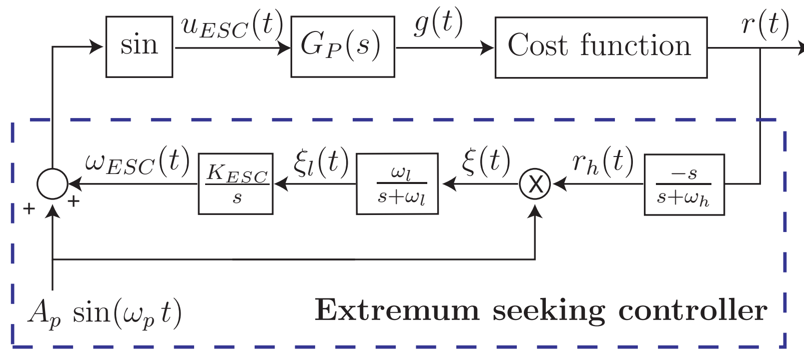

Figure 5.6: Extremum seeking controller to minimize cost function, based on perturbation methods, adapted from [15].

To implement Extremum Seeking Control, different approaches can be used [70]: there exist perturbation and averaging methods ([15], [98], [13], [17]), sliding mode model methods ([71], [70], [225], [141]) and numerical programming optimizer methods ([195], [227], [228], [229], [230]). No matter which approach is selected, the methodology is based on obtaining a gradient estimation by perturbing the input, the model or by optimizers techniques, and using it to drive the system to minimize the cost function.

Energy minimization has already been tested with extremum seeking controllers. There exist examples in asynchronous motors [54], actuators with change of stiffness [143] or wind energy generation [73]. These examples validate the applicability of the approach to the case of minimization of supplied energy to the electrostatically actuated MEMS resonator.

Moreover, in [87], an application of Extremum Seeking Controller that modifies variable gain of a controller is presented, with similar approach to what is needed to change the phase and frequency of the IMP Controller. And an application of Extremum Seeking

Controller has been tested in a MEMS gyroscope, [13], where the controller automatically handles the mode-matching of the frequencies of the gyroscope.

5.2.5 Conclusion

A novel three-stage controller has been proposed, in order to achieve the dissertation goals. The controller implements known strategies to the electrostatically actuated MEMS resonator problem. In the following Chapters the design and verification will be presented.

Chapter 6

Control architecture design

6.1 Introduction

In this Chapter, the strategies proposed in Chapter 5 are analyzed and tested to design a controller for pure-harmonic oscillation of a parallel-plate electrostatically actuated MEMS resonator, in a robust and energy efficient manner.

As has been stated in previous chapters, the nonlinearity of the system prevents it to produce a perfect sinus-like oscillation, unless it is forced. Moreover, stability of the system can vary extremely due to parameter uncertainty. Consequently, the right strategy has to be selected to obtain a perfect sinus-like oscillation that can remain stable under parameter variation.

In this Chapter, the design principles and tuning of the control algorithms are analyzed and tested, and stand-alone performance analysis is presented for the proposed controller in Figure 5.2. Combined global performance will be presented in Chapter 7.

6.2 System reformulation for control

Using the formulation previously introduced in Section 2.3, the oscillation of a parallel-plate electrostatically driven MEMS resonator behaves as a nonlinear mass-damper-system

$$\frac{d^2g}{dt^2} = -\frac{\omega_\mathrm{n}}{\mathrm{Q}}\frac{dg}{dt} + (\omega_\mathrm{n}^2 + \kappa) - (\omega_\mathrm{n}^2 + 3\kappa)g + 3\kappa g^2 - \kappa g^3 - \frac{\mathrm{f}_k\mathrm{g}_k}{g^2}V^2 \tag{6.1}$$

where $\mathrm{C}_0 = \frac{\epsilon \mathrm{A}_c}{\mathrm{g}_0}$, $\mathrm{f}_k = \frac{\mathrm{C}_0}{2\mathrm{g}_0}$, $\mathrm{g}_k = \frac{1}{\mathrm{g}_0\mathrm{M}}$, $\frac{\mathrm{B}}{\mathrm{M}} = \frac{\omega_\mathrm{n}}{\mathrm{Q}}$, $\frac{\mathrm{K}}{\mathrm{M}} = \omega_\mathrm{n}^2$ and $\kappa = \frac{\mathrm{K}_3\mathrm{g}_0^2}{\mathrm{M}}$, being ω_n the natural frequency of the system, $\mathrm{Q} = \frac{1}{2\zeta}$ the Quality factor and ζ the damping of the system.

The majority of control strategies are based on linear systems or systems linearized around an equilibrium point. In order to apply these standard control strategies, equation (6.1) needs to be linearized around an equilibrium point.

It is important to note, as happened in Chapter 4 in the Harmonic Balance analysis, that better formulation for control analysis is obtained if the square of the input voltage, V^2, is selected as the input of the system. If the voltage is directly taken instead, formulation is more complicated without advantages in the results. This selection has implications in the device design and implementation, as it is explained and solved in Chapter 7.

6.2.1 System linearization

The system nonlinear equation (6.1) can be rewritten in state-space formulation

$$\dot{\mathbf{x}} = f(\mathbf{x}, \mathbf{u}) \tag{6.2}$$

using the standard states for a mechanical system (gap position, $x_1 = g$, and its time variation, $x_2 = \frac{dg}{dt}$) and selecting the square of the driving voltage as the input for the system ($u_1 = V^2$):

$$\mathbf{x} = \begin{pmatrix} x_1 \\ x_2 \end{pmatrix}, \mathbf{u} = \begin{pmatrix} u_1 \end{pmatrix}.$$

Using these definitions, the equations are as follows

$$\begin{pmatrix} \dot{x_1} \\ \dot{x_2} \end{pmatrix} = \begin{pmatrix} x_2 \\ -\frac{\omega_\mathrm{n}}{\mathrm{Q}} x_2 - (\omega_\mathrm{n}^2 + 3\kappa)x_1 + 3\kappa x_1^2 - \kappa x_1^3 + (\omega_\mathrm{n}^2 + \kappa) - \frac{\mathrm{f}_k \mathrm{g}_k}{x_1^2} u_1 \end{pmatrix}. \tag{6.3}$$

As analyzed in Chapter 3, the MEMS resonator has different equilibrium points for each input voltage. Then, if $\mathbf{x}_0$ is the equilibrium point for the input voltage $\mathbf{u}_0$

$$\mathbf{x}_0 = \begin{pmatrix} x_{10} \\ x_{20} \end{pmatrix}, \mathbf{u}_0 = \begin{pmatrix} u_{10} \end{pmatrix}$$

and given that by definition $\dot{\mathbf{x}}_0 = 0$, it can be derived that

$$\dot{x}_{10} = x_{20} = 0 \text{ and } \dot{x}_{20} = 0.$$

Then, using equation (6.3), the equilibrium relationship between u_{10} and x_{10} is given by

$$\frac{\mathrm{f}_k \mathrm{g}_k}{x_{10}^2} u_{10} = (\omega_\mathrm{n}^2 + \kappa) - (\omega_\mathrm{n}^2 + 3\kappa)x_{10} + 3\kappa x_{10}^2 - \kappa x_{10}^3 \tag{6.4}$$

that allows to choose the fixed input voltage for a desired equilibrium position:

$$u_{10} = \frac{1}{\mathrm{f}_k \mathrm{g}_k} \left((\omega_\mathrm{n}^2 + \kappa)x_{10}^2 - (\omega_\mathrm{n}^2 + 3\kappa)x_{10}^3 + 3\kappa x_{10}^4 - \kappa x_{10}^5 \right). \tag{6.5}$$

The system around this equilibrium point, assuming small oscillations, can be approximated by its linearized version

$$\dot{\tilde{\mathbf{x}}} = \mathrm{A}\tilde{\mathbf{x}} + \mathbf{B}\tilde{\mathbf{u}} \tag{6.6}$$

where $\tilde{\mathbf{x}} = \mathbf{x} - \mathbf{x}_0$, $\tilde{\mathbf{u}} = \mathbf{u} - \mathbf{u}_0$ and the matrices are as follow

$$\mathbf{A} = \left.\frac{\partial f}{\partial \mathbf{x}}\right|_{\mathbf{x}_0,\mathbf{u}_0}, \quad \mathbf{B} = \left.\frac{\partial f}{\partial \mathbf{u}}\right|_{\mathbf{x}_0,\mathbf{u}_0}. \tag{6.7}$$

Consequently,

$$\begin{aligned}\mathbf{A} &= \left.\begin{pmatrix} 0 & 1 \\ -(\omega_{\mathrm{n}}^2 + 3\kappa) + 6\kappa x_1 - 3\kappa x_1^2 + 2\frac{\mathrm{f}_k \mathrm{g}_k}{x_1^3} u_1 & -\frac{\omega_{\mathrm{n}}}{\mathrm{Q}} \end{pmatrix}\right|_{\mathbf{x}_0,\mathbf{u}_0} \\ &= \begin{pmatrix} 0 & 1 \\ -(\omega_{\mathrm{n}}^2 + 3\kappa) + 6\kappa x_{10} - 3\kappa x_{10}^2 + 2\frac{\mathrm{f}_k \mathrm{g}_k}{x_{10}^3} u_{10} & -\frac{\omega_{\mathrm{n}}}{\mathrm{Q}} \end{pmatrix}\end{aligned} \tag{6.8}$$

$$\mathbf{B} = \left.\begin{pmatrix} 0 \\ -\frac{\mathrm{f}_k \mathrm{g}_k}{x_1^2} \end{pmatrix}\right|_{\mathbf{x}_0,\mathbf{u}_0} = \begin{pmatrix} 0 \\ -\frac{\mathrm{f}_k \mathrm{g}_k}{x_{10}^2} \end{pmatrix}. \tag{6.9}$$

And the system under the new variables $\tilde{\mathbf{x}}$ and $\tilde{\mathbf{u}}$ can be approximated by

$$\dot{\tilde{\mathbf{x}}} \approx \begin{pmatrix} 0 & 1 \\ -3(\omega_{\mathrm{n}}^2 + 3\kappa) + 12\kappa x_{10} - 5\kappa x_{10}^2 + 2\frac{(\omega_{\mathrm{n}}^2+\kappa)}{x_{10}} & -\frac{\omega_{\mathrm{n}}}{\mathrm{Q}} \end{pmatrix} \tilde{\mathbf{x}} + \begin{pmatrix} 0 \\ -\frac{\mathrm{f}_k \mathrm{g}_k}{x_{10}^2} \end{pmatrix} \tilde{\mathbf{u}}. \tag{6.10}$$

Finally, as the output of the system is directly the position, its transfer function, using $\tilde{Y}(s) = \begin{pmatrix} 1 & 0 \end{pmatrix} \tilde{X}(s)$ and $\tilde{U}(s)$, is

$$G_{Pn}(s) = \frac{\tilde{Y}(s)}{\tilde{U}(s)} \approx \frac{-\frac{\mathrm{f}_k \mathrm{g}_k}{x_{10}^2}}{s^2 + \frac{\omega_{\mathrm{n}}}{\mathrm{Q}} s + \left(3(\omega_{\mathrm{n}}^2 + 3\kappa) - 12\kappa x_{10} + 5\kappa x_{10}^2 - 2\frac{(\omega_{\mathrm{n}}^2+\kappa)}{x_{10}}\right)}. \tag{6.11}$$

This formulation will be used to derive the controllers.

6.3 Robust control strategy

This section defines the robustness analysis that has been performed and the final robust controller selection, based on Figure 5.2.

6.3.1 System uncertainties

Any MEMS resonator has some inherent uncertainties that can be grouped in four main types, with different effects on system parameters.

6.3.1.1 Fabrication uncertainties

Fabrication imperfections exist, and they come from the actual fabrication processes. Common processing techniques include bulk micromachining, wafer-to-wafer bonding, surface micromachining, and high-aspect ratio micromachining [96]. And these fabrication

techniques involve multiple steps. Typical examples are deposition of materials, chemical etching, patterning of materials and electrical bonding. Consequently, the achievable tolerance varies depending on the process and the design. As a general rule, every added fabrication step contributes to more imperfections in the final design. These imperfections have effects, for example, on the real size of the masses, the parallelism of electrostatic plates, the value of the spring constant and the linearity [188].

6.3.1.2 Environmental and external uncertainties

Environmental and external uncertainties include those external variables that cannot be tuned. Temperature [146], atmospheric pressure, material aging, leakage of vacuum environment [205], external vibrations and frame movement are in this group. All of them have important effects on the final performance of the system but cannot be predicted in advance in the model. Typical effects are changes on the damping of the system and changes on the spring constants.

6.3.1.3 Testing and variable identification uncertainties

The effect of fabrication imperfections and environmental uncertainties could be minimized if testing techniques could perfectly identify them. However, measuring techniques and testing equipment have their own tolerances. Typical system identification techniques involve atomic microscopy, optical microscopy, strobe video microscopy, white light interferometry and electrical testing. Depending on the needed parameters, one or all the techniques can be used, and tolerances will depend on it. The generated uncertainties are directly related to the variables that have been identified. Typical examples are mass of the devices, spring constants [91], damping value and electric parameters [240].

6.3.1.4 Control implementation uncertainties

Some uncertainties are directly related to the control system implementation. They can differ depending on the technologies that are used. The first level of uncertainties comes from the selection between analog or digital controller implementation. And depending on the selection, a second level of uncertainty is introduced depending on the implementation of the building blocks. Typical existing implementations that can be found in MEMS devices are: in-wafer control implementation, in-die interconnection of designed control, discrete components for the control included in-wafer and external

circuitry implementation of the control. Any of them have impact on different parameters, but they have special influence on electrical values. Examples of generated uncertainties are the electrical parasitics [239], the precision of control gains and the uncertainty of feedback acquisition variables [29].

6.3.1.5 Effect of the uncertainties

Based on the system equation (6.1), Table 6.1 summarizes the effect of the four types of uncertainty on the model parameters. Some parameters are related between them, in that case, both appear in the table to simplify variable search.

Fabrication	Environmental	Testing	Control implementation
M	ζ	ϵ	A_s
K	Q	ζ	g_0
K_3	K	ω_n	ω_n
A_c	K_3	M	g
g_0	ω_n	g_0	V
C_0	B	C_p	C_p
f_k			f_k
g_k			x_{10}
ω_n			
Q			
ζ			
κ			

Table 6.1: Classification of the effect of the uncertainties on model parameters. Each uncertainty source acts in different ways and affecting different parts of the model.

Fabrication uncertainty influences the capacity of knowing exactly the parameters of the model, and consequently, predicting with precision its behavior. For this reason, all the parameters related to the structural size and force generation appear on Table 6.1 as uncertain. Environmental uncertainties influence specially the damping of the system, but also the aging of the materials, an those parameters that can evolve with time. Testing uncertainty is clearly related to fabrication uncertainty, and the impossibility to compensate those uncertainties with proper identification techniques. In this case, the variables that are usually identified by testing of the final devices are included. And finally, controller implementation uncertainties are related to those parameters that interfere with the control loop. Specially, position sensing, control voltage generation and equilibrium point for linearization.

Based on the combined influences in Table 6.1, six parameters can be selected to summarize the existing uncertainties. In equation (6.1), the following parameters: Q, ω_n, κ, f_k and g_k will be considered with uncertainty. And they are complemented with the linearization position x_{10}. Table 6.2 shows the system parameters values used in the simulations, with indication of which ones are considered uncertain and their range. It is the same device used in Chapter 4.

Parameter	Value	Uncertainty
K	13.406 N/m	included in ω_n
K_3	$3.768 \cdot 10^{10}$ N/m^3	included in κ
M	$5.6 \cdot 10^{-7}$ Kg	included in ω_n , κ, $f_k g_k$
g_0	$5 \cdot 10^{-6}$ m	included in κ, $f_k g_k$
A_0	$3.86 \cdot 10^{-7}$ m^2	included in $f_k g_k$
ε	$8.85 \cdot 10^{-10}$	constant
C_0	$6.83 \cdot 10^{-13}$ F	included in $f_k g_k$
$\omega_n = \sqrt{\frac{K}{M}}$	4892 rad/s	30%
Q	10 - 100 - 1000	50%
$\kappa = \frac{K_3 g_0^2}{M}$	$1.6821 \cdot 10^6$ N/(m Kg)	30%
$f_k g_k = \frac{C_0}{2g_0}\frac{1}{g_0 M}$	$2.4401 \cdot 10^{-4}$ F/(m^2 Kg)	10%
x_{10}	g_0	20%

Table 6.2: MEMS Resonator parameters (AF07_resonator3 fabricated design) used for simulation

Large values of uncertainty are taken into account in order to formulate an approach that can be valid for different MEMS resonators without need of tuning it depending on fabrication outcome. For this reason, 30% variability is accepted in natural frequency and nonlinear spring, 50% on damping, 10% on force factor, and finally, the 20% on initial condition accounts for different static displacements than can be tolerated. All these values cover a sufficiently large range of values that could be accepted. However, it is clear that usual fabrication and system identification should lead to much lower values.

6.3.2 H_∞ robust control

The first approach was to use H_∞ techniques to obtain a robust behavior of the system against uncertainties, Figure 5.3, using previous schemes already applied on literature [244], [93], [193], [240], [186], [81]. Based on the existing uncertainties in the system (Table 6.2), we can model their effects as multiplicative uncertainty

$$G_P(s) = G_{Pn}(s)\,(1 + W_1(s)\Delta(s)) \quad \text{where} \quad \| \Delta(s) \|_\infty < 1 \tag{6.12}$$

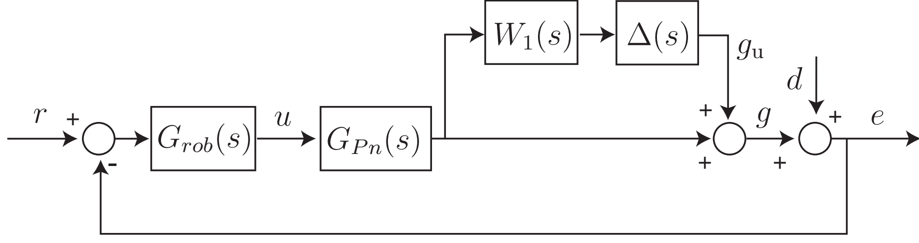

Figure 6.1: Robust control system framework

being $\Delta(s)$ the uncertainty matrix, $W_1(s)$ the uncertainty weighting function and $G_{Pn}(s)$ the system nominal transfer function. With this framework, following H_∞ Robust Control theory, the system is schematically represented as in Figure 6.1. Then, if we define the output sensitivity matrix and its complementary as

$$S_o(s) = \frac{1}{1 + G_{Pn}(s)G_{rob}(s)} \tag{6.13}$$

$$T_o(s) = 1 - S_o(s) = \frac{G_{Pn}(s)G_{rob}(s)}{1 + G_{Pn}(s)G_{rob}(s)} \tag{6.14}$$

the system is robustly stable if we can design a robust controller $G_{rob}(s)$ that satisfies the following stability condition [235]

$$\| W_1(s)\, T_o(s) \|_\infty \leq 1. \tag{6.15}$$

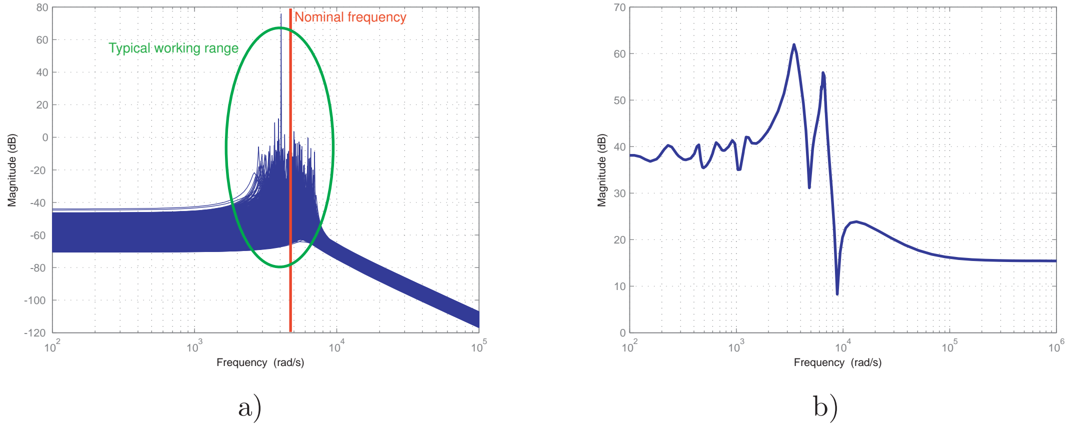

Figure 6.2: a) Magnitude bode plot of the response of a family of 5000 plants obtained with the parameters and the uncertainties in Table 6.2. b) Corresponding weighting function $W_1(s)$ of order 20 for the family of plants in a).

To apply robust stability tests and design a controller, identification of the uncertainty weighting function $W_1(s)$ is needed. Figure 6.2a shows a family of plants based on the

uncertainties and the model in Table 6.2. As can be observed, the existing uncertainties have a large impact in the frequency spectrum on the desired frequencies of oscillation. Moreover, identification of weighting function produces a result with large gain on the range of working frequencies, as observed in Figure 6.2b.

Consequently, trying to apply H_∞ approach to the global uncertainty would not be successful. The first reason is that the controller could not have large action force in the needed range of frequencies, due to the large uncertainty weighting gains in that range. And the second reason is that the range of uncertainty variation can turn the plant unstable, and that behavior cannot be captured by multiplicative uncertainty (6.12). For this reason, structured uncertainty is used instead.

6.3.3 μ-analysis

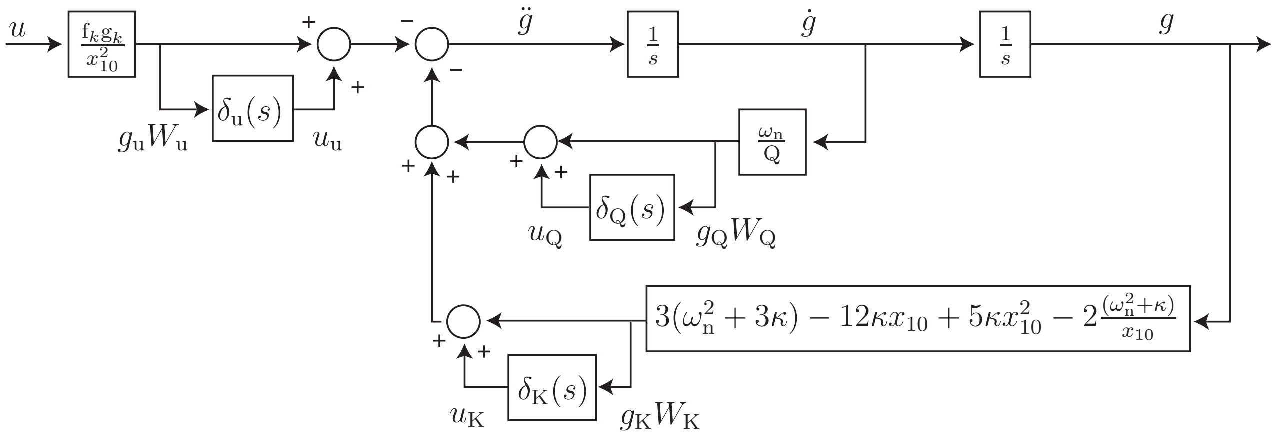

Figure 6.3: Structured uncertainty applied to the linearized system.

When different sources of uncertainty are present in a dynamic system, they usually have structure, meaning that they affect differently the system behavior. H_∞ optimal control treats the different uncertainties as a whole, and in order to obtain a controller the approach has to be too conservative to cover all the uncertain effects [235]. In some cases the strategy works, but when uncertainties are large and structured, better approaches exist. Structured singular value theory apply in this case, complemented with μ-analysis to define the stability dependence of each uncertainty, and μ-synthesis to obtain a robust controller.

First of all, the system equation (6.11) must be rewritten identifying the sources of

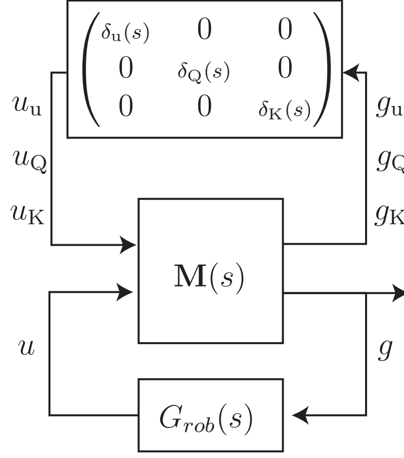

Figure 6.4: Structured uncertainty control system framework

structured uncertainty, Figure 6.3, and from this reconfiguration, matrix $\mathbf{M}(s)$

$$\mathbf{M}(s) = \begin{pmatrix} 0 & 0 & 0 & W_u \frac{f_k g_k}{x_{10}^2} \\ W_Q \frac{\omega_n}{Q}\, s\, \frac{x_{10}^2}{f_k g_k} G_{Pn}(s) & W_Q \frac{\omega_n}{Q}\, s\, \frac{x_{10}^2}{f_k g_k} G_{Pn}(s) & W_Q \frac{\omega_n}{Q}\, s\, \frac{x_{10}^2}{f_k g_k} G_{Pn}(s) & W_Q \frac{\omega_n}{Q}\, s\, G_{Pn}(s) \\ W_K\, \alpha_m \frac{x_{10}^2}{f_k g_k} G_{Pn}(s) & W_K\, \alpha_m \frac{x_{10}^2}{f_k g_k} G_{Pn}(s) & W_K\, \alpha_m \frac{x_{10}^2}{f_k g_k} G_{Pn}(s) & W_K\, \alpha_m\, G_{Pn}(s) \\ \frac{x_{10}^2}{f_k g_k} G_{Pn}(s) & \frac{x_{10}^2}{f_k g_k} G_{Pn}(s) & \frac{x_{10}^2}{f_k g_k} G_{Pn}(s) & G_{Pn}(s) \end{pmatrix} \tag{6.16}$$

where $\alpha_m = \left(3(\omega_n^2 + 3\kappa) - 12\kappa x_{10} + 5\kappa x_{10}^2 - 2\frac{(\omega_n^2+\kappa)}{x_{10}}\right)$, and the structure of $\mathbf{\Delta}(s)$ in Figure 6.4 are pulled out

$$\mathbf{\Delta}(s) = \begin{pmatrix} \delta_u(s) & 0 & 0 \\ 0 & \delta_Q(s) & 0 \\ 0 & 0 & \delta_K(s) \end{pmatrix}. \tag{6.17}$$

Although six parameters have been identified as uncertain, they combine to the three structured uncertainty actions in Table 6.3, where $\delta_i(j\omega) \leq 1$ and W_i are their uncertainty weightings based on the uncertainty range.

$\delta_u(s)$	includes $f_k g_k$ and x_{10}
$\delta_Q(s)$	includes Q and ω_{unc}
$\delta_K(s)$	includes κ, x_{10} and ω_{unc}

Table 6.3: Structured uncertainty components on linearized system model in Figure 6.3.

Based on the structured uncertainty, μ-analysis can be performed to identify the robustness of the system [235]. Given the system structure of Figure 6.4, the uncertain plant system poles are defined by

$$det(\mathbf{I} - \mathbf{M}(s)\mathbf{\Delta}(s)) = 0. \tag{6.18}$$

Consequently, using *singular value* theory, the maximum singular value of the system matrix $\bar{\sigma}(\mathbf{M}(j\omega))$ identifies the minimum destabilizing uncertainty matrix $\mathbf{\Delta}(j\omega)$ that leads the system to instability. Based on this reasoning, the *structured singular value* is the same concept applied to structured uncertainty matrices, and can be calculated as follows:

$$\mu_{\mathbf{\Delta}}(\mathbf{M}(j\omega)) = \frac{1}{min_{\mathbf{\Delta}(j\omega)}\{\bar{\sigma}(\mathbf{\Delta}(j\omega))\,|\,det(\mathbf{I}-\mathbf{M}(j\omega)\mathbf{\Delta}(j\omega))=0\}}. \tag{6.19}$$

Meaning that the *structured singular value*, $\mu_{\mathbf{\Delta}}(\mathbf{M}(j\omega))$, is the reciprocal of the singular value of the minimum structured uncertainty matrix that destabilizes the system. Consequently, as structured uncertainty matrices ($\delta_i(j\omega)$) are assumed normalized to the unity, a system is robustly stable if

$$\mu_{\mathbf{\Delta}}(\mathbf{M}(j\omega)) < 1\ ;\forall\,\omega. \tag{6.20}$$

In this case, the structured uncertainty matrix would need to have a singular value larger than one to destabilize the system, but this is not possible by definition.

The *structured singular value* can be difficult to calculate depending on the system matrix, but its upper bound can be computed numerically based on matrix transformations on $\mathbf{M}(s)$, and in some cases, like the present one, the bound is identical to the structured singular value. Using this approach, the upper-bound is as follows [235]

$$\mu_{\mathbf{\Delta}}(\mathbf{M}(j\omega)) \leq \inf_{\mathbf{D}} \bar{\sigma}(\mathbf{D}\,\mathbf{M}(j\omega)\,\mathbf{D}^{-1}) \tag{6.21}$$

where $\mathbf{D}$ is a block-diagonal scaling matrix with the last element being 1, that satisfies: $\mathbf{D}\,\mathbf{\Delta} = \mathbf{\Delta}\,\mathbf{D}$. And the robust stability condition is achieved if the μ upper-bound is lower than the unity for all the range of frequencies.

Figure 6.5 shows the μ upper-bound for the uncertain system plant, using the parameters in Table 6.2. As can be observed, there exist a range of frequencies where its value is larger than the unity, meaning that for the range of uncertainty that has been chosen some of the plants are unstable. This gives place to the necessity of analyzing what uncertainties lead the system to instability and obtaining a stabilizing controller.

6.3.3.1 Sensitivity analysis

Figure 6.5 shows that the open-loop system can become unstable in the range of chosen uncertainty. Given that six uncertainty sources have been defined, it is important to

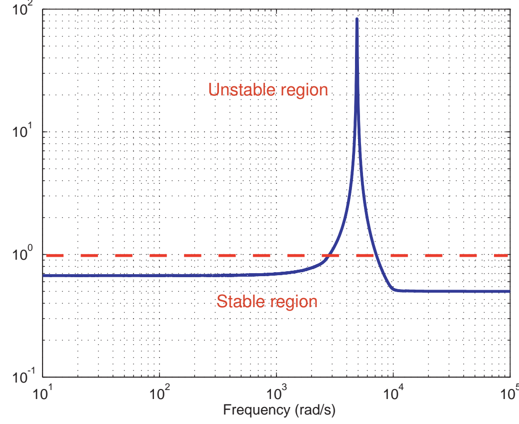

Figure 6.5: μ upper-bound for the open-loop system, using the parameters in Table 6.2.

---

understand which uncertainties and which ranges are the ones that are more critical to the stability of the system.

Associated to the *structured singular value*, the *Stability margin* is defined as

$$K_\mu = min_{K\geq 0}\{K \mid det(\mathbf{I} - K\mathbf{M}(j\omega)\mathbf{\Delta}(j\omega)) = 0\} = \frac{1}{\mu_{\mathbf{\Delta}}(\mathbf{M}(j\omega))} \tag{6.22}$$

in order to obtain a value to quantify the robust stability of the system. The stability margin calculates the minimum perturbation that converts the system plant unstable. The larger the value of the stability margin is, more robust the system is. Consequently, sensitivity analysis consists in identifying the effect of each uncertain parameter on the stability margin, and the probability that this parameter variation could drive the system to instability. Then, using this approach, the sensitivity of each parameter to the stability of the system can be analyzed.

Based on the uncertain ranges in Table 6.2, sensitivity analysis is calculated comparing relative variation of a parameter in the uncertain range and the decrease of the stability margin that generates. Table 6.4 shows the analysis done to the system using the three parameters in Table 6.3. Only the uncertainty that affects the spring constant of the model clearly generates stability margin reduction in the range of work. An increase of the 25% of the range on δ_{K} generates a reduction of 25% in the stability margin, while the same variation on δ_{Q} only generates a 1% reduction in the stability margin. The effect of variations in δ_{u} are not detectable in the stability margin. The sensitivity calculations have been performed using Matlab© *robuststab* command [18].

Given the large sensitivity detected, it is important to look in detail to the sensitivity

Parameter	Parameter variation	Stability margin variation	Sensitivity
δ_{Q}	25% of range	1% decrease in the margin	4%
δ_{K}	25% of range	25% decrease in the margin	100 %
δ_{u}	25% of range	0% decrease in the margin	0%

Table 6.4: Sensitivity of structured uncertainty components, based on example on Table 6.2.

results, and analyze which parameters are included in the δ_{K} term. For this reason, independent sensitivity analysis is carried on.

The calculation of the sensitivity of the system against the six initially defined parameters is presented in Table 6.5. The system is specially sensitive to the change of the natural frequency, ω_{n}, as an increase of 25% of its uncertainty range generates a 28% reduction of the stability margin. The next sensitive parameter is the linearization point, producing a 6% reduction of the stability margin, but clearly less sensitive than the frequency. Finally, the Quality factor has some effect (1%), and the rest have minor effect unless the variation is really important.

Parameter	Parameter variation	Stability margin variation	Sensitivity
Q	25% of range	0.2% decrease in the margin	1%
$\mathrm{f}_k\mathrm{g}_k$	25% of range	0% decrease in the margin	0 %
κ	25% of range	0% decrease in the margin	0%
ω_{n}	25% of range	28% decrease in the margin	110%
x_{10}	25% of range	6% decrease in the margin	22 %

Table 6.5: Sensitivity of uncertain parameters, based on example on Table 6.2.

Natural frequency uncertainty is then the most critical parameter in defining the robust controller. This result could be expected, as resonant frequency generates high gains and phase shifting in the system and can lead it to instability. Same analysis can be done for the equilibrium point chosen for linearization, as its variation changes the oscillation region and the energy profile in the gap, and it is directly related to the pull-in instability, as defined in Chapter 3.

6.3.3.2 μ-synthesis controller

Although the assumed uncertainty is large, in order to satisfy a large set of possible MEMS imperfections, following the control structure defined in Figure 6.4 a stabilizing controller can be designed.

Synthesis of stabilizing controllers using the so-called *D-K iteration* [235] is a well-known technique that produces good results in most cases. The only drawback is that in some

cases the controller can have large order. In the present case, the technique is able to produce a controller that leads the system to stability in the range of feasible uncertainty.

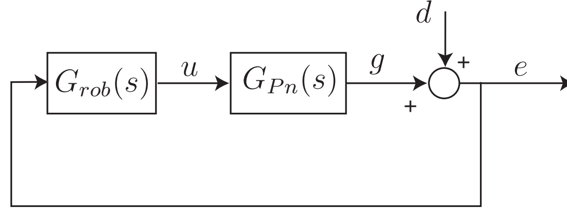

Figure 6.6: Control loop for disturbance rejection applied to obtain the *D-K iteration* controller, based on Matlab© *dksyn* command.

The *D-K iteration* is a two step iterative procedure that takes advantage of the H_∞-optimal control problem solution to obtain a controller that satisfies the stability criterion in (6.20). Using the μ upper-bound defined in (6.21), an initial **D** scaling is chosen and an H_∞-optimal controller is calculated. If the μ upper-bound doesn't satisfy the stability criteria with the new controller, new scalings are chosen to satisfy the bound, and another controller is calculated. This iteration process is continued until the closed-loop system with the controller is robustly stable with a μ upper-bound lower than one.
In the examples, μ-synthesis controller, $G_{rob}(s)$, is generated using the encapsulated Matlab© *dksyn* command [18], and the structure in Figure 6.6.
For the example of Table 6.2, the generated controller applying *D-K iteration* has the following transfer function:

$$G_{rob}(s) = \frac{2.731 \cdot 10^9 s + 6.465 \cdot 10^{11}}{s^2 + 4.268 \cdot 10^5 s + 7.543 \cdot 10^9} \tag{6.23}$$

It is important to notice that the plant has negative gain, for this reason the controller and the feedback loop are positive. The frequency response of the controller is presented in Figure 6.7, which obtains a μ upper-bound for the closed-looped system with the new controller of 0.9024 in the presented case, so stability is guaranteed for the uncertainty range. A minimum stability margin of 1.10 is obtained at frequency $0.5365\omega_\mathrm{n}$. The unitary step performance is shown in Figure 6.8 for a family of the uncertain plants with the new controller, confirming the stability requirements.
In the proposed control strategy, the robust control loop plays an important role. Given the fact that linear techniques are applied to a nonlinear plant, the Robust controller is the key to be able to apply the linearized controllers to the nonlinear system. In the proposed set-up, the linearization equilibrium has been included as uncertain covering most of the

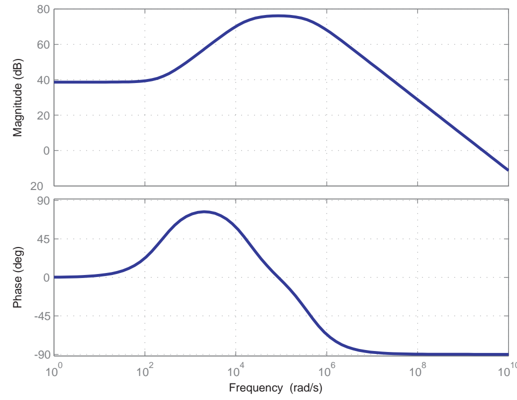

Figure 6.7: Frequency response of the designed robust controller.

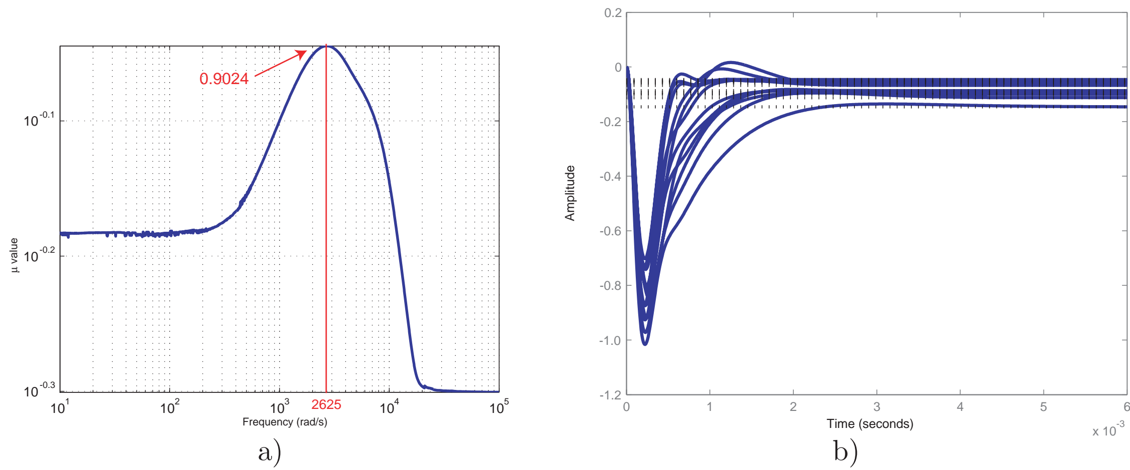

Figure 6.8: a) μ upper-bound of the closed-loop system with the designed μ-synthesis controller. b) Simulation of unitary step response of the closed-loop system with the μ-synthesis controller for a family of plants with uncertainties.

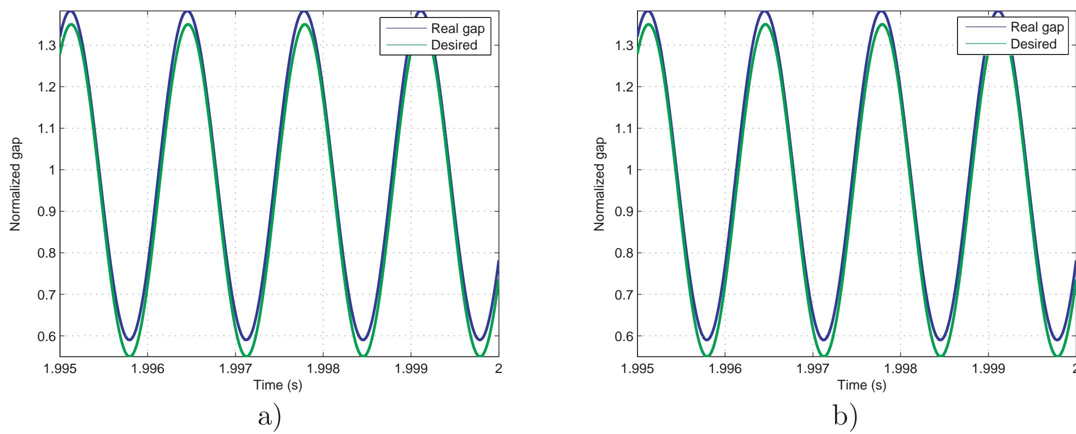

Figure 6.9: Simulations of nonlinear plant oscillation using the designed robust controller. a) The natural frequency is $w_k = 0.965$, or 3.5% different from nominal. b) κ is 20% higher than the nominal value.

range of oscillation. And the three elements related to the nonlinearity (x_{10}, κ, $\mathrm{f}_k\mathrm{g}_k$) are explicitly treated as uncertain, and with large range of uncertainty to guarantee robust stability. However, certain restrictions apply in the level of maximum uncertainty that can be handled [66], and must be thoroughly tested and validated.

In Figure 6.9, examples with 3.5% natural frequency variation and 20% nonlinear spring variation are presented, with stable performance. It is important to note that the controller has been purposely designed only for stability, and that is the reason of the steady-state error.

6.4 Internal-Model-Principle based control strategy

Once robustness of the system is assured in the working range, oscillation performance is the following goal. Based on the controller proposed in Chapter 5, Figure 5.2, an IMP Controller is designed.

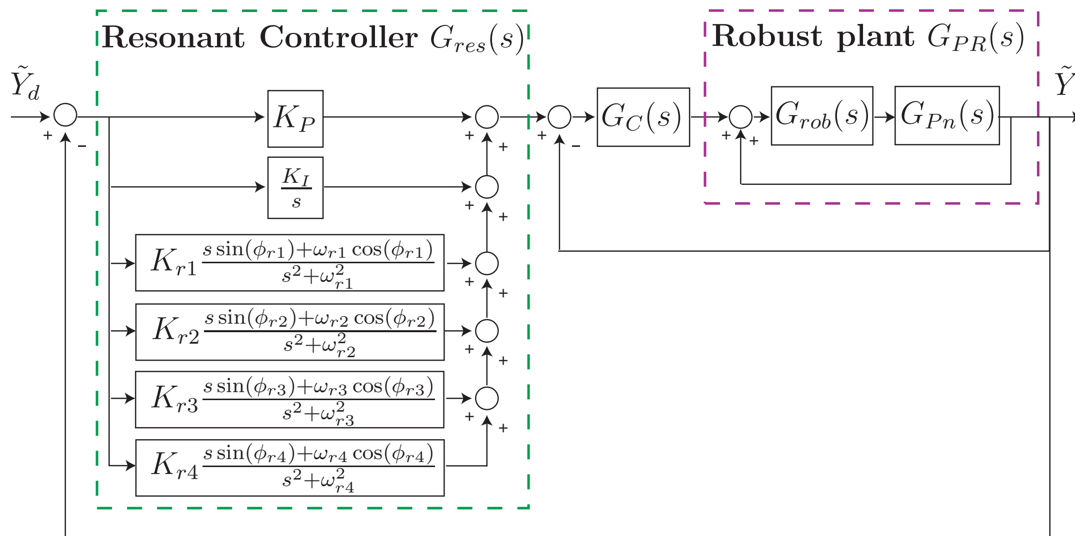

Figure 6.10: Resonant Controller with four resonators applied to the plant with the robust controller.

IMP Controllers have the ability to deal with oscillatory systems were certain harmonics are undesirable [69]. A MEMS resonator is a perfect example where these type of controllers can be applied. In the dissertation work, both Resonant Controllers and Repetitive Controllers have been analyzed. Both show the capability to be applied to MEMS, however, due to the low MEMS system gain and the design procedure, Resonant Controllers have been chosen.

6.4.1 Resonant control

When using MEMS devices in high performance inertial applications, the oscillation has to be as large as possible and as perfect sinus-like as possible. In Chapter 4 it has been shown that this goal is possible with the election of the right input. In this Section, a Resonant Controller [69] is shown to produce the needed input to generate the desired sinus-like oscillation at the desired amplitude.

Figure 6.10 shows the typical configuration of a Resonant Controller, given a plant represented by $G_{PR}(s)$. Two control loops are involved. In the inner loop, a first controller, $G_C(s)$ is designed to accomplish two goals: provide good stability margins and robustness and, at the same time, adjust the plant phase between given bounds at the working frequency bandwidth. The outer loop is the IMP based part. The resonant controller, $G_{res}(s)$, consists of a set of resonators in parallel, each one working at one of the desired working/rejecting frequencies and their harmonics. A complementary Proportional-Integral controller is applied in parallel to provide steady-state tracking performance [50].

With this set-up, the resulting closed-loop transfer function using the linearized model in (6.11) is

$$\frac{\tilde{Y}(s)}{\tilde{Y}_d(s)} = \frac{G_{res}(s)G_C(s)G_{PR}(s)}{1 + G_C(s)G_{PR}(s) + G_{res}(s)G_C(s)G_{PR}(s)} \tag{6.24}$$

where

$$G_{PR}(s) = \frac{G_{rob}(s)G_P(s)}{1 - G_{rob}(s)G_P(s)}. \tag{6.25}$$

In the system under study, the controller $G_C(s)$ is needed only to adjust the phase of the system, because the plant is already robust and stable thanks to the controller derived in the previous section, $G_{rob}(s)$, in (6.23). Including $G_C(s)$, the inner closed-loop transfer function is

$$P(s) = \frac{G_C(s)G_{PR}(s)}{1 + G_C(s)G_{PR}(s)}. \tag{6.26}$$

And to guarantee stability of the resonant controller and maximize the phase margin of the system, as explained in [34], the following condition on the phase of $P(s)$ must be satisfied in the working bandwidth

$$\angle P(j\omega) \in [-90^\circ, 90^\circ] \tag{6.27}$$

In the presented example, this condition is not satisfied unless $G_C(s)$ is added, as it can be observed in the Bode plot of Figure 6.11. The frequency working range is defined from under half natural frequency ($0.4\omega_\mathrm{n}$) up to the fifth harmonic of the natural frequency ($5\omega_\mathrm{n}$). Consequently, a filter $G_C(s)$ has been designed to correct the phase of $P(s)$ to satisfy the condition. For the system with the parameters in Table 6.2, it would have the following form

$$G_C(s) = -\left(\frac{\left(\frac{1}{3\,\omega_\mathrm{n}}\right)\ s+1}{\left(\frac{1}{7\,\omega_\mathrm{n}}\right)\ s+1}\right)^2. \qquad (6.28)$$

The negative term appears in order to move the phase that is placed at 180-degree to zero, and the filter adds some needed phase in the neighborhood of the fourth harmonic. With this filter, the phase of the nominal plant is corrected as observed in Figure 6.11. Moreover, the filter also guarantees that the phase variation of $P(s)$ due to the accepted uncertainty is also between bounds. Figure 6.12 shows the phase variation for a set of 2000 plants generated with the parameters in Table 6.2. In all cases the phase is between bounds in the frequency working range. This validation is important to guarantee the stability during frequency seeking in the energy minimization loop.

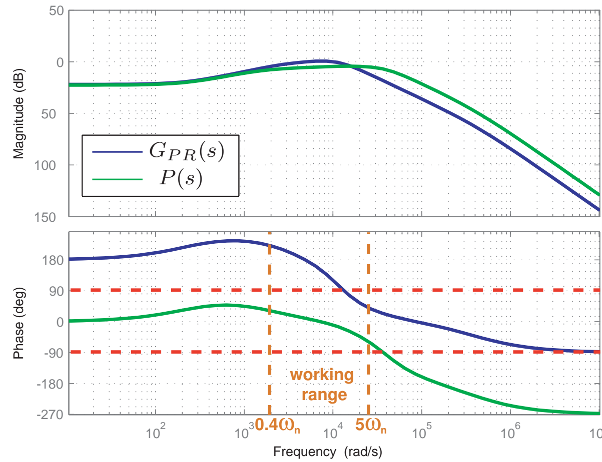

Figure 6.11: Bode plot comparing the nominal robust plant of $G_{PR}(s)$ and the plant $P(s)$ in (6.26), resulting of adding $G_C(s)$ to suit the Resonant Control needs.

Once $P(s)$ is adequately trimmed, the Resonant controller can be designed. As it is implied by the Internal Mode Principle, the reference or disturbance to be tracked or rejected must be included in the control loop. For sinusoidal signals, this translates to the introduction in the controller of a pair of poles at the desired frequency. With this

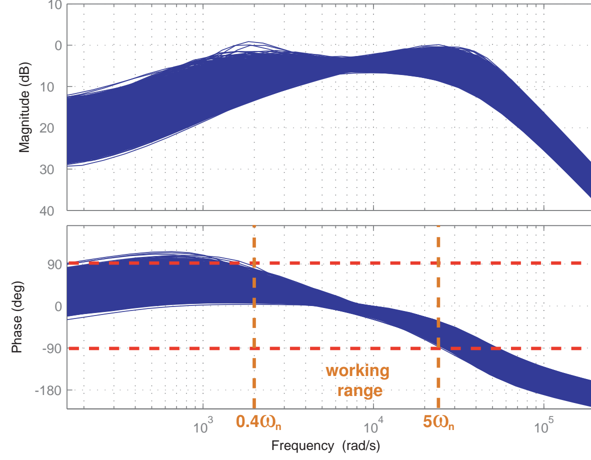

Figure 6.12: Analysis of $P(s)$ phase variation due to the range of chosen uncertainty in Table 6.2. A set of 2000 plants are presented.

inclusion, the controller has infinite gain at the desired frequency, leading to precise signal tracking or disturbance rejection at that frequency. Consequently, the resonator terms in the controller are chosen with the following form, using the adaptive feed-forward cancelation approach in [34] for the zeros:

$$\hat{R}_i(s) = K_{ri}\frac{s\sin(\phi_{ri}) + \omega_{ri}\cos(\phi_{ri})}{s^2 + \omega_{ri}^2} \tag{6.29}$$

where ω_{ri} is the desired working frequency and its harmonics in the thesis case, ϕ_{ri} is calculated as [124]

$$\phi_{ri} = -\angle P(j\omega_{ri}) \tag{6.30}$$

and K_{ri} is adjusted to have enough gain and performance. Finally, $K_P + \frac{K_I}{s}$ is a PI controller that is tuned with the rest of the controller resonator gains to produce a desired global performance, tracking and stability of the closed-loop transfer function (6.24).

Parameter	**Value**
K_P	5
K_I	100
K_{r1}	500
K_{r2}	200
K_{r3}	100
K_{r4}	50

Table 6.6: Resonant controller parameters for the model in Table 6.2.

Table 6.6 shows the selected controller parameters based on the MEMS resonator in Table 6.2. The Resonant controller is designed with four resonators, as Chapter 4

analysis indicates that in most cases four harmonics is enough to obtain a sinusoidal output. Moreover, in terms of final design, more than four resonators could be difficult to implement in commonly available technology. Figure 6.13 shows the resulting controller Bode plot for a desired frequency of oscillation at $0.96\omega_{\mathrm{n}}$. In the Bode plot the four resonators are clearly visible.

The PI controller parameters have been selected to achieve a quick error settlement under one second. And the resonator gains have been selected to achieve that the oscillation error is at least six times lower than the oscillation magnitude without any of the first four harmonics present on it. The rest of parameters depend on the selected frequency of oscillation.

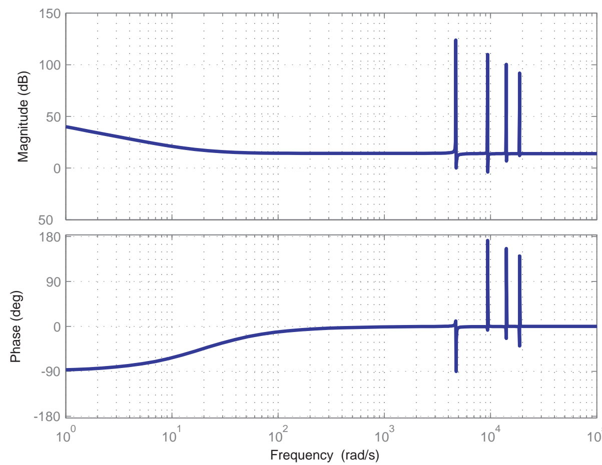

Figure 6.13: Bode plot of the Resonant controller, $G_{res}(s)$, with four resonators for a desired oscillation frequency of $0.96\omega_{\mathrm{n}}$.

With these parameters, the resulting closed-loop system is stable, as it is obtained from the nominal transfer function poles (6.24) in Table 6.7. Moreover, applying μ-analysis to the closed-loop system, it can be obtained that the system with the resonant controller is robustly stable for the range of uncertainties, Figure 6.14, with a stability margin of 1.053. The stabilizing effect of the resonant controller can be observed in the working frequency range, where the μ-bound is flat and lower than the previous values of Figure 6.8.

To verify that the linearized control solution is applicable to the non-linear system, simulation has been carried on the actual non-linear model. In the simulations, the designed resonant controller with the four resonators is used. The system parameters are

Closed-loop poles
-422780
-630
-10
$-21390 \pm 73070i$
$-14580 \pm 2740i$
$-10 \pm 4730i$
$\pm 9410i$
$\pm 14100i$
$\pm 18790i$

Table 6.7: Poles of the nominal closed-loop transfer function including the resonant controller, for a desired frequency of oscillation at $0.96\omega_{\mathrm{n}}$.

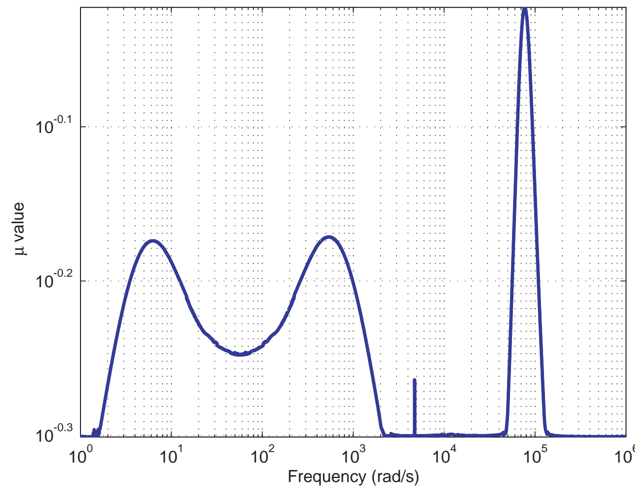

Figure 6.14: μ-bound of the closed-loop system with the Resonant controller, $G_{res}(s)$, for a desired oscillation frequency of $0.96\omega_{\mathrm{n}}$.

---

the same previously used from Table 6.2.

The results of the simulations show that the controller is stable and obtains good performance. This could be expected, as the designed robust controller handles the nonlinearities, and the resonant controller is designed based on the robust plant. Figure 6.15 shows the simulation results for a desired sinusoidal output with a normalized amplitude of 0.4, a normalized steady-state bias gap of 0.95 and a normalized frequency of 0.96. The system obtains the desired amplitude, bias and frequency of oscillation with a fast transient response.

The generated input voltage is shown in Figure 6.16, as well as, its transient dynamics. As can be observed, at the beginning of the simulation large voltages are applied, but no snapping occurs. The tuning of the PI-controller plays an important role in this transient

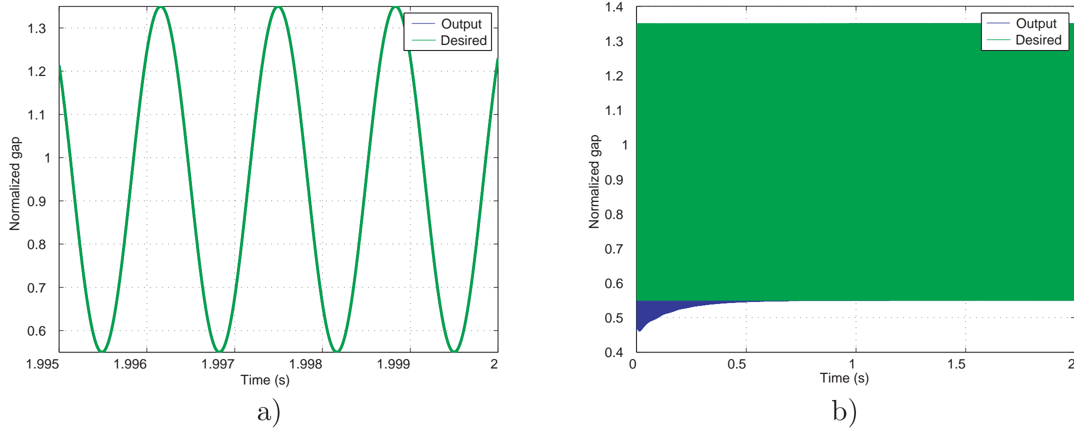

Figure 6.15: a) Detail of the normalized gap oscillation after applying the resonant control, for a set-point with $G_1 = 0.4$ as amplitude of oscillation, $G_0 = 0.95$ as static bias and $\omega_d = 0.96\omega_\mathrm{n}$ as oscillation frequency. b) Long time normalized gap oscillation showing transient evolution and steady-state convergence in less than a second.

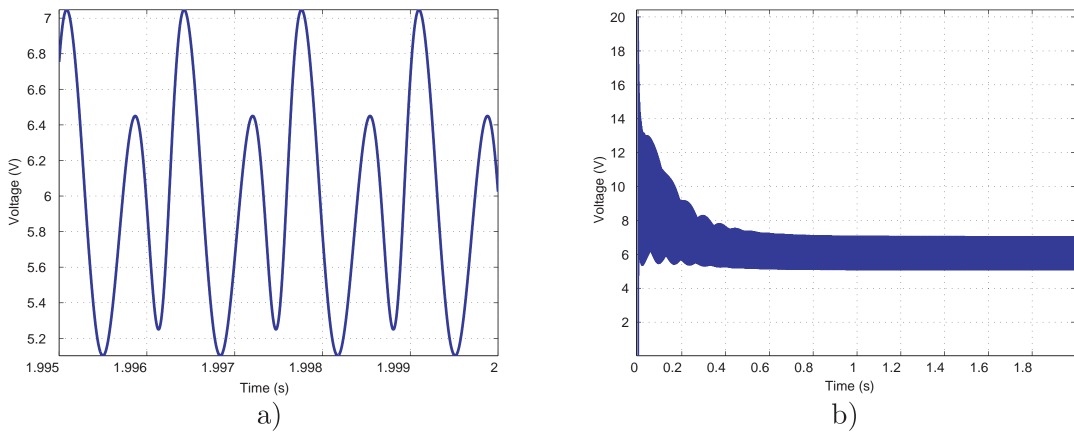

Figure 6.16: a) Close-up of the control voltage generated by the controller to obtain the desired oscillation. b) Control voltage long time simulation, showing transient evolution and steady-state.

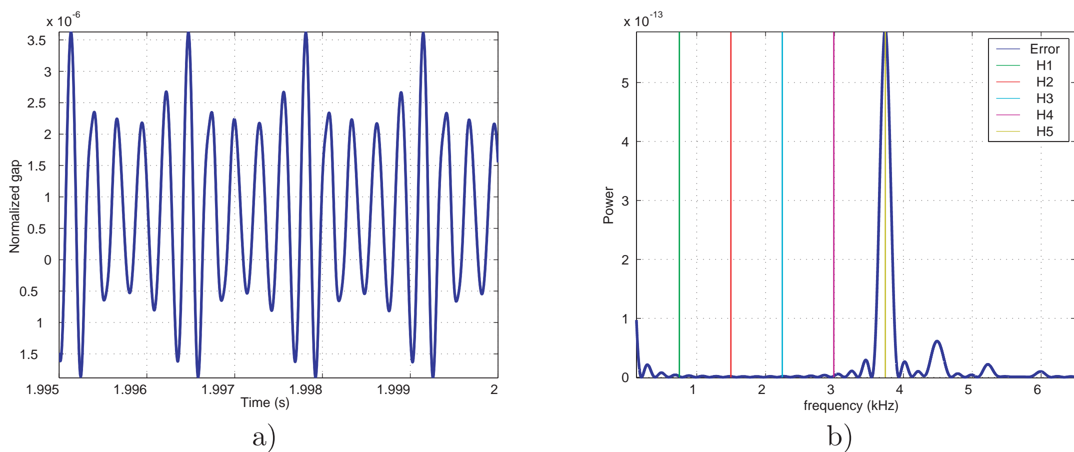

Figure 6.17: a) Oscillation error comparing system output and pure sinusoidal set-point. b) Frequency analysis of the oscillation error.

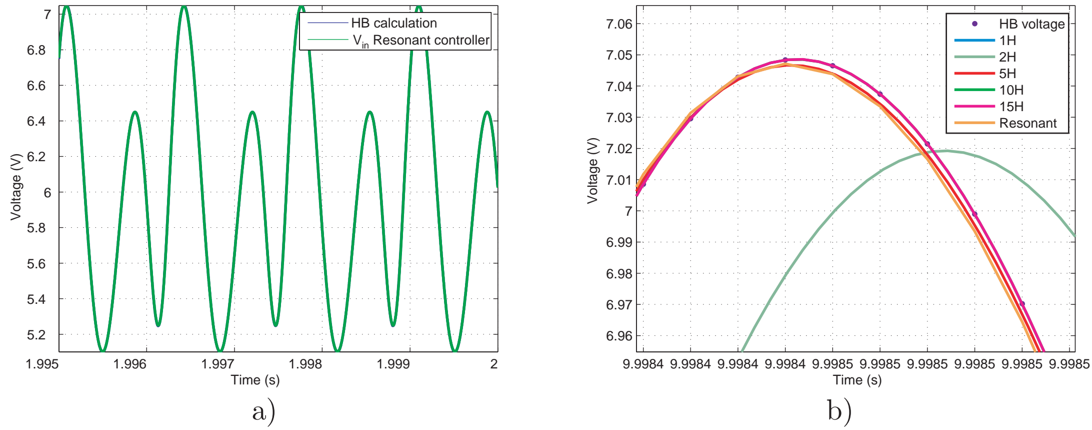

a) b)

Figure 6.18: a) Harmonic Balance predicted input voltage compared to the voltage generated by the controller. b) Close-up of the voltage comparison showing that some difference exists.

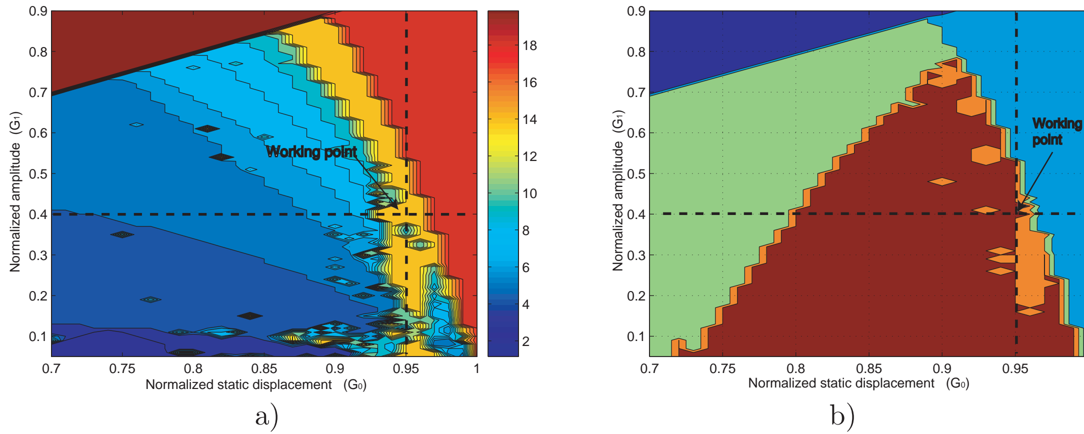

a) b)

Figure 6.19: Comparison of current simulations with Chapter 4 results. a) Harmonic Balance predicts that more than 10 harmonics are needed for a perfect driving voltage reproduction. b) The oscillation is predicted stable when the Harmonic Balance voltage is applied.

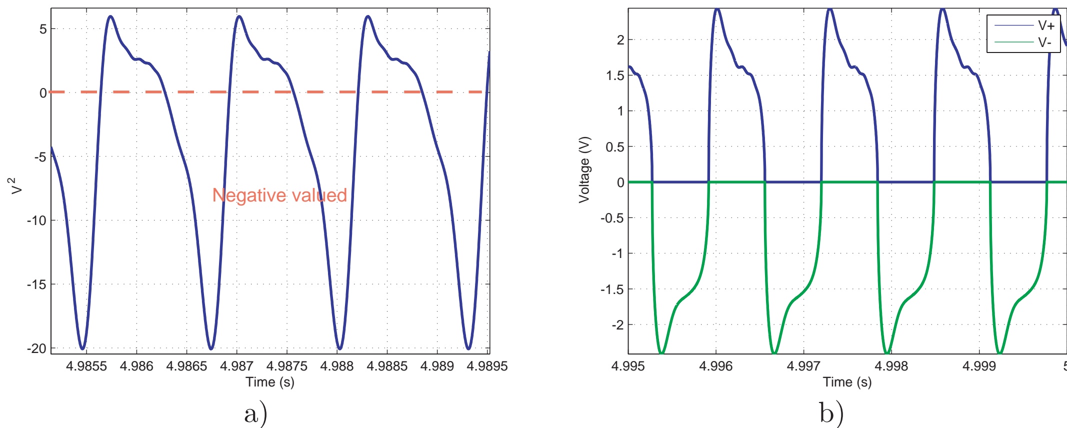

a) b)

Figure 6.20: a) Example of V^2 generated by proposed controller with negative values, for an amplitude of oscillation of 0.5 and no static bias, Quality factor 100 and normalized frequency $w_k = 1$. b) Voltages applied to the two-sided actuator to produce the desired actuation, as described in detail in Section 7.3.1. V^+ is applied to one side and $|V^-|$ is applied to the other side.

behavior.

The generated input voltage produces an almost null steady-state error, as can be seen in Figure 6.17. The highest error component is in the fifth harmonic, as expected, as four resonators have been used in the control and their gains have been tuned to achieve this goal. And the steady-state error is six times lower than the absolute amplitude g_0, what implies that the output is an almost perfect sinusoid.

If we analyze the correspondence of the results with the predicted Harmonic Balance voltage in Chapter 4, Figure 6.18 shows that both input voltages are almost identical. The discrepancy comes from the number of harmonics used in the controller. For the desired oscillation, the chart in Figure 6.19a indicates that more than ten harmonics are needed for perfect sinusoidal recovery. The same result can be seen in Figure 6.18b, where a fifteen harmonics fitting is needed to perfectly reproduce the Harmonic Balance ideal voltage.

However, while Harmonic Balance prediction was expecting more harmonics in the driving voltage to generate the perfect sinusoid, simulation shows that the Resonant Controller with just four resonators is able to produce outputs with errors six orders of magnitude lower than the oscillation gap, what could be considered almost perfect for a real application. This discrepancy is due to the fact that both analysis are not equivalent: the chart in Figure 6.19a has been generated assuming a perfect sinusoid output and fitting a signal to the drive input, while the Resonant Controller generates the voltage by eliminating harmonics of the output but limiting the number of them.

To close the analysis, Figure 6.19b shows that the system was predicted stable by the Harmonic Balance with the desired oscillation, and the simulations in Figure 6.15 show that the controller generates a stable oscillation.

Finally, as described in Chapter 4, the selection of V^2 as control action implies that the output of the controller cannot be directly applied to the MEMS resonator. The control action must be converted to a voltage signal. However, the controller output can lead to negative V^2 control actions that cannot be directly converted to driving voltages, Figure 6.20. This problem has been solved improving the MEMS design introducing two-sided actuation to the MEMS resonator as explained in detail in Section 7.1.3.

6.5 Extremum seeking control strategy

To complete the proposed control strategy in Figure 5.2, the last controller loop include an energy minimization extremum seeking controller that must be designed. As described in Chapter 5, Extremum seeking control allows to optimize a cost function even when it is not analytically known [56], [71], [70]. Energy efficiency is sought in all aspects of life, and in electrostatically actuated MEMS, this is specially needed when they must act as stand-alone sensors. And in this case, extremum seeking control would minimize the energy consumption of the electrostatically actuated MEMS resonator.

Between the different existing approaches describer in Chapter 5, perturbation-based extremum seeking is chosen [15]. This approach is well-tested, easily implementable, and don't interfere with the desired dynamics due to the time-scales. Moreover, stability of the approach has been demonstrated [98] and a real application has been tested in a MEMS gyroscope [13].

The critical part in the implementation is the fact that the variable to be optimized is the desired oscillation frequency, ω_d. The goal is to select the frequency where the desired amplitude of oscillation consumes less energy. However, that frequency is a design value for the Resonant controller implementation, and this issue must be treated carefully. The results in [87], where ESC is used to tune the variable gain of a controller, are used as example to change the phase and frequency of the proposed Resonant controller.

Figure 6.21 shows the control scheme connected to the previously presented system with the Robust controller and the Resonant controller.

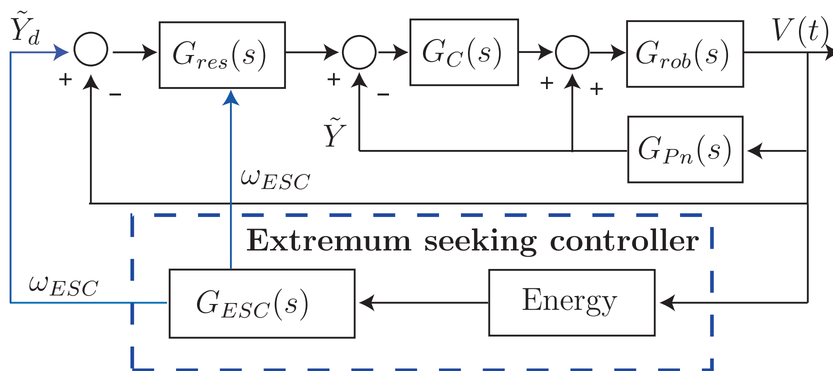

Figure 6.21: Extremum Seeking Control applied to the system framework, using Energy in one oscillation cycle as Cost Function.

6.5.1 Energy calculation

The selection of the *Cost function* is the basis of the minimization process. In order to effectively minimize a variable, the values of the variable have to change smoothly and a local extremum must exist.

As presented in Chapter 4, the energy consumption in one oscillation corresponds to the energy losses in equation (4.51)

$$E_{consumption} = \frac{\mathrm{B}\,\pi}{\mathrm{C}_0}\,\hat{Y}_1^2\,\omega + \mathrm{R}_{vs}\int_0^{\frac{2\pi}{\omega}} I_{vs}(\omega, t)^2 dt \tag{6.31}$$

where a negligible fraction comes from mechanical losses and the main part is associated to the driving voltage and the power supply. With this formulation, the energy consumption is frequency dependent, smooth and have a clear minimum for each desired oscillation, as showed in Figures 4.48 and 4.49.

Based on equation (6.31), and dropping the mechanical term as negligible, the *Cost function* for the Extremum seeking controller is defined with the following formula:

$$\text{Cost function} = \int_t^{t+\frac{2\pi}{\omega}} \left(\frac{d\,V(t)}{dt}\right)^2 dt \tag{6.32}$$

where $T_d = \frac{2\pi}{\omega_d}$ is the time of one oscillation cycle at the desired frequency, and $V(t)$ is the voltage that is really fed into the MEMS resonator, as shown in Figure 6.21. Consequently, the selected voltage is not only related to the device, but to the whole control action that is built around it.

Although the energy calculation includes the source resistance, the resistance is not included in the cost function because its magnitude is constant and has no effect on the minimization process.

Figure 6.22 shows two simulated examples of time evolution of the energy cost function calculation. As can be seen, the cost function can be calculated continuously to be fed into the ESC controller. Moreover, the system has a fast response, and the energy calculation is also fast allowing to implement the ESC controller without added restrictions. The time response of the cost function calculation is a key parameter when designing the ESC controller, due to the necessity to separate time scales.

Finally, Figure 6.23 compares the cost function frequency profile obtained via simulation with the values from the Harmonic Balance energy calculation. As can be seen, both profiles present similar results. Although the energy levels are not identical, the minimum

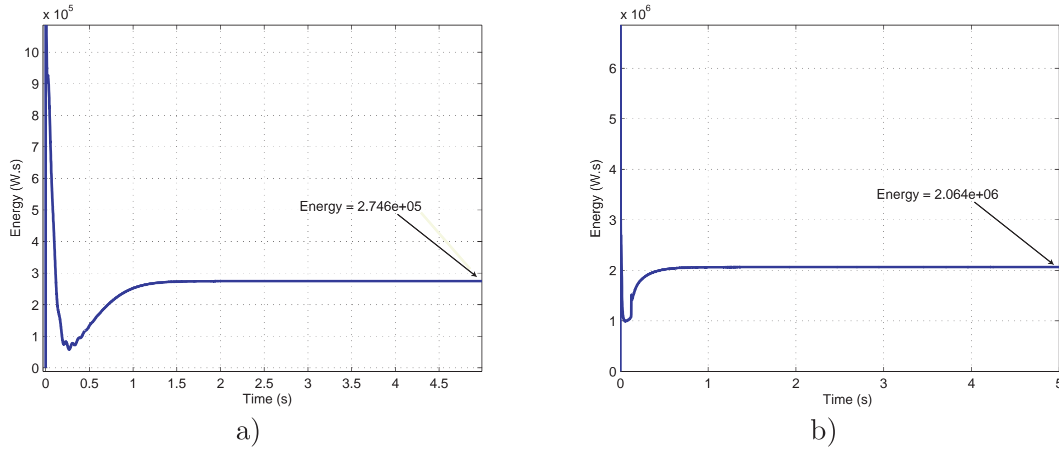

Figure 6.22: Time evolution of energy cost function calculation for two different oscillation frequencies. The desired oscillation is fixed at an amplitude of 0.4 and a static bias of 0.95. a) $w_k = 0.94$ b) $w_k = 1.1$.

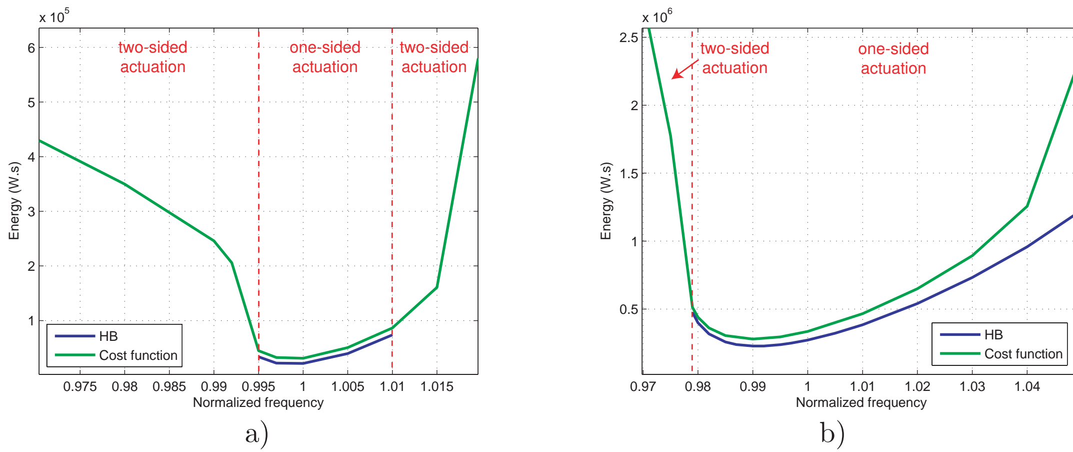

Figure 6.23: Energy consumption curves comparing Harmonic balance energy calculation and controller Cost function calculation, for fixed damping at Q = 100. a) Amplitude of desired oscillation $0.4g_0$ with 0.99 gap bias. b) Amplitude of desired oscillation $0.7g_0$ with 0.95 gap bias.

energy frequency obtained from the Cost function is approximately at the same value predicted by Harmonic Balance. The discrepancies come from the differences between the Harmonic Balance voltage and the output of the Resonant Controller as indicated in the previous section. Moreover, with the two-sided actuation improvement presented in Section 7.1.3 to handle the negative valued V^2 output, the energy cost function is expanded to the whole frequency range, allowing smooth operation of the ESC controller. As can be observed, the values corresponding to the zone where one-sided actuation is possible are almost identical to the Harmonic Balance ones, except when they get far from the minimum energy point. And when the actuation gets to the two-sided zone, energy increases quickly. This indicate that the system will be driven by the extremum seeking

controller to work in the one-sided frequency range.

6.5.2 Extremum seeking controller

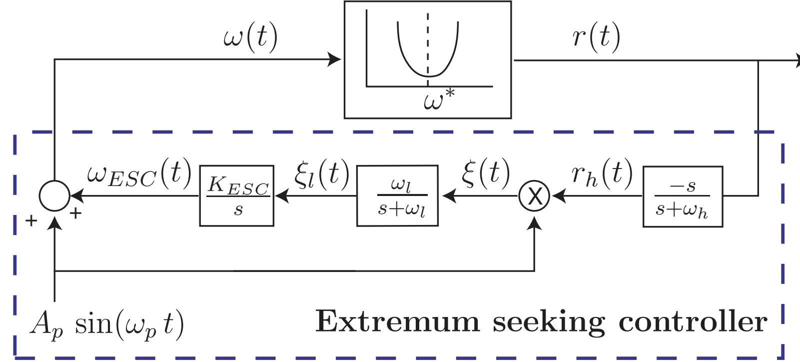

Figure 6.24: Extremum seeking controller to minimize cost function, based on perturbation methods, adapted from [15]. Due to time scales, the plant is treated as an static map from the controller point of view.

The ESC controller defined in Figure 6.24 includes four main stages:

- A perturbation that is fed into the system in order to extract the cost function gradient, with a frequency of ω_p and an amplitude of A_p.

$$u_p(t) = A_p \sin(\omega_p t) \tag{6.33}$$

- A high-pass filter to eliminate the DC content of the energy followed by demodulation of the perturbation to generate an estimate of the gradient, with frequency of ω_h.

$$F_h(s) = \frac{-s}{s + \omega_h} \tag{6.34}$$

- A low-pass filter, with frequency of ω_l, to extract the DC content of the estimated gradient.

$$F_l(s) = \frac{\omega_l}{s + \omega_l} \tag{6.35}$$

- And an integrator of the gradient to generate the optimal input estimate for the plant, to which the perturbation is added.

$$G_{ESC}(s) = \frac{K_{ESC}}{s}. \tag{6.36}$$

Consequently, the input to the system is

$$\omega(t) = \omega_{ESC}(t) + u_p(t). \tag{6.37}$$

In order to work properly and with stability, the five parameters ($A_p, \omega_p, \omega_h, \omega_l,\ K_{ESC}$) must be selected appropriately. This selection must guarantee the time scales separation between the different stages of the controller. In particular, there exists three velocities in the system [15]:

- A fast response is given by the system and the two-inner loops. In order to be able to identify the system as a static map, in the extremum seeking scheme, the system has to be an order of magnitude quicker than the perturbation.
- A medium time response must be provided by the perturbation, which must be quick enough to respond to changes but must not interfere with the system performance.
- An a slow time response of the filters, that will extract the gradient estimate. The filters must be an order of magnitude lower than the perturbation signal.

In the final controller, for the system parameters in Table 6.2, the chosen values are presented in Table 6.8. The main reference is T_f, the settling time of the system, that must be chosen to guarantee that the dynamics of the system is separated of the rest of the extremum seeking dynamics. From this value, the rest come out automatically.

T_f	$3.85\,s$
ω_f	$2\,\pi\ /\ \mathrm{T}_f$
K_{ESC}	0.001
A_p	0.001
ω_p	$\omega_f/20$
ω_h	$\omega_p/10$
ω_l	$\omega_p/10$

Table 6.8: Extremum seeking controller parameters used in the examples.

Figure 6.25 shows the different stages of the controller in an example. The plots allow to see the evolution of the energy and how it is driven to its minimum with the continuous frequency variation generated by the controller. In the example, a desired amplitude of 0.4, a bias of 0.95, a damping of 100 and an initial frequency of $0.97\omega_{\mathrm{n}}$ have been chosen. Based on Figure 4.48a, the more efficient frequency for the desired oscillation and damping is $0.968\omega_{\mathrm{n}}$, so the controller should lead the frequency to this value. Figure 6.25a shows how the Cost function value is minimized while, at the same time, Figure 6.25b shows how the set-point frequency is decreased with time from the initial 0.97 value in search of

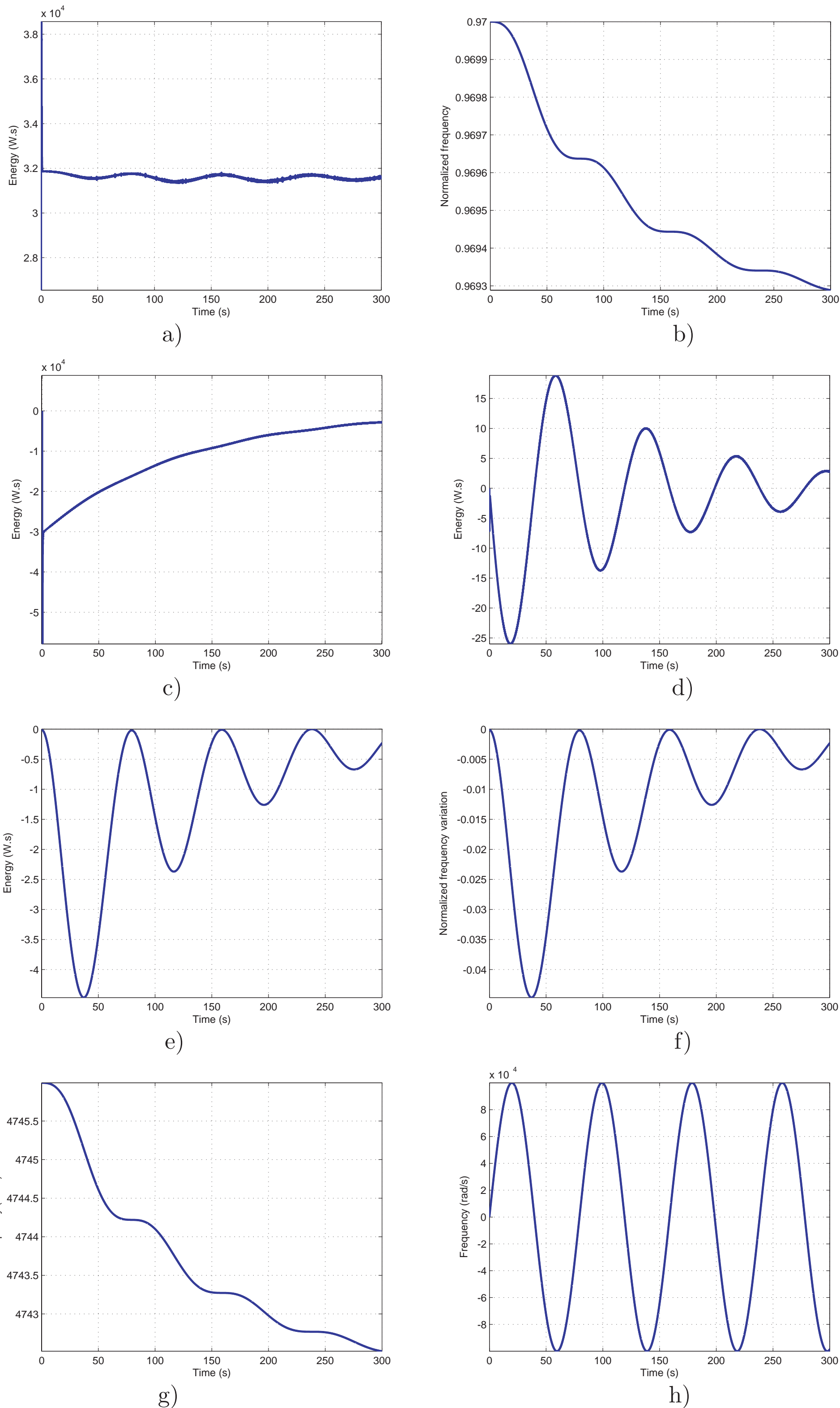

Figure 6.25: ESC performance with a desired amplitude of 0.4, a gap bias of 0.95, a damping of Q = 100 and an initial frequency of w_k = 0.97. a) Energy Cost function time evolution. b) Frequency set-point generated by the ESC controller, including the perturbation. c) High-pass filtered Cost function, with DC elimination. d) Demodulation of c)-signal with the perturbation. e) Gradient estimation obtained through low-pass filtering. f) Scaled gradient estimation. g) ESC frequency output through integration of scaled gradient. h) Perturbation signal.

the optimal 0.968 value. Due to the time scales separation, the frequency variation has to be very slow in order to prevent transients in the system oscillation. For this reason in 300 seconds the frequency change is so small.

Figure 6.25c presents the effect of the high-pass filter that incorporates the ESC controller. As can be seen, the cost function value is recentered around zero, by extraction of the cost function DC bias. After this filtering, the signal is demodulated with the perturbation in order to extract the effect generated by the perturbation, as can be seen in Figure 6.25d. Low pass filtering of the demodulated signal generates the gradient estimate, Figure 6.25e, that is scaled in order to define convergence velocity, Figure 6.25f. Final integration of the scaled gradient generates the frequency output of the controller, Figure 6.25g, that is summed up with the perturbation, Figure 6.25h, in order to generate the input to the system as presented in Figure 6.25b.

In a real application, the seeking time should be even slower than the one presented in simulations, what would lead to a gradient estimation that monotonically decreases until reaching the optimal frequency.

6.5.3 Convergence analysis

The mode of operation, the controller steps presented in Figure 6.25 and the controller convergence can be analytically explained, in a simplified manner, following the same reasoning as in [12]. The explanation assumes that the system works as a static map (Example in Figure 6.23) referencing the frequency to its consumption energy. With this assumption, the controller loop is redefined as in Figure 6.24. This simplification holds if the adaptation dynamics is sufficiently slow, as previously stated, due to selected time scales. Then, the output of the static map, $r(t)$, is the value of the cost function and can be represented as

$$r(t) = f(\omega(t)) \tag{6.38}$$

where the static map is assumed C^2 around its minimum ω^*. The input to the system is the new estimate of the optimal frequency obtained by the controller, $\omega_{ESC}(t)$, plus the seeking perturbation, so that the output of the cost function is

$$r(t) = f(\omega_{ESC}(t) + A_p \sin(\omega_p t)). \tag{6.39}$$

As the perturbation is small, the output can be approximated by

$$r(t) \approx f(\omega_{ESC}(t)) + A_p \frac{\partial f}{\partial \omega}|_{\omega=\omega_{ESC}} \sin(\omega_p t). \tag{6.40}$$

Consequently, the high pass filter allows to separate the variation introduced by the perturbation from the constant output term

$$r_h(t) \approx A_p \frac{\partial f}{\partial \omega}|_{\omega=\omega_{ESC}} \sin(\omega_p t) \tag{6.41}$$

and if the resulting signal is demodulated with the perturbation, $A_p \sin(\omega_p t)$

$$\xi(t) \approx \frac{1}{2} A_p^2 \frac{\partial f}{\partial \omega}|_{\omega=\omega_{ESC}} - \frac{1}{2} A_p^2 \frac{\partial f}{\partial \omega}|_{\omega=\omega_{ESC}} \cos(2\omega_p t) \tag{6.42}$$

using the low pass filter, the estimation of the gradient at the actual input value can be obtained

$$\xi_l(t) \approx \frac{1}{2} A_p^2 \frac{\partial f}{\partial \omega}|_{\omega=\omega_{ESC}}. \tag{6.43}$$

Then, the input to the system is updated based on the following law, using the estimation gradient in (6.43)

$$\dot{\omega}(t) = K_{ESC} \frac{1}{2} A_p^2 \frac{\partial f}{\partial \omega}|_{\omega=\omega_{ESC}}. \tag{6.44}$$

As we have assumed that the map is C^2 locally around ω^*, the law guarantees convergence of the controller frequency estimate to the optimum of the system.

This can be seen in detail if the map f is approximated as a Taylor polynomial of second order in a small neighborhood of ω^*

$$f(\omega) \approx f(\omega^*) + f'(\omega^*)(\omega - \omega^*) + \frac{1}{2} f''(\omega^*)(\omega - \omega^*)^2 \tag{6.45}$$

where $f'(\omega^*) = 0$ because ω^* is an extremum point. Then the resulting gradient is

$$\frac{\partial f}{\partial \omega}|_{\omega} \approx f''(\omega^*)(\omega - \omega^*). \tag{6.46}$$

Defining the convergence error as $\tilde{\omega} = (\omega - \omega^*)$, its behavior with the chosen updating law (6.44) is

$$\dot{\tilde{\omega}} \approx \left(\frac{1}{2} K_{ESC} A_p^2 f''(\omega^*) \right) \tilde{\omega} \tag{6.47}$$

meaning that the controller is locally asymptotically stable with the appropriate election of parameters

$$K_{ESC} A_p^2 f''(\omega^*) < 0 \tag{6.48}$$

The full detailed justification of the stability and convergence of the method is discussed in [98]. As can be seen, all the steps of the convergence analysis have their counterpart in Figure 6.25.

6.6 Conclusion

The proposed controller with three control loops for robustness, stability, sinus-like oscillation and minimum energy actuation has been designed. Based on the linearized system approach, the controller has been formulated and analyzed. The stability and robustness of the combined controller has been validated with μ-analysis. Applicability of the designed controller to the nonlinear plant has been verified via simulation.
The performance of the global controller is tested in Chapter 7, what allows to confirm that the controller based on the linearized system is effective on the real nonlinear plant and to track oscillation trajectories.

Chapter 7

Verification of control strategy

7.1 Introduction

This Chapter performs the verification of the proposed control strategy. In the first part, a series of simulation tests of the complete set-up are presented, and its stability, robustness and performance analyzed.

In the second part, the needed steps for a real implementation are analyzed. First of all, design modifications are presented to overcome possible implementation difficulties. A two-sided actuation for full-range amplitude and bias oscillation selection is presented. And a modification of standard Electromechanical Amplitude Modulation is analyzed and validated for position feedback implementation.

Finally, a MEMS resonator with the desired specifications for testing the proposed control is designed for fabrication. Based on this design, testing procedure is discussed, as well as, actual laboratory set-up. The fabrication and laboratory testing is included as Future Work.

7.2 System performance

A set of simulations has been executed to validate the whole range of behaviors of the system using the proposed controller. The simulations follow the same approach presented in Section 4.2 in Chapter 4, and the same system model (Table 4.1).

In detail, good performance of the controller imply that the four main goals defined in Chapter 5 are accomplished:

- Stability of the oscillation in amplitude and frequency.
- Robustness of the oscillation against inherent MEMS fabrication uncertainties.

- Perfect sinus-like oscillation for high precision applications.
- Minimum energy consumption to sustain the oscillation.

Each of the items is analyzed individually.

7.2.1 Stability

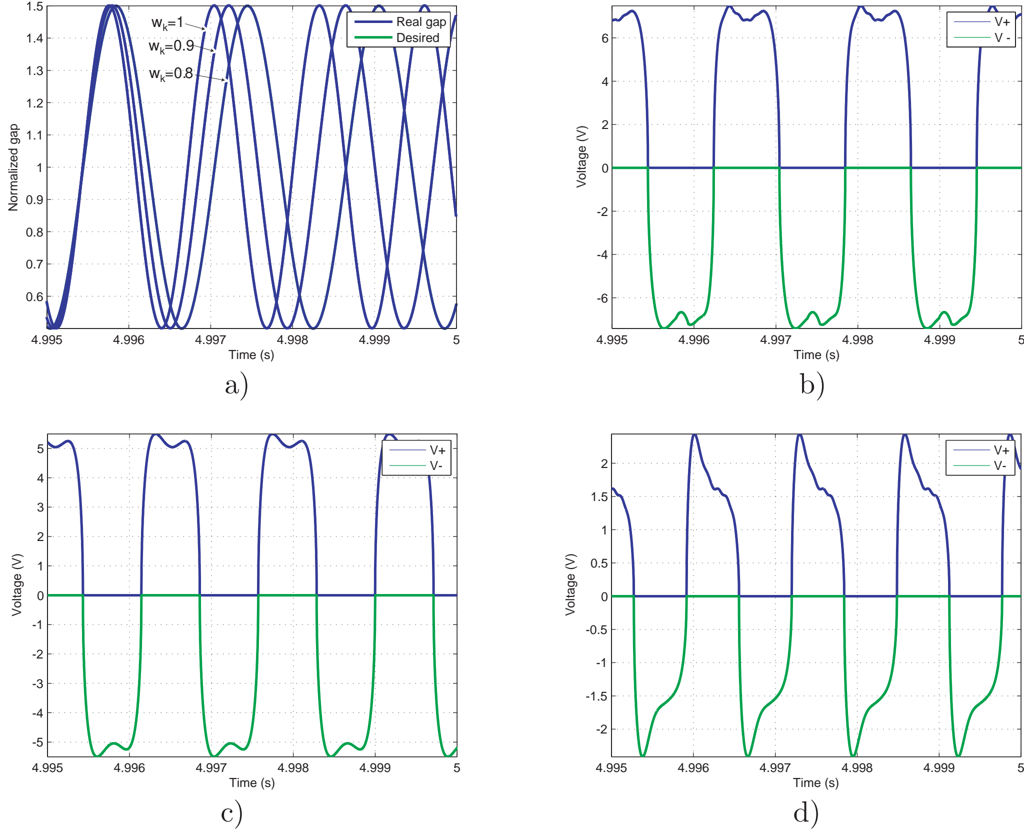

Figure 7.1: Time response of the oscillation of the MEMS resonator with 0.5 amplitude set-point and bias fixed at 1. Damping fixed at Q = 100. a) Output of the MEMS resonator compared to oscillation reference for three different frequencies: $w_k = 0.80$, $w_k = 0.90$ and $w_k = 1.00$. b) Input to the MEMS resonator for $w_k = 0.80$. c) Input to the MEMS resonator for $w_k = 0.90$. d) Input to the MEMS resonator for $w_k = 1.00$.

One of the main goals of any controller is to guarantee stability. In the present case, the controller must be able to oscillate the MEMS resonator at any desired amplitude and with any desired static bias. For this reason, a set of simulations has been performed to analyze oscillation ranging from small amplitudes ($0.1\mathrm{g}_0$) to almost full gap amplitudes ($0.9\mathrm{g}_0$), and with different steady-state biases (g_0 to $0.8\mathrm{g}_0$). At the same time, the whole range of oscillation frequencies has been analyzed. Usual working frequencies have been defined as those ranging from $0.8\omega_\mathrm{n}$ to $1.1\omega_\mathrm{n}$. The work of the controller with subharmonic and

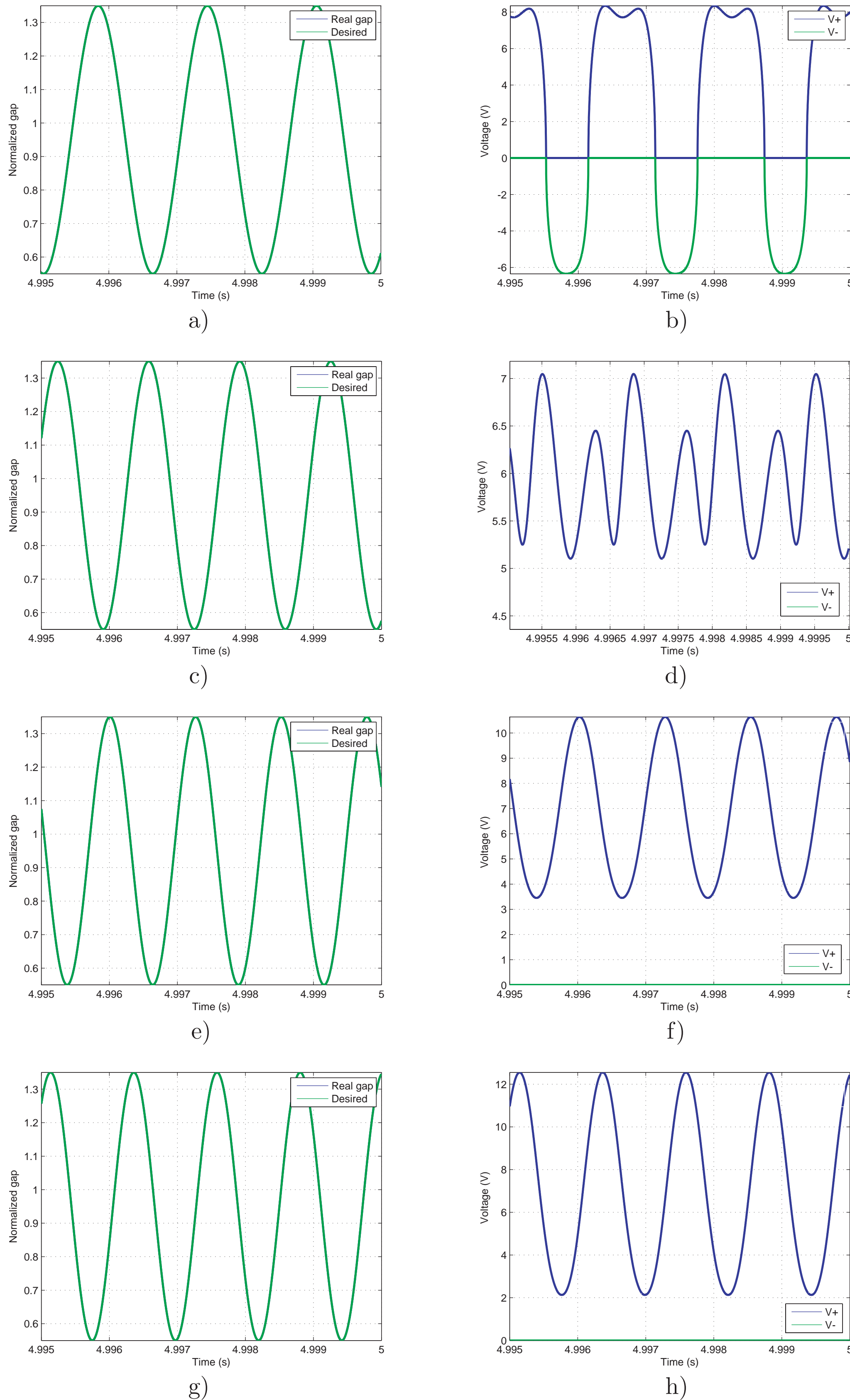

Figure 7.2: Time response of the oscillation of the MEMS resonator with 0.4 amplitude set-point and bias fixed at 0.95. Damping fixed at Q = 100. a) Oscillation for $w_k = 0.80$. b) Voltage input for $w_k = 0.80$. c) Oscillation for $w_k = 0.96$. d) Voltage input for $w_k = 0.96$ e) Oscillation for $w_k = 1.02$. f) Voltage input for $w_k = 1.02$. g) Oscillation for $w_k = 1.05$. h) Voltage input for $w_k = 1.05$.

superharmonic frequencies have also been investigated. And finally, the oscillations have been simulated with damping varying from over-damped systems (Q = 1) to low vacuum systems (Q = 1000). Simulations include steady-state oscillation as well its transients, as they can lead to pull-in of the structure.

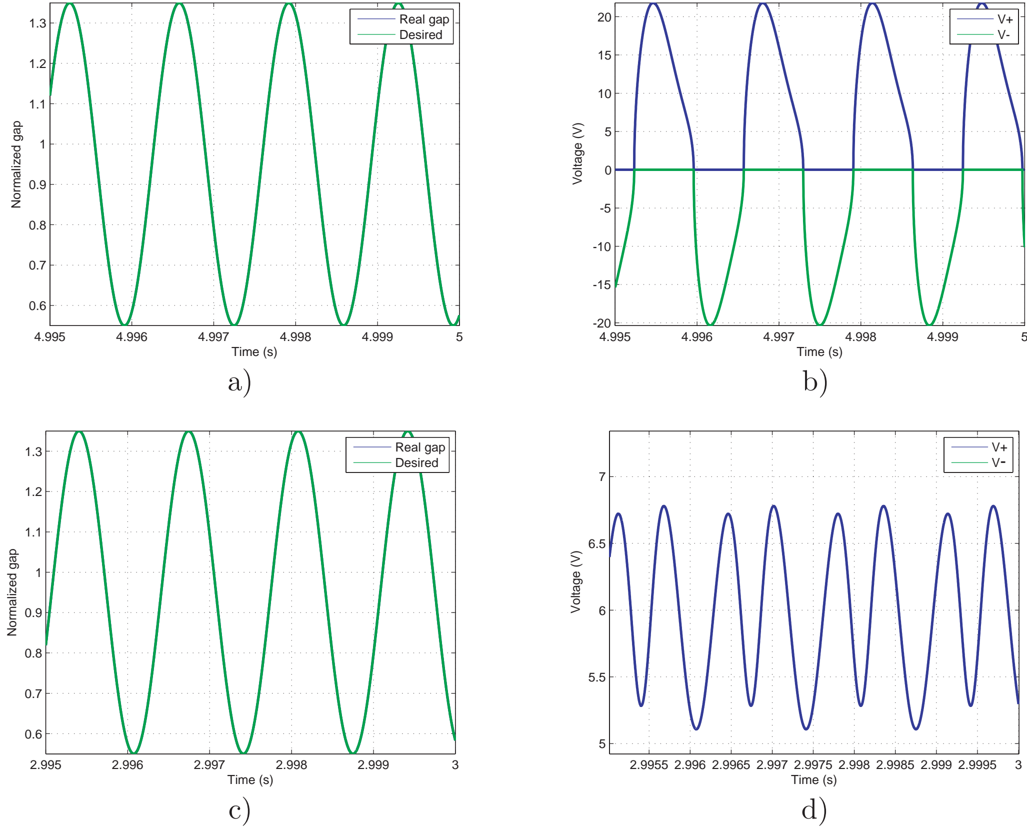

Figure 7.3: Time response of the oscillation of the MEMS resonator with 0.4 amplitude set-point and bias fixed at 0.95. The normalized frequency is fixed at $w_k = 0.96$. a) Oscillation for Q = 1. b) Voltage input for Q = 1. c) Oscillation for Q = 1000. d) Voltage input for Q = 1000.

With this framework, Figure 7.1a shows an example of normalized oscillation of the MEMS resonator for different frequency set-points. At rest, gap is assumed to be one (g_0 in real values). In the example, the simulations have an oscillation set-point with amplitude of half the gap (0.5) and centered at rest position (bias is one), with a Quality-factor of 100. Different normalized frequencies are tested ($w_k = 0.80$ to $w_k = 1.00$). In all cases stable oscillation of the desired amplitude is achieved, as the controller automatically generates the needed voltage to reach the target (the same predicted by harmonic balance in Chapter 4), Figures 7.1b, 7.1c, 7.1d. In all cases, two-sided actuation is needed to achieve the desired set-point, V^+ is applied to one side and $|V^-|$ is applied to the other side (See Section 7.3.1).

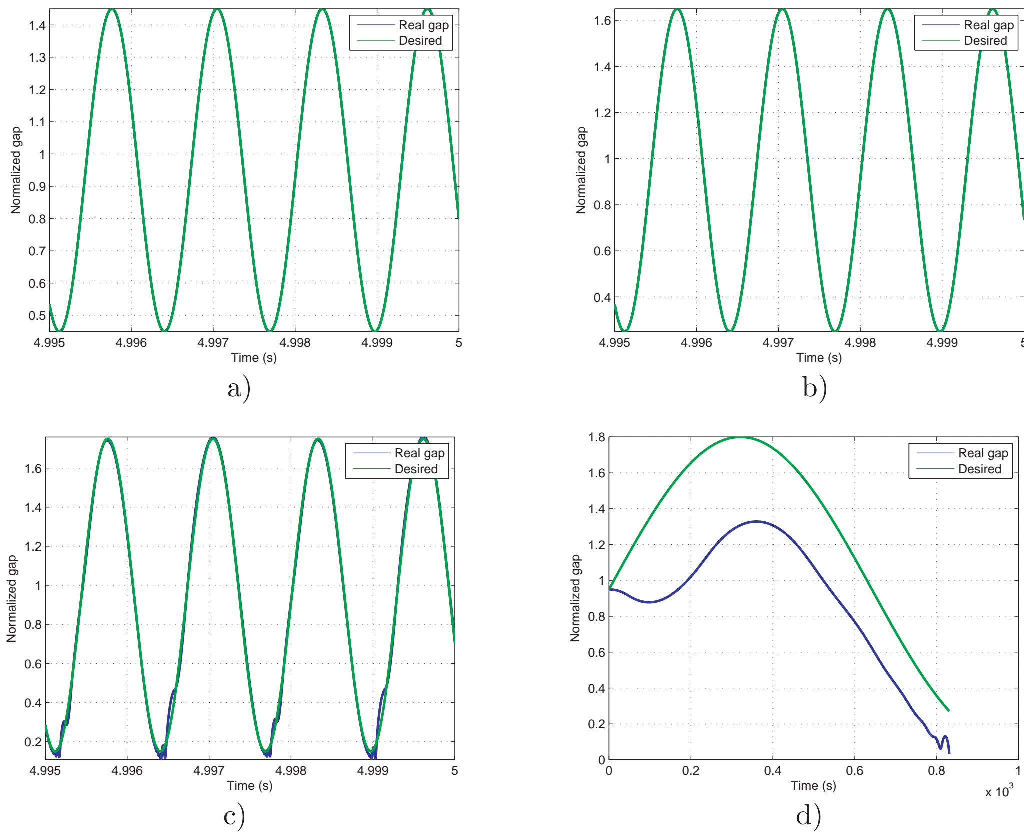

Figure 7.4: Time response of the oscillation of the MEMS resonator frequency fixed at $w_k = 1$ with changing amplitude set-point and fixed bias at 0.95. Fixed damping at Q = 100. a) Amplitude of 0.50. b) Amplitude of 0.70. c) Amplitude of 0.80. d) Amplitude of 0.85.

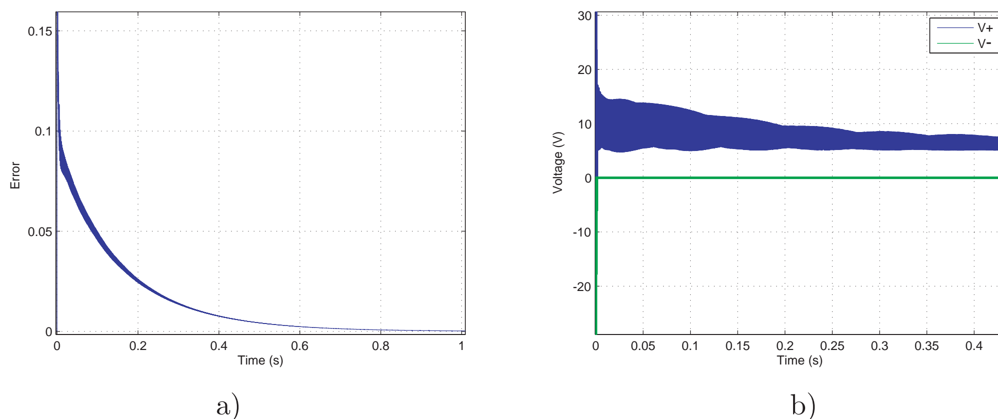

Figure 7.5: Transient oscillation performance of the MEMS resonator with 0.4 amplitude set-point and bias fixed at 0.95. The normalized frequency is fixed at $w_k = 0.96$ and Quality factor at Q = 100. a) Oscillation error. b) Close-up of the input voltage during transient.

Figure 7.2 shows similar simulations with increased range of normalized frequencies from $w_k = 0.80$ to $w_k = 1.05$. In this case, set-point is fixed at lower amplitude (0.4), and not centered at rest position (bias is 0.95), with same Quality factor (100). Again all oscillations are stable at steady-state and during transient. As can be seen, stability is not affected by set-point or frequency of oscillation. Moreover, Figures 7.2b and 7.2d show that depending on desired frequency, oscillation is achieved with one-sided or two-sided voltage driving.

In Figure 7.3 the effects of damping are analyzed. The example shows the same set-point oscillation with normalized frequency close to resonance ($w_k = 0.96$), amplitude of 0.4 and bias of 0.95. Changing the damping conditions from over-damped (Q = 1) to low vacuum (Q = 1000) don't change stability of the system with the proposed controller, and in all cases the desired oscillation is achieved with the controller automatically providing the needed voltage.

As analyzed in Chapter 3, pull-in of electrostatic driven parallel-plate actuators is a limiting factor for gap oscillation. At the same time, large amplitudes are needed to improve sensitivity of MEMS resonators working as sensors. Figure 7.4 shows oscillations with amplitude set-point up to $0.85g_0$. In the simulations, bias is fixed at 0.95, frequency at $w_k = 1$ and Quality factor at 100. As a reference, the MEMS resonator nonlinear *Static Pull-in* occurs at $0.336g_0$, and the *Resonant Pull-in Condition* fixes maximum amplitude of oscillation around $0.59g_0$ for the chosen bias, with a square function. Given these pull-in limits, the simulations show that stable oscillations are achieved well beyond them. However, pull-in can still occur if set-point is fixed with steady-state oscillations reaching more than 80% of the gap. In Figure 7.4b, total gap oscillation of $0.75g_0$ is achieved with 0.7 as amplitude and 0.95 as bias. But Figure 7.4c shows unstable oscillation that leads to pull-in with an amplitude of 0.8 plus 0.95 bias (equivalent to 0.85 total gap oscillation), and 7.4d shows pull-in with a set-point with a total gap amplitude of 0.95.

Figure 7.5 shows transient behavior of the controller, with amplitude set-point fixed at 0.4 and bias fixed at 0.95. The normalized frequency is fixed at $w_k = 0.96$ and Quality factor at Q = 100. Transient stability is accomplished for the tested conditions, with settling times under one second. In the example, Figure 7.5a shows that the output error is close to zero (10^{-6}) after one second. And in Figure 7.5b, a close-up of the needed control action is shown. This behavior has been detected all over the different simulations and is not affected by Q changes, what satisfies the needed smooth transient performance for a

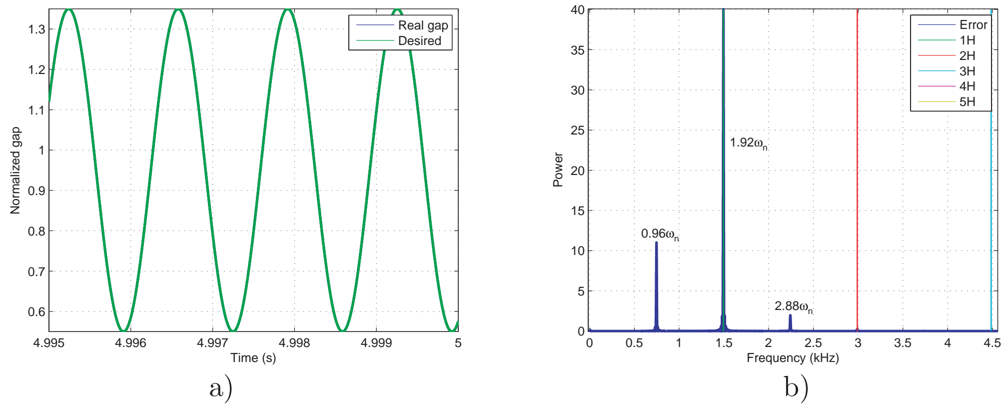

a) b)

Figure 7.6: Subharmonic oscillation of the MEMS resonator with frequency design fixed at $w_k = 1.92$, amplitude set-point fixed at 0.40 and fixed bias at 0.95. With damping at Q = 100. Desired set-point frequency fixed at $w_k = 0.96$. a) Stable oscillation output at $w_k = 0.96$. b) Power spectrum of the generated input voltage.

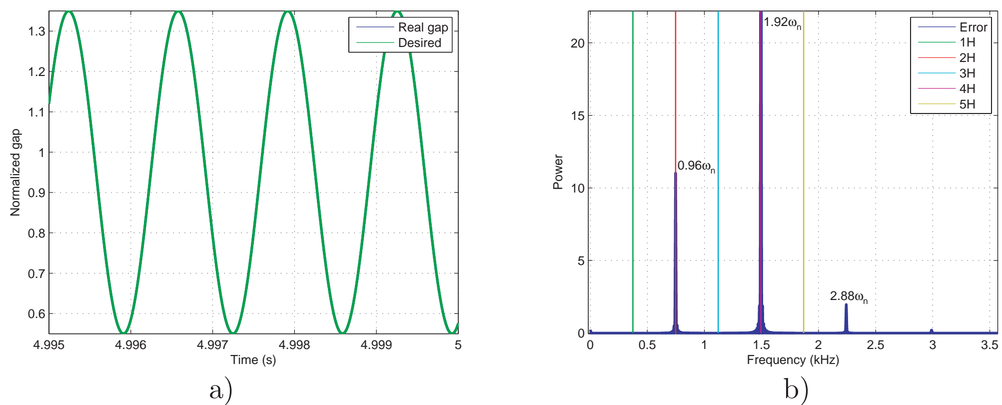

a) b)

Figure 7.7: Superharmonic oscillation of the MEMS resonator with frequency design fixed at $w_k = 0.48$, amplitude set-point fixed at 0.40 and fixed bias at 0.95. With damping at Q = 100. Desired set-point frequency fixed at $w_k = 0.96$. a) Stable oscillation output at $w_k = 0.96$. b) Power spectrum of the generated input voltage.

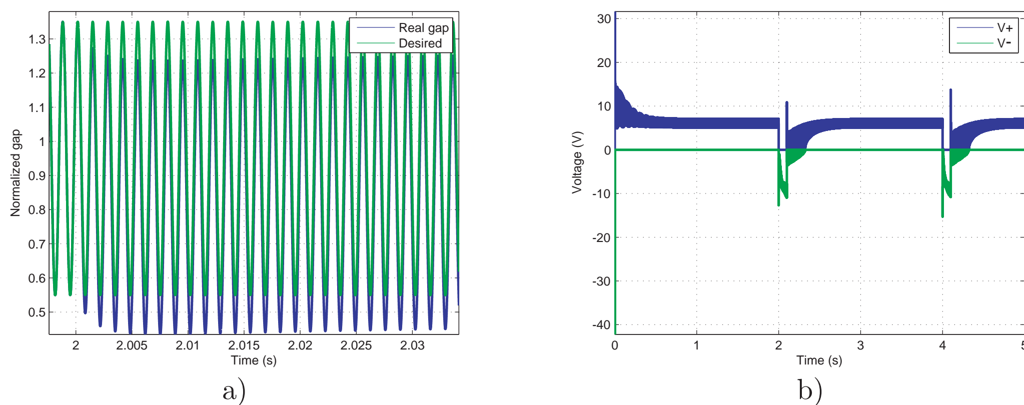

a) b)

Figure 7.8: Position shock performance when a 20% position displacement is created in the oscillation, with an amplitude set-point of 0.4, bias fixed at 0.95, normalized frequency at $w_k = 0.96$ and Q-factor at 100. a) Detail of the oscillation response. b) Controller generated voltage.

MEMS resonator.

The controller has also been tested with superharmonic and subharmonic driving schemes, to analyze its feasibility. In the case of subharmonic oscillation, the controller has been implemented with four harmonics at frequencies $1.92\omega_\mathrm{n}$, $2 \cdot 1.92\omega_\mathrm{n}$, $3 \cdot 1.92\omega_\mathrm{n}$, $4 \cdot 1.92\omega_\mathrm{n}$, while the set-point has been fixed at $0.96\omega_\mathrm{n}$. The choice of frequencies is based on Chapter 4 results. In this case, stable sinusoidal oscillation is achieved with small error but frequency component at the oscillation frequency appears at the input voltage, Figure 7.6, although the controller doesn't include a resonator at that frequency. This feature is related to the known capability of IMP-based controllers to perform better than its defined parameters [27]. In the case of superharmonic oscillation, the controller has been implemented with four harmonics at frequencies $0.48\omega_\mathrm{n}$, $2 \cdot 0.48\omega_\mathrm{n}$, $3 \cdot 0.48\omega_\mathrm{n}$, $4 \cdot 0.48\omega_\mathrm{n}$, while the set-point has been fixed at $0.96\omega_\mathrm{n}$. The choice of frequencies is based on Chapter 4 results. In this case, stable sinusoidal oscillation is achieved with small error and again driving voltage has frequency component in the oscillation frequency, Figure 7.7. This was expected as the controller has a resonator in the desired frequency. Consequently, the controller generates stable oscillation but superharmonic or subharmonic schemes are not possible, as the controller generates an input with all the frequencies to obtain a sinusoidal output, as indicated by the Harmonic Balance, even when the frequency is not explicitly included.

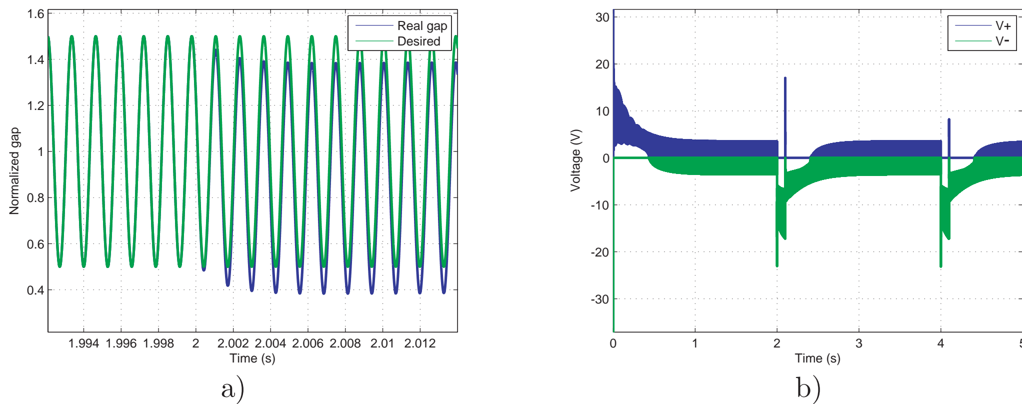

Figure 7.9: Position shock performance when a 20% position displacement is created in the oscillation, with an amplitude set-point of 0.5, bias fixed at 1.00, normalized frequency at $w_k = 1.00$ and Q-factor at 1000. a) Detail of the oscillation response when it suffers the shock. b) Generated voltage by the controller.

And finally, the controller stability has been tested against shock response. To analyze shock response, a 20% gap jump is simulated in the system with a duration of 0.1 seconds,

and the transient response of the system is analyzed. Figure 7.8 shows the oscillation evolution for a an amplitude set-point of 0.4, bias fixed at 0.95, normalized frequency at $w_k = 0.96$ and Q-factor at 100. The controller is able to handle the shock and drive back the system to desired oscillation. In this case, although one-sided actuation could be enough at steady-state oscillation, the shock response shows that two-sided actuation is important even in this cases, because the two-sided control capability allows the controller to work smoothly to drive the system back to unperturbed oscillation. In Figure 7.9 a similar case is presented for low damping operation. The simulation shows the oscillation evolution for a an amplitude set-point of 0.5, bias fixed at 1.00, normalized frequency at $w_k = 1.00$ and Q-factor at 10000. The controller is able to handle the shock and drive back the system to desired oscillation even in low damping conditions. In this case, two-sided actuation is already needed at steady-state oscillation.
As a conclusion, using the thesis controller, stable oscillation is achieved for any desired combinations of amplitude of oscillation, bias, Quality factor and frequency. Only oscillations reaching amplitudes larger than 80% gap size are forbidden, but this is an acceptable range for MEMS resonator amplitudes.

7.2.2 Robustness

As already discussed, robustness is necessary to handle the imperfections of MEMS fabrication techniques. Moreover, parameter variation with time and non-accounted nonlinearities add up to the uncertainty of the system. The design of the controller has been selected taking into account all possible parameter uncertainties and with large range of variation, to guarantee long-time stable actuation.
In order to test robustness of the controller a set of simulations has been generated that cover the majority of predictable uncertainties. The plots is Figure 7.10 show the sinus-like oscillations of the system with a set-point of amplitude 0.4, a bias of 0.95, normalized frequency of 0.96 and a design Quality factor of 100. The presented uncertainties cover the whole range of design uncertainties in frequency (ω_{n}), damping (Q), nonlinear spring (κ) and electrostatic force ($\mathrm{f}_k\mathrm{g}_k$). The linearization parameter (x_{10}) is fixed in all this simulations at $x_{10u} = 0.95x_{10}$. All the performed simulations show stable oscillations at the desired set-point, for all the different uncertainties. It is important to observe that for the same output oscillation, the controller is able to generate different voltage inputs to guarantee that the set-point is achieved depending on the system variation.

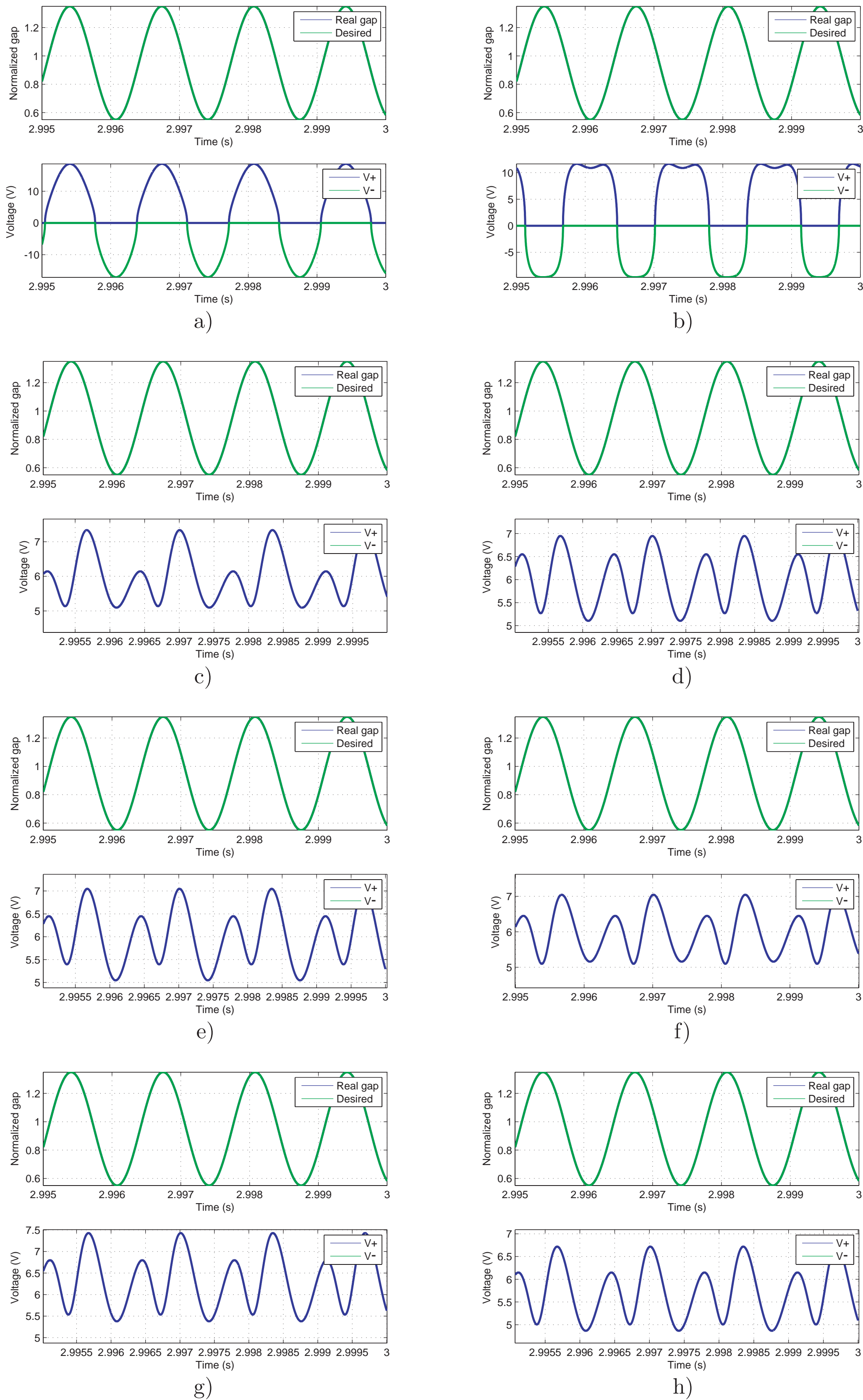

Figure 7.10: Oscillation performance of the MEMS resonator with 0.4 amplitude set-point and bias fixed at 0.95. Predicted damping fixed at Q = 100, and normalized frequency set-point at $w_k = 0.96$. The oscillations are presented with the following parameter variations: $x_{10u} = 0.95x_{10}$ and a) $\omega_u = 0.7\omega_{\rm n}$. b) $\omega_u = 1.3\omega_{\rm n}$. c) $\mathrm{Q}_u = 0.5\mathrm{Q} = 50$. d) $\mathrm{Q}_u = 1.5\mathrm{Q} = 150$. e) $\kappa_u = 0.7\kappa$. f) $\kappa_u = 1.3\kappa$. g) $(\mathrm{f}_k\mathrm{g}_k)_u = 0.9\mathrm{f}_k\mathrm{g}_k$. h) $(\mathrm{f}_k\mathrm{g}_k)_u = 1.1\mathrm{f}_k\mathrm{g}_k$.

This fact is important, as the controller don't generate a predefined voltage as the one calculated by the Harmonic Balance, but generates the needed voltage to adapt to the system uncertainty.
As identified in the sensitivity analysis, the natural frequency change is the one that has more effect on the system. The input voltage changes completely from the rest of voltage actuations when the natural frequency is varied from the nominal one. Moreover, it even forces two-sided actuation in front of one-sided actuation in the other cases. Increasing the Quality factor is the next parameter with clear influence, and the rest of uncertainties have minor effects on the input voltage.
As a conclusion, the controller presents robustness against the chosen existing uncertainties, allowing a large amount of parameter variation.

7.2.3 Sinus-like oscillation

Parallel-plate electrostatic actuators are often avoided in MEMS designs because they are extremely nonlinear and introduce a second order harmonic in the oscillation of the device if a sinusoidal voltage is used as driving force. However, as stated in Chapter 4, a pure harmonic oscillation can be achieved, if the right control action is provided. The proposed controller is able to generate the needed control action as predicted by Harmonic Balance to produce an almost perfect sinusoidal oscillation, and not only that, allowing to select any amplitude of oscillation, static bias, oscillation frequency and with any damping conditions.
Figure 7.11 shows that the selected frequency of the set-point has no influence in the performance of the controller. The presented oscillation has an amplitude set-point of 0.5, bias fixed at 1.00 and Q-factor at 100. With frequencies ranging from $0.8\omega_{\mathrm{n}}$ to ω_{n}, all oscillations have null error in the first four harmonics, and the fifth harmonic is at least eight orders of magnitudes lower than oscillation. It is interesting to note that the output has different higher harmonics for each set-point frequency, related to the complexity of the needed driving voltage, the number of harmonics it contains and its significance.
Similar analysis is performed in Figure 7.12, with set-point oscillation with an amplitude of 0.4, bias fixed at 0.95 and normalized frequency at 0.96. The variation of damping has no effect on the performance of the controller, obtaining almost identical output for both cases. All oscillations have null error in the first four harmonics, and the fifth harmonic is twelve orders of magnitudes lower than oscillation, leaving the actual oscillation close

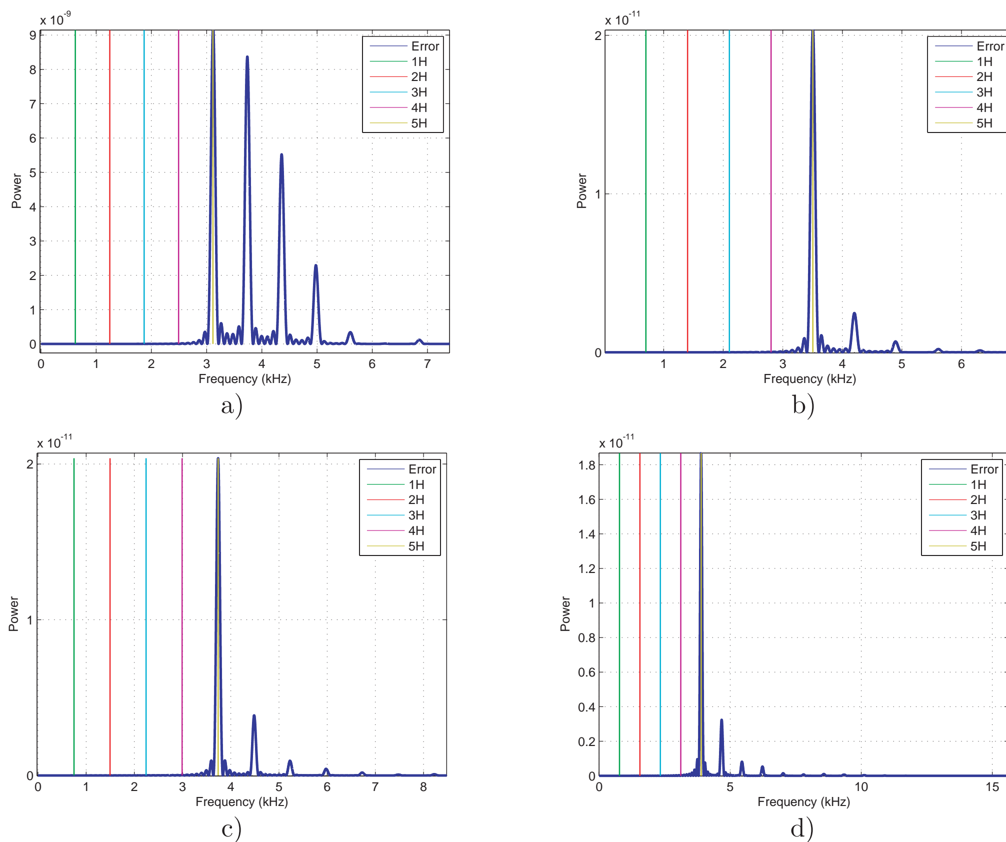

Figure 7.11: Analysis of frequency content of the output. The presented oscillation is with an amplitude set-point of 0.5, bias fixed at 1.00, normalized frequency varying and Q-factor at 100. a) $w_k = 0.80$. b) $w_k = 0.90$. c) $w_k = 0.96$. d) $w_k = 1.00$.

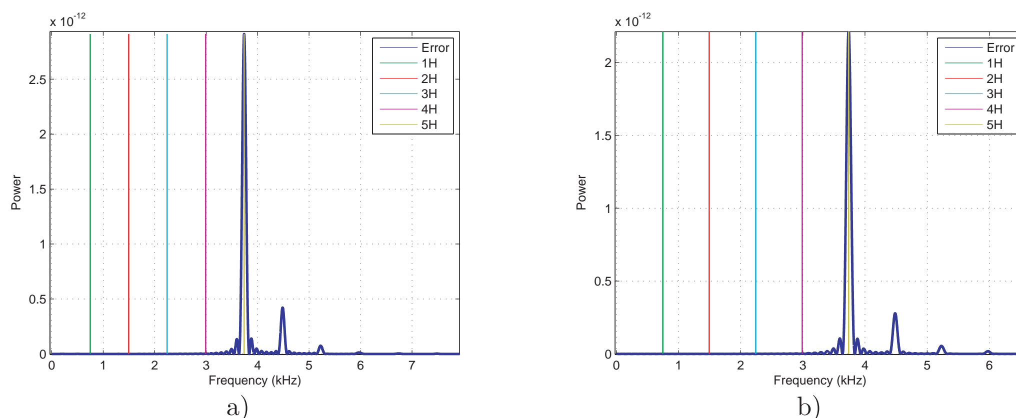

Figure 7.12: Analysis of frequency content of the output depending on Quality factor. The presented oscillation is with an amplitude set-point of 0.5, bias fixed at 1.00, normalized frequency $w_k = 0.96$ and varying Q-factor. a) Q = 1. b) Q = 1000.

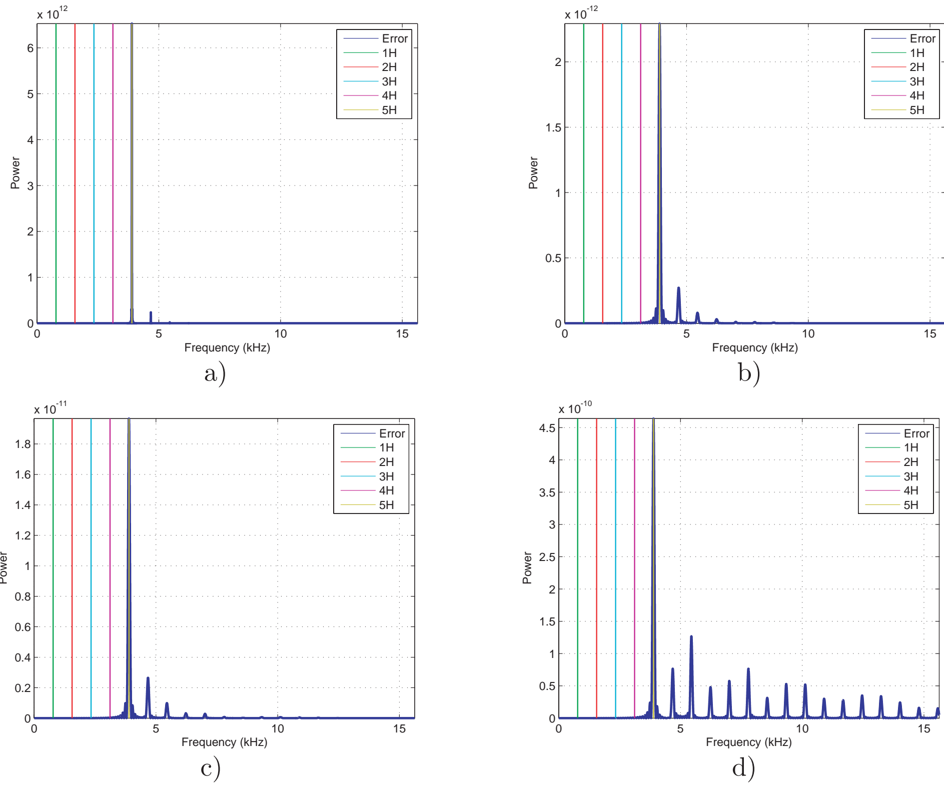

Figure 7.13: Analysis of frequency content of the output. The presented oscillation is with an with varying amplitude set-point, bias fixed at 0.95, normalized frequency $w_k = 1.00$ and Q-factor at 100. Amplitudes: a) 0.30. b) 0.40. c) 0.50. d) 0.70.

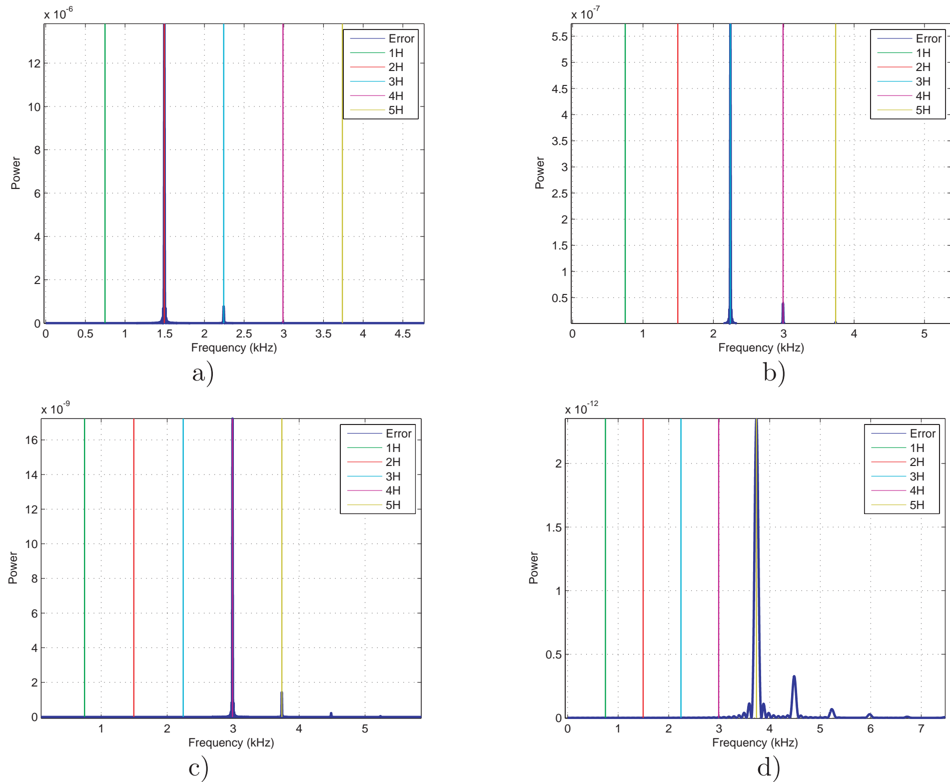

Figure 7.14: Analysis of frequency content of the output depending on the number of harmonics used in the controller. The presented oscillation is with an amplitude set-point of 0.5, bias fixed at 1.00, normalized frequency $w_k = 0.96$ and Q-factor at 100. a) Only first harmonic. b) Two harmonics included. c) Three harmonics included. d) Proposed controller with four harmonics.

to a pure sinusoidal.

In Figure 7.13, comparison of sinusoidal output depending on amplitude of oscillation is presented. In this case, set-point oscillation is chosen with bias fixed at 0.95, normalized frequency at 1.00 and Quality factor at 100. The amplitude selection again has no impact in the sinusoidal output of the MEMS resonator, as the controller behaves identically in all cases. The first four harmonics are almost null in all four examples, and fifth harmonic is more than ten times smaller than oscillation.

Finally, Figure 7.14 presents the effect of using less harmonics in the Resonant Controller. As can be seen, the inclusion of each harmonic in the controller eliminates its matching frequency in the output error. Then, depending on the desired output, the number of harmonics can be chosen. For an almost pure sinus-like oscillation, four harmonics guarantee that error is ten times smaller than oscillation magnitude.

7.2.4 Minimum energy

Energy consumption minimization is basic for stand-alone devices, or for sensors for mobile applications. As MEMS sensors have inherent uncertainties and aging contributes to these uncertainties, it is vital to guarantee that the MEMS resonator works at the most energy efficient frequency. This frequency is the resonance frequency in linear mechanical models. However, in nonlinear systems electrostatically actuated, this resonance frequency doesn't explicitly exists. A resonant-like frequency is obtained via testing, but changes in driving scheme or environmental factors can make it change. The extremum seeking loop overcomes these difficulties.

As presented in Chapter 6, the *Cost function* provides the energy consumption estimate for the whole range of working frequencies, Figure 7.15, allowing to implement a real-time minimum search algorithm. In order to verify the effectiveness of the energy minimization, long time simulations have been performed to analyze the convergence of the system to its minimum. At the same time, the effects of the seeking perturbation on the system are also studied.

Figure 7.16 shows the energy evolution of the system when an initial normalized frequency of 0.965 is selected. The system is oscillated with amplitude set-point of 0.4, bias fixed at 0.95 and Q-factor at 100. As is shown in Figure 7.15, the minimum of the energy is around 0.968, and the evolution of the input frequency in Figure 7.16b shows how the ESC scheme drives the value to its minimum. In the evolution in Figure 7.16a, the

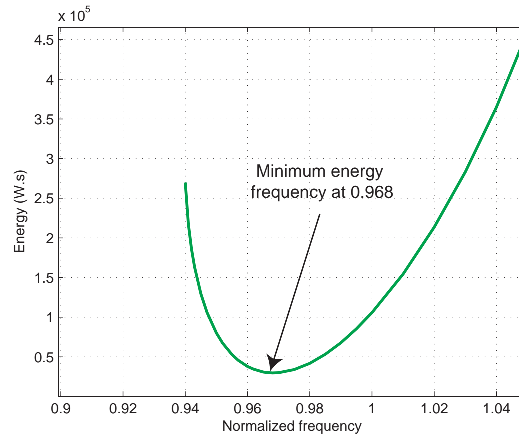

Figure 7.15: Energy profile for the presented example, with an oscillation with an amplitude set-point of 0.4, bias fixed at 0.95 and Q-factor at 100. The profile has its minimum at the normalized frequency $w_k = 0.968$

---

calculated cost function, an estimate of the consumed energy, decreases continuously to the optimum. In Figure 7.16b, the input frequency smoothly evolves from 0.965 in search of the minimum at 0.968. The gains of the perturbation and controller are small in order to avoid interfering with the rest of the controller, that is the reason why the evolution is so slow. However, that is not a problem, because as the frequency gets close to the optimum the energy consumption variation is small, consequently no large energy reductions are gained. When the system is far away from the optimum the controller works quicker, but when the optimum is close, the reaction is slow. This behavior is given by the use of the gradient.

Details of the evolution of all the ESC steps are also presented. Figure 7.16c presents the high-pass filtered cost function and Figure 7.16d shows this value once it has been demodulated with the seeking perturbation. Then, the gradient estimate is obtained via low-pass filtering, Figure 7.16e. Finally, the gradient estimate is scaled, Figure 7.16f, and integrated to produce the ESC optimum frequency estimate, Figure 7.16g. This value is added to the perturbation, Figure 7.16h, to generate the input frequency to the controller in Figure 7.16b.

Figure 7.17 shows similar energy evolution of the system for the same desired oscillation when the initial normalized frequency is 0.97, at the other side of the optimum. As is shown in Figure 7.16b, the ESC again drives the frequency again to its minimum. All the ESC steps are again presented.

The ESC controller has time scales separation, as can be seen in Figure 7.18. The plots

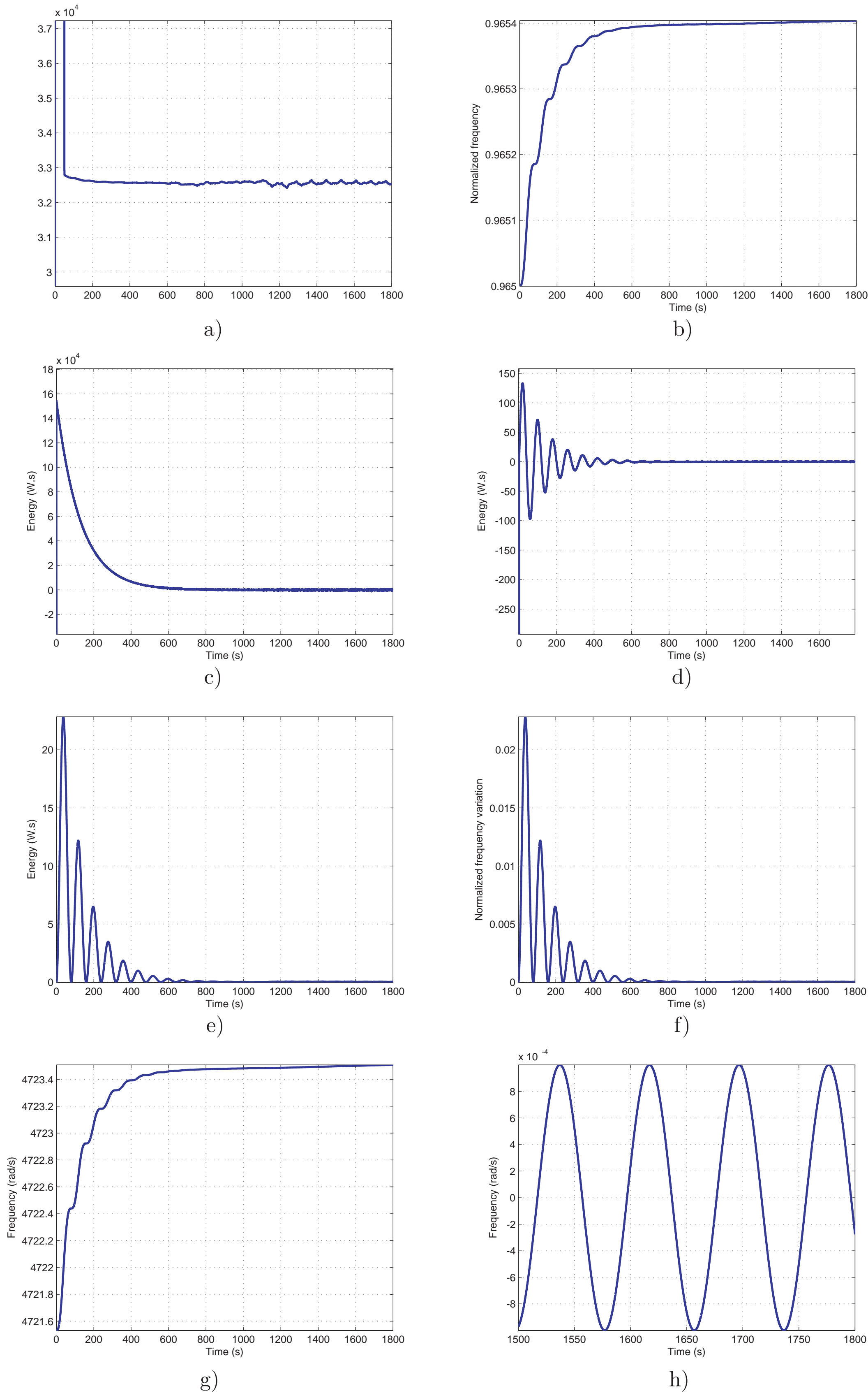

Figure 7.16: ESC controller performance for an oscillation with an amplitude of 0.4, bias fixed at 0.95, initial frequency at $w_k = 0.965$ and Q-factor at 100. a) Energy evolution. b) Applied set-point frequency. c) High-pass filtered energy. d) Demodulated energy. e) Gradient estimate. f) Scaled gradient to modify the frequency set-point. g) Controller optimum frequency estimate. h) Close-up of perturbation.

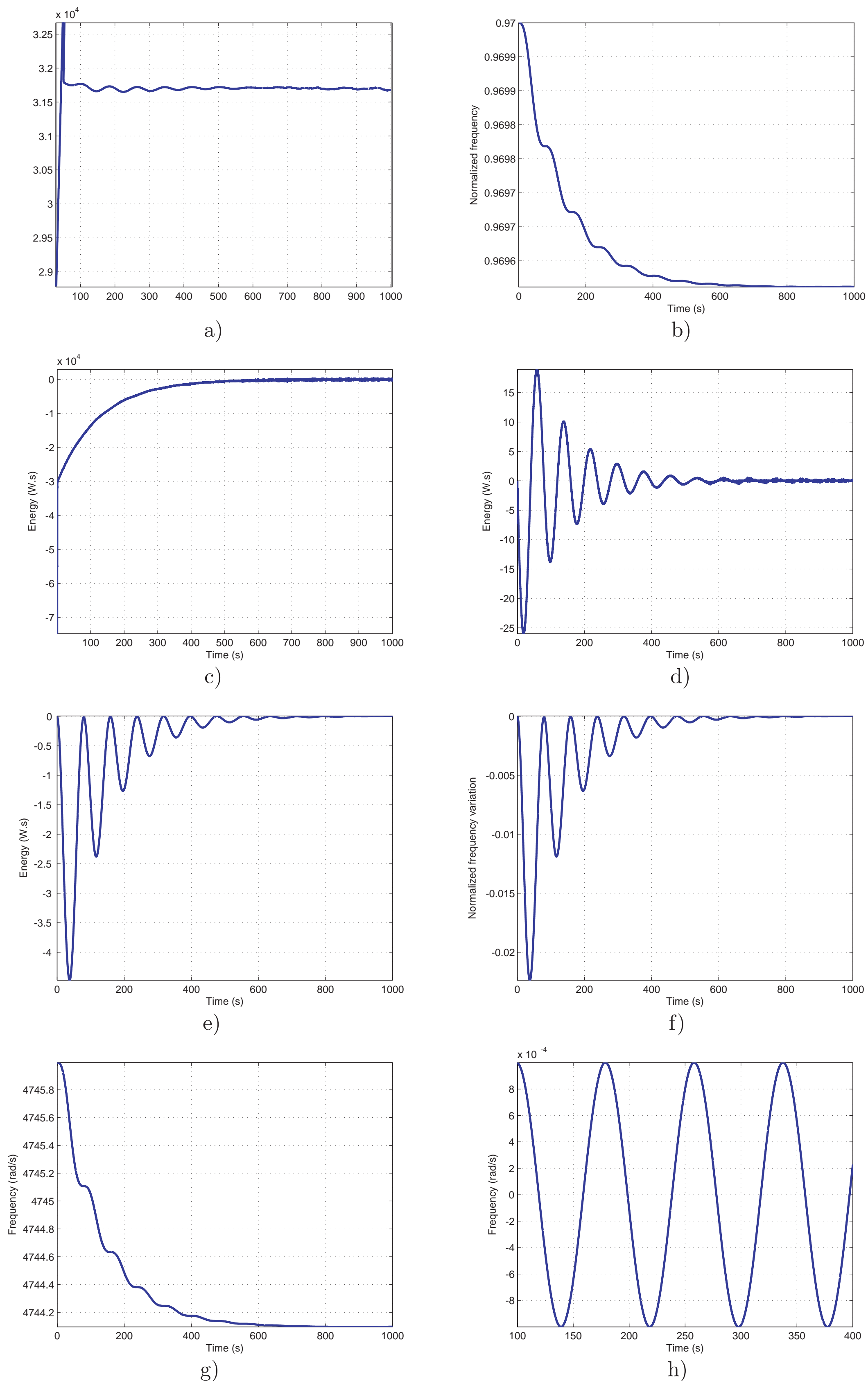

Figure 7.17: ESC controller performance for an oscillation with an amplitude set-point of 0.4, bias fixed at 0.95, initial frequency at $w_k = 0.97$ and Q-factor at 100. a) Energy evolution. b) Applied set-point frequency. c) High-pass filtered energy. d) Demodulated energy. e) Gradient estimate. f) Scaled gradient to modify the frequency set-point. g) Controller optimum frequency estimate. h) Close-up of perturbation.

show a close up of the evolution in Figure 7.16 at time 500 seconds. The oscillation is almost a perfect sinusoidal, Figure 7.18a, like the reference, while the input frequency is continuously changing as can be seen in Figure 7.18b. However, the change is slow enough to not interfere with the MEMS resonator oscillation. Figure 7.18c shows that the input voltage is stable and doesn't show any effect of the ESC perturbation or the frequency seeking. Figure 7.18d shows the descending evolution of the cost function.

The only drawback of the slow evolution is that as the frequency variation is decreased, the cost function calculation becomes more jittery due to simulation limitations, but that wouldn't affect in a real device. The sharp variations in the voltage generate large current variations, and this behavior makes it difficult to evaluate with precision the energy consumed in one cycle, Figure 7.18d, but this not interfere with the optimum search.

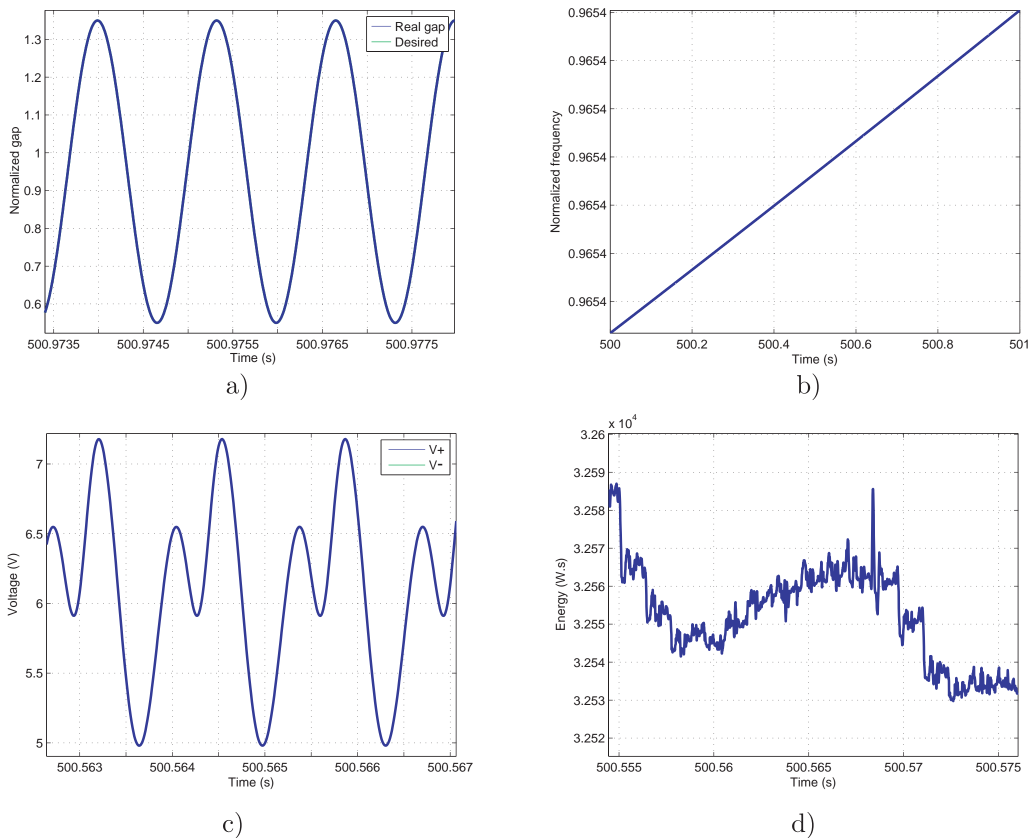

Figure 7.18: Detail of the behavior of the MEMS resonator under ESC controller. It is a close-up of the simulation in Figure 7.16 at time 500 s. a) Normalized oscillation. b) Frequency input. c) Voltage input. d) Cost function.

7.2.5 Conclusion

Simulations show that the controller fulfils the four goals that had been established in Chapter 5 for the controller. Stable robust pure-sinusoidal oscillations with minimum energy consumption can be achieved, and the controller is able to handle large uncertainties without affecting the desired output. Moreover, the adaptation provided by the extremum seeking guarantees low energy without interfering with the oscillation and performance of the system.

From simulations it is identified that the controller in most cases outperforms its working range. That can be seen in Figure 7.6, where it is able to generate a perfect sinus without including the first harmonic as a resonator in the controller in the loop, or in Figure 7.19, where the simulated uncertainties are well beyond the controller design.

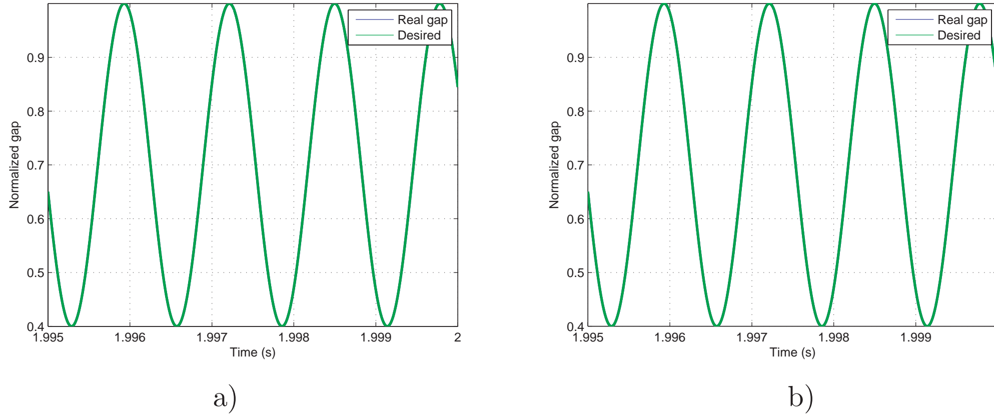

Figure 7.19: Controller performance for an oscillation with an amplitude set-point of 0.3, bias fixed at 0.7, initial normalized frequency at $w_k = 1.00$ and Q-factor at 100. a) The bias is fixed at $0.7\mathrm{g}_0$, well beyond the 20% uncertainty in $x_{10} = \mathrm{g}_0$. b) In this simulation, apart from the bias, the following parameters have been changed without affecting system performance: $\omega_u = 0.6\omega_\mathrm{n}$, $\mathrm{Q}_u = 3\mathrm{Q} = 300$, $\kappa_u = 1.5\kappa$ and $(\mathrm{f}_k\mathrm{g}_k)_u = 1.2\mathrm{f}_k\mathrm{g}_k$.

7.3 Improvement of MEMS drive and sense for control applications

In order to implement the proposed control strategy, two main issues appear.

The first issue is outlined in Chapter 4, and it has appeared again in the controller implementation in Chapter 6. It involves the fact that a closed form for the ideal actuation only exists if the square voltage is used as the control action. But calculations lead to negative V^2 control actions that cannot be directly converted to driving voltages.

The second issue is related to the position feedback that is needed to generate the control action. Typical implementations in the literature don't take into account the need of actual real position with all the existing harmonics in order to be fed back. Consequently, a position readout strategy must be implemented.

7.3.1 Full range oscillation

7.3.1.1 One-sided actuation

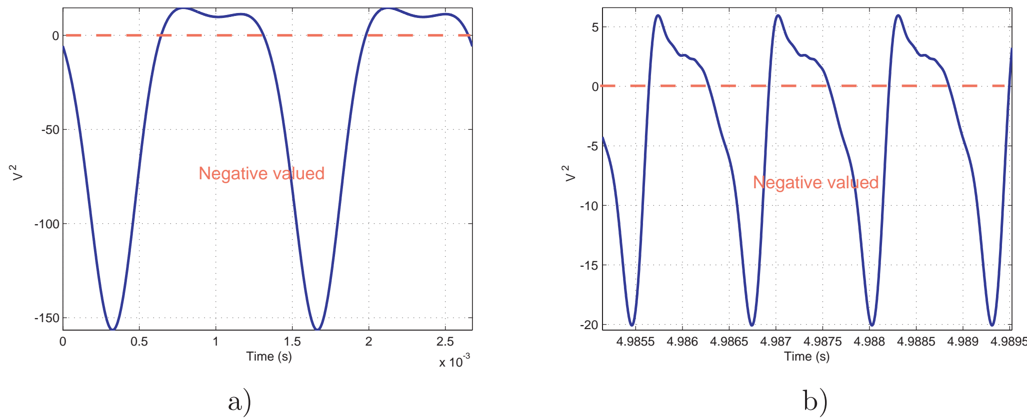

Figure 7.20: a) Example of V^2 Harmonic Balance calculation with negative values for an amplitude of oscillation of 0.6 and no static bias, Quality factor 100 and normalized frequency $w_k = 0.96$. b) Example of V^2 generated by proposed controller with negative values, for an amplitude of oscillation of 0.5 and no static bias, Quality factor 100 and normalized frequency $w_k = 1$.

The whole control strategy is based on choosing the V^2 driving action. Harmonic Balance Analysis and the control study show that this driving selection simplifies the control architecture. However, the selected control scheme can produce V^2 driving actions with negative component, see examples in Figure 7.20.

If the MEMS resonator uses one-sided actuation, Figure 7.21, the voltage driving signal (V) can only be generated by performing a square-root of the V^2 signal. In those cases where V^2 is negative valued, it means that the driving signal cannot be generated.

An option could be truncating the V^2 signal to zero for the negative valued part, but the results are not satisfactory, as the desired oscillation is not achieved.

Consequently, with one-sided actuation, as stated in Chapter 4, there exists desired oscillation areas that are not reachable. In actual implementations that leads to delimit the working zone to reachable areas, and avoid those that cannot be reached. This could be applicable for pre-set actuation, but it is not a choice in real-time closed loop controllers.

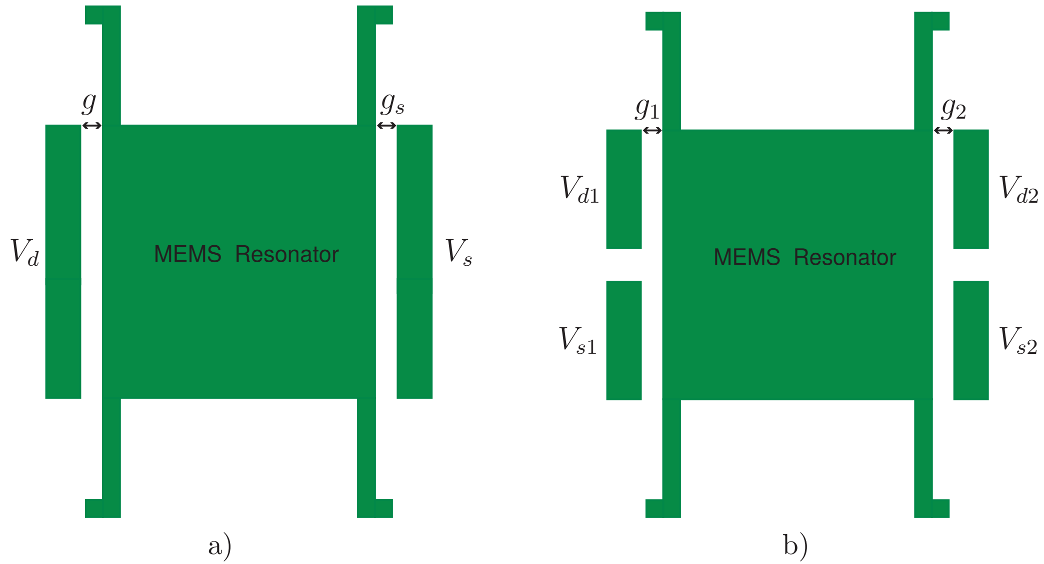

Figure 7.21: a) Schematic MEMS resonator with one driving port (V_d) and one sensing port (V_s). b) Schematic MEMS resonator with two driving ports (V_{d1} and V_{d2}) and two sensing ports (V_{s1} and V_{s2}).

Figure 7.22a shows that even in those cases where the steady-state actuation doesn't need negative-valued V^2 actuation, it can be needed in the transient to control the evolution.

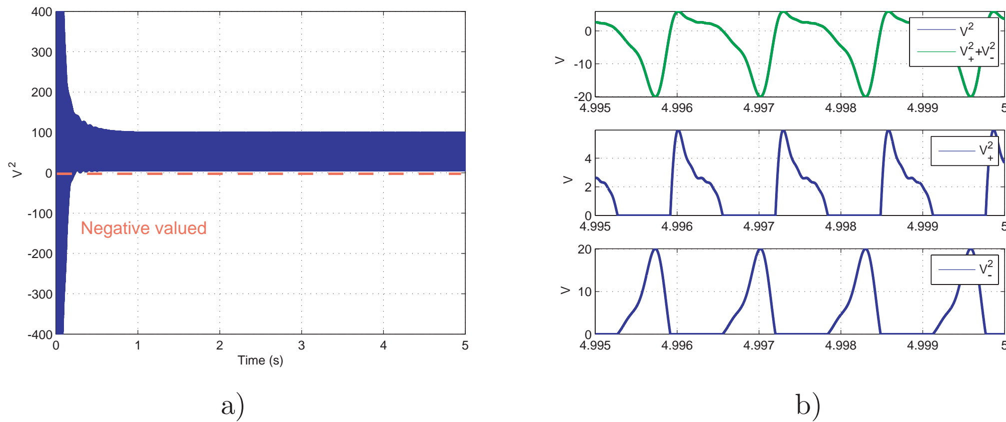

Figure 7.22: a) Example of V^2 generated by proposed controller with negative values in the transient but positive-valued in steady-state, for an amplitude of oscillation of 0.7 and static bias of 0.95, Quality factor 100 and normalized frequency $w_k = 1$. b) Decomposition of V^2 signal in V_+^2 and V_-^2 components.

7.3.1.2 Double-sided actuation

A new approach is presented to overcome the limitation of one-sided actuation. The approach is based on understanding the force that must be generated by the V^2 action, instead of trying to generate the needed voltage. The desired actuation has the following

form:

$$F = \frac{\mathrm{f}_k \mathrm{g}_k}{g^2} V^2. \tag{7.1}$$

If the device, instead of being actuated just by one side as Figure 7.21a, is actuated by two opposite sides, Figure 7.21b, the total force can be reproduced. Consequently, it is needed to have a two-sided actuator in the MEMS device to overcome the problem, splitting the needed voltage between the actuators and generating the desired driving force into the MEMS resonator.

Assume that the V^2 driving force is divided in V_+^2, its positive part, and V_-^2, its absolute value negative part, Figure 7.22b.

$$V^2 = V_+^2 - V_-^2$$

Assume that V_{d1} is applied to one side and V_{d2} to the other side, and that the gap for each actuator is $g_1 = g$ and $g_2 = 2 - g$. Then, the desired force is divided between actuators in the following way:

$$\frac{\mathrm{f}_k \mathrm{g}_k}{g^2} V^2 = \frac{\mathrm{f}_k \mathrm{g}_k}{g_1^2} V_{d1}^2 - \frac{\mathrm{f}_k \mathrm{g}_k}{g_2^2} V_{d2}^2. \tag{7.2}$$

The negative signs appears because the two generated forces are in opposed directions. So, the key is choosing the right V_{d1} and V_{d2} actuation. If we choose

$$V_{d1} = \sqrt{V_+^2} \tag{7.3}$$

$$V_{d2} = \frac{g_2 \sqrt{V_-^2}}{g_1} = \frac{(2-g)\sqrt{V_-^2}}{g} \tag{7.4}$$

the generated force over the MEMS resonator with the two-sided actuation is the desired one

$$\begin{aligned} \frac{\mathrm{f}_k \mathrm{g}_k}{g^2} V^2 &= \frac{\mathrm{f}_k \mathrm{g}_k}{g^2} \sqrt{V_+^2}^2 - \frac{\mathrm{f}_k \mathrm{g}_k}{(2-g)^2} \left(\frac{(2-g)\sqrt{V_-^2}}{g} \right)^2 \\ &= \frac{\mathrm{f}_k \mathrm{g}_k}{g^2} V_+^2 - \frac{\mathrm{f}_k \mathrm{g}_k}{g^2} V_-^2 \\ &= \frac{\mathrm{f}_k \mathrm{g}_k}{g^2} (V_+^2 - V_-^2). \end{aligned} \tag{7.5}$$

This approach has been successfully tested in the simulations, as can be seen in Figure 7.23.

As a conclusion, the new drive approach overcomes the limitations of the one-sided actuation. Two-sided actuation with separated voltage action to each electrode allows to oscillate any MEMS resonator at any desired amplitude and bias, within physical

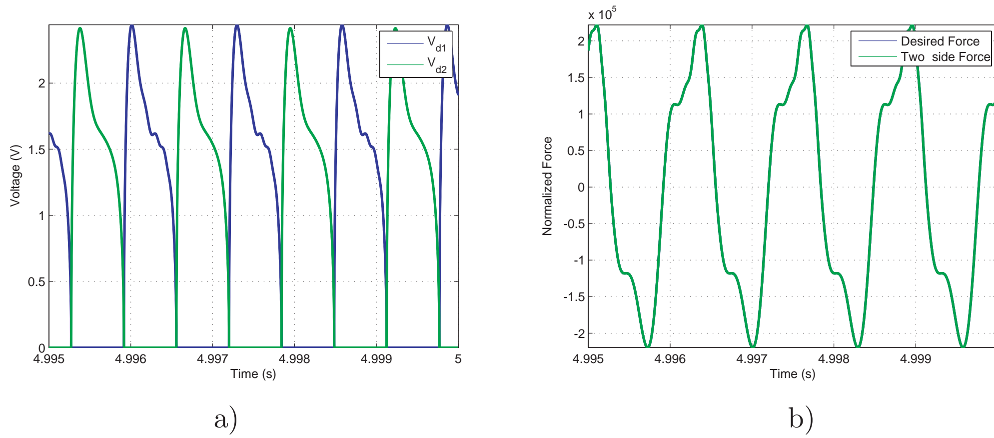

Figure 7.23: a) New voltages for the two opposite ports (V_{d1} and V_{d2}). b) Comparison of desired force and force applied with two-side actuator.

constrains. Moreover, two-sided actuation is necessary to design controllers that can work smoothly to control the stable oscillation of the MEMS resonators.

This approach has been used and verified in all the simulations where negative-valued V^2 voltage was needed through the dissertation.

7.3.2 Full position feedback

The proposed controller design relies on real position feedback to generate the control action. Position feedback is not a new issue in MEMS. Several approaches try to obtain position parameters on-line to fed them back to the controller. In Phase-lock-loop controllers, frequency or phase is extracted. In AGC controllers amplitude of oscillation is extracted. And in some cases, more parameters are obtained, as is the case in gyroscopes. However, all tested approaches that could apply to the proposed MEMS resonator only obtain information of one harmonic, the one that is considered more significant: main harmonic in most cases, but examples of second harmonic is detected in subharmonic oscillation and other cases can be found in parametric oscillation.

Complete position oscillation output, without high harmonics filtering, is not an usual feedback variable in existing approaches. Only cases where complete position information is obtained is in out-of-plane MEMS resonators, where laser interferometry can be used to analyze the position. However, the technology cannot work in a real-time loop, as position and harmonics are extracted via post-processing.

Examples of implementation of optical interferometry on-chip exist, but they haven't been fully developed, only experimentally. In [90], adaptive control approach to solve

uncertainties and faulty conditions is done with optical position feedback. An in [173], the optical signal is used for on-chip system characterization. But both implementations don't generate the needed feedback.

The best applicable approach to robust extraction of position is done in [198] using electrostatic sensing. The approach is adapted on this section to fulfill the thesis needs and produce full position readout.

7.3.2.1 Electrostatic sensing basics

To measure displacement using electrostatics, motional current is usually read. As capacitance changes due to the movement of the MEMS resonator, charge flows and current is generated:

$$Q_s(t) = \mathrm{C}_s(t)\, V_s \tag{7.6}$$

$$I_s(t) = \frac{d(\mathrm{C}_s(t)\, V_s)}{dt}\,, \tag{7.7}$$

being $Q_s(t)$ the charge stored in the capacitor, $\mathrm{C}_s(t)$ the sense capacitance, V_s the fixed voltage applied across the capacitor and $I_s(t)$ the motional sensed current. Two kind of

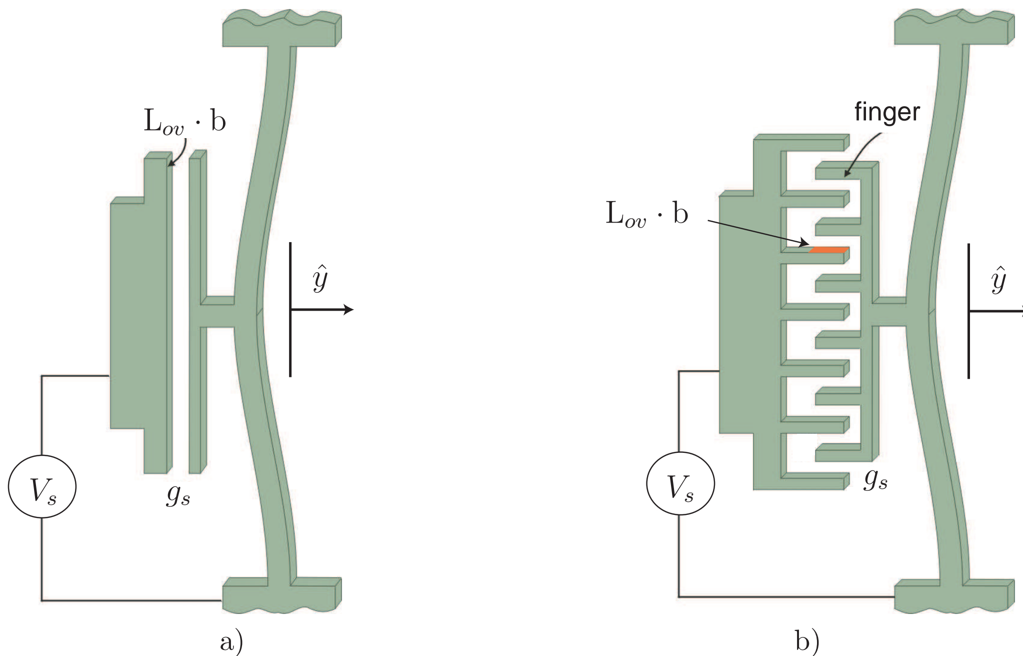

Figure 7.24: Electrostatic sensing techniques. a) Parallel-plate capacitor. b) Lateral comb capacitor.

sensing capacitors can be used. In parallel plate capacitors, Figure 7.24a, capacitance variation is generated while the capacitor plates move one against the other. In lateral

comb capacitors, Figure 7.24b, capacitance variation is generated by the displacement of one plate in parallel to the other plate, producing change in the overlap of the plates. Taking this scheme into account, the parallel-plate capacitor sensing capacitance is

$$\mathrm{C}_s(t) = \frac{\varepsilon\,\mathrm{b}\,\mathrm{L}_{ov}\,\mathrm{N}_p}{(\mathrm{g}_s + \hat{y}(t))^2} = \mathrm{C}_{snp}\,\frac{1}{\left(1 + \frac{\hat{y}(t)}{\mathrm{g}_s}\right)^2} \tag{7.8}$$

where $\mathrm{C}_{snp} = \frac{\varepsilon\,\mathrm{b}\,\mathrm{L}_{ov}\,\mathrm{N}_p}{\mathrm{g}_s^2}$, ε is the dielectric constant, b is the MEMS resonator width, L_{ov} is the overlap length, N_p is the number of sensing parallel plates in the MEMS resonator, g_s is gap distance between the capacitor plates and $\hat{y}(t)$ is the movement of the MEMS resonator. The sign of the movement of the MEMS resonator is assumed to be positive for the actuator (plates approach) and negative for the sensor (plates separate). If the motion is sensed with lateral combs instead, [138], the sensing capacitance is:

$$\mathrm{C}_s(t) = \frac{\varepsilon\,\mathrm{b}\,\mathrm{N}_l\,(\mathrm{L}_{ov} - \hat{y}(t))}{\mathrm{g}_s} = \mathrm{C}_{snl}\left(1 - \frac{\hat{y}(t)}{\mathrm{L}_{ov}}\right) \tag{7.9}$$

where $\mathrm{C}_{snl} = \frac{\varepsilon\,\mathrm{b}\,\mathrm{N}_l\,\mathrm{L}_{ov}}{\mathrm{g}_s}$ and N_l as the number of lateral comb fingers pairs.
If the voltage across the sensing capacitor (V_s) is assumed constant, the motional current is

$$I_s(t) = \frac{d\mathrm{C}_s(t)}{dt} V_s = V_s\,\mathrm{C}_{snp}\,\frac{-2}{\mathrm{g}_s\left(1 + \frac{\hat{y}(t)}{\mathrm{g}_s}\right)^3}\,\frac{d\hat{y}(t)}{dt} \tag{7.10}$$

for the parallel plate case, and

$$I_s(t) = \frac{d\mathrm{C}_s(t)}{dt} V_s = -\frac{V_s\,\mathrm{C}_{snl}}{\mathrm{L}_{ov}}\,\frac{d\hat{y}(t)}{dt} \tag{7.11}$$

for the lateral comb case. In both cases, the sensed current is proportional to the velocity of the MEMS resonator. However, in the lateral comb capacitors the relationship is linear, and in the parallel plate capacitors is nonlinear on the position. For this reason, lateral comb capacitors are preferred when can be used. And parallel-plates are limited to small oscillations where the nonlinear term can be approximated to be 1.
Usually, this current is extracted using a transimpedance amplifier, Figure 7.25, and in that case the output voltage is

$$V_{out}(t) = -\mathrm{R}_{amp}\,I_s(t) \tag{7.12}$$

being R_{amp} the resistance used in the transimpedance amplifier set-up.
This sensing approach is theoretically ideal for velocity feedback, but real application is influenced by parasitics. When using electrostatics as sensing technology, parasitics

must be taken into account, as parasitic capacitances can be even higher than the sensing capacitance. Figure 7.25 shows a typical sensing scheme with parasitics. The problem with parasitics is that the driving voltage is fed through to the sensing port, masking the desired position output, as they share the same frequency.

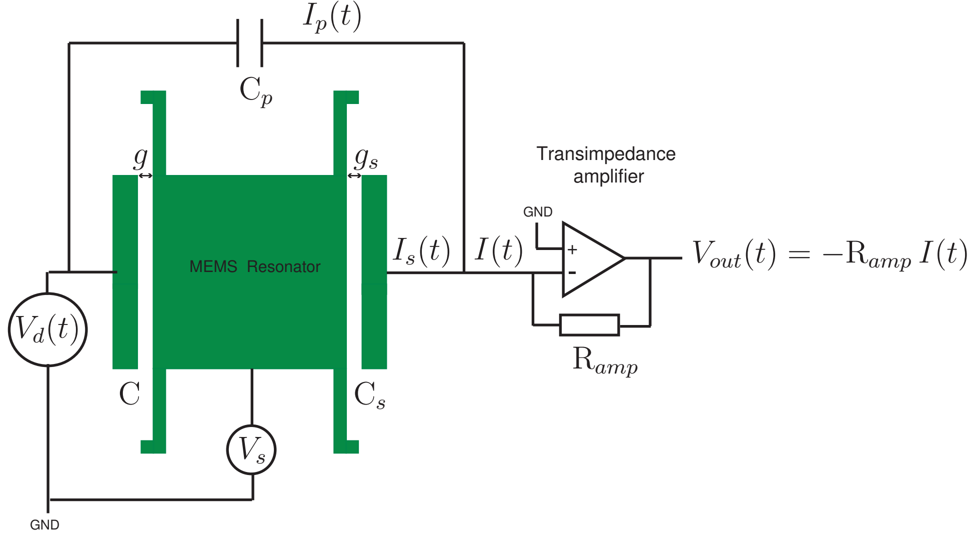

Figure 7.25: Device with parasitics and transimpedance amplifier voltage pick-up.

Consequently, Equation (7.6) must be corrected adding the parasitics term

$$I(t) = I_s(t) + I_p(t) = \frac{d(C_s(t)V_s)}{dt} + C_p \frac{dV_d(t)}{dt} \tag{7.13}$$

where C_p is the parasitics capacitance between the input port of the MEMS resonator and the output port of the MEMS resonator, and $V_d(t)$ is the MEMS driving voltage. To be able to use this current output, the parasitics must be minimized either by decreasing the parasitics capacitance or the driving voltage. The parasitics capacitance can be reduced improving fabrication techniques, the materials used or separating as much as possible input and output ports. And the driving voltage is usually decreased by oscillating the MEMS resonators in vacuum. Vacuum sealing of the devices reduces the damping of the system, allowing to drive the MEMS resonators with low voltages, while keeping high voltages for the sensing part.

7.3.2.2 Electromechanical Amplitude Modulation standard approach

To solve the parasitics issue, different signal processing techniques are used in the literature. Between them, Electromechanical Amplitude Modulation (EAM) is the reference in robust extraction of position in electrostatically actuated MEMS [138], [198],

[202], [199]. In these works, EAM is presented, developed and tested for electrostatic lateral combs and for electrostatic parallel-plate combs.

EAM allows frequency-domain separation of the position signal from the parasitics signal, using a high frequency carrier signal. The standard EAM set-up is shown in Figure 7.26.

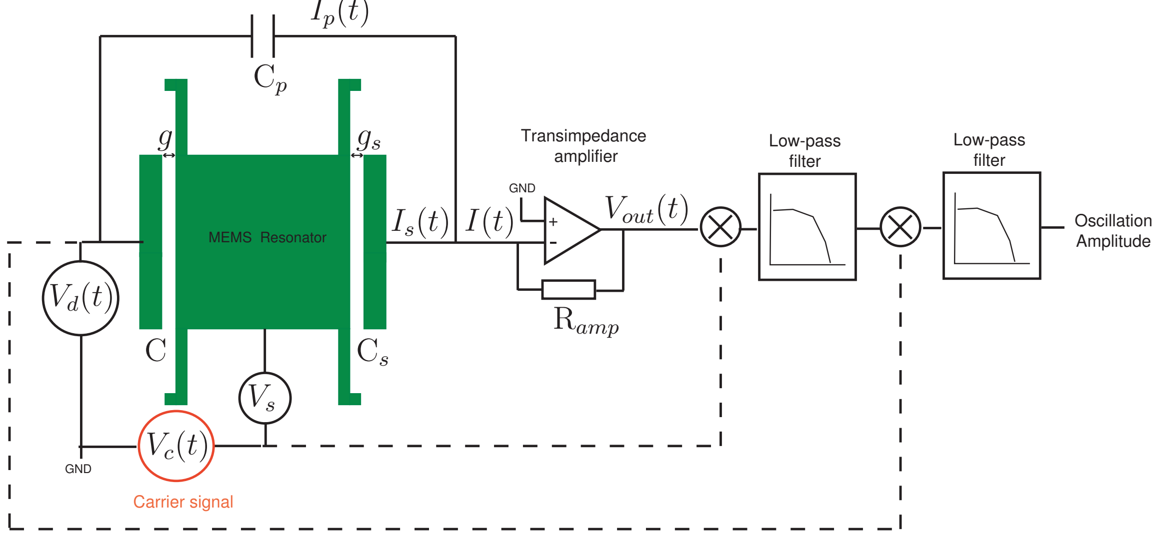

Figure 7.26: EAM output signal extraction set-up.

If we assume that the MEMS resonator is oscillated sinusoidally at driving frequency

$$\hat{y}(t) = \hat{Y}_1 \sin(\omega_d t + \phi_d) \tag{7.14}$$

given driving and carrier voltages as follows

$$V_d(t) = V_d \sin(\omega_d t) \tag{7.15}$$

$$V_c(t) = V_c \sin(\omega_c t) \tag{7.16}$$

the new sensed current is

$$\begin{aligned} I(t) &= I_s(t) + I_p(t) \\ &= \frac{d(\mathrm{C}_s(t)\,(V_s + V_c(t)))}{dt} + \mathrm{C}_p \frac{dV_d(t)}{dt} \\ &= \frac{d\mathrm{C}_s(t)}{dt}\,(V_s + V_c(t)) + \mathrm{C}_s(t)\frac{dV_c(t)}{dt} + \mathrm{C}_p \frac{dV_d(t)}{dt}. \end{aligned} \tag{7.17}$$

In the case of lateral comb sensing, the capacitance is defined on (7.9), and then the output of the system is

$$\begin{aligned} I(t) = &-\mathrm{C}_{snl}\,\check{Y}_1\,V_s\,\omega_d \cos(\omega_d t + \phi_d) - \mathrm{C}_{snl}\,\check{Y}_1\,V_c\,\omega_d \cos(\omega_d t + \phi_d)\sin(\omega_c t) \\ &+ \mathrm{C}_{snl}\,V_c\,\omega_c \cos(\omega_c t) - \mathrm{C}_{snl}\,\check{Y}_1\,V_c\,\omega_c \sin(\omega_d t + \phi_d)\cos(\omega_c t) + \mathrm{C}_p\,V_d\,\omega_d \cos(\omega_d t) \end{aligned} \tag{7.18}$$

where $\check{Y}_1 = \frac{\hat{Y}_1}{\mathrm{L}_{ov}}$ is the normalized comb movement. Rearranging terms, four frequencies are observed in the power spectrum of the extracted current, Figure 7.27

$$\begin{aligned} I(t) = -V_s\,\mathrm{C}_{snl}\,\check{Y}_1\,\omega_d\,\cos(\omega_d\,t + \,\phi_d) + \mathrm{C}_p\,V_d\,\omega_d\cos(\omega_d\,t) \\ + \mathrm{C}_{snl}V_c\,\omega_c\cos(\omega_c\,t) \\ - \frac{1}{2}\,\mathrm{C}_{snl}\,\check{Y}_1\,V_c(\omega_c + \omega_d)\sin((\omega_c + \omega_d)t + \,\phi_d) \\ + \frac{1}{2}\,\mathrm{C}_{snl}\,\check{Y}_1\,V_c(\omega_c - \omega_d)\sin((\omega_c - \omega_d)t - \,\phi_d). \end{aligned} \tag{7.19}$$

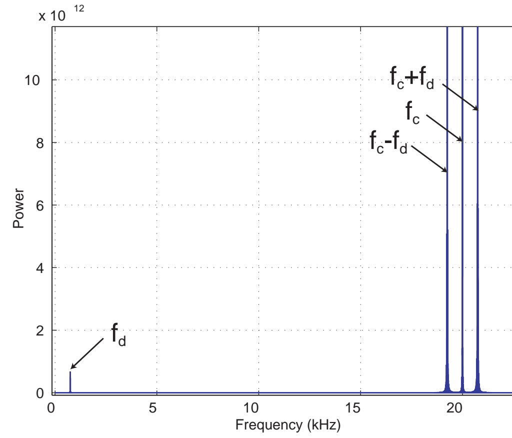

Figure 7.27: Power spectrum of the output voltage with identification of the four frequencies that appear due to electromechanical modulation.

Once the output voltage is obtained through a transimpedance amplifier, the position is extracted with four steps:

1. Mixing of the output voltage with the carrier signal to map the side-bands back to driving frequency: $V(t) \otimes V_c \sin(\omega_c t)$. The mixing or signal multiplying operation is identified with the $\otimes$ operator.

2. Low-pass filtering of the resulting signal to attenuate frequencies higher than drive frequency.

3. Mixing of the resulting voltage with drive signal to map the oscillation into oscillation amplitude: $V(t) \otimes V_d \sin(\omega_d t)$.

4. Low-pass filtering of the final signal to extract DC signal proportional to amplitude of oscillation.

In Figure 7.26 the procedure is outlined. This set-up can be implemented with two high-precision lock-in amplifiers in series, each one implementing one mixing step and its low-pass filtering [146].

Improved demodulation procedure with parallel-plate capacitors is as shown in [202]. Although the current is more complex, as infinite side-bands appear for each oscillation frequency, the proposed amplitude extraction is more robust than the linear one. The procedure is based in parallel demodulation of two side-bands to extract amplitude from their ratio.

7.3.2.3 EAM for full position extraction

In order to be used as position feedback for the thesis controller, the presented EAM procedure can be modified for full position extraction, Figure 7.28.

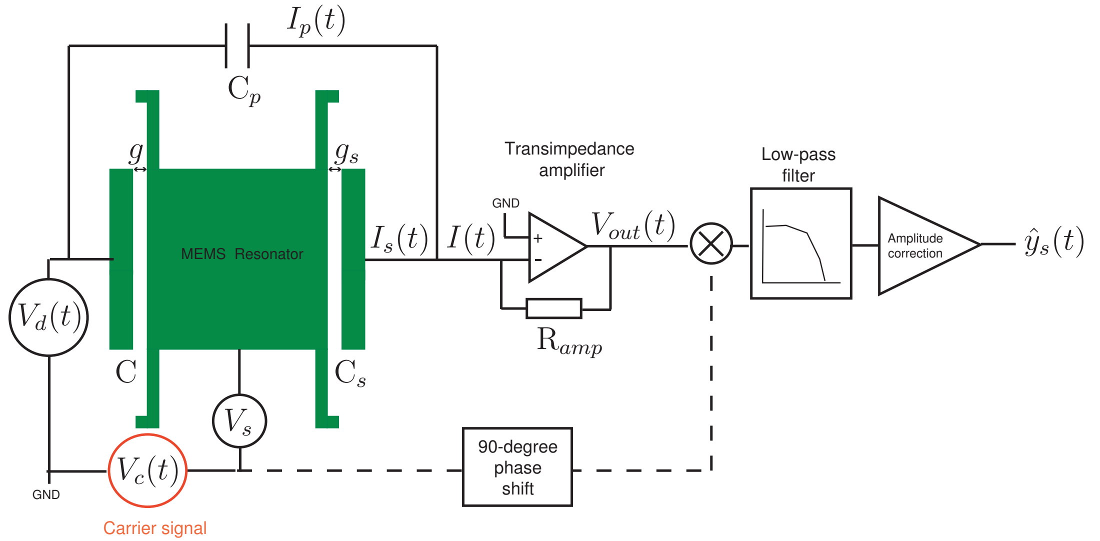

Figure 7.28: EAM scheme modification for full-position extraction.

Assume that the MEMS resonator oscillates with four harmonics and a static bias

$$\begin{aligned}\hat{y}(t) = \hat{Y}_0 + \hat{Y}_1 \sin(\omega_d t + \phi_{d1}) + \hat{Y}_2 \sin(2\omega_d t + \phi_{d2})\\ + \hat{Y}_3 \sin(3\omega_d t + \phi_{d3}) + \hat{Y}_4 \sin(4\omega_d t + \phi_{d4}).\end{aligned} \tag{7.20}$$

The driving voltage has also four harmonics

$$\begin{aligned}V_d(t) = V_0 + V_1 \sin(\omega_d t + \theta_{d1}) + V_2 \sin(2\omega_d t + \theta_{d2})\\ + V_3 \sin(3\omega_d t + \theta_{d3}) + V_4 \sin(4\omega_d t + \theta_{d4})\end{aligned} \tag{7.21}$$

and the applied carrier is

$$V_c(t) = V_c \sin(\omega_c t) \tag{7.22}$$

complemented with a fixed sensing voltage, V_s. Then, assuming lateral comb sensing, the capacitance variation is

$$\begin{aligned}\frac{\mathrm{C}_s(t)}{dt} =& -\mathrm{C}_{snl}\,\omega_d\Big(\check{Y}_1\cos(\omega_d t+\phi_{d1})+2\check{Y}_2\cos(2\omega_d t+\phi_{d2})\\ &+3\check{Y}_3\cos(3\omega_d t+\phi_{d3})+4\check{Y}_4\cos(4\omega_d t+\phi_{d4})\Big)\end{aligned} \tag{7.23}$$

where $\check{Y}_i = \frac{\hat{Y}_i}{\mathrm{L}_{ov}}$ is the normalized position amplitude of the i-harmonic. From this capacitance variation, following equations (7.17) and (7.12), the output voltage is

$$\begin{aligned}V(t) =& -\mathrm{R}_{amp}\left(\frac{d\mathrm{C}_s(t)}{dt}V_s+\frac{d\mathrm{C}_s(t)}{dt}V_c(t)+\mathrm{C}_s(t)\frac{dV_c(t)}{dt}+\mathrm{C}_p\frac{dV_d(t)}{dt}\right)\\ =& +\mathrm{R}_{amp}\,V_s\,\mathrm{C}_{snl}\,\omega_d\Big(\check{Y}_1\cos(\omega_d t+\phi_{d1})+2\check{Y}_2\cos(2\omega_d t+\phi_{d2})\\ &+3\check{Y}_3\cos(3\omega_d t+\phi_{d3})+4\check{Y}_4\cos(4\omega_d t+\phi_{d4})\Big)\\ &+\mathrm{R}_{amp}\,\mathrm{C}_{snl}\,\omega_d\,V_c\sin(\omega_c t)\Big(\check{Y}_1\cos(\omega_d t+\phi_{d1})+2\check{Y}_2\cos(2\omega_d t+\phi_{d2})\\ &+3\check{Y}_3\cos(3\omega_d t+\phi_{d3})+4\check{Y}_4\cos(4\omega_d t+\phi_{d4})\Big)\\ &-\mathrm{R}_{amp}\,\mathrm{C}_{snl}\,V_c\,\omega_c\cos(\omega_c t)\\ &+\mathrm{R}_{amp}\,\mathrm{C}_{snl}\,V_c\,\omega_c\cos(\omega_c t)\Big(\check{Y}_0+\check{Y}_1\sin(\omega_d t+\phi_{d1})+\check{Y}_2\sin(2\omega_d t+\phi_{d2})\\ &+\check{Y}_3\sin(3\omega_d t+\phi_{d3})+\check{Y}_4\sin(4\omega_d t+\phi_{d4})\Big)\\ &-\mathrm{R}_{amp}\,\mathrm{C}_p\,V_d\,\omega_d\cos(\omega_d t).\end{aligned} \tag{7.24}$$

Once this voltage is obtained, mixing the voltage with the phased-shifted carrier, $V_c\cos(\omega_c t)$, maps back the full position to the original frequency

$$\begin{aligned}V_m(t) =& V(t)\otimes V_c\cos(\omega_c t)\\ =& +\mathrm{R}_{amp}\,\mathrm{C}_{snl}\,V_c^2\,\omega_c\cos(\omega_c t)^2\Big(\check{Y}_0+\check{Y}_1\sin(\omega_d t+\phi_{d1})+\check{Y}_2\sin(2\omega_d t+\phi_{d2})\\ &+\check{Y}_3\sin(3\omega_d t+\phi_{d3})+\check{Y}_4\sin(4\omega_d t+\phi_{d4})\Big)\\ &+\mathrm{R}_{amp}\,V_s\,\mathrm{C}_{snl}\,\omega_d\,V_c\cos(\omega_c t)\Big(\check{Y}_1\cos(\omega_d t+\phi_{d1})+2\check{Y}_2\cos(2\omega_d t+\phi_{d2})\\ &+3\check{Y}_3\cos(3\omega_d t+\phi_{d3})+4\check{Y}_4\cos(4\omega_d t+\phi_{d4})\Big)\\ &+\mathrm{R}_{amp}\,\mathrm{C}_{snl}\,\omega_d\,V_c^2\cos(\omega_c t)\sin(\omega_c t)\Big(\check{Y}_1\cos(\omega_d t+\phi_{d1})+2\check{Y}_2\cos(2\omega_d t+\phi_{d2})\\ &+3\check{Y}_3\cos(3\omega_d t+\phi_{d3})+4\check{Y}_4\cos(4\omega_d t+\phi_{d4})\Big)\\ &-\mathrm{R}_{amp}\,\mathrm{C}_{snl}\,V_c^2\,\omega_c\cos(\omega_c t)^2\\ &-\mathrm{R}_{amp}\,\mathrm{C}_p\,V_d\,\omega_d V_c\cos(\omega_d t)\cos(\omega_c t).\end{aligned} \tag{7.25}$$

Using trigonometric equivalences

$$\cos(\omega_c t)^2 = \frac{1}{2} - \frac{\cos(2\omega_c t)}{2}$$
$$\cos(\omega_c t)\sin(\omega_c t) = \frac{\sin(2\omega_c t)}{2}$$

the resulting voltage is

$$\begin{aligned} V_m(t) = &+ \frac{1}{2}\mathrm{R}_{amp}\,\mathrm{C}_{snl}\,V_c^2\,\omega_c\Big(\check{Y}_0 + \check{Y}_1\,\sin(\omega_d t + \phi_{d1}) + \check{Y}_2\,\sin(2\omega_d t + \phi_{d2}) \\ &+ \check{Y}_3\,\sin(3\omega_d t + \phi_{d3}) + \check{Y}_4\,\sin(4\omega_d t + \phi_{d4})\Big) \\ &- \frac{1}{2}\mathrm{R}_{amp}\,\mathrm{C}_{snl}\,V_c^2\,\omega_c \\ &+ \textit{higher harmonics}. \end{aligned} \tag{7.26}$$

And the scaled full position with a fixed bias is obtained after low-pass filtering

$$\begin{aligned} V_{pos}(t) =& \frac{1}{2}\mathrm{R}_{amp}\,\mathrm{C}_{snl}\,V_c^2\,\omega_c\Big(\check{Y}_0 + \check{Y}_1\,\sin(\omega_d t + \phi_{d1}) + \check{Y}_2\,\sin(2\omega_d t + \phi_{d2}) \\ &+ \check{Y}_3\,\sin(3\omega_d t + \phi_{d3}) + \check{Y}_4\,\sin(4\omega_d t + \phi_{d4}) - 1\Big) \qquad (7.27) \\ =& \frac{1}{2}\mathrm{R}_{amp}\,\mathrm{C}_{snl}\,V_c^2\,\omega_c\Big(\frac{\hat{y}(t)}{\mathrm{L}_{ov}} - 1\Big). \qquad (7.28) \end{aligned}$$

Finally, the full position of the MEMS resonator is calculated as

$$\hat{y}(t) = \mathrm{L}_{ov}\Big(\frac{2V_{pos}(t)}{\mathrm{R}_{amp}\,\mathrm{C}_{snl}\,V_c^2\,\omega_c} + 1\Big). \tag{7.29}$$

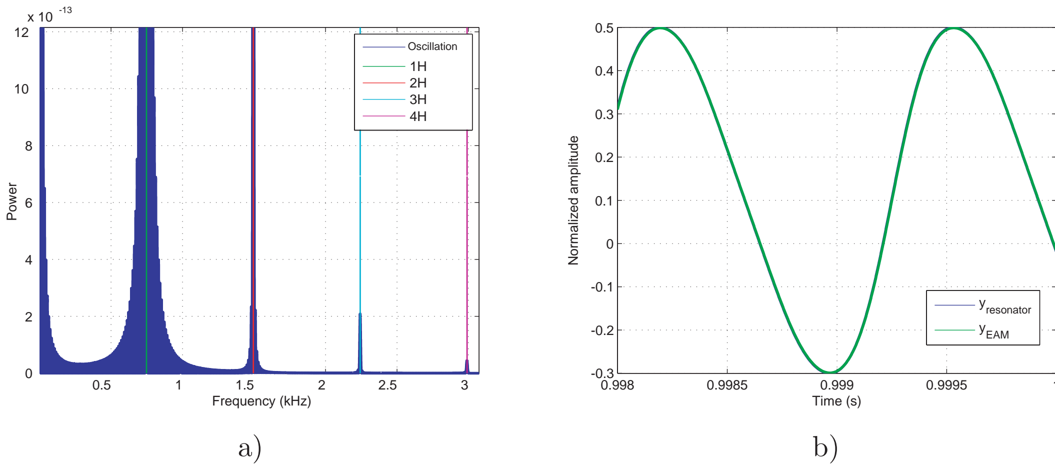

Figure 7.29: a) Power spectrum of the oscillation to be sensed including four harmonics. b) Comparison between the sensed position and the position signal extracted using EAM position sensing.

Consequently, with a simplified version of the Electromechanical Amplitude Modulation the full position can be extracted with electrostatic sensing using lateral comb capacitors.

EAM procedure is well-known and tested, what guarantees that the position can be extracted. The procedure can be extended to parallel-plate capacitors for small amplitudes of oscillation.

Figures 7.29 and 7.30 show the effectiveness of the procedure via simulation. The oscillation of the MEMS resonator with four harmonics, Figure 7.29a, is perfectly extracted and suitable for position feedback, Figure 7.29b. Figures 7.30a and 7.30b detail the effect of the EAM modulation on the oscillation signal and how the mixing with the 90°-phase shifted carrier signal allows to extract the full oscillation of the MEMS resonator from the masked signals with parasitics. In the example simulation, the parasitics capacitance is $C_s = 6.8322 \cdot 10^{-12}\,F$, and the carrier signal is chosen with an amplitude of $10\,V$ and a frequency of $20\,kHz$. The selection of the carrier signal frequency must be done carefully, in order to correctly separate the frequencies with the low-pass filter. And the MEMS design has to be checked to verify that the generated frequencies don't excite undesired mechanical oscillation modes [199].

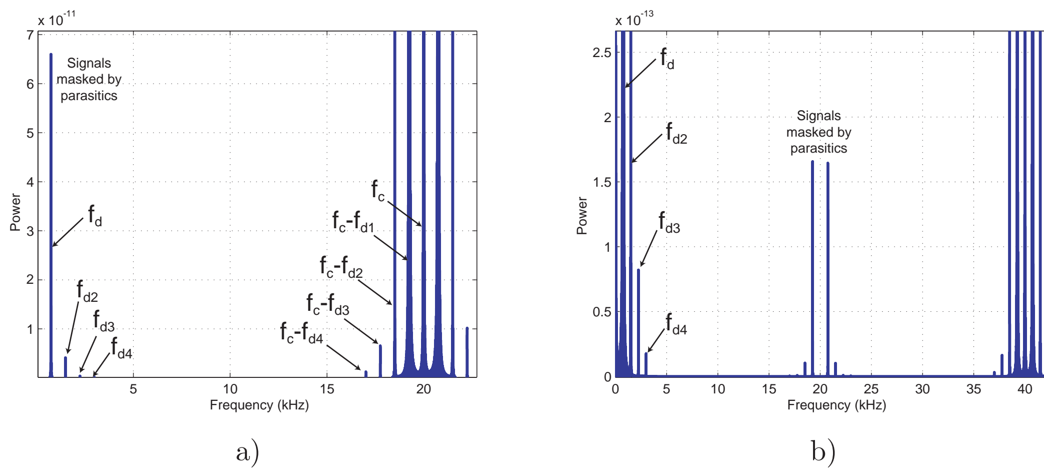

Figure 7.30: a) Power spectrum of the EAM signal that is extracted from the transimpedance amplifier with four side-bands of the carrier signal. b) Power spectrum of the EAM signal after mixing with the 90°-phase shifted carrier signal.

7.4 Proposed laboratory testing

In order to fully test the controller capabilities, an appropriate MEMS test resonator must be designed. Usual MEMS resonators designs cannot completely adapt to validate the control approach. New design with two-sided independent parallel-plate actuation and position feedback with lateral-comb or parallel-plate is presented. The design is prepared

for in-plane laser interferometry.

In the same way, some adaptation must be done in usual laboratory set-up to accommodate the tests. The proposed final set-up is presented, and the test procedure is outlined.

7.4.1 MEMS resonator design

To test the results presented in the dissertation, these main characteristics must be included in the MEMS test resonator:

1. Low natural frequency of the MEMS resonator (around 300 Hz) to be able to excite and detect up to four harmonics in the oscillations. The natural frequency affects the needed sampling frequency of the electronic board where the controller is implemented.

2. Non-linear spring design, with β-factor smaller than 5, to verify the suitability of the controller in nonlinear MEMS resonators.

3. Two-sided independent driving with parallel plates capacitors, in order to verify full-gap oscillation selection, with the proposed controller.

4. Voltage extraction with lateral comb fingers and parallel-plate capacitors, in order to test the EAM full position signal extraction approach.

5. A large planar area must be free of obstacles in order to implement in-plane position extraction with laser interferometry. This approach is under technical study as Future Work.

Using the same fabrication technology used in the MEMS resonator (*AF07_resonator3*) that has been used in the simulations, Figure 4.1, the necessary MEMS test resonator can be fabricated. The design is based on *UCI Microsystems* in-house wafer-level silicon-on-insulator (SOI) process. For the design fabrication, a silicon wafer with 50μm thickness is patterned using the design mask and a photoresist layer. Once the photoresist is developed, deep-reactive-ion-etching (DRIE) is applied using a Surface Technology Systems (STS) tool and then released in a HF-acid bath [198]. The minimal gap feature is 5μm. The minimal structural feature is 8μm. And maximum solid area is 20μm, with etch holes of size 20 μm $\times$ 20 μm.

Parameter	Value
Spring beam height b_K	$50\,\mu m$
Spring beam length L_K	$2\,mm$
Spring beam thickness h_K	$8\,\mu m$
Drive gap g_0	$5\,\mu m$
Sense gap g_s	$5\,\mu m$
Number of parallel-plates driveN_{dp}	40
Number of parallel-plates senseN_{sp}	20
Length of parallel-plates drive L_{dp}	$305\,\mu m$
Length of parallel-plates sense L_{sp}	$360\,\mu m$
Number lateral comb fingers N_{sl}	238
Lateral combs overlap L_{ov}	$20\,\mu m$
Resonator thickness b	$50\,\mu m$

Table 7.1: Design parameters of the MEMS resonator in Figure 7.31a.

The proposed MEMS resonator is presented in Figure 7.31. It is composed of four one-leg suspensions that suspend the proof-mass over the substrate. Two-sided independent parallel-plate electrostatic driving can be used to drive the MEMS resonator from the two sides of the mass. Lateral comb fingers are present in one-side for position feedback. And at the other side parallel-plate capacitors can also be used for position feedback. The basic design features are described in Table 7.1.

The equivalent model parameters are summarized in Table 7.2. As can be seen, the MEMS resonator is designed for $278\,Hz$ natural frequency, meaning that the fourth harmonic would be at $1.112\,kHz$, well in standard control equipment working frequencies. Driving capacitors are large and allow low-voltage driving, to avoid parasitics. Pull-in voltage is placed at $3.43\,V$, with the non-linear β-factor clearly on the nonlinear regime.

Parameter	Value
Linear spring K	$1.716\,N/m$
Non-linear spring K_3	$1.929 \cdot 10^{10}\ N/m^3$
Mass M	$5.6 \cdot 10^{-7}$ Kg
Oscillation gap g_0	$5 \cdot 10^{-6}$ m
Driving capacity (each side) C_0	$1.0797 \cdot 10^{-12}$ F
Lateral comb sensing capacity C_{snl}	$1.626 \cdot 10^{-10}$ F
Parallel-plate sensing capacity C_{snl}	$6.83 \cdot 10^{-13}$ F
Frequency ω_n	$1750\,rad/s$
Frequency f_n	$0.278\,kHz$
$\beta - factor = K/(K_3\, g_0^2)$	3.56

Table 7.2: New MEMS resonator model characteristic parameters designed for testing the control approach.

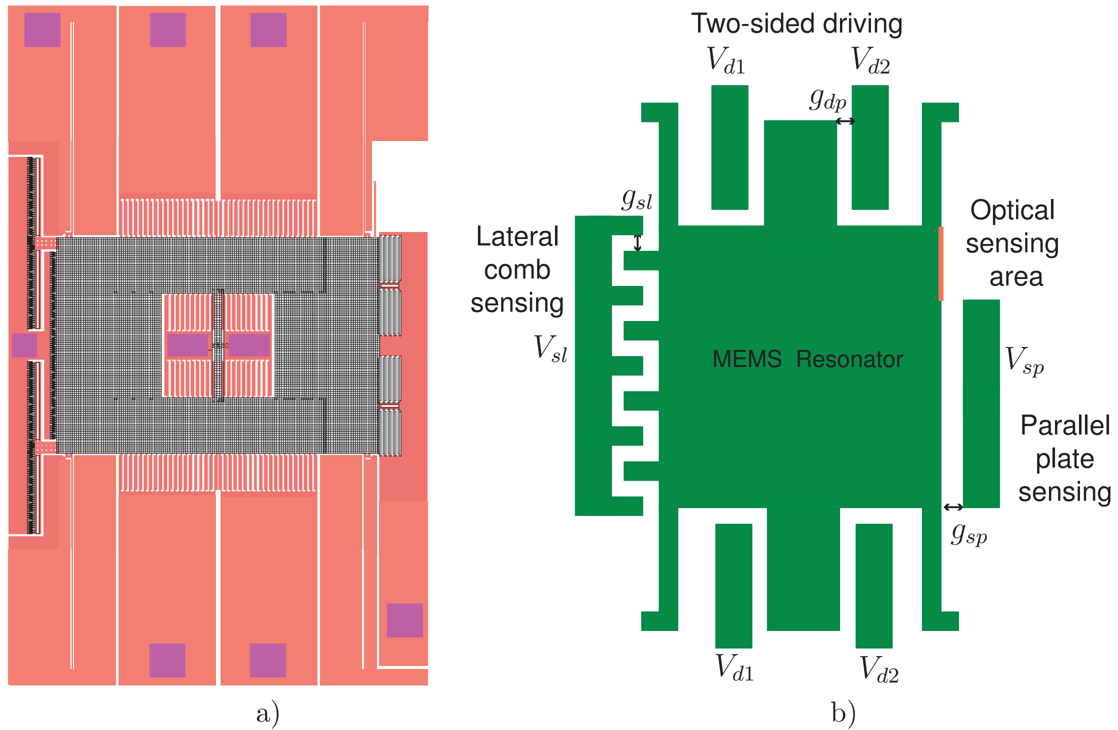

Figure 7.31: a) Capture of the L-Edit® fabrication design program with the proposed MEMS resonator. Design values in Table 7.1. b) Schematic of the MEMS resonator, indicating electrostatic driving and sensing ports, in the same positions designed in a). The surface prepared for optical detection is also indicated.

A large area has been cleaned in one of the sides to allow in-plane laser position detection against a flat lateral surface. In the process of wire-bonding the device to the dip-package, that area would be left clear in order to glue a 45° mirror to redirect laser from an laser Doppler vibrometer to measure real in-plane displacement, to validate electrostatic measuring.

7.4.2 Laboratory test set-up

In order to test the fabricated device, the proposed laboratory set-up is presented in Figure 7.32. The fabricated device would be diced and wire-bonded to a 48-pin DIP-package. The output of the MEMS resonator would be connected to a signal processing board, with a tansimpedance amplifier. In some cases, the transimpedance amplifier can be implemented on board and wire-bonded at wafer level, this lowers the parasitics and the Signal-to-Noise Ratio (SNR). The output would be processed by a Lock-in Amplifier, that would generate the carrier signal used to demodulate and filter out the MEMS resonator oscillation. This output would be processed by a FPGA/DSP board, where all the control would be implemented. The control board would generate the two driving signals for the

two-sided oscillation driving of the MEMS resonator. Depending on final implementation and capability of the control board, the lock-in amplifier processing can be integrated in the control board.

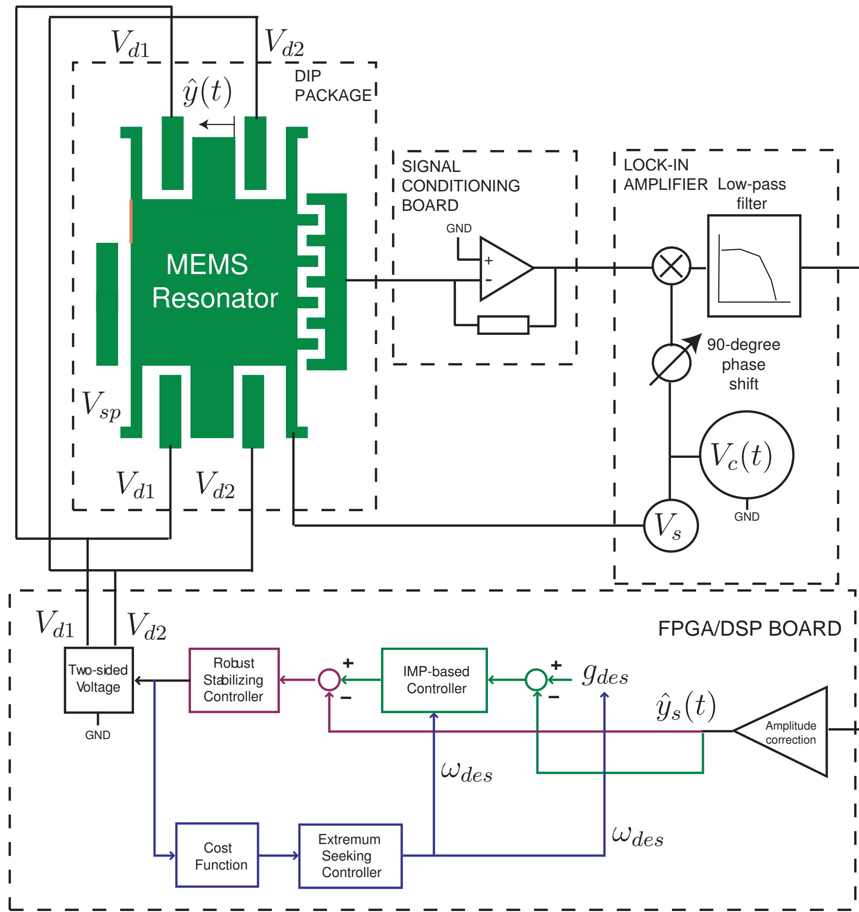

Figure 7.32: Proposed test-setup with the interconnections and the necessary laboratory equipment.

It is important to summarize the key features that must be included in the FPGA or DSP Control board, as this board would implement the proposed control strategy. The board must work on a clock of at least 100 kHz. It would implement a first step of signal processing to extract the real position, by correcting the output of the lock-in amplifier. After that, the three control levels would be implemented. The desired oscillation amplitude and bias would be a parameter, and from those values, the control loop would generate the driving voltages, at the minimum energy frequency. The controller would be implemented with a minimum of four resonators.

To validate the strategy, the tests that must be performed can be divided in four different areas:

Fabricated device identification

The first step is to fully identify the MEMS resonator parameters. Optical identification of key features would define fabrication imperfections and delimit the final mass, spring and gap information. Then, with electrostatic identification, the model parameters are extracted: resonant frequency, working Q, driving force and sensing capacity. With all this data the model parameters are fine-tuned to generate the controller parameters.

EAM full position extraction implementation and validation

Once the system is identified, validation of the EAM full position extraction scheme would be tested. This step is crucial to guarantee that the closed-loop control can be implemented with satisfactory results.

Different tests would be carried on, where multiple-harmonic driving voltages are applied, and the real oscillation is extracted. The test must guarantee that the generated output is the actual oscillation of the device.

In order to specifically validate that the EAM position feedback works as desired, an optical validation is proposed. This implementation is challenging and would need to be verified on the laboratory. The idea is to insert a 45-degree mirror in the dip package in the space already prepared for it. With this mirror, the laser beam of a laser Doppler vibrometry measuring table could be redirected to the MEMS resonator lateral surface, Figure 7.33. This implementation could allow optical position extraction, as in out-of-plane MEMS resonators. Another option could be fabrication of a MEMS mirror together with the MEMS resonator, but this is limited by the fabrication technique that is used. In the proposed SOI fabrication, this is not possible.

Robust controller with pure-sinusoidal oscillation implementation

Next step would be to validate robust pure-sinusoidal oscillation with full range of amplitudes and bias selection. Using the controller implemented in the Control board, different set-points with frequencies ranging from $0.8\omega_\mathrm{n}$ to $1.05\omega_\mathrm{n}$, amplitudes of oscillation ranging from $0.1\mathrm{g}_0$ to $0.6\mathrm{g}_0$ and bias ranging g_0 to $0.8\mathrm{g}_0$ would be tested. Pure-sinusoidal

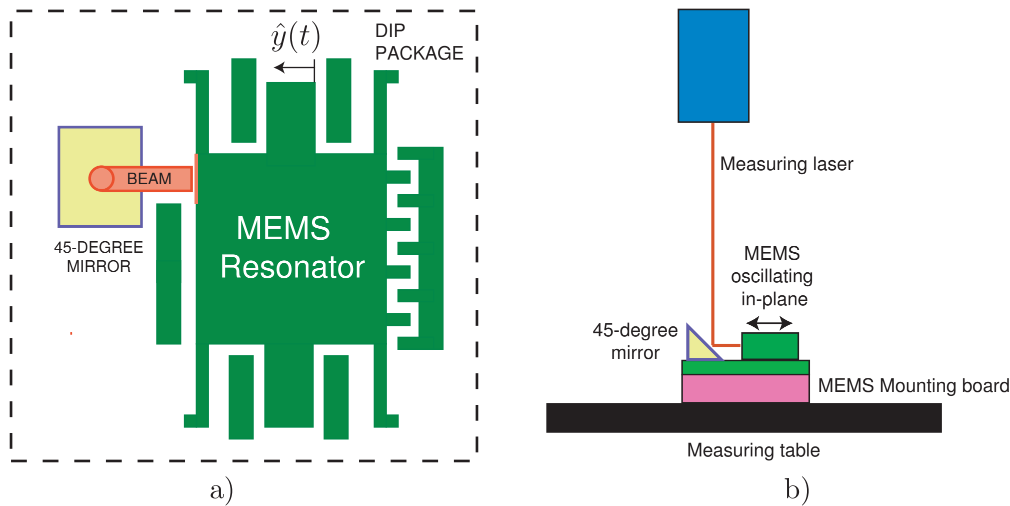

Figure 7.33: a) Detail of the insertion of a 45-degree mirror to redirect the laser beam for optical identification. b) Measuring implementation with an laser Doppler vibrometry measuring table.

oscillation should be verified in all cases. Also, two-sided actuation should be verified. To validated the robustness of the control, changes on Q-factor would be applied, as well as, shock tests.

Energy Efficient Control implementation

Finally, long-term tests would be done on the controller to validate the minimum energy control loop. For the same oscillation patterns of previous tests, where energy consumption would have been recorded, the control loop has to be able to reach the lowest energy consumption frequency.

In conclusion, a full validation of the control strategy is proposed with four incremental tests, that would verify control viability.

Chapter 8

Conclusions

The field of Micro-Electro-Mechanical Systems (MEMS) is nowadays a reality. Lots of designs already exist, and some of them are not a concept anymore. We can find them in devices around us. However, there are still challenges that prevent them to be used in high grade performance applications.

Plenty of MEMS devices are actuated using electrostatic forces, and specially, parallel-plate actuators are extensively used due to the simplicity of their design. Nevertheless, parallel-plate actuators have some limitations due to the nonlinearity of the generated force. Their robustness, stability, performance and energy consumption are issues that are not completely solved. This dissertation has tried to bring some light to them.

Taking the focus away from the application, and analyzing the MEMS resonator as it is, different approaches have been studied. The results change the way some of the issues were understood or extend their domain to nonlinear mechanical spring models. The *Resonant Pull-in Condition*, the definition of the *Harmonic Balance Voltage*, the two-sided actuation for full-range oscillation selection or the minimum energy frequency selection are between them.

Challenges are still there, but the search for better solutions are a step closer.

8.1 Contributions of the dissertation

Nonlinear extension of Pull-in derivations

Based on energy analysis, a unified framework for Static, Dynamic and Resonant Pull-in has been derived. Their definitions have been extended including a nonlinear mechanical spring in the model, and comparison of behaviors between linear and nonlinear behaviors have been provided. Nonlinear spring inclusion is important as it reduces or increases the maximum voltage that can be applied depending on the application, and at the same time, increases the stable maximum oscillation amplitude.
The energy analysis has shown the importance of potential energy curves. Their profile bound the range of feasible stable positions and oscillations. This has been shown graphically and analytically.

Definition of ***Resonant Pull-in Condition***

The energy analysis developed in the dissertation has lead to the definition of the Resonant Pull-in Condition [62]. For the first time, a general analytical formula to delimit the maximum combination of AC and DC voltage that can be applied without leading the MEMS resonator to pull-in was derived. The formula is defined for the nonlinear mechanical spring model, and unifies previous results.
The concept of Resonant Pull-in Condition was extended in [36] to define the minimum voltage combination for bistable actuation of MEMS switches.

Harmonic Balance oscillation characteristics analysis

Harmonic Balance has been shown to be an excellent tool to analyze and predict the steady-state behavior of the electrostatically actuated MEMS resonators. Insight on the limitations of first harmonic, superharmonic and subharmonic actuation schemes in terms of oscillation performance has been provided. Depending on chosen actuation, the number of harmonics that can be controlled on the oscillation output are limited.
Pure sinusoidal oscillation can only be achieved with appropriate voltage selection with at least three harmonics in the linear case and five harmonics in the nonlinear case. Closed-form oscillation solution cannot be obtained, but harmonic balance coupled to implicit numerical solver allows to predict expected oscillations for a given oscillation scheme.

Harmonic Balance predicts existence of steady-state oscillations when working between in stable bounds.

Harmonic Balance voltage definition

Using the square of the input voltage (V^2) as control action leads to simplification of the Harmonic Balance analysis. Moreover, it has been demonstrated that for any desired oscillation pattern, there exists a V^2 control action that leads the system to that oscillation. Harmonic Balance equations directly provide the V^2 needed voltage for a given oscillation pattern. The only limitation is the ability to convert that control action in a voltage applied to the MEMS resonator. With usual one-sided actuation, there are regions of oscillation that cannot be reached due to the impossibility of producing the V^2 voltage when it is negative-valued.

Full range oscillation with new two-sided actuation

Full range selection of oscillation amplitude and bias, as predicted by Harmonic Balance analysis, cannot be reached with one-sided actuation. For this reason, a new two-sided actuation scheme with individually selected input voltage to each side of the MEMS resonator has been defined. With the new actuation scheme, the desired action force is perfectly achieved, allowing the MEMS resonator to oscillate at the desired set-point.

The proposed scheme divides and scales the V^2 voltage into two different input voltages, one for each side.

Minimum energy oscillation frequency

Based on the Harmonic Balance voltage, energy analysis allows to define the minimum energy frequency for each desired oscillation. The approach shows that minimum energy frequency is dependent on desired bias and amplitude. Increasing the bias reduces the minimum energy frequency, but increasing the amplitude woks on the opposite direction.

Minimum energy is always obtained in the range of frequencies where one-sided actuation is possible, as two-sided actuation demands more energy. Nevertheless, two-sided actuation is important to allow smooth control over the whole range of frequencies.

Surprisingly, as the bias is reduced, frequencies higher than the mechanical natural frequency are more energy efficient than the lower frequencies.

New controller for energy efficient robust sinusoidal oscillation

A new controller with three hierarchical control schemes has been designed to automatically generate sinus-like oscillations in the full range of desired amplitudes. The driving voltage has been shown to match with the analytically predicted Harmonic Balance voltage. The proposed controller is able to produce the driving action needed to obtain the desired set-point oscillation with robustness over a large range of system parameters variations. And it seeks the lowest energy frequency for the desired amplitude of oscillation.

Consequently, it allows to obtain a pure sinus-like oscillation with the desired amplitude, with robustness and with minimum energy consumption.

8.2 Publications in the field

- Snap-Action Bistable Micromechanisms Actuated by Nonlinear Resonance. J. Casals-Terre, A. Fargas-Marques and A.M. Shkel, Journal of Microelectromechanical Systems. Oct. 2008 Volume: 17, Issue: 5. DOI: 10.1109/JMEMS.2008.2003054

- Resonant Pull-In Condition in Parallel-Plate Electrostatic Actuators. A. Fargas-Marques, J. Casals-Terre and A.M. Shkel, Journal of Microelectromechanical Systems. Oct. 2007 Volume: 16, Issue: 5. DOI: 10.1109/JMEMS.2007.900893

- Using interactive tools to teach and understand MEMS. A. Fargas-Marques and R. Costa-Castelló. ACE06. 7th IFAC Symposium on Advances in Control Education. 21 23 June 2006, Madrid, Spain. DOI: 10.3182/20060621-3-ES-2905.00101.

- Describing function analysis in MEMS resonators. A. Fargas-Marques and R. Costa-Castelló. 2ndas Jornadas UPC de Investigación en Automática, Visión y Robótica (AVR'06). Camps Nord - UPC. Barcelona, July 2006.

- Modeling the electrostatic actuation of MEMS: state of art 2005. A. Fargas-Marques, R. Costa-Castelló and A.M. Shkel. IOC-DT-P-2005-18 - Technical report - Institut d'Organització i Control. Universitat Politècnica de Catalunya. 2005. URI: http://hdl.handle.net/2117/119

- On Electrostatic Actuation Beyond Snapping Condition. A. Fargas-Marques and A. M. Shkel. Proceedings IEEE SENSORS'05, pp.4, Irvine, Oct. 30 2005-Nov. 3

2005. DOI: 10.1109/ICSENS.2005.1597770

- On Electrostatic Actuation Beyond Snapping Condition. A. Fargas-Marques and A. M. Shkel. Preprint of Eurosensors XIX: The 19th European Conference on Solid-State Transducers, Barcelona, Spain, 11 - 14 September 2005.

8.3 Future work

Laboratory testing

In the current work, a test MEMS resonator has been specially designed for testing the new control approach. The device has been designed with low natural frequency, two-sided independent actuation and prepared for EAM position feedback. The device must be fabricated and tested.

Once fabricated the device, the controller must be implemented in a control board in order to validate the approach. The control board must include the EAM position feedback, the three control loops and the two-sided actuation voltage generation.

The complete testing procedure to validate the control approach and the laboratory set-up have been detailed in Chapter 7.

Optical position extraction

In the laboratory testing, a new approach to extract in-plane position has been proposed with the installation of a 45-degree mirror on die. The proposed MEMS resonator for testing has been specially designed to use this approach.

The approach is designed to validate EAM position extraction with a non-parasitic affected measuring method. This would be a new way to use interferometry in on-plane resonators.

New control feedback scheme would be investigated, using similar techniques as presented in [90], depending on the testing results. The testing procedure has been detailed in Chapter 7.

Stability formulation and control

The proposed control strategy has shown good performance to obtain the set-point oscillation, robustness and minimum energy seeking. However, stability for amplitudes

larger than 80% of the gap cannot be guaranteed.

Harmonic Balance predicts that steady-state oscillations are feasible, but the transient dynamics make it difficult to achieve them. Moreover, the energy analysis in the Harmonic Balance formulation links directly to the Resonant Pull-in Condition formulation, but the interconnection between results has not fully developed in order to obtain a closed-form formula that could be possible.

In parallel, a control loop for pull-in avoidance should be added if those amplitudes are desired. New approaches to deal with large amplitudes have been presented in literature, as in [30], where a polynomial linear parameter varying model is used for full gap positioning. Similar approaches could be added to the proposed controller.

Robust EAM adaptation to full position

The effectiveness of EAM position feedback has to be tested and validated to be able to implement the controller and the full range oscillation. The approach relies on lateral combs electrostatic position extraction. In order to be able to oscillate with large amplitudes devices where lateral combs cannot be used, an extension of the Robust EAM extraction for parallel-plate position sensing should be derived [199]. Moreover, the parallel plate extension is robust against parameters variation, and it would be a perfect combination for the controller.

Extension to two degrees-of-freedom MEMS resonators

The presented results have the potential to be extended to 2-DOF MEMS resonators, as in the case of gyroscopes. The effect of the proposed controller should be analyzed, and the improvement in sensitivity gained by large amplitude pure-sinusoidal oscillation should be quantified. Interaction of oscillation controller with sensing precession or oscillation should also be analyzed.

Bibliography

[1] E. M. Abdel-Rahman, A. H. Nayfeh, and M. I. Younis. Dynamics of an electrically actuated resonant microsensor. In *Proceedings of the International Conference on MEMS, NANO and Smart Systems*, pages 188–196, July 2003.

[2] E. M. Abdel-Rahman, M. I. Younis, and A. H. Nayfeh. Characterization of the mechanical behavior of an electrically actuated microbeam. *Journal of Micromechanics and Microengineering*, 12:759–766, 2002.

[3] C. Acar, S. Eler, and A.M. Shkel. Concept, implementation, and control of wide bandwidth mems gyroscopes. In *Proceedings of the American Control Conference*, volume 2, pages 1229–1234, 2001.

[4] C. Acar and A. M. Shkel. Inherently robust micromachined gyroscopes with 2-DOF sense-mode oscillator. *IEEE/ASME Journal of Microelectromechanical Systems*, 15:380–387, 2006.

[5] C.G. Agudelo, M. Packirisamy, G. Zhu, and L. Saydy. Nonlinear control of an electrostatic micromirror beyond pull-in with experimental validation. *IEEE/ASME Journal of Microelectromechanical Systems*, 18(4):914–923, Aug 2009.

[6] M. Aikele, K. Bauer, W. Ficker, F. Neubauer, U. Prechtel, J. Schalk, and H. Seidel. Resonant accelerometer with self-test. *Sensors and Actuators A: Physical*, 92(1-3):161–167, August 2001.

[7] A. Al-Mamun, E. Keikha, C. S. Bhatia, and T. H. Lee. Integral resonant control for suppression of resonance in piezoelectric micro-actuator used in precision servomechanism. *Mechatronics*, 23(1):1 – 9, 2013.

[8] F. M. Alsaleem, M. I. Younis, and H. M. Ouakad. On the nonlinear resonances and dynamic pull-in of electrostatically actuated resonators. *Journal of Micromechanics and Microengineering*, 19(4):045013, 2009.

[9] N. R. Aluru and J. White. A multilevel newton method for mixed-energy domain simulation of mems. *IEEE/ASME Journal of Microelectromechanical Systems*, 8(3):299–308, 1999.

[10] G. K. Ananthasuresh, R. K. Gupta, and S. D. Senturia. An approach to macromodeling of mems for nonlinear dynamic simulation. In *Proceedings of the International Conference on Solid State Sensors and Actuators, TRANSDUCERS*, volume 59, pages 401–407, Atlanta, Nov. 17-22 1996. ASME.

[11] M. Andrews, I. Harris, and G. Turner. A comparison of squeeze-film theory with measurements on a microstructure. *Sensors and Actuators A: Physical*, 36(1):79–87, 1993.

[12] R. Antonello and R. Oboe. Mode-matching in vibrating microgyros using extremum seeking control. In *33rd Annual Conference of the IEEE Industrial Electronics Society*, pages 2301–2306, Nov 2007.

[13] R. Antonello, R. Oboe, L. Prandi, and F. Biganzoli. Automatic mode matching in mems vibrating gyroscopes using extremum-seeking control. *IEEE Transactions on Industrial Electronics*, 56(10):3880–3891, Oct 2009.

[14] S. S. Aphale, A. J. Fleming, and S. O. Reza Moheimani. Integral resonant control of collocated smart structures. *Smart Materials and Structures*, 16(2):439, 2007.

[15] K. B. Ariyur and M. Krstic. *Real-Time Optimization by Extremum-Seeking Control*. Wiley, 2003. 978-0-471-46859-2.

[16] M. Ashhab, M. V. Salapaka, M. Dahleh, and I. Mezic. Dynamical analysis and control of microcantilevers. *Automatica*, 35(10):1663–1670, October 1999.

[17] K. T. Atta, A. Johansson, and T. Gustafsson. Extremum seeking control based on phasor estimation. *Systems & Control Letters*, 85:37 – 45, 2015.

[18] G. Balas, R. Chiang, A. Packard, and M. Safonov. *MATLAB Robust Control Toolboox. Reference*. MATLAB, 2013.

[19] C. Batur, T. Sreeramreddy, and Q. Khasawneh. Sliding mode control of a simulated mems gyroscope. In *Proceedings of the American Control Conference*, volume 6, pages 4160–4165, 2005.

[20] D.S. Bayard. A general theory of linear time-invariant adaptive feedforward systems with harmonic regressors. *IEEE Transactions on Automatic Control*, 45(11):1983–1996, Nov 2000.

[21] D. Bernstein, P. Guidotti, and J.A. Pelesko. Mathematical analysis of an electrostatically actuated mems devices. In *Proceedings of Modeling and Simulation of Microsystems*, pages 489–492, 2000.

[22] G. Besançon, A. Voda, and E. Colinet. Towards oscillation control in a vibrating cantilever nonlinear NEMS. In *Proceedings of the European Control Conference*, pages 2582 – 2586, 2007.

[23] J. Bienstman, R. Puers, and J. Vandewalle. Periodic and chaotic behaviour of the autonomous impact resonator. In *Proceedings of the IEEE Annual International Conference on MEMS*, pages 562–567, 1998.

[24] J.J. Blech. On isothermal squeeze films. *Journal of Lubrication Technology*, 105(4):615–620, 1983.

[25] M. Bodson. Rejection of periodic disturbances of unknown and time-varying frequency. *International Journal of Adaptive Control and Signal Processing*, 19(2-3):67–88, 2005.

[26] M. Bodson, A. Sacks, and P. Khosla. Harmonic generation in adaptive feedforward cancellation schemes. In *IEEE Conference on Decision and Control*, pages 1261–1266 vol.2, 1992.

[27] M. Bodson, A. Sacks, and P. Khosla. Harmonic generation in adaptive feedforward cancellation schemes. *IEEE Transactions on Automatic Control*, 39(9):1939–1944, Sep 1994.

[28] B. Borovic, C. Hong, A.Q. Liu, L. Xie, and F.L. Lewis. Control of a mems optical switch. In *Proceedings of the IEEE Conference on Decision and Control*, volume 3, pages 3039–3044, 2004.

[29] B. Borovic, A.Q. Liu, D. Popa, H. Cai, and F.L. Lewis. Open-loop versus closed-loop control of mems devices: choices and issues. *Journal of Micromechanics and Microengineering*, 15(10):1917–1924, 2005.

[30] M. Boudaoud, Y. Le Gorrec, Y. Haddab, and P. Lutz. Gain scheduling control of a nonlinear electrostatic microgripper: Design by an eigenstructure assignment with an observer-based structure. *IEEE Transactions on Control Systems Technology*, 23(4), July 2015.

[31] C. Burrer, J. Esteve, and E. Lora-Tamayo. Resonant silicon accelerometers in bulk micromachining technology-an approach. *IEEE/ASME Journal of Microelectromechanical Systems*, 5(2):122–130, 1996.

[32] H. Busta, R. Amantea, D. Furst, J. M. Chen, M. Turowski, and C. Mueller. A MEMS shield structure for controlling pull-in forces and obtaining increased pull-in voltages. *Journal of Micromechanics and Microengineering*, 11(6):720–725, 2001.

[33] E. I. Butikov. Parametric excitation of a linear oscillator. *European Journal of Physics*, 25(4):535, 2004.

[34] M. F. Byl, S. J. Ludwick, and D. L. Trumper. A loop shaping perspective for tuning controllers with adaptive feedforward cancellation. *Precision Engineering*, 29(1):27–40, January 2005.

[35] B. Cagdaser and B.E. Boser. Resonant drive for stabilizing parallel-plate actuators beyond the pull-in point. In *Proceedings of the International Conference on Solid State Sensors and Actuators, TRANSDUCERS*, volume 1, pages 688–692, 2005.

[36] J. Casals-Terré, A. Fargas-Marquès, and A. M. Shkel. Snap-action bistable micromechanisms actuated by nonlinear resonance. *IEEE/ASME Journal of Microelectromechanical Systems*, 17(5):1082–1093, October 2008.

[37] L. Castañer, J. Pons, R. Nadal-Guardia, and A. Rodríguez. Analysis of extended actuation range of electrostatic actuators by current pulse drive. *Sensors and Actuators A: Physical*, 90(3):181–190, 2001.

[38] L. Castañer, A. Rodríguez, J. Pons, and S. D. Senturia. Pull-in time-energy product of electrostatic actuators: comparison of experiments with simulation. *Sensors and Actuators A: Physical*, 83(1-3):263–269, 1999.

[39] L M. Castañer and S. D. Senturia. Speed-energy optimization of electrostatic actuators based on pull-in. *IEEE/ASME Journal of Microelectromechanical Systems*, 8(3):290–298, September 1999.

[40] E.K. Chan and R.W. Dutton. Electrostatic micromechanical actuator with extended range of travel. *IEEE/ASME Journal of Microelectromechanical Systems*, 9(3):321–328, 2000.

[41] F. Chen, W. Yuan, H. Chang, G. Yuan, J. Xie, and M. Kraft. Design and implementation of an optimized double closed-loop control system for mems vibratory gyroscope. *IEEE Sensors Journal*, 14(1):184–196, Jan 2014.

[42] J. Chen, W. Weingartner, A. Azarov, and R.C. Giles. Tilt-angle stabilization of electrostatically actuated micromechanical mirrors beyond the pull-in point. *IEEE/ASME Journal of Microelectromechanical Systems*, 13(6):988–997, 2004.

[43] K.K. Chew and M. Tomizuka. Digital control of repetitive errors in disk drive systems. *IEEE Control Systems Magazine*, 10(1):16–20, 1990.

[44] Y. Cho, B. M. Kwak, A. P. Pisano, and R. T. Howe. Slide film damping in laterally driven microstructures. *Sensors and Actuators A: Physical*, 40(1):31–39, 1994.

[45] P. B. Chu, P. R. Nelson, M. L. Tachiki, and K. S. J. Pister. Dynamics of polysilicon parallel-plate electrostatic actuators. *Sensors and Actuators A: Physical*, 52:216–220, 1996.

[46] P.B. Chu, I. Brener, C. Pu, S.-S. Lee, J.I. Dadap, S. Park, K. Bergman, N.H. Bonadeo, T. Chau, M. Chou, R.A. Doran, R. Gibson, R. Harel, J.J. Johnson, C.D. Lee, D.R. Peale, B. Tang, D.T.K. Tong, M.-J. Tsai, Q. Wu, W. Zhong, E.L. Goldstein, L.Y. Lin, and J.A. Walker. Design and nonlinear servo control of mems mirrors and their performance in a large port-count optical switch. *IEEE/ASME Journal of Microelectromechanical Systems*, 14(2):261–273, 2005.

[47] P.B. Chu and S.J. Pister. Analysis of closed-loop control of parallel-plate electrostatic microgrippers. In *Proceedings of the IEEE International Conference on Robotics and Automation*, volume 1, pages 820–825, 1994.

[48] W. A. Clark. *Micromachined Vibratory Rate Gyroscopes*. PhD thesis, U.C. Berkeley, 1997.

[49] R. Costa-Castelló, R. Griñó, and E. Fossas. Resonant control of a single-phase full-bridge unity power factor boost rectifier. In *IEEE International Conference on Control Applications*, pages 599–604, 2007.

[50] R. Costa-Castelló, J. M. Olm, H. Vargas, and G. A. Ramos. An educational approach to the internal model principle for periodic signals. *International Jounal of Innovative Computing, Information and Control*, 8(8):5591–5606, August 2012.

[51] M.F. Daqaq, C.K. Reddy, and A.H. Nayfeh. Input-shaping control of nonlinear mems. *Nonlinear Dynamics*, 54(1-2):167–179, 2008.

[52] S. K. De and N.R. Aluru. Complex nonlinear oscillations in electrostatically actuated microstrucures. *IEEE/ASME Journal of Microelectromechanical Systems*, 15(2):355–369, April 2006.

[53] R.N. Dean Jr., J.Y. Hung, and B.M. Wilamowski. Advanced controllers for microelectromechanical actuators. In *IEEE International Conference on Industrial Technology*, pages 899–904, 2005.

[54] T. Devos, F. Malrait, and R. Sepulchre. Energy saving for induction motor control by extremum seeking. In *International Conference on Electrical Machines (ICEM)*, pages 934–938, Sept 2012.

[55] H. Ding, Z. Yang, G. Yan, M. Kraft, and R. Wilcock. MEMS gyroscope control system using a band-pass continuous-time sigma-delta modulator. In *IEEE Sensors*, pages 868–872, Nov 2010.

[56] D. Dochain, M. Perrier, and M. Guay. Extremum seeking control and its application to process and reaction systems: A survey. *Mathematics and Computers in Simulation*, 82(3):369 – 380, 2011. 6th Vienna International Conference on Mathematical Modelling.

[57] A. Duwel, J. Gorman, M. Weinstein, J. Borenstein, and P. Ward. Experimental study of thermoelastic damping in mems gyros. *Sensors and Actuators A: Physical*, 103(1):70–75, 2003.

[58] A. Ebrahimi. Regulated model-based and non-model-based sliding mode control of a mems vibratory gyroscope. *Journal of Mechanical Science and Technology*, 28(6):2343–2349, 2014.

[59] D. Elata, O. Bochobza-Degani, S. Feldman, and Y. Nemirovsky. Secondary dof and their effect on the instability of electrostatic mems devices. In *Proceedings of the IEEE Annual International Conference on MEMS*, pages 177–180, 2003.

[60] X. Fang, X. Li, J. Wang, and L. Dong. Repetitive control of rehabilitation robot with multi-channel periodic input signal. In *8th World Congress on Intelligent Control and Automation (WCICA)*, pages 6605–6609, July 2010.

[61] A. Fargas-Marquès. Stable electrostatic actuation of mems double-ended tuning fork oscillators. Master's thesis, University of California, Irvine, 2001. Advisor: Dr. Shkel.

[62] A. Fargas-Marquès, J. Casals-Terre, and A. M. Shkel. Resonant pull-in condition in parallel-plate electrostatic actuators. *IEEE/ASME Journal of Microelectromechanical Systems*, 16(5):1044–1053, October 2007.

[63] A. Fargas-Marquès and A. M. Shkel. On electrostatic actuation beyond snapping condition. In *Proceedings of IEEE Sensors*, pages 600–603, Irvine, CA, November 2005.

[64] A. Fargas-Marquès and A. M. Shkel. On electrostatic actuation beyond snapping condition. In *Proceedings of Eurosensors XIX*, page MB13, Barcelona, September 2005.

[65] J. Fei and D. Wu. Adaptive sliding mode control using robust feedback compensator for mems gyroscope. *Mathematical Problems in Engineering*, 2013, 2013.

[66] S. Fekri, D.G. Bates, and I. Postlethwaite. Linear vs. nonlinear robustness analysis: A case study. In *IEEE International Conference on Control Applications*, pages 753–758, Oct 2007.

[67] Z. C. Feng, M. Fan, and V. Chellaboina. Adaptive input estimation methods for improving the bandwidth of microgyroscopes. *IEEE Sensors Journal*, 7(4):562–567, 2007.

[68] G. Flores, G.A. Mercado, and J.A. Pelesko. Dynamics and touchdown in electrostatic mems. In *Proceedings of the International Conference on MEMS, NANO and Smart Systems*, pages 182– 187, July 2003.

[69] B. A. Francis and W. M. Wonham. The internal model principle of control theory. *Automatica*, 12(5):457–465, 1976.

[70] L. Fu. *Model-based Extremum Seeking for a Class of Nonlinear Systems*. PhD thesis, The Ohio State University, 2010.

[71] L. Fu and Ü. Özgüner. Extremum seeking with sliding mode gradient estimation and asymptotic regulation for a class of nonlinear systems. *Automatica*, 47(12):2595 – 2603, 2011.

[72] B. J. Gallacher, J. S. Burdess, and K. M. Harish. A control scheme for a mems electrostatic resonant gyroscope excited using combined parametric excitation and harmonic forcing. *Journal of Micromechanics and Microengineering*, 16(2):320–331, 2006.

[73] A. Ghaffari, M. Krstic, and S. Seshagiri. Power optimization and control in wind energy conversion systems using extremum seeking. *IEEE Transactions on Control Systems Technology*, 22(5):1684–1695, Sept 2014.

[74] M.-A. Gretillat, Y.-J. Yang, E.S. Hung, V. Rabinovich, G.K. Ananthasuresh, N.F. De Rooij, and S.D. Senturia. Nonlinear electromechanical behaviour of an electrostatic microrelay. In *Proceedings of the International Conference on Solid State Sensors and Actuators, TRANSDUCERS*, volume 2, pages 1141–1144, 1997.

[75] C. Gui, R. Legtenberg, H. A. C. Tilmans, J. H. J. Fluitman, and M. Elwenspoek. Nonlinearity and hysteresis of resonant strain gauges. *IEEE/ASME Journal of Microelectromechanical Systems*, 7(1):122–127, 1998.

[76] R. K. Gupta, E.S. Hung, Y.J. Yang, G.K. Ananthasuresh, and S.D. Senturia. Pull-in dynamics of electrostatically-actuated beams. In *Solid-State Sensors and Actuators Workshop, Late News Session*, pages 1–2, 1996.

[77] R. K. Gupta and S.D. Senturia. Pull-in time dynamics as a measure of absolute pressure. In *Proceedings of the IEEE Annual International Conference on MEMS*, pages 290–294, 1997.

[78] B.J. Hamrock. *Fundamentals of fluid film lubrication*. McGraw Hill, 1994.

[79] J. S. Han, E. B. Rudnyi, and J. G. Korvink. Efficient optimization of transient dynamic problems in mems devices using model order reduction. *Journal of Micromechanics and Microengineering*, 15(4):822, 2005.

[80] M. Handtmann, R. Aigner, A. Meckes, and G. Wachutka. Sensitivity enhacement of mems inertial sensors using negative spring and active control. *Sensors and Actuators A: Physical*, 97-98:153–160, 2002.

[81] T. Hiller, L.L. Li, E.L. Holthoff, B. Bamieh, and K.L. Turner. System identification, design, and implementation of amplitude feedback control on a nonlinear parametric mem resonator for trace nerve agent sensing. *IEEE/ASME Journal of Microelectromechanical Systems*, PP(99):1–1, 2015.

[82] G. Hillerstrom. Adaptive suppression of vibrations - a repetitive control approach. *IEEE Transactions on Control Systems Technology*, 4(1):72–78, 1996.

[83] J.-M. Huang, A.Q. Liu, C. Lu, and J. Ahn. Mechanical characterization of micromachined capacitive switches: design consideration and experimental verification. *Sensors and Actuators A: Physical*, 108:36–48, 2003.

[84] J.M. Huang, K.M. Liew, C.H. Wong, S. Rajendran, M.J. Tan, and A. Q. Liu. Mechanical design and optimization of capacitive micromachined switch. *Sensors and Actuators A: Physical*, 93:273–285, 2001.

[85] E. S. Hung and S. D. Senturia. Extending the travel range of analog-tuned electrostatic actuators. *IEEE/ASME Journal of Microelectromechanical Systems*, 8:497–505, 1999.

[86] E. S. Hung and S. D. Senturia. Generating efficient dynamical models for microelectromechanical systems from a few finite-element simulation runs. *IEEE/ASME Journal of Microelectromechanical Systems*, 8(3):280–289, 1999.

[87] B. Hunnekens, A. Di Dino, N. van de Wouw, N. van Dijk, and H. Nijmeijer. Extremum-seeking control for the adaptive design of variable gain controllers. *IEEE Transactions on Control Systems Technology*, 23(3):1041–1051, May 2015.

[88] D. J. Ijntema and H. A. C. Tilmans. Static and dynamic aspects of an air-gap capacitor. *Sensors and Actuators A: Physical*, 35:121–128, 1992.

[89] M. Itik. Repetitive control of a trilayer conjugated polymer actuator. *Sensors and Actuators A: Physical*, 194:149–159, 2013.

[90] A. Izadian and P. Famouri. Reliability enhancement of mems lateral comb resonators under fault conditions. *IEEE Transactions on Control Systems Technology*, 16(4):726–734, July 2008.

[91] S. Jagannathan and M. Hameed. Adaptive force-balancing control of mems gyroscope with actuator limits. In *Proceedings of the American Control Conference*, volume 2, pages 1862–1867, 2004.

[92] A. Jimenez-Triana, G. Zhu, and L. Saydy. Oscillation amplitude enhancement of an electrostatic mems resonator via chaos control. In *American Control Conference*, pages 6269–6274, June 2013.

[93] M. Khammash, L. Oropeza-Ramos, and K.L. Turner. Robust feedback control design of an ultra-sensitive, high bandwidth tunneling accelerometer. In *Proceedings of the American Control Conference*, volume 6, pages 4176–4180, 2005.

[94] Q. Khasawneh and C. Batur. Design and control of a vibrating gyroscope. In *Proceedings of the American Control Conference*, volume 3, pages 2505–2510, 2004.

[95] E.-R. König and G. Wachutka. Multi-parameter homotopy for the numerical analysis of MEMS. *Sensors and Actuators A: Physical*, 110(1):39–51, 2004.

[96] G. Kovacs. *Micromachined Transducers Sourcebook*. McGraw-Hill, 1998.

[97] M. Kranz, S. Burgett, T. Hudson, M. Buncick, P. Ruffin, P. Ashley, and J. McKee. Performance of a silicon-on-insulator mems gyroscope with digital force feedback. In *Proceedings of IEEE Position Location and Navigation Symposium, PLANS*, pages 7–14, 2004.

[98] M. Krstic and H.-H. Wang. Stability of extremum seeking feedback for general nonlinear dynamic systems. *Automatica*, 36(4):595 – 601, 2000.

[99] S. Krylov. Lyapunov exponents as a criterion for the dynamic pull-in instability of electrostatically actuated microstructures. *International Journal of Non-Linear Mechanics*, 42(4):626–642, 2007.

[100] S. Krylov, I. Harari, and Y. Cohen. Stabilization of electrostatically actuated microstructures using parametric excitation. *Journal of Micromechanics and Microengineering*, 15:1188–1204, 2005.

[101] S. Krylov and R. Maimon. Pull-in dynamics of an elastic beam actuated by continuously distributed electrostatic force. *Journal of Vibration and Acoustics. Transactions of the ASME*, 126(3):332–342, 2004.

[102] A. Kumar, A. Dikshit, B. Clark, and J. Yan. A frequency scan scheme for pll-based locking to high-q mems resonators. In *VLSI Design (VLSID), 2015 28th International Conference on*, pages 71–74, Jan 2015.

[103] R. C.H. Lee and M. C. Smith. Robustness and trade-offs in repetitive control. *Automatica*, 34(7):889 – 896, 1998.

[104] R. C.H. Lee and M. C. Smith. Nonlinear control for robust rejection of periodic disturbances. *Systems & Control Letters*, 39(2):97 – 107, 2000.

[105] R.P. Leland. Adaptive mode tuning for vibrational gyroscopes. *IEEE Transactions on Control Systems Technology*, 11(2):242–247, 2003.

[106] R.P. Leland. Adaptive control of a mems gyroscope using lyapunov methods. *IEEE Transactions on Control Systems Technology*, 14(2):278–283, 2006.

[107] S. Lenci and G. Rega. Control of pull-in dynamics in a nonlinear thermoelastic electrically actuated microbeam. *Journal of Micromechanics and Microengineering*, 16(2):390–401, 2006.

[108] J. Li and T.C. Tsao. Robust performance repetitive control systems. *Journal of Dynamic Systems, Measurement, and Control*, 123(3):330–337, 2001.

[109] N.E. Ligterink, M. Patrascu, P.C. Breedveld, and S. Stramigioli. An energy-based electroelastic beam model for mems applications. *Sensors and Actuators A: Physical*, 121(2):500–507, June 2005.

[110] S. Liu, A. Davidson, and Q. Lin. Simulation studies on nonlinear dynamics and chaos in a mems cantilever control system. *Journal of Micromechanics and Microengineering*, 14:1064–1073, 2004.

[111] P. W. Loveday and C. A. Rogers. The influence of control system design on the performance of vibratory gyroscopes. *Journal of Sound and Vibration*, 255(3):417–432, 2002.

[112] C. Lu, M. Lemkin, and B. E. Boser. A monolithic surface micromachined accelerometer with digital output. *IEEE Journal of Solid-State Circuits*, 30(12):1367–1373, 1995.

[113] M.S.-C. Lu and G.K. Fedder. Position control of parallel-plate microactuators for probe-based data storage. *IEEE/ASME Journal of Microelectromechanical Systems*, 13(5):759–769, 2004.

[114] H. Luo, G.K. Fedder, and L.R. Carley. A 1 mg lateral cmos-mems accelerometer. In *Proceedings of the IEEE Annual International Conference on MEMS*, pages 502–507, 2000.

[115] D. H. S. Maithripala, B. D. Kawade, J. M. Berg, and W. P. Dayawansa. A general modelling and control framework for electrostatically actuated mechanical systems. *International Journal of Robust and Nonlinear Control*, 15(16):839–857, 2005.

[116] D.H.S. Maithripala, J.M. Berg, and W.P. Dayawansa. Control of an electrostatic microelectromechanical system using static and dynamic output feedback. *Journal of Dynamic Systems, Measurement and Control.*, 127(3):443 – 50, 2005.

[117] D.H.S. Maithripala, B. D. Kawade, J. M. Berg, and W.P. Dayawansa. Passivity-based control of electrostatic mems in the presence of parasitics. In *Proceedings*

of the IEEE Conference on Decision and Control, volume control, parasitics, pages 615–620, San Diego, CA, USA, December 2006.

[118] S. Maithripala. *Nonlinear control of an electrostatically actuated MEMS*. PhD thesis, Texas Tech University, 2003.

[119] S. Malo and R. Griñó. Adaptive feed-forward cancellation control of a full-bridge dc-ac voltage inverter. In *17th IFAC World Congress*, pages 4571–4576, 2008.

[120] R. M'Closkey and A.D. Challoner. Modeling, identification, and control of micro-sensor prototypes. In *Proceedings of the American Control Conference*, volume 1, pages 9–24, 2004.

[121] R. T. M'Closkey, A. Vakakis, and R. Gutierrez. Mode localization induced by a nonlinear control loop. *Nonlinear Dynamics*, 25:221–236, 2001.

[122] R.T. M'Closkey and A. Vakakis. Analysis of a microsensor automatic gain control loop. In *Proceedings of the American Control Conference*, volume 5, pages 3307–3311, 1999.

[123] J. E. Mehner, L. D. Gabbay, and S. D. Senturia. Computer-aided generation of nonlinear reduced-order dynamic macromodels II: Stress-stiffened case. *IEEE/ASME Journal of Microelectromechanical Systems*, 9(2):262–269, 2000.

[124] W. Messner and M. Bodson. Design of adaptive feedforward controllers using internal model equivalence. In *American Control Conference*, volume 2, pages 1619–1623 vol.2, June 1994.

[125] K. Minami, T. Matsunaga, and M. Esashi. Simple modeling and simulation of the squeeze film effect and transient response of the mems device. In *Proceedings of the IEEE Annual International Conference on MEMS*, pages 338–343, 1999.

[126] F. Najar, S. Choura, S. El-Borgi, E. M. Abdel-Rahman, and A. H. Nayfeh. Modeling and design of variable-geometry electrostatic microactuators. *Journal of Micromechanics and Microengineering*, 15(3):419, 2005.

[127] M. Napoli, B. Bamieh, and K. Turner. Mathematical modeling, experimental validation and observer design for a capacitively actuated microcantilever. In *Proceedings of the American Control Conference*, volume 5, pages 3732–3737, 2003.

[128] M. Napoli, B. Bamieh, and K. Turner. A capacitive microcantilever: Modelling, validation, and estimation using current measurements. *Journal of Dynamic Systems, Measurement and Control*, 126(2):319–326, 2004.

[129] M. Napoli, K. Turner, and B. Bamieh. Understanding mechanical domain parametric resonance in microcantilevers. In *Proceedings of the IEEE Annual International Conference on MEMS*, pages 169–172, Kyoto, 2003.

[130] M. Napoli, W. Zhang, K. Turner, and B. Bamieh. Dynamics of mechanically and electrostatically coupled microcantilevers. In *Proceedings of the International Conference on Solid State Sensors and Actuators, TRANSDUCERS*, volume 2, pages 1088–1091, 2003.

[131] H.C. Nathanson, W.E. Newell, R.A. Wickstrom, and J.R. Davis Jr. The resonant gate transistor. *IEEE Transactions on Electron Devices*, 14(3):117–133, 1967.

[132] A. H. Nayfeh and M. I. Younis. A new approach to the modeling and simulation of flexible microstructures under the effect of squeeze-film damping. *Journal of Micromechanics and Microengineering*, 14:170–181, 2004.

[133] A. H. Nayfeh and M. I. Younis. Dynamics of MEMS resonators under superharmonic and subharmonic excitations. *Journal of Micromechanics and Microengineering*, 15(10):1840–1847, 2005.

[134] A. H. Nayfeh, M. I. Younis, and E. M. Abdel-Rahman. Dynamic analysis of MEMS resonators under primary-resonance excitation. In *ASME International Design Engineering Technical Conferences & Computers and Information in Engineering Conference, IDETC/CIE* , volume DETC2005-84146, pages 397–404, 2005.

[135] A. H. Nayfeh, M. I. Younis, and E. M. Abdel-Rahman. Dynamic pull-in phenomenon in MEMS resonators. *Nonlinear Dynamics*, 48:153–163, 2007.

[136] Y. Nemirovsky and O. Bochobza-Degani. A methodology and model for the pull-in parameters of electrostatic actuators. *IEEE/ASME Journal of Microelectromechanical Systems*, 10(4):601–615, 2001.

[137] W.E. Newell. Miniaturization of tuning forks. *Science*, 161(3848):1320–1326, 1968.

[138] C. T.-C. Nguyen. Electromechanical characterization of microresonators for circuit applications. Master's thesis, Dept. of Electrical Engineering and Computer Sciences, University of California at Berkeley, 1991.

[139] H. Nishiyama and M. Nakamura. Capacitance of a strip capacitor. *IEEE Transactions on Components, Hybrids, and Manufacturing Technology*, 13(2):417–423, 1990.

[140] K. Nonaka, T. Sugimoto, J. Baillieul, and M. Horenstein. Bi-directional extension of the travel range of electrostatic actuators by open loop periodically switched oscillatory control. In *Proceedings of the IEEE Conference on Decision and Control*, volume 2, pages 1964–1969, 2004.

[141] Nusawardhana and S.H. Zak. Extremum seeking using analog nonderivative optimizers. In *American Control Conference*, volume 4, pages 3242–3247 vol.4, June 2003.

[142] R. Oboe, R. Antonello, E. Lasalandra, G.S. Durante, and L. Prandi. Control of a z-axis mems vibrational gyroscope. *IEEE/ASME Transactions on Mechatronics*, 10(4):364–370, 2005.

[143] T. Okubo and H. Ohmori. Energy saving by extremum-seeking control using an actuator with adjustable stiffness (AwAS). In *Proceedings of SICE Annual Conference*, pages 1836–1841, Sept 2013.

[144] E. Omidi and S. N. Mahmoodi. Sensitivity analysis of the nonlinear integral positive position feedback and integral resonant controllers on vibration suppression of nonlinear oscillatory systems. *Communications in Nonlinear Science and Numerical Simulation*, 22(13):149 – 166, 2015.

[145] R. Ortega, A.J. Van Der Schaft, I. Mareels, and B. Maschke. Putting energy back in control. *IEEE Control Systems Magazine*, 21(2):18–33, 2001.

[146] C. Painter. *Micromachined Vibratory Gyroscopes with Imperfections*. PhD thesis, University of California, Irvine, 2005.

[147] C. Painter and A.M. Shkel. Micromachined vibratory rate integrating gyroscope, micromachined inertial sensors. Patent. UC Office of Technology Transfer, UC Case No. 2003-135-1, 2003.

[148] C. C. Painter and A. M. Shkel. Active structural error suppression in MEMS vibratory rate integrating gyroscopes. *IEEE Sensors Journal*, 3(5):595–606, 2003.

[149] S. Park. *Adaptative Control Strategies for MEMS Gyroscopes*. PhD thesis, U.C. Berkeley, 2000.

[150] S. Park and R. Horowitz. Adaptive control for the conventional mode of operation of mems gyroscopes. *IEEE/ASME Journal of Microelectromechanical Systems*, 12(1):101–108, 2003.

[151] S. Park and R. Horowitz. New adaptive mode of operation for mems gyroscopes. *Transactions of the ASME*, 126(4):800–810, 2004.

[152] S. Park and R. Horowitz. Discrete time adaptive control for a mems gyroscope. *International Journal of Adaptive Control and Signal Processing*, 19(6):485–503, 2005.

[153] J. A. Pelesko and D. H. Bernstein. *Modeling MEMS and NEMS*. Chapman & Hall/CRC, 2003.

[154] J.A. Pelesko. Electrostatic field aproximations and implications for mems devices. In *Proceedings of ESA*, pages 126–137, 2001.

[155] J.A. Pelesko. Multiple solutions in electrostatic MEMS. In *Proceedings of Modeling and Simulation of Microsystems*, pages 290–293, Hilton Head Island, 2001.

[156] J.A. Pelesko and A.A. Triolo. Nonlocal problems in mems device control. In *Technical Proceedings of the International Conference on Modeling and Simulation of Microsystems*, 2000.

[157] J.A. Pelesko and A.A. Triolo. Nonlocal problems in mems device control. *Journal of Engineering Mathematics*, 41:345–366, 2001.

[158] M. F. Perez Polo and M. Perez Molina. Regular self-oscillating and chaotic behaviour of a pid controlled gimbal suspension gyro. *Chaos, Solitons & Fractals*, 21(5):1057–1074, 2004.

[159] S. Pigg and M. Bodson. Adaptive algorithms for the rejection of sinusoidal disturbances acting on unknown plants. *IEEE Transactions on Control Systems Technology*, 18(4):822–836, July 2010.

[160] D. Piyabongkarn, R. Rajamani, and M. Greminger. The development of a mems gyroscope for absolute angle measurement. *IEEE Transactions on Control Systems Technology*, 13(2):185–195, 2005.

[161] D. Piyabongkarn, Y. Sun, R. Rajamani, A. Sezen, and B.J. Nelson. Travel range extension of a mems electrostatic microactuator. *IEEE Transactions on Control Systems Technology*, 13(1):138–145, 2005.

[162] G.V. Rao and K.K. Raju. Large amplitude free vibrations of beams - an energy approach. *Journal of Applied Mathematics and Mechanics*, 83(7):493 – 498, 2003.

[163] S.S. Rao. *Mechanical Vibrations*. Addison-Wesley, 2nd edition, 1990.

[164] J. F. Rhoads, S. W. Shaw, and K. L. Turner. The nonlinear response of resonant microbeam systems with purely-parametric electrostatic actuation. *Journal of Micromechanics and Microengineering*, 16(5):890–899, 2006.

[165] L. A. Rocha, E. Cretu, and R. F. Wolffenbuttel. Using dynamic voltage drive in a parallel-plate electrostatic actuator for full-gap travel range and positioning. *IEEE/ASME Journal of Microelectromechanical Systems*, 15(1):69–83, February 2006.

[166] L.A. Rocha, E. Cretu, and R.F. Wolffenbuttel. Pull-in dynamics: analysis and modeling of the transitional regime. In *Proceedings of the IEEE Annual International Conference on MEMS*, pages 249–252, 2004.

[167] H. Rodjegard, D. Sandstrom, P. Pelin, M. Carlsson, M. Bohman, N. Hedenstierna, and G.I. Andersson. A novel architecture for digital control of mems gyros. In *Proceedings of IEEE Sensors*, volume 3, pages 1403–1406, 2004.

[168] H. Rodjegard, D. Sandstrom, P. Pelin, N. Hedenstierna, D. Eckerbert, and G.I. Andersson. A digitally controlled mems gyroscope with 3.2 deg/hr stability. In *Proceedings of the International Conference on Solid State Sensors and Actuators, TRANSDUCERS*, volume 1, pages 535–538, 2005.

[169] T. Roessig, A.P. Pisano, R.T. Howe, and J.H. Smith. Surface-micromachined resonant accelerometer. In *Proceedings of the International Conference on Solid State Sensors and Actuators, TRANSDUCERS*, volume 2, pages 859–862, June 1997.

[170] T.A. W. Roessig. *Integrated MEMS Tuning Fork Oscillators for Sensor Applications*. PhD thesis, U.C. Berkeley, 1998.

[171] H. Rong, Q.-A. Huang, M. Nie, and W. Li. An analytical model for pull-in voltage of clamped-clamped multilayer beams. *Sensors and Actuators A: Physical*, 116(1):15–21, October 2004.

[172] M. A. Rosa, D. De Bruyker, A. R. Vlkel, E. Peeters, and J. Dunec. A novel external electrode configuration for the electrostatic actuation of mems based devices. *Journal of Micromechanics and Microengineering*, 14:446–451, 2004.

[173] Y. Sabry, M. Medhat, B. Saadany, A. Safwat, and D. Khalil. Optical characterization technique for mems comb-drive resonators. In *IEEE/LEOS International Conference on Optical MEMS and Nanophotonics*, pages 127–128, Aug 2009.

[174] M. Saif, B. Ebrahimi, and M. Vali. Terminal sliding mode control of z-axis mems gyroscope with observer based rotation rate estimation. In *American Control Conference (ACC), 2011*, pages 3483–3489, June 2011.

[175] A. Salian, H. Kulah, N. Yazdi, G. He, and K. Najafi. Hybrid silicon microaccelerometer system with cmos interface circuit. In *Proceedings of the 43rd IEEE Midwest Symposium on Circuits and Systems*, volume 1, pages 228–231, 2000.

[176] H.S. Sane. Energy-based control for mems with one-sided actuation. In *Proceedings of the American Control Conference*, pages 6–pp, 2006.

[177] H.S. Sane, N. Yazdi, and C.H. Mastrangelo. Application of sliding mode control to electrostatically actuated two-axis gimbaled micromirrors. In *Proceedings of the American Control Conference*, volume 5, pages 3726–3731, 2003.

[178] H.S. Sane, N. Yazdi, and C.H. Mastrangelo. Modified sliding mode control and its application to electrostatically controlled dual-axis micromirrors. In *Proceedings of the American Control Conference*, volume 3, pages 1934–1939, 2004.

[179] E. Saucedo-Flores, R. Ruelas, M. Flores, C. Ying, and C. Jung-chih. Dynamic behavior modeling of MEMS parallel plate capacitors. In *Proceedings of IEEE Position Location and Navigation Symposium, PLANS*, pages 15–19, 2004.

[180] J. I. Seeger and B. E. Boser. Parallel-plate driven oscillations and resonant pull-in. In *Solid-State Sensor, Actuator and Microsystems Workshop, Hilton Head Island*, pages 313–316, 2002.

[181] J.I. Seeger and B.E. Boser. Charge control of parallel-plate, electrostatic actuators and the tip-in instability. *IEEE/ASME Journal of Microelectromechanical Systems*, 12(5):656–671, 2003.

[182] J.I. Seeger and S.B. Crary. Stabilization of electrostatically actuated mechanical devices. In *Proceedings of the International Conference on Solid State Sensors and Actuators, TRANSDUCERS*, volume 2, pages 1133–1136, 1997.

[183] S.D. Senturia. *Microsystem Design*. Kluwer Academic Publishers, 1st edition, 2001.

[184] S.D. Senturia, R.M. Harris, B.P. Johnson, S. Kim, K. Nabors, M.A. Shulman, and J.K. White. A computer-aided design system for microelectromechanical systems (memcad). *IEEE/ASME Journal of Microelectromechanical Systems*, 1(1):3–13, Mar 1992.

[185] F. Shi, P. Ramesh, and S. Mukherjee. Dynamic analysis of micro-electro-mechanical systems. *International Journal for Numerical Methods in Engineering*, 39(24):4119–4139, 1996.

[186] F.A. Shirazi, J.V. Mohammadpour, and K.M. Grigoriadis. An lpv design approach for voltage control of an electrostatic MEMS actuator. *IEEE/ASME Journal of Microelectromechanical Systems*, 20(1):302–311, Feb 2011.

[187] A. Shkel, R. Horowitz, A. Seshia, S. Park, and R. T. Howe. Dynamics and control of micromachined gyroscopes. In *Proceedings of the American Control Conference*, volume 3, pages 2119–2124, 1999.

[188] A. Shkel, R.T. Howe, and R. Horowitz. Modeling and simulation of micromachined gyroscopes in the presence of imperfections. *International Conference on Modeling and Simulation of Microsystems*, pages 605–608, 1999,.

[189] T. Sugimoto, K. Nonaka, and M.N. Horenstein. Bidirectional electrostatic actuator operated with charge control. *IEEE/ASME Journal of Microelectromechanical Systems*, 14(4):718–724, 2005.

[190] W. Sun, J.T.W. Yeow, and Z. Sun. Robust adaptive control of a one degree of freedom electrostatic microelectromechanical systems model with output-error-constrained tracking. *Control Theory Applications, IET*, 6(1):111–119, January 2012.

[191] S. Sung, J. G. Lee, and T. Kang. Development and test of MEMS accelerometer with self-sustatined oscillation loop. *Sensors and Actuators A: Physical*, 109(1):1–8, 2003.

[192] S. Sung, J.G. Lee, T. Kang, and J. W. Song. Development of a tunable resonant accelerometer with self-sustained oscillation loop. In *IEEE National Aerospace and Electronics Conference*, pages 354–361, 2000.

[193] W.-T. Sung, J. G. Lee, J. W. Song, and T. Kang. H-infinity controller design of mems gyroscope and its performance test. In *Proceedings of IEEE Position Location and Navigation Symposium, PLANS*, pages 63–69, 2004.

[194] M.A. Tadayon, M. Rajaei, H. Sayyaadi, G. N. Jazar, and A. Alasty. Nonlinear dynamics of microresonators. *Journal of Physics: Conference Series*, 34:961–966, 2006.

[195] A.R. Teel and D. Popovic. Solving smooth and nonsmooth multivariable extremum seeking problems by the methods of nonlinear programming. In *American Control Conference*, volume 3, pages 2394–2399 vol.3, 2001.

[196] R. Teodorescu, F. Blaabjerg, M. Liserre, and P.C. Loh. Proportional-resonant controllers and filters for grid-connected voltage-source converters. *IEEE Proceedings on Electric Power Applications*, 153(5):750–762, 2006.

[197] H. A. C. Tilmans and R. Legtenberg. Electrostatically driven vacuum-encapsulated polysilicon resonators part II. theory and performance. *Sensors and Actuators A: Physical*, 45:67–84, 1994.

[198] A. Trusov. *Investigation of Factors Affecting Bias Stability and Scale Factor Drifts in Coriolis Vibratory MEMS Gyroscopes*. PhD thesis, University of California Irvine, 2009.

[199] A. A. Trusov. Nonlinear effects in control of capacitive resonant microstructures. Master's thesis, University of california, Irvine, 2006.

[200] A. A. Trusov and A. M. Shkel. Capacitive detection in resonant mems with arbitrary amplitude of motion. *Journal of Micromechanics and Microengineering*, 17(8):1583–1592, 2007.

[201] A.A. Trusov, G. Atikyan, D.M. Rozelle, A.D. Meyer, S.A. Zotov, B.R. Simon, and A.M. Shkel. Force rebalance, whole angle, and self-calibration mechanization of silicon mems quad mass gyro. In *Inertial Sensors and Systems (ISISS), 2014 International Symposium on*, pages 1–2, Feb 2014.

[202] A.A. Trusov and A.M. Shkel. A novel capacitive detection scheme with inherent self-calibration. *IEEE/ASME Journal of Microelectromechanical Systems*, 16(6):1324–1333, Dec 2007.

[203] T.-C. Tsao, Y.-X. Qian, and M. Nemani. Repetitive control for asymptotic tracking of periodic signals with an unknown period. *Journal of Dynamic Systems, Measurement, and Control*, 122(2):364–369, 2000.

[204] M. Varghese, R. Amantea, D. Sauer, and S. D. Senturia. Resistive damping of pulse-sensed capacitive position sensors. In *Proceedings of the International Conference on Solid State Sensors and Actuators, TRANSDUCERS*, volume 2, pages 1121–1124, 1997.

[205] T. Veijola, H. Kuisma, and J. Lahdenper. The influence of gas-surface interaction on gas-film damping in a silicon accelerometer. *Sensors and Actuators A: Physical*, 66(1):83–92, 1998.

[206] T. Veijola, H. Kuisma, J. Lahdenper, and T. Ryhnen. Equivalent-circuit model of the squeezed gas film in a silicon accelerometer. *Sensors and Actuators A: Physical*, 48(3):239–248, 1995.

[207] T. Veijola and M. Turowski. Compact damping models for laterally moving microstructures with gas-rarefaction effects. *IEEE/ASME Journal of Microelectromechanical Systems*, 10(2):263–273, 2001.

[208] R. Y. Vinokur. Feasible analytical solutions for electrostatic parallel-plate actuator or sensor. *Journal of Vibration and Control*, 10(3):359–369, 2002.

[209] C. Wang, H.-H. Yu, M. Wu, and W. Fang. Implementation of phase-locked loop control for MEMS scanning mirror using DSP. *Sensors and Actuators A: Physical*, 133(1):243–249, 2006.

[210] L. D. Wang, J.M. Hornak, L.A. Famouri, and R. P. Ghaffarian. Real-time translational control of a mems comb resonator. *IEEE Transactions on Aerospace and Electronic Systems*, 40(2):567 – 575, April 2004.

[211] P. K. C. Wang. Feedback control of vibrations in a micromachined cantilever beam with electrostatic actuators. *Journal of Sound and Vibration*, 213(3), 1998.

[212] X. Wang, Y. Liu, M. Wang, and X. Chen. The effect of air damping on the planar mems structures. In *Proceeding of the Sixth IEEE CPMT Conference on High Density Microsystem Design and Packaging and Component Failure Analysis, HDP'04*, pages 349–352, 2004.

[213] Y. C. Wang, S. G. Adams, J. S. Thorp, N. C. MacDonald, P. Hartwell, and F. Bertsch. Chaos in MEMS, parameter estimation and its potential application. *IEEE Transactions on Circuits and Systems*, 45(10):1013–1020, 1998.

[214] J. Wu and L.R. Carley. Electromechanical $\Delta\Sigma$ modulation with high-q micromechanical accelerometers and pulse density modulated force feedback. *IEEE Transactions on Circuits and Systems I: Regular Papers*, 53(2):274–287, 2006.

[215] W. C. Xie, H. P. Lee, and S. P. Lim. Nonlinear dynamic analysis of MEMS switches by nonlinear modal analysis. *Nonlinear Dynamics*, 31:243–256, 2003.

[216] M. Yamada, Z. Riadh, and Y. Funahashi. Design of discrete-time repetitive control system for pole placement and application. *IEEE/ASME Transactions on Mechatronics*, 4(2):110–118, 1999.

[217] S. Yamauchi and T. Watanabe. All-digital MEMS tuning-fork self-excited vibration control by phase-relation using TAD-based ADPLL. In *IEEE 13th International New Circuits and Systems Conference (NEWCAS)*, pages 1–4, June 2015.

[218] Y.-J. Yang, M.-A. Gretillat, and S.D. Senturia. Effect of air damping on the dynamics of nonuniform deformations of microstructures. In *Proceedings of the International Conference on Solid State Sensors and Actuators, TRANSDUCERS*, volume 2, pages 1093–1096, 1997.

[219] Y.J. Yang and S.D. Senturia. Numerical simulations of compressible squeezed-film damping. In *Solid-State Sensors and Actuators Workshop, Late News Session*, pages 76–79, 1996.

[220] N. Yazdi, H. Sane, T.D. Kudrle, and C.H. Mastrangelo. Robust sliding-mode control of electrostatic torsional micromirrors beyond the pull-in limit. In *Proceedings of the International Conference on Solid State Sensors and Actuators, TRANSDUCERS*, volume 2, pages 1450–1453, 2003.

[221] B. Y. Yeh, Y. C. Liang, and F. E. H. Tay. Mathematical modelling on the quadrature error of low-rate microgyroscope for aerospace applications. *Analog Integrated Circuits and Signal Processing*, 29(1-2):85–94, 2001.

[222] M. I. Younis and A. H. Nayfeh. A study of the nonlinear response of a resonant microbeam to an electric actuation. *Nonlinear Dynamics*, 31:91–117, 2003.

[223] M.I. Younis, E.M. Abdel-Rahman, and A. H. Nayfeh. A reduced-order model for electrically actuated microbeam-based MEMS. *IEEE/ASME Journal of Microelectromechanical Systems*, 12:672–680, 2003.

[224] M.I. Younis, E.M. Abdel-Rahman, and A. H. Nayfeh. Global dynamics of MEMS resonators under superharmonic excitation. In *Proceedings of the International Conference on MEMS, NANO and Smart Systems*, pages 694–699, 2004.

[225] H. Yu and U. Ozguner. Extremum-seeking control via sliding mode with periodic search signals. In *IEEE Conference on Decision and Control*, volume 1, pages 323–328 vol.1, Dec 2002.

[226] Q. Yuan, B. Peng, W. Luo, J. Zhao, J. Yang, and F. Yang. Frequency stability of rf oscillator with mems-based encapsulated resonator. In *18th International Conference on Solid-State Sensors, Actuators and Microsystems (TRANSDUCERS)*, pages 1969–1972, June 2015.

[227] C. Zhang and R. Ordonez. Numerical optimization-based extremum seeking control of LTI systems. In *IEEE Conference on Decision and Control*, pages 4428–4433, Dec 2005.

[228] C. Zhang and R. Ordonez. Extremum seeking control based on numerical optimization and state regulation - part I: Theory and framework. In *IEEE Conference on Decision and Control*, pages 4466–4471, Dec 2006.

[229] C. Zhang and R. Ordonez. Extremum seeking control based on numerical optimization and state regulation - part II: Robust and adaptive control design. In *IEEE Conference on Decision and Control*, pages 4460–4465, Dec 2006.

[230] C. Zhang and R. Ordonez. Numerical optimization-based extremum seeking control with application to ABS design. *IEEE Transactions on Automatic Control*, 52(3):454–467, March 2007.

[231] W. Zhang, R. Baskaran, and K.L. Turner. Effect of cubic nonlinearity on auto-parametrically amplified resonant mems mass sensor. *Sensors and Actuators A: Physical*, 102:139–150, 2002.

[232] H. Zhao. *Passive, Iterative, and Repetitive Control for Flexible Distributed Parameter Systems*. PhD thesis, The Pennsylvania State University, 2005.

[233] X. Zhao, C. K. Redd, and A. H. Nayfeh. Nonlinear dynamics of an electrically driven impact microactuator. *Nonlinear Dynamics*, 40(3):227–239, 2005.

[234] Y. Zhao, F. E.H. Tay, G. Zhou, and F. S. Chau. Fast and precise positioning of electrostatically actuated dual-axis micromirror by multi-loop digital control. *Sensors and Actuators A: Physical*, 132(2):421–428, November 2006.

[235] K. Zhou and J. C. Doyle. *Essentials Of Robust Control*. Prentice Hall, 1997.

[236] Y.-H. Zhou and X. Yang. Numerical analysis on snapping induced by electromechanical interaction of shuffling actuator with nonlinear plate. *Computers and Structures*, 81:255–264, 2003.

[237] G. Zhu, J. Levine, and L. Praly. Improving the performance of an electrostatically actuated mems by nonlinear control: Some advances and comparisons. In *Proceedings of the IEEE Conference on Decision and Control*, pages 7534–7539, 2005.

[238] G. Zhu, J. Levine, and L. Praly. On the differential flatness and control of electrostatically actuated MEMS. In *Proceedings of the American Control Conference*, pages 2493–2498, 2005.

[239] G. Zhu, J. Penet, and L. Saydy. Robust control of an electrostatically actuated mems in the presence of parasitics and parametric uncertainties. In *Proceedings of the American Control Conference*, pages 6–pp, 2006.

[240] G. Zhu, L. Saydy, M. Hosseini, J.-F. Chianetta, and Y.-A. Peter. A robustness approach for handling modeling errors in parallel-plate electrostatic mems control. *IEEE/ASME Journal of Microelectromechanical Systems*, 17(6):1302–1314, Dec 2008.

[241] H. Zhu, Z. Jin, S. Hu, and Y. Liu. Constant-frequency oscillation control for vibratory micro-machined gyroscopes. *Sensors and Actuators A: Physical*, 193(0):193 – 200, 2013.

[242] V.F. Zhuravlev. Oscillation shape control in resonant systems. *Journal of Applied Mathematics and Mechanics*, 56(5):827–836, 1992.

[243] V.F. Zhuravlev. Global evolution of state of the generalized foucault pendulum. *Mechanics of Solids*, 33(6):1–6, 1998.

[244] A. C. Zolotas, A. Tzes, and M. Vagia. Robust control design for an uncertain electrostatic micro-mechanical system via loop shaping. In *Proceedings of the European Control Conference*, pages 389–394, 2007.

[245] Z.-X. Zou, K. Zhou, Z. Wang, and M. Cheng. Frequency-adaptive fractional-order repetitive control of shunt active power filters. *IEEE Transactions on Industrial Electronics*, 62(3):1659–1668, March 2015.

Appendix A

Harmonic Balance formulations

In this Appendix, the development of the set of equations including the second harmonic in the oscillation response are presented. These formulations complement the ones presented in Chapter 4.

In both cases, the system evolution is assumed to be composed of the natural frequency and the second harmonic

$$\begin{aligned} g(t) &= G_0 + G_1 \sin(\omega\, t + \phi_1) + G_2 \sin(2\,\omega\, t + \phi_2) \\ &= \breve{G}_0 + \breve{G}_1 e^{j\omega t} + \breve{G}_{-1} e^{-j\omega t} + \breve{G}_2 e^{j2\omega t} + \breve{G}_{-2} e^{-j2\omega t} \end{aligned} \tag{A.1}$$

where $\breve{G}_0 = G_0$, $\breve{G}_1 = \frac{G_1}{2j}\, e^{j\,\phi_1}$, $\breve{G}_2 = \frac{G_2}{2j}\, e^{j\,\phi_2}$, $\breve{G}_{-1} = \overline{\breve{G}_1}$ and $\breve{G}_{-2} = \overline{\breve{G}_2}$.

A.1 Linear case - second harmonic

The complete set of equations is as follows:

$$\begin{aligned} \beta_0 =& \frac{1}{\mathrm{f}_k \mathrm{g}_k}\Big(-\omega_\mathrm{n}^2 \breve{G}_0^3 + \omega_\mathrm{n}^2 \breve{G}_0^2 + \big(4\omega^2 - 6\omega_\mathrm{n}^2\big)|\breve{G}_1|^2 \breve{G}_0 + 2\omega_\mathrm{n}^2 |\breve{G}_1|^2\Big) \\ &+ \frac{1}{\mathrm{f}_k \mathrm{g}_k}\Big(\big(16\omega^2 - 6\omega_\mathrm{n}^2\big)|\breve{G}_2|^2 \breve{G}_0 + 2\omega_\mathrm{n}^2 |\breve{G}_2|^2 + \big(6\omega^2 - 3\omega_\mathrm{n}^2\big)\breve{G}_1^2 \overline{\breve{G}_2} + \big(6\omega^2 - 3\omega_\mathrm{n}^2\big)\overline{\breve{G}_1}^2 \breve{G}_2\Big) \\ \beta_1 =& \frac{1}{\mathrm{f}_k \mathrm{g}_k}\Big(\big(3\omega^2 - j\frac{\omega_\mathrm{n}}{\mathrm{Q}}\omega - 3\omega_\mathrm{n}^2\big)|\breve{G}_1|^2 + \big(\omega^2 - j\frac{\omega_\mathrm{n}}{\mathrm{Q}}\omega - 3\omega_\mathrm{n}^2\big)\breve{G}_0^2 + 2\omega_\mathrm{n}^2 \breve{G}_0\Big)\breve{G}_1 \\ &+ \frac{1}{\mathrm{f}_k \mathrm{g}_k}\Big(\big(18\omega^2 - 2j\frac{\omega_\mathrm{n}}{\mathrm{Q}}\omega - 6\omega_\mathrm{n}^2\big)\overline{\breve{G}_2}\breve{G}_1 + \big(10\omega^2 - 2j\frac{\omega_\mathrm{n}}{\mathrm{Q}}\omega - 6\omega_\mathrm{n}^2\big)\breve{G}_0 \overline{\breve{G}_1} + 2\omega_\mathrm{n}^2 \overline{\breve{G}_1}\Big)\breve{G}_2 \\ \beta_2 =& \frac{1}{\mathrm{f}_k \mathrm{g}_k}\Big(\big(2\omega^2 - 2j\frac{\omega_\mathrm{n}}{\mathrm{Q}}\omega - 3\omega_\mathrm{n}^2\big)\breve{G}_0 + \omega_\mathrm{n}^2\Big)\breve{G}_1^2 + \frac{1}{\mathrm{f}_k \mathrm{g}_k}\Big(\big(12\omega^2 - 2j\frac{\omega_\mathrm{n}}{\mathrm{Q}}\omega - 3\omega_\mathrm{n}^2\big)|\breve{G}_2|^2\Big)\breve{G}_2 \\ &+ \frac{1}{\mathrm{f}_k \mathrm{g}_k}\Big(\big(12\omega^2 - 4j\frac{\omega_\mathrm{n}}{\mathrm{Q}}\omega - 6\omega_\mathrm{n}^2\big)|\breve{G}_1|^2 + \big(4\omega^2 - 2j\frac{\omega_\mathrm{n}}{\mathrm{Q}}\omega - 3\omega_\mathrm{n}^2\big)\breve{G}_0^2 + 2\omega_\mathrm{n}^2 \breve{G}_0\Big)\breve{G}_2 \end{aligned}$$

$$
\begin{aligned}
\beta_3 =& \frac{1}{\mathrm{f}_k \mathrm{g}_k}\big(\omega^2 - j\frac{\omega_\mathrm{n}}{\mathrm{Q}}\omega - \omega_\mathrm{n}^2\big)\breve{G}_1^3 \\
&+ \frac{1}{\mathrm{f}_k \mathrm{g}_k}\Big(\big(9\omega^2 - 3j\frac{\omega_\mathrm{n}}{\mathrm{Q}}\omega - 3\omega_\mathrm{n}^2\big)\breve{G}_2\overline{\breve{G}_1} + \big(10\omega^2 - 6j\frac{\omega_\mathrm{n}}{\mathrm{Q}}\omega - 6\omega_\mathrm{n}^2\big)\breve{G}_0\breve{G}_1 + 2\omega_\mathrm{n}^2\breve{G}_1\Big)\breve{G}_2 \\
\beta_4 =& \frac{1}{\mathrm{f}_k \mathrm{g}_k}\Big(\big(8\omega^2 - 4j\frac{\omega_\mathrm{n}}{\mathrm{Q}}\omega - 3\omega_\mathrm{n}^2\big)\breve{G}_2\breve{G}_0 + \big(6\omega^2 - 4j\frac{\omega_\mathrm{n}}{\mathrm{Q}}\omega - 3\omega_\mathrm{n}^2\big)\breve{G}_1^2 + \omega_\mathrm{n}^2\breve{G}_2\Big)\breve{G}_2 \\
\beta_5 =& \frac{1}{\mathrm{f}_k \mathrm{g}_k}\big(9\omega^2 - 5j\frac{\omega_\mathrm{n}}{\mathrm{Q}}\omega - 3\omega_\mathrm{n}^2\big)\breve{G}_1\breve{G}_2^2 \\
\beta_6 =& \frac{1}{\mathrm{f}_k \mathrm{g}_k}\big(4\omega^2 - 2j\frac{\omega_\mathrm{n}}{\mathrm{Q}}\omega - \omega_\mathrm{n}^2\big)\breve{G}_2^3
\end{aligned}
$$

A.2 Nonlinear case - second harmonic

The complete set of equations is as follows:

$$
\begin{aligned}
\beta_0 =& \frac{1}{\mathrm{f}_k \mathrm{g}_k}\Big(-\omega_\mathrm{n}^2\breve{G}_0^3 + \omega_\mathrm{n}^2\breve{G}_0^2 + \big(4\omega^2 - 6\omega_\mathrm{n}^2\big)|\breve{G}_1|^2\breve{G}_0 + 2\omega_\mathrm{n}^2|\breve{G}_1|^2\Big) \\
&+ \frac{1}{\mathrm{f}_k \mathrm{g}_k}\Big(\big(16\omega^2 - 6\omega_\mathrm{n}^2\big)|\breve{G}_2|^2\breve{G}_0 + 2\omega_\mathrm{n}^2|\breve{G}_2|^2 + \big(6\omega^2 - 3\omega_\mathrm{n}^2\big)\breve{G}_1^2\overline{\breve{G}_2} + \big(6\omega^2 - 3\omega_\mathrm{n}^2\big)\overline{\breve{G}_1}^2\breve{G}_2\Big) \\
&+ \frac{\kappa}{\mathrm{f}_k \mathrm{g}_k}\Big(\big(-\breve{G}_0^5 + 3\breve{G}_0^4 - 3\breve{G}_0^3 + \breve{G}_0^2\big) + \big(-120\breve{G}_0 + 72\big)|\breve{G}_1|^2|\breve{G}_2|^2\Big) \\
&+ \frac{\kappa}{\mathrm{f}_k \mathrm{g}_k}\Big(\big(-30\breve{G}_0 + 18\big)|\breve{G}_1|^4 + \big(-20\breve{G}_0^3 + 36\breve{G}_0^2 - 18\breve{G}_0 + 2\big)|\breve{G}_1|^2\Big) \\
&+ \frac{\kappa}{\mathrm{f}_k \mathrm{g}_k}\Big(\big(-30\breve{G}_0 + 18\big)|\breve{G}_2|^4 + \big(-20\breve{G}_0^3 + 36\breve{G}_0^2 - 18\breve{G}_0 + 2\big)|\breve{G}_2|^2\Big) \\
&+ \frac{\kappa}{\mathrm{f}_k \mathrm{g}_k}\big(-30|\breve{G}_2|^2 - 20|\breve{G}_1|^2 - 30\breve{G}_0^2 + 36\breve{G}_0 - 9\big)\breve{G}_1^2\overline{\breve{G}_2} \\
&+ \frac{\kappa}{\mathrm{f}_k \mathrm{g}_k}\big(-30|\breve{G}_2|^2 - 20|\breve{G}_1|^2 - 30\breve{G}_0^2 + 36\breve{G}_0 - 9\big)\overline{\breve{G}_1}^2\breve{G}_2 \\
\beta_1 =& \frac{1}{\mathrm{f}_k \mathrm{g}_k}\Big(\big(3\omega^2 - j\frac{\omega_\mathrm{n}}{\mathrm{Q}}\omega - 3\omega_\mathrm{n}^2\big)|\breve{G}_1|^2 + \big(\omega^2 - j\frac{\omega_\mathrm{n}}{\mathrm{Q}}\omega - 3\omega_\mathrm{n}^2\big)\breve{G}_0^2 + 2\omega_\mathrm{n}^2\breve{G}_0\Big)\breve{G}_1 \\
&+ \frac{1}{\mathrm{f}_k \mathrm{g}_k}\Big(\big(18\omega^2 - 2j\frac{\omega_\mathrm{n}}{\mathrm{Q}}\omega - 6\omega_\mathrm{n}^2\big)\overline{\breve{G}_2}\breve{G}_1 + \big(10\omega^2 - 2j\frac{\omega_\mathrm{n}}{\mathrm{Q}}\omega - 6\omega_\mathrm{n}^2\big)\breve{G}_0\overline{\breve{G}_1} + 2\omega_\mathrm{n}^2\overline{\breve{G}_1}\Big)\breve{G}_2 \\
&+ \frac{\kappa}{\mathrm{f}_k \mathrm{g}_k}\Big(\big(-48|\breve{G}_2|^2 - 60|\breve{G}_1|^2 - 60\breve{G}_0^2\breve{G}_0 + 72\big)|\breve{G}_2|^2 + \big(-10|\breve{G}_1|^2 - 30\breve{G}_0^2 + 36\breve{G}_0 - 9\big)|\breve{G}_1|^2\Big)\breve{G}_1 \\
&+ \frac{\kappa}{\mathrm{f}_k \mathrm{g}_k}\Big(\big(-5\breve{G}_0^4 + 12\breve{G}_0^3 - 9\breve{G}_0^2 + 2\breve{G}_0\big)\breve{G}_1 + \big(-20\breve{G}_0 + 12\big)\breve{G}_1^3\overline{\breve{G}_2} - 10\overline{\breve{G}_1}^3\breve{G}_2^2\Big) \\
&+ \frac{\kappa}{\mathrm{f}_k \mathrm{g}_k}\Big(\big(-60\breve{G}_0 + 36\big)|\breve{G}_2|^2 + \big(-60\breve{G}_0 + 36\big)|\breve{G}_1|^2 - 20\breve{G}_0^3 + 36\breve{G}_0^2 - 18\breve{G}_0 + 2\Big)\overline{\breve{G}_1}\breve{G}_2
\end{aligned}
$$

$$
\begin{aligned}
\beta_2 =& \frac{1}{\mathrm{f}_k \mathrm{g}_k}\Big(\big(2\omega^2 - 2j\frac{\omega_\mathrm{n}}{\mathrm{Q}}\omega - 3\omega_\mathrm{n}^2\big)\breve{G}_0 + \omega_\mathrm{n}^2\Big)\breve{G}_1^2 + \frac{1}{\mathrm{f}_k \mathrm{g}_k}\Big(\big(12\omega^2 - 2j\frac{\omega_\mathrm{n}}{\mathrm{Q}}\omega - 3\omega_\mathrm{n}^2\big)|\breve{G}_2|^2\Big)\breve{G}_2 \\
&+ \frac{1}{\mathrm{f}_k \mathrm{g}_k}\Big(\big(12\omega^2 - 4j\frac{\omega_\mathrm{n}}{\mathrm{Q}}\omega - 6\omega_\mathrm{n}^2\big)|\breve{G}_1|^2 + \big(4\omega^2 - 2j\frac{\omega_\mathrm{n}}{\mathrm{Q}}\omega - 3\omega_\mathrm{n}^2\big)\breve{G}_0^2 + 2\omega_\mathrm{n}^2\breve{G}_0\Big)\breve{G}_2 \\
&+ \frac{\kappa}{\mathrm{f}_k \mathrm{g}_k}\big(-10|\breve{G}_2|^2 - 60|\breve{G}_1|^2 - 30\breve{G}_0^2 + 36\breve{G}_0 - 9\big)|\breve{G}_2|^2\breve{G}_2 \\
&+ \frac{\kappa}{\mathrm{f}_k \mathrm{g}_k}\big(-30|\breve{G}_1|^2 - 60\breve{G}_0^2 + 72\breve{G}_0 - 18\big)|\breve{G}_1|^2\breve{G}_2 \\
&+ \frac{\kappa}{\mathrm{f}_k \mathrm{g}_k}\big(-20|\breve{G}_1|^2\breve{G}_0 - 9\breve{G}_0 - 60|\breve{G}_2|^2\breve{G}_0 - 10\breve{G}_0^3 + 18\breve{G}_0^2 + 36|\breve{G}_2|^2 + 12|\breve{G}_1|^2 + 1\big)\breve{G}_1^2 \\
&+ \frac{\kappa}{\mathrm{f}_k \mathrm{g}_k}\Big(-5\overline{\breve{G}_2}\breve{G}_1^4 + \big(-5\breve{G}_0^4 + 12\breve{G}_0^3 - 9\breve{G}_0^2 + 2\breve{G}_0\big)\breve{G}_2 + \big(-30\breve{G}_0 + 18\big)\overline{\breve{G}_1}^2\breve{G}_2^2\Big) \\
\beta_3 =& \frac{1}{\mathrm{f}_k \mathrm{g}_k}\big(\omega^2 - j\frac{\omega_\mathrm{n}}{\mathrm{Q}}\omega - \omega_\mathrm{n}^2\big)\breve{G}_1^3 + \frac{1}{\mathrm{f}_k \mathrm{g}_k}\Big(\big(10\omega^2 - 6j\frac{\omega_\mathrm{n}}{\mathrm{Q}}\omega - 6\omega_\mathrm{n}^2\big)\breve{G}_0 + 2\omega_\mathrm{n}^2\Big)\breve{G}_1\breve{G}_2 \\
&+ \frac{1}{\mathrm{f}_k \mathrm{g}_k}\big(9\omega^2 - 3j\frac{\omega_\mathrm{n}}{\mathrm{Q}}\omega - 3\omega_\mathrm{n}^2\big)\overline{\breve{G}_1}\breve{G}_2^2 + \frac{\kappa}{\mathrm{f}_k \mathrm{g}_k}\Big(-20|\breve{G}_2|^2 - 30|\breve{G}_1|^2 - 30\breve{G}_0^2 + 36\breve{G}_0 - 9\Big)\overline{\breve{G}_1}\breve{G}_2^2 \\
&+ \frac{\kappa}{\mathrm{f}_k \mathrm{g}_k}\big(+36|\breve{G}_2|^2 - 60\breve{G}_0|\breve{G}_2|^2 + 36|\breve{G}_1|^2 - 60\breve{G}_0|\breve{G}_1|^2 - 20\breve{G}_0^3 + 36\breve{G}_0^2 - 18\breve{G}_0 + 2\big)\breve{G}_1\breve{G}_2 \\
&+ \frac{\kappa}{\mathrm{f}_k \mathrm{g}_k}\big(-20|\breve{G}_2|^2 - 5|\breve{G}_1|^2 - 10\breve{G}_0^2 + 12\breve{G}_0 - 3\big)\breve{G}_1^3 \\
\beta_4 =& \frac{1}{\mathrm{f}_k \mathrm{g}_k}\Big(\big(8\omega^2 - 4j\frac{\omega_\mathrm{n}}{\mathrm{Q}}\omega - 3\omega_\mathrm{n}^2\big)\breve{G}_2\breve{G}_0 + \big(6\omega^2 - 4j\frac{\omega_\mathrm{n}}{\mathrm{Q}}\omega - 3\omega_\mathrm{n}^2\big)\breve{G}_1^2 + \omega_\mathrm{n}^2\breve{G}_2\Big)\breve{G}_2 \\
&+ \frac{\kappa}{\mathrm{f}_k \mathrm{g}_k}\Big(-10\overline{\breve{G}_1}^2\breve{G}_2^3 + \big(-30|\breve{G}_2|^2 - 20|\breve{G}_1|^2 - 30\breve{G}_0^2 - 9 + 36\breve{G}_0\big)\breve{G}_1^2\breve{G}_2 + \big(-5\breve{G}_0 + 3\big)\breve{G}_1^4\Big) \\
&+ \frac{\kappa}{\mathrm{f}_k \mathrm{g}_k}\big(12|\breve{G}_2|^2 - 20|\breve{G}_2|^2\breve{G}_0 + 36|\breve{G}_1|^2 - 60\overline{\breve{G}_1}^2\breve{G}_0 - 10\breve{G}_0^3 + 18\breve{G}_0^2 - 9\breve{G}_0 + 1\big)\breve{G}_2^2 \\
\beta_5 =& \frac{1}{\mathrm{f}_k \mathrm{g}_k}\big(9\omega^2 - 5j\frac{\omega_\mathrm{n}}{\mathrm{Q}}\omega - 3\omega_\mathrm{n}^2\big)\breve{G}_1\breve{G}_2^2 + \frac{\kappa}{\mathrm{f}_k \mathrm{g}_k}\big(-20|\breve{G}_2|^2 - 30|\breve{G}_1|^2 - 30\breve{G}_0^2 + 36\breve{G}_0 - 9\big)\breve{G}_1\breve{G}_2^2 \\
&+ \frac{\kappa}{\mathrm{f}_k \mathrm{g}_k}\Big(\big(-20\breve{G}_0 + 12\big)\overline{\breve{G}_1}\breve{G}_2^3 + \big(-20\breve{G}_0 + 12\big)\breve{G}_1^3\breve{G}_2 - \breve{G}_1^5\Big) \\
\beta_6 =& \frac{1}{\mathrm{f}_k \mathrm{g}_k}\big(4\omega^2 - 2j\frac{\omega_\mathrm{n}}{\mathrm{Q}}\omega - \omega_\mathrm{n}^2\big)\breve{G}_2^3 + \frac{\kappa}{\mathrm{f}_k \mathrm{g}_k}\big(-5|\breve{G}_2|^2 - 20|\breve{G}_1|^2 - 10\breve{G}_0^2 + 12\breve{G}_0 - 3\big)\breve{G}_2^3 \\
&+ \frac{\kappa}{\mathrm{f}_k \mathrm{g}_k}\Big(\big(-30\breve{G}_0 + 18\big)\breve{G}_1^2\breve{G}_2^2 - 5\breve{G}_1^4\breve{G}_2\Big) \\
\beta_7 =& \frac{\kappa}{\mathrm{f}_k \mathrm{g}_k}\Big(-5\overline{\breve{G}_1}\breve{G}_2^4 + \big(-20\breve{G}_1\breve{G}_0 + 12\breve{G}_1\big)\breve{G}_2^3 - 10\breve{G}_1^3\breve{G}_2^2\Big) \\
\beta_8 =& \frac{\kappa}{\mathrm{f}_k \mathrm{g}_k}\Big(\big(-5\breve{G}_0 + 3\big)\breve{G}_2^4 - 10\breve{G}_1^2\breve{G}_2^3\Big) \\
\beta_9 =& -\frac{5\kappa}{\mathrm{f}_k \mathrm{g}_k}\breve{G}_1\,\breve{G}_2^4 \\
\beta_{10} =& -\frac{\kappa}{\mathrm{f}_k \mathrm{g}_k}\breve{G}_2^5
\end{aligned}
$$